

**Influence of Energy Input in Friction Stir Welding
on Structure Evolution and Mechanical Behaviour
of Precipitation-Hardening in Aluminium Alloys
(AA2024-T351, AA6013-T6 and Al-Mg-Sc)**

(Von der Fakultät für Maschinenbau der Ruhr-Universität Bochum als
Dissertation angenommene Arbeit)

Author:
C. A. Weis Olea

wissen
schafft
nutzen

GKSS 2008/8

**Influence of Energy Input in Friction Stir Welding
on Structure Evolution and Mechanical Behaviour
of Precipitation-Hardening in Aluminium Alloys
(AA2024-T351, AA6013-T6 and Al-Mg-Sc)**

(Von der Fakultät für Maschinenbau der Ruhr-Universität Bochum als
Dissertation angenommene Arbeit)

Author:

C. A. Weis Olea

(Institute of Materials Research)

Die Berichte der GKSS werden kostenlos abgegeben.
The delivery of the GKSS reports is free of charge.

Anforderungen/Requests:

GKSS-Forschungszentrum Geesthacht GmbH
Bibliothek/Library
Postfach 11 60
21494 Geesthacht
Germany
Fax.: +49 04152 87 17 17

Als Manuskript vervielfältigt.
Für diesen Bericht behalten wir uns alle Rechte vor.

ISSN 0344-9629

GKSS-Forschungszentrum Geesthacht GmbH · Telefon (04152) 87-0
Max-Planck-Straße 1 · 21502 Geesthacht / Postfach 11 60 · 21494 Geesthacht

GKSS 2008/8

Influence of Energy Input in Friction Stir Welding on Structure Evolution and Mechanical Behaviour of Precipitation-Hardening in Aluminium Alloys (AA2024-T351, AA6013-T6 and Al-Mg-Sc)

(Von der Fakultät für Maschinenbau der Ruhr-Universität Bochum als Dissertation angenommene Arbeit)

Cesar Afonso Weis Olea

156 pages with 78 figures and 10 tables

Abstract

Aluminium alloys AA2024 T351, AA6013 T6 and the recently developed Al-Mg-Sc for aircraft industry applications, which are usually considered difficult to weld by conventional fusion welding processes, demonstrate outstanding performance when joined by friction stir welding (FSW). The main feature of the process is to produce solid-state welds, where the maximum temperatures attained during the process are about 80 % that of the melting temperature of the base material. The process generates substantial plastic deformation, due to the solid-state stirring, and consequently creates a high dislocation density, which is a precursor to dynamic recrystallization, a metallurgical feature that characterizes the stir zone (weld centre). A relevant aspect considered, regarding precipitation-hardening aluminium alloys, is the deterioration of the mechanical properties in the weld zones, which are fundamentally attributed to changes in the characteristics of strengthening precipitates. Among the strengthening mechanisms acting in these aluminium alloys, the most important is basically dependent on the morphology, size and population of the precipitates. The thermal cycle and deformation generated during the FSW process alter the precipitation characteristics previously present in the base material. FSW input energy regulates the magnitude of the thermal cycle and the intensity of deformation taking place during the process, and it can be controlled by the welding parameters, affecting the precipitates evolution and consequently the mechanical properties of the joint. Nevertheless, there remains a lack of knowledge about the substructural evolution of these alloys during FSW, and its correlation with weld energy input and their respective mechanical properties, particularly for the Al-Mg-Sc alloy. The main objective of this work is to explain the micro and substructural evolution (emphasizing precipitates evolution) of AA2024-T351, AA6013-T6 and Al-Mg-Sc alloys in similar friction stir welded joints, produced using different weld energy inputs. In addition, it is intended to establish the microstructure/properties/weld energy input relationships of the resultant joints, in order to understand the precipitates evolution and its consequences. Metallurgical characterization of the base material and welded joints was performed using optical microscopy and scanning and transmission electron microscopy. Mechanical assessment was carried out using microhardness, conventional flat tensile and microflat tensile testing. Microstructural investigation of the friction stir welded joints showed similar weld zone formation (heat affected zone – HAZ, thermomechanical affected zone – TMAZ, and stir zone – SZ) for the different Al alloys, but presented specific precipitation features, according to weld zone and energy input. In the case of Al-Mg-Sc joints, Al₃Sc precipitates present in the base material were very stable and the thermal cycle produced during welding was not able to significantly deteriorate the strengthening effect, as evidenced by mechanical testing. The Al-Mg-Sc joints presented, in general, a similar mechanical behaviour to the base material. Strengthening precipitates S'' type and Guinier Preston Bagariastkij (GPB) zones, previously present in the base material of AA2024 T351 joints were dissolved in the SZ and coarse round-type precipitates were found. In the TMAZ, overaging was observed with rod and lath-type precipitates beyond precipitate free zones, which resulted in deteriorated mechanical properties in this region. Joints in AA2024 T351 showed a loss of strength in the TMAZ of up to 30 %, compared to the base material. In AA6013 T6 joints, needle-type β'' precipitates (Mg-Si) were fully dissolved in the SZ. TMAZ was characterized essentially by lath-type Q' (Mg-Si-Cu) precipitates and particularly rod-type precipitates for the lower heat inputs, beyond the presence of dispersoids. Such precipitate dissolution and coarsening along the weld zones resulted in significant material softening. Joints in AA6013 T6 showed an average loss of strength of approximately 48 %, compared to the base material.

Einfluss der durch das Reibrührschweißen eingebrachten Energie auf die strukturelle Entwicklung und das mechanische Verhältnis der Ausscheidungshärtung in Aluminiumlegierungen (AA2024-T351, AA6013-T6 und Al-Mg-Sc)

Zusammenfassung

Aluminiumlegierungen AA2024 T351, AA6013 T6 und die neue, für die Luftfahrtindustrie entwickelte Legierung Al-Mg-Sc, welche durch konventionelles Reibschweißen eine begrenzte Schweißbarkeit haben, zeigen eine außergewöhnliche Leistung beim Reibrührschweißen. Da der Prozess ein Festphasenschweißverfahren ist, erreichen die maximalen Temperaturen lediglich bis zu 80 % des Schmelzpunktes des Grundmaterials. Durch das Rühren in der Festphase generiert der Prozess eine erhebliche plastische Verformung und infolgedessen eine hohe Versetzungsdichte, welche dynamische Rekristallisation verursacht, die ein metallurgisches Merkmal der Rührzone ist. Bei ausscheidungsgehärteten Aluminiumlegierungen, ist eine Verschlechterung der mechanischen Eigenschaften in der Schweißnaht zu sehen, die grundsätzlich mit den Merkmalen der Verfestigungsteilchen korreliert. Unter den in Aluminiumlegierungen wirkenden Aushärtungsmechanismen ist der, welcher von Morphologie, Größe und Dichte der Ausscheidungen abhängig ist, am wichtigsten. Der Temperaturzyklus und die Verformung ändern während des Reibrührschweißvorgangs die Merkmale der im Grundmaterial vorliegenden Verfestigungsteilchen. Die durch das Reibrührschweißen generierte Energieeinbringung, die die Entwicklung der Ausscheidungen und infolgedessen die mechanischen Eigenschaften der Verbindung bestimmt, reguliert den Temperaturzyklus, die Verformungsintensität und kann durch die Schweißparameter kontrolliert werden. Dennoch ist die substrukturelle Entwicklung dieser Legierung während des Schweißens sowie deren Korrelationen mit Energieeinbringung und die infolgedessen mechanischen Eigenschaften noch nicht komplett geklärt worden, vor allem für Al-Mg-Sc-Legierungen. Das Hauptziel dieser Arbeit ist die Erklärung der mikro- und substrukturelle Entwicklung von AA2024-T351-, AA6013-T6- und Al-Mg-Sc-Legierungen in artgleich reibrührgeschweißten Verbindungen, die mit unterschiedlichen Energieeinbringungen hergestellt wurden. Zusätzlich wurden die Beziehungen zwischen Mikrostruktur/Eigenschaften/Energieeinbringungen untersucht, um die Entwicklung der Ausscheidungen sowie deren Folgen besser verstehen zu können. Die metallurgische Charakterisierung des Grundmaterials und der geschweißten Verbindungen wurden mittels Licht-, Raster und Transmissionselektronenmikroskop durchgeführt. Die mechanischen Eigenschaften wurden mittels Mikrohärtprüfung, Flach- und Mikroflachzugproben bestimmt. Mikrostrukturelle Untersuchungen reibrührgeschweißter Verbindungen zeigten eine ähnliche Ausbildung der Schweißnaht (Wärme beeinflusste Zone – WBZ, Thermomechanische beeinflusste Zone – TMBZ und Rührzone – RZ) der verschiedenen Al-Legierungen, stellen aber spezifische Ausscheidungsmerkmale abhängig von Schweißzone und Energieeinbringung dar. In Al-Mg-Sc-Verbindungen, waren die im Grundmaterial enthaltenen Al₃Sc-Ausscheidungen sehr stabil, und der während des Schweißens induzierte Temperaturzyklus war nicht in der Lage, den Verfestigungseffekt negativ zu beeinflussen, wie schon durch die mechanische Charakterisierung festgestellt wurde. Al-Mg-Sc-Verbindungen zeigten vergleichbare mechanische Eigenschaften im Vergleich zum Grundwerkstoff. S''-Ausscheidungen und Guinier Preston Bagariastkij (GPB)-Zonen, die ursprünglich im AA2024 T351-Mikrogefüge beobachtet wurden, wurden in der Rührzone aufgelöst, und grobe rundliche Ausscheidungen wurden gefunden. In der TMBZ wurde eine Überalterung mit stab- und lattenförmigen Ausscheidungen hinter ausscheidungsfreien Zonen beobachtet, was zu verschlechterten mechanischen Eigenschaften in dieser Region führte. Die AA2024 T351-Verbindungen zeigten in der TMBZ im Vergleich zum Grundwerkstoff einen Abfall der Festigkeit um bis zu 30 %. In den AA6013 T6-Verbindungen waren nadelförmige Typ β'' -Ausscheidungen (Mg-Si) vollständig in der RZ gelöst. Die TMBZ war weitgehend durch lattenförmige Q' (Mg-Si-Cu)-Ausscheidungen und teilweise stabförmige Ausscheidungen für die niedrigeren Streckenenergien neben dem Vorhandensein von Dispersoiden gekennzeichnet. Diese Ausscheidungsauflösung und -vergrößerung entlang der Schweißzonen führte zu einer signifikanten Entfestigung der Struktur. Verbindungen in AA6013 T6 zeigten, verglichen mit dem Grundwerkstoff, einen durchschnittlichen Festigkeitsabfall von annähernd 48 %.

ACKNOWLEDGEMENTS

I would like to thank Prof. Dr. Anke Pyzalla and Prof. Dr. Norbert Huber for the supervision of this work and important contributions.

I would like to thank GKSS Forschungszentrum GmbH for giving me the opportunity to develop and perform this work, particularly to the Head of the WMP department, Dr. Jorge Fernandez dos Santos for the valuable support exerted during the developing of my work.

I would like to acknowledge Dipl.-Ing. Rudolf Zettler and Dr. Silvia Lomolino for their valuable contributions to the progress of this work and for their relevant discussions and support during development of this investigation.

I would like to acknowledge Mr. Uwe Lorenz for the important assistance during the use of GKSS electron microscopy facilities. I would like also to thank Mrs. Roisina from TUHH for the support during the TEM samples preparation.

Many thanks to Prof. Dr. Telmo Roberto Strohaecker and Prof. Afonso Reguly from LAMEF/UFRGS for the valuable opportunities and support since the accomplishment of my M.Sc. degree and during the development of this work.

I would like to acknowledge a number of colleagues from GKSS and from LAMEF for their technical support and above all the friendship during all these years.

I would like to conclude with special thanks to all my family, in particular to my lovely Arelise, my father Afonso, my mother Terezinha and my brothers Alexandre, Eduardo e Lisiane that even far away in Brazil understood my absence and supplied me all the energy needed to go further and accomplish this stage of my life.

CONTENTS
*ABSTRACT**ZUSAMMENFASSUNG**ACKNOWLEDGEMENTS* _____ *v**CONTENTS* _____ *vii*

1. INTRODUCTION	1
2. STATE OF THE ART	4
2.1 Friction Stir Welding (FSW)	4
2.2 Heat Transfer during FSW	6
2.3 Weldability of Aluminium Alloys through FSW Process	8
2.4 Aluminium-Magnesium-Scandium Alloys	12
2.5 Aluminium-Magnesium-Silicon-Copper Alloys	17
2.6 Aluminium-Copper-Magnesium Alloys	21
3. OBJECTIVES	26
4. EXPERIMENTAL PROCEDURE	27
4.1 Overview of the Methodology	27
4.2 Materials and Heat Treatment	28
4.3 Friction Stir Welding Process	29
4.4 Temperature Measurements	32
4.5 Mechanical Testing	34
4.5.1 Microhardness	34
4.5.2 Tensile Test	34
4.5.3 Microflat Tensile Test	35
4.6 Metallurgical Characterization	37
4.6.1 Macrostructure Characterization	37
4.6.2 Microstructure Characterization	37
4.6.3 Substructure characterization	38
4.6.4 Image Processing	40
5. RESULTS AND DISCUSSION	41
5.1 Characterization of the Al-Mg-Sc Friction Stir Welded Joints	41
5.1.1 Thermal history during FSW Process	41
5.1.2 Mechanical Characterization	44
5.1.2.1 Microhardness Test	44

5.1.2.2	Conventional Flat Tensile Test _____	46
5.1.2.3	Microflat Tensile Test _____	48
5.1.3	Metallurgical Characterization _____	52
5.1.3.1	Macro and Microstructural Investigation _____	52
5.1.3.2	Substructural Investigation _____	55
5.1.3.3	Analogy of Al-Mg-Sc FSW joints / strengthening predictions _____	70
5.2	Characterization of the AA2024 T351 Friction Stir Welded Joints _____	73
5.2.1	Thermal history during FSW Process _____	73
5.2.2	Mechanical Characterization _____	76
5.2.2.1	Microhardness Test _____	76
5.2.2.2	Transverse Flat Tensile Test _____	77
5.2.2.3	Microflat Tensile Test _____	79
5.2.3	Metallurgical Characterization _____	83
5.2.3.1	Macro and Microstructural Investigation _____	83
5.2.3.2	Substructural Investigation _____	87
5.2.3.3	Substructural evolution _____	96
5.3	Characterization of the AA6013 T6 Friction Stir Welded Joints _____	98
5.3.1	Thermal history during FSW Process _____	98
5.3.2	Mechanical Characterization _____	101
5.3.2.1	Microhardness Test _____	101
5.3.2.2	Transverse Flat Tensile Test _____	103
5.3.2.3	Microflat Tensile Test _____	105
5.3.3	Metallurgical Characterization _____	108
5.3.3.1	Macro and Microstructural Investigation _____	108
5.3.3.2	Substructural Investigation _____	113
5.3.3.3	Substructural evolution _____	123
6.	<i>SUMMARY</i> _____	126
7.	<i>CONCLUSIONS</i> _____	132
8.	<i>REFERENCES</i> _____	135
	<i>LIST OF FIGURES</i> _____	141
	<i>LIST OF TABLES</i> _____	147
	<i>LIST OF SYMBOLS AND ABBREVIATIONS</i> _____	148

1. INTRODUCTION

Aluminium and aluminium alloys have played an important role in the development of human civilization. Important applications include automotive, aeronautical and food packaging industries. The 2xxx alloys are widely used in the aeronautical and space industry, as well as for machine parts, bolts and rivets. The 6xxx alloys are most frequently used for extrusion applications and the 7xxx series alloys are used for structural applications where high mechanical strength is needed. The combination of low density with strength, high corrosion resistance, thermal and electrical conductivity, hot and warm formability, are in general the main characteristics that assure versatility for aluminium and its alloys [1,2]. The use of Al alloys is very attractive to industry, usually for applications where their versatility can be applied to great advantage, exploiting their desirable properties and abilities. However, the difficulties in welding aluminium alloys by fusion welding processes has hindered the development of new applications for years.

Since its invention, the friction stir welding (FSW) process has received worldwide attention. When compared to fusion welding processes, FSW causes less distortion, changes in metallurgical and mechanical properties are minimized and the associated residual stresses are reduced [3,4]. Additionally, Mishra et al. [5] reported that the effect of intense plastic deformation and temperature rise, promoted by FSW, result in fine recrystallized grains, precipitate dissolution and coarsening with a magnitude much lower than that in traditional fusion welding. The FSW process is not only an emerging solid-state welding process. This friction-based technology is now extensively employed in several sectors such as the automotive and aerospace industries. A significant amount of knowledge has been gathered in the last few years, related to the global performance of the aluminium alloys welded by FSW. However, the main emphasis of recent studies has moved a step towards better understanding of the local behaviour, involving thermal cycles and plastic flow observed in the microstructure of the welded region after processing.

Many important properties of Al alloys, such as their mechanical strength, toughness, creep and stress-corrosion cracking are largely affected by the presence of precipitated particles of a second phase. In the FSW of Al alloys, changes in microstructure and properties of the base material (BM) occur not only in the stir zone (SZ) but also in the heat affected zone (HAZ) and in the thermo-mechanically affected zone (TMAZ) due to the coarsening and dissolution of hardening precipitates and the effects related to dynamic grain recovery [6]. Since FSW efficiency levels and quality is rising, a better understanding of the factors affecting the

weldability and properties of friction stir welded precipitation hardening alloys is required. The successful engineering application of precipitation-hardening Al alloys relies on FSW process control, in order to produce high quality joints.

1.1. Alloys Selection

In the present work, three age-hardening Al alloys were selected for investigation by considering scientific and technological criterias. The scientific criteria was based on the alloying elements present in the alloy, the resulting phase formation and their effects on the microstructure and material properties, as well as the dominant strengthening mechanisms and susceptibility of the material to thermomechanical processing. The technological criteria basically considered the functionality of the alloys, allied to the field of applications. The Al alloys chosen included the robust AA2024 T351, where the addition of Cu and Mg increase the natural aging and assure material strength. Such an alloy has a wide range of applications in medium and small size aircraft production (including companies like Eclipse Aviation, Embraer and Bombardier). The AA6013 artificially aged to T6, which is characterized by the high susceptibility to precipitation hardening due the formation of Mg-Si(-Cu) precipitates, is largely used in large-sized aircraft production (i.e. Airbus). The Sc addition in the Al-Mg-Sc alloy has the ability to increase recrystallisation resistance, due to solid solution hardening and the formation of Al-Sc precipitates, which results in a fine grain structure and consequently good mechanical properties. The new Al-Mg-Sc alloy has already a considerable range of applications and can be considered “the alloy of the future”, since it combines several attractive properties with stability at high temperatures (up to 350°C).

The utilization of FSW in the aircraft industry is nowadays a reality and a *systematic study*, as in the present work, concerning the Al alloys above described is expected to contribute to the development of FSW process implementation, without changes to the alloys currently used, beyond the FSW process optimization. Several studies have been conducted relating the physics (experimental) and modelling (mathematical) of material flow, thermal cycle and correlation of FSW process parameters [7-10]. However, there is no known methodology able to *explain precisely how the combination of certain welding parameters and tool geometries provides, at the optimal deformation rate, the resultant microstructural evolution*, which generally generates degradation of the mechanical properties in Al FSW joints. The main focus of this work is aimed at understanding the interrelation among FSW parameters, microstructural evolution and resulting mechanical properties.

1.2. Outline of the Work

The general presentation of this work is divided into chapters, which include an introduction, a literature survey, an experimental procedure, the results and discussion, the summary of the results as well as the conclusions. The introductory section presents a general description about Al and its alloys, paying attention especially to precipitation hardening alloys and a brief description of the FSW process, in conjunction with the weldability of such alloys. In this chapter, the importance of this solid state joining technique on precipitation strengthened Al alloys applications is elucidated as well as the motivation and objectives of the work. Chapter 2 presents a literature review of the friction stir welding process, including the principles, applications and advantages of the process with notes on the consequent heat generation during the welding process. The weldability of Al alloys through FSW, with the resulting microstructure and properties of welded joints, is also presented in this chapter, as well as the main metallurgical features of the investigated Al alloys, emphasizing the second phase particles formation, their features, including precipitation sequence and their particular role played, in terms of material strengthening. Chapter 3 presents a detailed description of the experimental procedure employed in this work, presenting the process monitoring and the welding parameter matrix of the joining process, with all the different conditions used to perform the welds, as well as mechanical and metallurgical techniques and methodologies utilized to characterize the welded joints and base material. Chapter 4 presents the results and discussion of this investigation, in terms of temperature measurements, detailed mechanical and metallurgical characterization of the Al-Mg-Sc (section 4.1), AA2024 T351 (section 4.2) and AA6013 T6 (section 4.3) base material and FSW joints, resulting in the establishment of process energy input/structure/properties relationships. Subsequently, a summary of the results is presented for the different Al alloys followed by the conclusions of the thesis. Suggestions for future work are listed, according to the needs observed at the end of the work.

2. STATE OF THE ART

2.1 Friction Stir Welding (FSW)

Friction stir welding (FSW) is an innovative solid phase joining process, developed and patented by TWI Ltd. of Cambridge, England in 1991 [11]. FSW is a derivative of conventional friction welding techniques, which enables the advantages of solid-phase welding to produce long butt and lap joints [12]. In the FSW process, a wear-resistant, non-consumable rotating tool is used to join sheet and plate materials such as aluminium, aluminium based metal matrix composites, magnesium alloys, copper, zinc, titanium alloys, lead and steel, among others. The workpieces have to be properly clamped onto a backing bar and secured against vertical, longitudinal and lateral forces, which will tend to lift them and push them apart. The outstanding mechanical properties and low distortion are attributed to the low heat input and the absence of melting. As it is a solid-state process, FSW allows joining of materials that cannot be welded with a conventional fusion welding process [13]. Since its invention, the process has received worldwide attention and today many companies around the world are using the technology in production, particularly for joining aluminium alloys [14].

In an FSW process, a rotating tool consisting of one protruding part (pin) fixed in the centre of one thicker cylindrical part (shoulder) is forced down into the join line, under conditions where frictional heating is sufficient to locally raise the temperature of the material to a range where it is easily plastically deformed. The plasticised material is transferred from the leading edge of the tool to the trailing edge of the tool pin and is forged by the intimate contact of the tool shoulder and the pin profile. The transversal tool movement produces a material flow around the tool in a complex flow pattern, which varies according on the tool geometry, rotational and transverse speed. It leaves a solid phase bond between the two pieces. For butt joint, the length of the pin approximates to the thickness of the workpiece. The FSW process can be illustrated as shown in Figure 2-1.

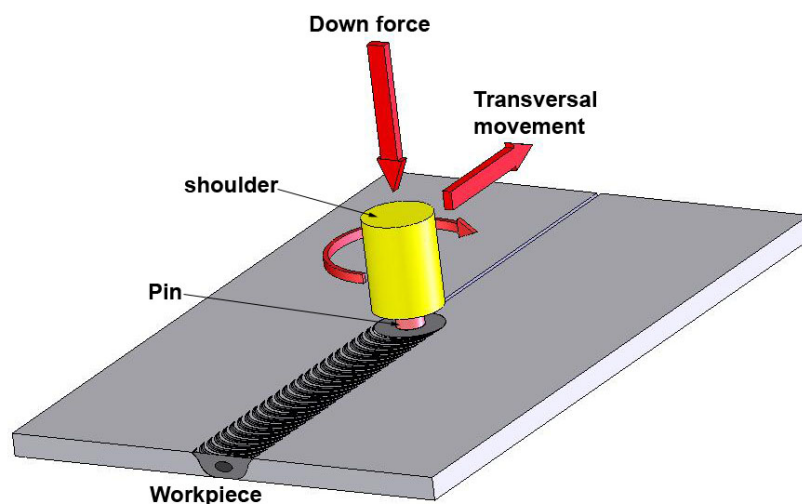


Figure 2-1 – Friction stir welding principle.

The FSW tools are generally manufactured from a wear-resistant material with good static and dynamic mechanical properties at an elevated temperature. They are made in a manner that permits up to 1000 m of weld to be produced in 5 mm thick aluminium extrusions without changing the tool. The design of FSW tools is a critical characteristic of this remarkable and relatively new joining process. Different tool designs have been developed, always aiming to improve the weld performance, to enhance the weld metal flow path, and achieve higher welding speeds and superior penetration [13].

This welding process brings great benefits, mainly for aircraft applications, with regards to cost, weight and joint quality. The FSW process advantages include “production cost savings” due to the simple welding operation, which is energy efficient and eliminates the need for costly consumables. The weld quality provides opportunities for improved and new product designs, i.e. welds can be made in Al alloys which cannot be fusion welded, because of crack sensitivities; high joint strengths can be achieved in heat treatable alloys, no porosity, dissimilar material and conditions can be joined, the elimination of solidification defects, lower residual stresses, etc. The process is completely mechanical and therefore the welding operation and weld energy input are accurately controlled. The process is clean and does not produce any major safety hazards, such as welding fume or radiation. Nevertheless, the FSW process does have some disadvantages: the single pass welding speeds in some sheet alloys are slower than for some mechanised arc welding techniques; the pieces must be rigidly clamped against the backing bar to prevent metal breakout when full penetration welds are required; at the end of the weld run, a hole is left where the tool pin is withdrawn [12].

The FSW process attains a wide field of applications. The first commercial application of the process concerned the manufacture of hollow aluminium panels for shipbuilding applications. Wide aluminium panels made by joining extrusions for high-speed ferryboats are commercially available. The application of FSW extends to the production of high-strength aluminium tanks and boosters for spacecraft. FSW procedures for welding end domes into cylindrical, high-quality tanks have been developed for cryogenic oxygen storage vessels. In aircraft production, the FSW process offers a huge potential for the low-cost joining of lightweight aluminium airframe structures. The Eclipse Aviation Corporation decided to use FSW to replace traditional riveting and bonding processes for the majority of the aircraft's primary structure on the Eclipse 500 jets. In the automotive industry, applications include the Ford GT aluminium tunnel, joining a 6061-T6 extrusion to a 5182 sheet panel as a continuous lap joint. Spot friction welding (SFW) is also applied to produce the rear aluminium door of the Mazda RX-8. In the railway industry, hollow profiles and T-stiffener extrusions are currently being friction stir welded for the manufacture of commuter and high-speed trains [12,13].

2.2 Heat Transfer during FSW

The large plastic deformation around the rotating tool during the welding process and friction between tool and workpieces are the two main sources generating heat in FSW. Both aspects contribute to the temperature increase within and around the stirred zone, but the friction is considered the major heat source [7,8]. As the temperature distribution along the weld zones directly controls the microstructure of the welds, such as grain size, grain boundary character, coarsening and dissolution of precipitates, and consequently the resultant mechanical properties of the welds, it is important to obtain information about temperature distribution during FSW. Temperature measurement is difficult to perform within the stirred zone, due to the intense plastic deformation generated by the rotation and translation of the tool. Therefore, the maximum temperatures attained in the stir zone and adjacent regions have been estimated from the microstructure of the weld or measured using embedding thermocouple as close as possible to the stir zone [5,8]. The thermo-cycle prediction during FSW should assist in understanding the metallurgical evolution and related mechanical properties' behaviour along the weld zones. The yield-strength variation with temperature, represented by aluminium alloys along the different weld zones, is illustrated in Figure 2-2. If the maximum temperature in an element exceeds 400°C, which are generally the stir zone and TMAZ during the FSW process, the path **abicefgh** in Figure 2-2 is followed: **abice** during the heating stage and **efgh** during the cooling stage. In the case where the maximum temperature exceeds 250°C, commonly in the HAZ, the path **abijk** in

Figure 2-2 is followed: represented by the heating (**abi**) and cooling (**ijk**) stages. However, this is a general consideration and, depending on the alloy, the decrease of the yield strength promoted by the thermal cycles sometimes can be even higher in the HAZ, in comparison with the SZ and TMAZ.

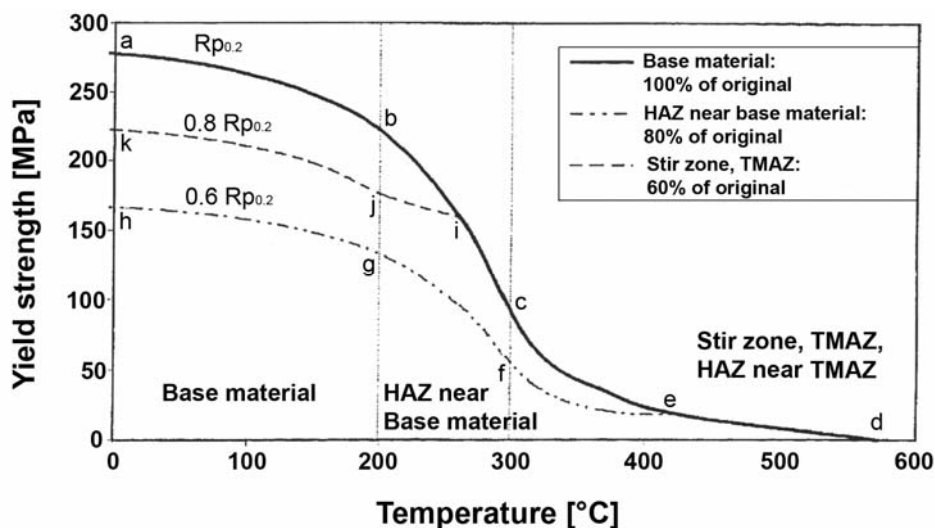


Figure 2-2 – Yield-strength variation along the different FSW zones [8].

The heat flow in the workpiece is characteristically three-dimensional, being necessary to use a 3D solid element in a finite element model. Some authors assume the heat input as being linearly proportional to the distance from the center of the tool, which is derived from the assumptions that the downward force applied to the workpiece from the tool creates a uniform pressure between the shoulder and the workpiece, and the heat is generated from the work done by the frictional force. The heat generated from the friction between the tool shoulder and the workpiece produces a rate of heat input to the workpiece (Watt/m^2), which is represented by [8]

$$q(r) = \frac{3Q_T r}{2\pi(r_0^3 - r_i^3)} \quad \text{for } r_i \leq r \leq r_0 \quad (1)$$

Where Q_T is the total rate of heat input to the workpiece (i.e. Watt), r_0 and r_i are the radius of the shoulder and the tool pin. The heat term $q(r)$ can be further related to the process parameters by

$$q(r) = \frac{F\mu}{\pi(r_0^2 - r_i^2)} \frac{2\pi\omega r}{60} \quad (2)$$

Where F is the downward force, ω is the tool rotation speed (rpm), and μ is the frictional coefficient correspondent to the relative speed at the interface at r .

Figure 2-3 represents schematically the heat distribution, simulating the heat generated from the friction at the interface between the shoulder and the workpiece. Even considering the

temperature field as insensitive to the diameter of the pin of the tool, it is believed that the tool pin also generates heat from the friction of the pin surface and the workpiece. In order to also consider such heat produced among these interfaces, simulations used assume r_i as zero for analytical analysis.

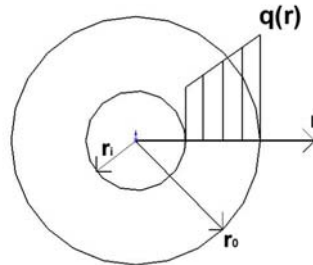


Figure 2-3 – Schematics of the heat distribution along the interface tool shoulder and workpiece adapted from [8].

The heat flux in FSW is conducted to both the tool and the workpiece. The amount of heat conducted into the workpiece dictates a successful FSW process, the quality of the weld, shape of the weld, microstructure of the weld, as well as the residual stress and distortion of the workpiece [7,8]. The amount of heat flowing to the tool will determine the life of the tool and its capability for the joining process [7]. Chao and co-workers [7] reported that only about 5% of the heat generated by the friction process flows to the tool and the rest flows to the workpiece. The heat efficiency in FSW is thus 95%, which is very high compared to traditional fusion welding (typically 60 to 80%). Therefore, the heat input will affect directly the resulting thermal cycle, heating and cooling rate, peak temperatures and dwell time. In the present work, the heat input applied during the weld is controlled in terms of transverse welding speed. The faster welding speed leaves less heat to the workpiece and thus is generally called “cold weld”. Slower welding speed would produce larger dwell time, which consequently increases peak temperature and enlarges the thermal cycle.

2.3 Weldability of Aluminium Alloys through FSW Process

FSW process has emerged as a promising solid-state process with the potential to join aluminium alloys traditionally considered difficult to weld. The most attractive reasons for joining aluminium alloys through this process is the avoidance of solidification defects formed by conventional fusion weld processes, the low distortion and the inferior remaining residual stresses after FSW. Consequently, friction stir welding is effective and has been systematically developed for joining aluminium alloys, especially for those usually considered unweldable such as 2xxx and 7xxx series alloys [9,10]. During the process, thermo-mechanical conditions vary

along the weld seam, promoting a corresponding variation of the microstructure. Work to date has concentrated on single-pass welds in material thicknesses from 1.6 mm to 10 mm but it has been shown that a thickness of up to 50 mm can be joined with one pass, and up to 75 mm with 2 passes, one in each side [12].

Solid-state stirring leads to fine equiaxed grains in the weld centre, produced due to dynamic recrystallization (stir zone - SZ), followed by a typically recovered microstructure around the stir zone, which is affected by lower levels of deformation and temperature in comparison to the weld centre (thermo-mechanical affected zone - TMAZ) and a region affected only by temperature, with a microstructure similar to the base material (heat affected zone - HAZ). The stir zone (SZ) often contains a well-defined onion ring type of inner structure, consisting of concentric ovals, however, in some alloys this feature is not visible. It is dependent on the alloy used and the process conditions. The diameter of the stir zone is typically slightly larger than that of the tool pin and significantly less than the shoulder diameter. The stir zone also typically extends to the bottom of the weld, but not always. The prediction of the SZ shape is directly dependent on the tool design and welding parameters, beyond the hot strength of the material being welded. The macrostructure outside of the stir zone generally present an area adjacent to the SZ where severe plastic deformation of the material occurs, such that the elongated grain structure previously present in the base material of the majority of rolled plates can be rotated by as much as 90°. It has been possible to correlate these welded regions with variations in mechanical properties. For example, in several previous studies the hardness profiles correlate to metallurgical and mechanical aspects [15]. Normally the mechanical properties of precipitate strengthened aluminium alloys tend to deteriorate in the weld zones and generally, they depend on the dissolution and/or coarsening of strengthening second phase particles [16].

Figure 2-4 shows, from top to bottom, the superficial features of the weld, typically presenting a remaining hole at the end. A macrograph of the transversal segment of the welded joint reveals a well-developed stir zone in the centre of the weld, which indicates a good quality weld with the correspondent FSW zones and microhardness profile performed in the mid-thickness of the base material and welded joint. The overall shape of the stir zone is variable, depending on the alloy used and the actual process conditions. This kind of hardness decrease in the weld zones is usual in friction stir welds of artificially aged aluminium 6xxx series.

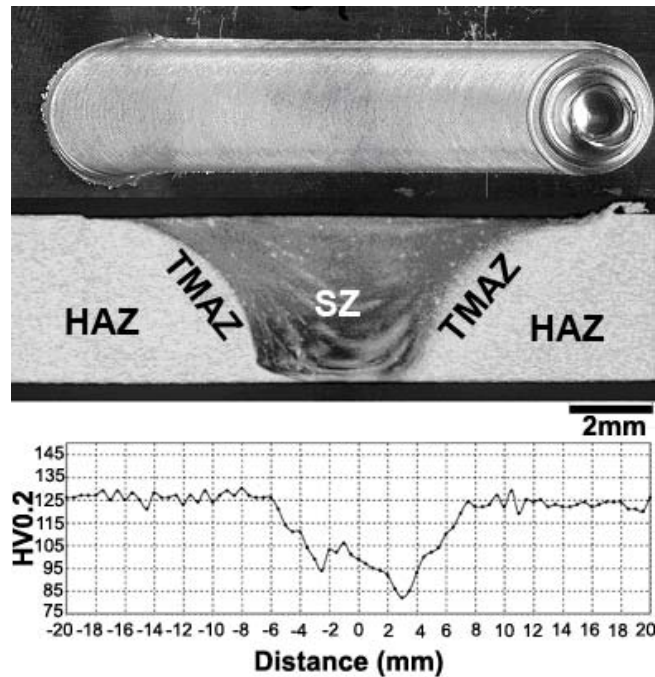


Figure 2-4- Surface aspect of the FSW joint in Al 6xxx series alloy, macrograph of the weld transversal section and microhardness profile typical, respectively from top to bottom.

The microstructure of FSW aluminium alloys, in the heat affected zone (HAZ) usually shows no apparent difference from the base material. In age-hardened alloys, the hardness level tends to decrease in this zone, indicating clearly that the thermal cycle during the welding process has a significant influence, either by overaging, or by decreasing dislocation density, probably by both in fully aged alloys. In the thermomechanically-affected zone (TMAZ), through optical microscopy it is perceived that the FSW causes bending of the pancake grains, and occasionally some local recrystallisation. The heat also accelerates the aging and annealing processes, although the latter will compete with some degree of work hardening. Typical hardness profiles for age-hardened alloys have shown that the hardness usually reaches a minimum in this region. Work hardening is the dominant effect close to the stir zone, while overaging/annealing is the most important effect towards the HAZ. It is also possible that local areas may reach a sufficiently high temperature to allow partial precipitate dissolution, particularly in the TMAZ [5,6,15]. There is usually considerable evidence for partial recrystallization close to the interface with the stir zone. It is remarkable to note that this interface is generally very sharply defined, especially on the side where the direction of the tool rotation is the same as the direction of travel (advancing side). The interface on the side where the direction of the tool rotation is contrary to the direction of travel (retreating side) usually shows a wider gradient of microstructure. The microstructure of the SZ is clearly equiaxed and very fine, varying the grain size according to the alloy and FSW process parameters. These fine grains are difficult to investigate by optical

microscopy due to their diameter, presenting typically a few microns or less. Hardness levels are usually below the base material level in age hardened and mechanically hardened alloys [15]. Typical interfaces between TMAZ and SZ for the advancing and retreating sides of friction stir welded aluminium alloys are illustrated in Figure 2-5.

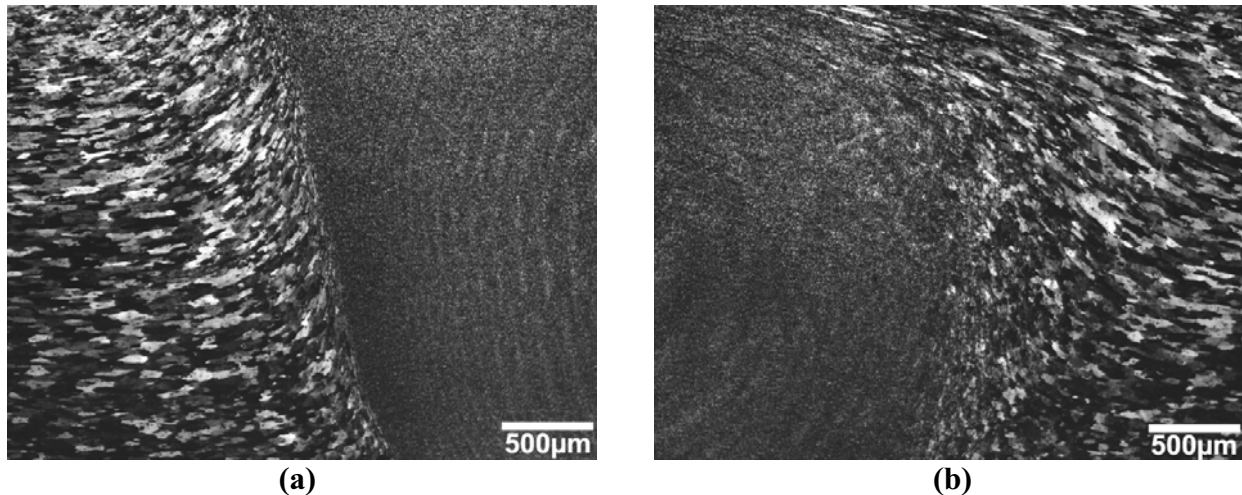


Figure 2-5 – Micrographs showing the interface TMAZ/SZ of 2024 T351 alloy joint in detail. (a) Advancing side and (b) retreating side.

Deeper investigations using electron microscopy of the individual weld regions have shown the particular effects of the weld energy input on the substructure of several aluminium alloys. Usually a considerable reduction in dislocation density in the SZ is reported, compared to the other regions, as a consequence of the recrystallization phenomenon [5,6,10]. Different kinds of precipitates have been observed along the different FSW zones, from dispersoids to very thin strengthening precipitates, occurring intragranular and/or intergranular, depending essentially on the alloying elements present. The coarsening and dissolution of the precipitates along the TMAZ and SZ has been reported for several age-hardened alloys [15]. The different second phase particles formed in different strengthening precipitate alloys vary in chemical composition, size, morphology and distribution, depending on the aluminium alloy and process parameter employed to produce the joint. The different precipitation features for different precipitate strengthened alloys are described in detail in the following sections.

The FSW of aluminium alloys provided three main metallurgical advantages when compared to fusion welds: joining in the solid state eliminates cracking; there is no loss of alloying elements through weld metal evaporation, preserving the alloy composition in the weld region; the crushing, stirring and forging action of the welding tool produces a weld metal with a finer grain structure than that of the base material. The friction stir weld metal (stir zone) and HAZ in solution heat-treated and artificially aged aluminium alloys (i.e. 2xxx and 6xxx series)

can be returned to a strength close to the fully heat-treated base material, by applying a post-weld heat treatment [12].

2.4 Aluminium-Magnesium-Scandium Alloys

Excellent mechanical properties at room temperature have been reported for aluminium alloyed with scandium. This is due to the presence of nanometer size Al_3Sc precipitates which are effective in pinning mobile dislocations and stabilizing a fine grain structure [17]. The solubility of scandium in solid aluminium is about 0.22, 0.15 and 0.05% at 645, 600 and 500°C, respectively. The Al_3Sc phase has about 35.7% Sc and is in equilibrium with the aluminium solid solution, having an FCC lattice with the following parameters: $a = 0.4106$ nm, space group $\text{Pm}\bar{3}\text{m}$, 4 atoms per unit cel. The scandium tends to form supersaturated solid solutions with aluminium, even at relatively low cooling rates. A polythermal section for the Al-Mg-Sc is represented in Figure 2-6 from Al-17% Mg to Al-1% Sc. The solubility of scandium and the mutual solubility of scandium and magnesium in aluminium were determined in the temperature range 430 to 640°C. The Al_3Sc and Al_3Mg_2 phases were found to be in equilibrium with the aluminium solid solution, and no ternary phase was found in this concentration range [17].

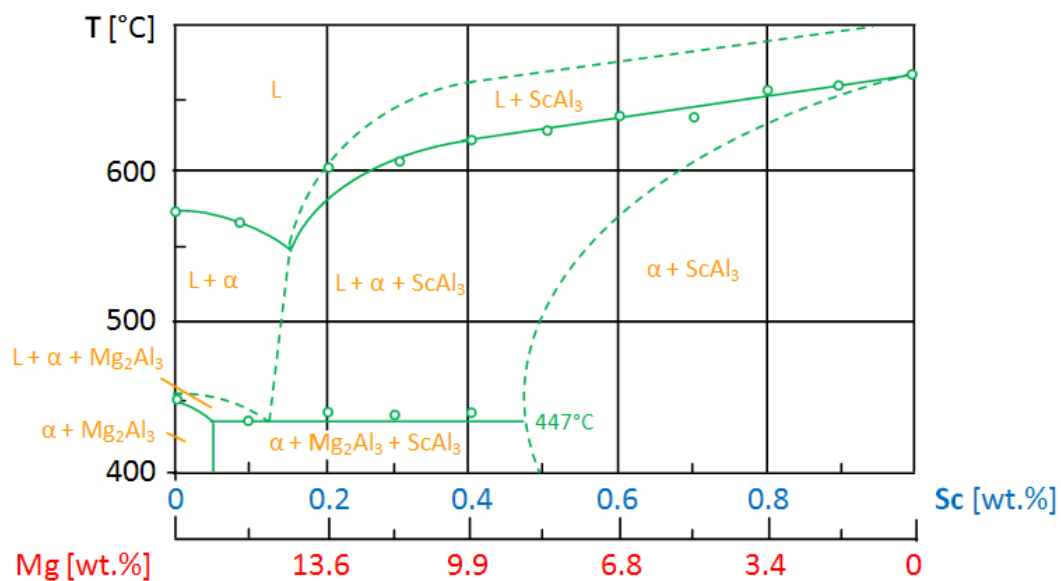


Figure 2-6 – Al-Mg-Sc system from Al - 17% Mg to Al - 1% Sc [adapted from 17].

The phase diagram above includes a single phase of the aluminium-based solid solution, two two-phase fields (Al) + Al_3Mg_2 and (Al) + Al_3Sc , and a three-phase field (Al) + Al_3Mg_2 + Al_3Sc . A eutectic reaction occurs in the concentration range 0.1 to 0.5% Sc at $447 \pm 3^\circ\text{C}$: $\text{L} \rightarrow (\text{Al}) + \text{Al}_3\text{Mg}_2 + \text{Al}_3\text{Sc}$. The solidus is the bottom of the solidification surface for the (Al) + Al_3Mg_2 eutectic in alloys containing up to 0.1% Sc, and of the (Al) + Al_3Sc eutectic in alloys

containing more than 0.5% Sc. Alloy structures in different phase ranges demonstrate a degenerated (Al) + Al_3Mg_2 eutectic and a highly dispersed (Al) + Al_3Sc constitution [17].

The Al_3Sc precipitates are usually stable against coarsening, up to temperatures of 350°C and the decomposition temperature sometimes can reach 650°C , depending on the alloying elements [17,18]. Precipitates formed in solid state are coherent with the aluminium lattice, normally have a spherical appearance and the volume fraction of precipitates is small due to the low solubility of scandium in aluminium. Therefore, Sc containing particles are generally known to increase the recrystallization resistance, and consequently grain refinement. The recrystallization of aluminium alloys containing scandium can be observed through the effect of the scandium concentration on the temperature range of recrystallization and the recrystallization of alloys containing Al_3Sc precipitates, prior to plastic deformation and annealing. The effect of scandium on recrystallization temperatures of an Al-Mg-Sc containing 6.5% Mg and up to 0.7% Sc is shown in Figure 2-7. The maximum recrystallization temperature is achieved at 0.2% Sc, further increasing the scandium content has virtually no effect on t_r^s (recrystallization start temperature). The temperature at which recrystallization finishes (t_r^f) has been determined only for alloys with $< 0.2\%$ Sc. This temperature has been estimated as 540°C for an Al-6.5% Mg-1.8% Sc alloy.

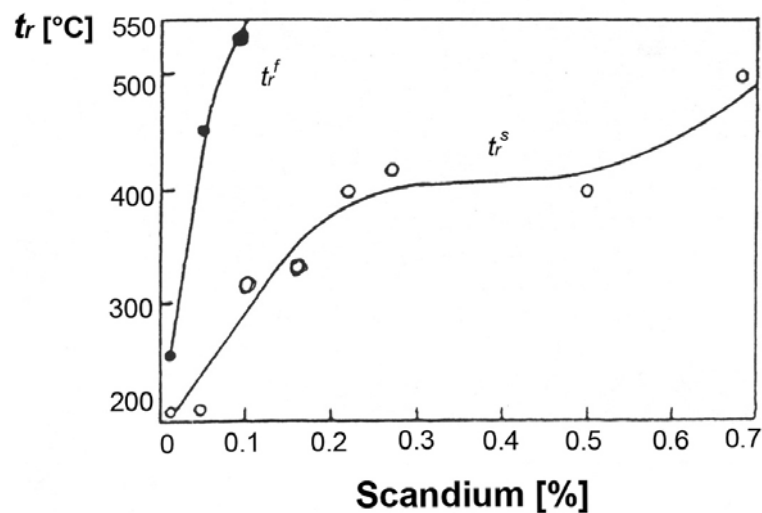


Figure 2-7 – Effect of scandium addition on recrystallization temperatures [17]

The relationship between the presence of Al_3Sc precipitates and the recrystallization starting temperature can be represented for an Al-6.5% Mg-Sc containing 0.15 and 0.32% Sc with the values presented in Table 2-1. At a given volume fraction of precipitates (f) with average

radius (r), finer particles have a stronger effect on the retardation of (sub)boundary migration, and the hindering force F is given by [17,19]:

$$F \approx \frac{f}{r} \quad (3)$$

In precipitation-hardening alloys, such as the Al-Mg-Sc alloy, fine precipitates mainly hinder the nucleation of recrystallization centers, not their growth. The main parameter is the interparticle spacing L . According to Orowan model, the resistance to dislocation motion in an alloy with precipitates is inversely proportional to the interparticle spacing (see Figure 2-8). In the case where the elastic parameters of the particles remain constant upon recrystallization, the forces hindering recrystallization are determined by the f/r (according to Zener) and $1/L$ (according to Orowan) ratios, which characterize the precipitation parameters. There is no contradiction, because all these parameters interrelate as [17]:

$$L = 4/3r(1 - f)/f \quad (4)$$

Table 2-1 - Al₃Sc precipitate features and recrystallization temperature (t_r^s) [17].

Al-Mg-Sc Alloy	T [°C] (1h)	r [nm]	L [nm]	f [%]	$1/L \times 10^{-3}$ [nm ⁻¹]	$f/r \times 10^{-2}$ [%nm ⁻¹]	t_r^s [°C]
0.15% Sc	300	4.0	79.0	0.41	12.6	10.2	400
	350	8.2	110	0.39	9.1	4.76	400
	400	13.1	231	0.37	4.3	2.82	325
	450	25.6	521	0.37	2.4	1.92	275
	550	82.1	1930	0.32	0.52	0.39	220
0.32% Sc	300	4.3	105	0.78	9.5	18.1	400
	350	7.9	175	0.74	6.3	9.36	400
	400	10.1	488	0.74	2.1	7.33	350
	450	24.6	687	0.74	1.45	0.3	220
	550	55.1	2980	0.74	0.33	0.134	220

The Al₃Sc precipitates presenting $r = 8$ nm and $L \leq 170$ nm have the greatest hampering effect. When the particles coarsen to $r \geq 24$ nm and $L \geq 600$ nm, the recrystallization commencement temperature decreases to 220°C.

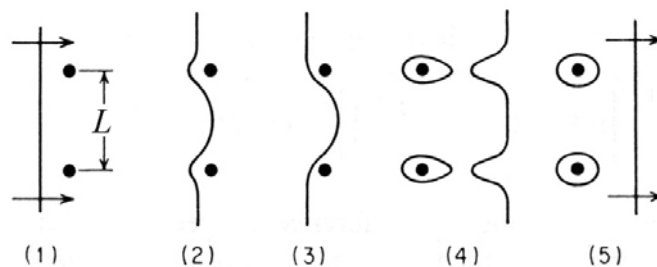


Figure 2-8 – Orowan’s mechanism of dispersion hardening [19].

Stage 1 of Figure 2-8 shows a straight dislocation line approaching two precipitates. At stage 2 the line is beginning to bend, and at stage 3 it has reached the critical curvature. The dislocation can then move forward without further decreasing its radius of curvature, if the stress required to force the dislocation between the obstacles is attained. At stage 4, the segments of the dislocation that meet on the other side of the precipitate are of the opposite sign; they can annihilate each other over part of their length, leaving a dislocation loop around each precipitate. In stage 5 the original dislocation is free to move on. Every dislocation gliding over the slip plane adds one loop around the precipitate. Consequently, an increase in shear stress will be required, with the result that L can be reduced and also noncoherent particles can cause the matrix to strain-harden [19].

The influence of scandium on the tensile properties has been shown to be effective in terms of increasing the yield strength and tensile strength, reducing the elongation of Al-Mg alloys, but remaining sufficient in high levels. The effect of scandium in ternary alloys can be estimated as [17]

$$\Delta\sigma_{0.2} = \sigma_{0.2}^T - \sigma_{0.2}^B \quad (5)$$

Where $\sigma_{0.2}^T$ is the yield strength of an Al-Mg-Sc alloy and $\sigma_{0.2}^B$ is the yield strength of a relevant binary Al-Mg alloy. Even small additions of scandium can sharply increase the yield strength. The increment becomes lower for further increases of the scandium concentration. The influence of different scandium concentrations on the mechanical properties of annealed Al-Mg extruded rods and rolled sheets are shown in Table 2-2.

Table 2-2 – Effect of scandium on Tensile properties of annealed Al-Mg alloy [17].

Content [wt.%]	Rm [MPa]		Rp _{0.2} [MPa]		A [%]	
	rod	sheet	rod	sheet	rod	Sheet
2% Mg	180	155	80	80	38.5	33
2% Mg, 0.18% Sc	225	-	135	-	27.5	-
2% Mg, 0.3% Sc	255	220	150	130	22	26
2% Mg, 0.4% Sc	260	-	165	-	23.1	-
5% Mg	270	260	115	115	37	34.5
5% Mg, 0.15% Sc	335	-	180	-	24	-
5% Mg, 0.25% Sc	360	320	215	170	20	23
5% Mg, 0.5% Sc	370	340	235	195	19.5	22.5
8.5% Mg	345	340	160	160	27.5	28
8.5% Mg, 0.13% Sc	410	-	265	-	16.2	-
8.5% Mg, 0.27% Sc	455	-	280	-	13	-
8.5% Mg, 0.45% Sc	470	420	285	255	13	17

The strengthening mechanisms that act in Al-Mg-Sc alloys are mainly precipitation and structural (solid solution) hardening due to the Al₃Sc phase, solid-solution hardening due to magnesium and precipitation hardening with respect to the Al₃Mg₂ phase in alloys containing more than 8% Mg. The decreased difference in lattice parameters makes it possible to preserve the coherence of Al₃Sc precipitates at higher temperatures and for longer exposures. Thus, the yield strength of a deformed alloy can be analytically determined according to the contribution of precipitates and dislocation structures to strengthening:

$$\sigma_{0.2}^{calc} = \sigma_{0.2}^0 + \sigma_{0.2}' + \sigma_{0.2}'' \quad (6)$$

where $\sigma_{0.2}^0$ is the yield strength of an Al-Mg single crystal, $\sigma_{0.2}'$ represents the strengthening contribution due to a substructure with an increased dislocation density, and $\sigma_{0.2}''$ represents the strengthening contribution due to the Al₃Sc precipitates. The $\sigma_{0.2}^0$ can be determined by the Hall-Petch relationship [17]

$$\sigma_{0.2}^0 = \sigma_i + KD^{-1/2} \quad (7)$$

σ_i being the stress required to move the dislocation inside the grain and equal to the yield strength of a single crystal, D is the grain size, and K is a coefficient characterizing the ability for plastic deformation to be transferred between grains. The $\sigma_{0.2}^0 - D^{-1/2}$ dependence has been shown to be linear for an Al-6.5% Mg alloy. This dependence has been extrapolated to $D^{-1/2} = 0$ to obtain $\sigma_{0.2}^0 = 78.7 \text{ MPa}$. The substructure strengthening $\sigma_{0.2}'$ is determined by

$$\sigma_{0.2}' = Kd^{-1/2} \quad (8)$$

for d representing the subgrain size and $K = 3.8 \text{ MPa mm}^{1/2}$ for hot-extruded aluminium alloys, tensile tested in the longitudinal direction [17].

The strengthening promoted by the precipitates depends on the interaction mechanism acting between precipitates and dislocations. The main factor in such an interaction is the mean free path or interparticle spacing. Precipitates are sheared by dislocations when the mean free path is about $100b$ (b is the Burgers vector) and dislocations bow out between precipitates when the spacing is larger. It has been estimated $\sigma_{0.2}'' = 3.06\sigma$ from the Orowan bypassing [17].

When compared to commercial age-hardening 2xxx and 6xxx series alloys containing Cu, Mg and Si, where precipitates usually coarsen rapidly above 250°C, it is reasonable to assume that Al₃Sc precipitates are much more stable. Thus, aluminium alloys containing scandium

precipitation strengthening, can be used at temperatures significantly higher than conventional precipitate-hardened aluminium alloys [20]. The homogeneous structure and fine grain size promoted by scandium addition improves fabricability, yield strength and toughness. The material applications include defense (especially in Soviet Union), sporting goods, transportation, and the aerospace industry [16]. The excellent control of the grain structure in thermomechanical treatments produced by Al_3Sc precipitates and significant particle strengthening are indications of good performance in welding applications.

The benefits produced by the Sc addition in Al-Mg-Sc alloys previously mentioned, such as: the effective influence on its tensile properties, in terms of increasing yield and tensile strengths, retaining elongation in sufficiently high levels and formation of phases with decreased difference in lattice parameters, which preserves the stability of Al_3Sc precipitates to higher temperatures and for longer exposures, make the Al-Mg-Sc alloy a potential material for thermomechanical processing applications, like FSW. However, so far little information is available regarding FSW for such an alloy. *The development of the FSW process for joining the new Al-Mg-Sc alloy by means of understanding the metallurgical reactions during welding will improve the joining quality of future applications.*

2.5 Aluminium-Magnesium-Silicon-Copper Alloys

The 6xxx-series wrought Al-Mg-Si(-Cu) alloys are widely used as medium-strength structural alloys because of their good weldability, corrosion resistance, and immunity to stress-corrosion cracking, and are therefore used for the majority of extrusions [21,22]. They are considered to be the most promising candidates for the heat-treatable body sheet materials for autobody applications [21,23]. Typical applications range from window frames to heavily loaded structures, like body panels in the automotive industry and for particularly highly stressed components in the aviation and space industries such as airplane fuselage skin [24,25]. Such wide ranges of applications results from the ability that these alloys have to increase mechanical strengthening by aging after forming processes. In this type of alloy, the highest strengthening results are expected to be promoted by the interaction of dislocations with fine precipitates. Strengthening models include parameters such as particle size, volume fraction and distribution of the precipitates. The presence of Cu leads to the formation of an additional hardening phase in these quaternary alloys. Moreover, it also modifies the composition of some second phase particles due to a change in phase stability. This quaternary phase is commonly designated as the “Q” phase (and its precursor metastable phases) and it plays a key role in controlling the

properties in Al-Mg-Si-Cu alloys, because of its ubiquitous and often dominant presence [25,26]. Chakrabarti *et al* [26] reported that one of the most important phases present in these 6xxx alloys with Cu to varying amounts is a quaternary phase, denoted as Q containing Al, Cu, Mg, and Si, which forms as an equilibrium phase. Matsuda *et al* (2001) [27] explains that the Q' is a metastable version of the Q phase and has the same crystal structure as the equilibrium Q phase. For many commercial alloy compositions, the relative amount of Q' is expected to be higher than the other strengthening phases. Indeed, Denquin *et al* [28] present an SAED pattern of a precipitate in an AA6056 T4 alloy, which gives a good correlation with the Q phase. Additionally, Vivas *et al* [25], investigating an AA6056 T6 alloy, observed that the number of elongated precipitates (length in the range of 40-120 nm) is smaller than that of circular and rectangular ones (length limit of 2-5 nm).

The precipitation sequence in the Al-Mg-Si alloys is: α solubilized solid solution (SSS) \rightarrow Guinier Preston zones (GP'z) \rightarrow needle-type β'' \rightarrow rod-type β + lath-type Q' \rightarrow β + Si. On the other hand, the Cu addition changes the precipitation sequence to α (SSS) \rightarrow GP zones \rightarrow needle type β'' \rightarrow lath-type Q' \rightarrow Q + Si. It was concluded that Cu induces the formation of Q and its precursor metastable phases and has a beneficial effect on the kinetics of artificial aging [29,30]. Additionally, prior investigations regarding Al-Mg-Si alloys, Blanc and Mankowski (1997) [31] and later Edwards *et al* (1998) [32] had already proposed a precipitation sequence, as follows: separate clusters of Mg and Si atoms - co-clusters that contain both Mg and Si atoms - β'' precipitates - β'' and β' precipitates - β' precipitates - β Mg₂Si precipitates. Vivas *et al* [25] added that the yield strength of the AA6056 T6 alloy decreased slowly from -196°C to 125°C (375 to 305 MPa for the respective temperatures). As already mentioned, lath and needle shape precipitates were also found in AA6056 alloy. It has also been reported that evidence suggests several other precipitates may form in addition to those listed above [32].

As previously mentioned, this series of alloys is mainly characterized by the high susceptibility to age under heat treatment or thermomechanical processing. The precipitation hardening that results from natural aging (T4) alone produces tempers that are characterized by high ratios of tensile to yield strength, high fracture toughness and resistance to fatigue. The alloys that are used in these tempers, have relatively high supersaturation of vacancies retained by fast quenching, resulting in rapid formation of Guinier-Preston (GP) zones; strength increases rapidly, attaining nearly maximum stable values after four or five days [33]. The T6 temper or artificial aging produces a fully heat-treated condition (maximum strength), i.e. maximum precipitation. Aluminium alloys in T6-type tempers generally have the highest strengths,

practically without the sacrifice of minimum levels of other properties and characteristics [33,34].

2.5.1 FSW of 6xxx alloys

As previously mentioned in section 2.3, the localized heating produced during FSW creates significant microstructural changes, and this can be associated with local variations in mechanical properties across the welded joint. Precipitates in the welded joint can be fully or partially redissolved during FSW as well as coarsened [35,36]. The process parameters will dictate the amount of energy (thermal cycle and deformation levels) generated during the process and, consequently, the resulting microstructure and mechanical properties of the weld joint. The effect of different shoulder geometries on the mechanical and microstructural properties on 6082 T6 friction stir welded joints was studied by Scialpi and co-workers [37]. It was verified that the tool working at 460 mm/min and 1810 rpm, increases the longitudinal and transverse strength of the joint and provides the best crown surface due to the combination of fillet and cavity. Nevertheless, Fujii *et al.* [38], prospecting the optimal tool design for 5 mm thick welded aluminium plates, concluded that for 6061-T6, whose deformation resistance is relatively low, the tool shape does not significantly affect the microstructures and mechanical properties. Murr and co-workers [39,40] have observed from friction stir welded 6061 aluminium alloys that the extreme plastic deformation, associated with the friction straining, characterizes the metal flow in solid state. A comparison of the microstructures between friction stir welded aluminium alloy 6061 and 1100 (considering that cast aluminium alloy 1100 slabs contain large columnar grains) provides evidence for dynamic recrystallization as a principal feature of FSW development. In aluminium alloy 6061, the plastic deformation, accompanied by temperature variations within and across the weld zone (which approach a maximum around 250°C), produce a wide variation of precipitation structures, ranging from Guinier-Preston-type zones to Widmanstätten structures and other, more irregular precipitates [41]. Lienert *et al.* [42] investigated friction stir welded AA6061-T651. It was observed that the microstructural development in each region of the weld is a strong function of the local thermomechanical cycle experienced during welding. Olea *et al.* [43] working on AA6056 alloy in three heat-treatment conditions (T4, T6 and a PWHT - post weld heat treatment), also found microstructural changes in various zones. TEM observations showed precipitate dissolution and coarsening after FSW, followed by reprecipitation of a very thin structure in the stir zone of the PWHT condition. Furthermore, it was suggested that the presence of a subgrain network developed in the base metal, formed during thermomechanical processing and/or after T6 temper. The β'' strengthening precipitates were found only in the base

metal, while Si-O and Al-Fe-Si particles were found in all regions studied. It was also observed that the stir zone experienced the highest temperature, the greatest strain and the highest strain rate. The absence of precipitates of any kind in the stir zone suggest that the temperatures exceeded the dissolution temperature for the equilibrium β precipitates and the local cooling rates were sufficiently fast to avoid appreciable precipitation. Sato *et al.* [35] observed on 6063 weld regions that the hardness profile depends slightly on the grain size, but strongly on the precipitate distribution. It is known that the mechanical properties of 6063 depend more on the needle-type precipitates rather than on the rod-type precipitates. I.e. needle-type precipitates are about 20 to 50 nm in length and partially or completely coherent with the matrix. On the other hand, rod-type precipitates are from 50 to 700 nm in length and have a low coherency with the matrix. Moreover, the stability of the needle-type precipitates depends very much on the temperature. With an increase in temperature, needle-type precipitates are dissolved, which leads to softening, as seen in Figure 2-9.

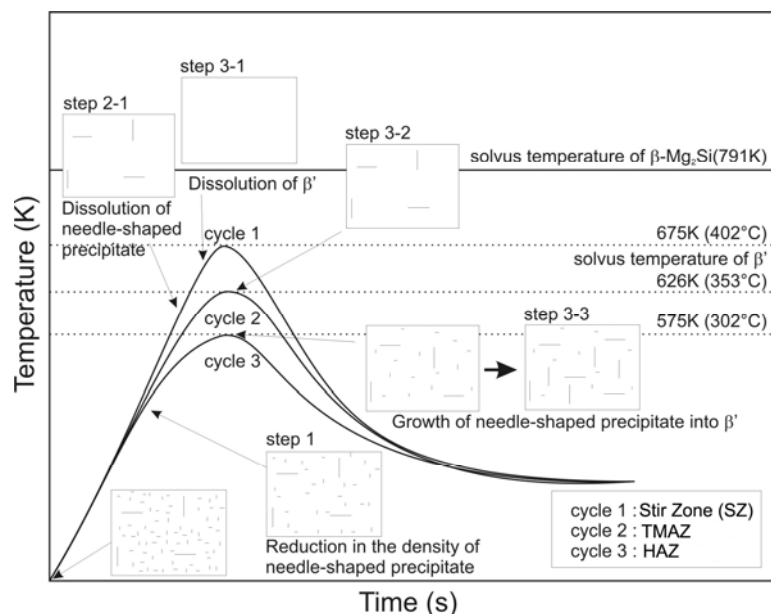


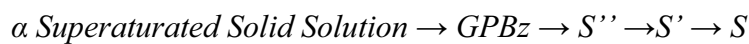
Figure 2-9 – Schematic illustration of the precipitation sequence during FSW [35].

Thermo-mechanical analysis of FSW heat-treatable aluminium alloy 6061 T6 using a finite element method has been reported [44]. The results indicated that the maximum residual stress in the joint was inferior to these resulting from conventional welding processes involving melting. Furthermore, two characteristics that produced a significant effect on residual stress and distortion of the workpiece were verified: (a) the fixture used to clamp the workpiece to the backing, and (b) the reduction of the weld strength at the SZ, TMAZ and HAZ of the heat-treatable Al alloys during cooling.

The microstructural changes associated with deterioration in mechanical properties across the welded joint produced during FSW of 6xxx artificially aged alloy, as has been mentioned above, is mainly due to the precipitate instability generated by the local heating. Strengthening precipitates in the welded joint can be fully or partially redissolved during FSW as well as coarsened, and the avoidance of such a phenomenon is still lacking in FSW technology. *A systematic investigation of the influence of energy input (thermal cycle and deformation levels) on 6xxx artificially aged FSW joints, regarding the understanding of the strengthening precipitates evolution during welding, can control the resulting microstructure and mechanical properties of the weld joint, in order to improve the joint performance.*

2.6 Aluminium-Copper-Magnesium Alloys

In 2xxx series alloys, copper is the prime hardening element. Magnesium is often added to increase the natural aging and tensile strength. The alloys are characterised by high strength, poor corrosion resistance, very low extrudability (typical extrusion speeds are as low as 1/6 m/min) and poor weldability by fusion techniques [24]. These alloys obtain their very high strength fundamentally by formation of GPB zones and precipitation of the phase “S” (Al₂MgCu). The precipitation sequence of aluminium alloys with this composition follows [45-51]:



where GPBz are the Cu-Mg Guinier-Preston-Bagariastkij zones, S'' and S' are the precursor metastable phase of the stable S phase. The clusters (GPBz) first precipitate out from an oversaturated α solid solution and their appearance in the first minutes of aging in a broad temperature range (110°C-240°C) has been based frequently on the interpretation of X-ray scattering. GPB zones are cylindrical (rod-type), 1-2 nm width and 4 nm length [45,46,47]. Thus, several attempts to observe them at this stage by means of strain field contrast in conventional transmission electron microscopy (TEM), selected area diffraction (SAD) and high resolution transmission electron microscopy (HRTEM) have failed. Differential scanning calorimetry (DSC) exothermal (50-150°C) and endothermal (150-280°C) peaks have been assigned to the GPB zones formation and dissolution. The schematic representation of the GPB zones morphology and respective crystal structure is shown in Figure 2-10. The stable Al₂MgCu phase, designed as S phase has an orthorhombic face centered structure with lattice parameters $a = 4.00$, $b = 9.23$ and $c = 7.14$ Å. The two intermediate structures (S'' and S'), both with slightly distorted S structure, present different degrees of matrix-precipitate coherence. Large stresses are

considered to be associated with the coherence of S'' . The S' phase has the same structure as the S phase, but slightly different lattice parameters, i.e. $a = 4.04$, $b = 9.25$ and $c = 7.18\text{\AA}$ [45].

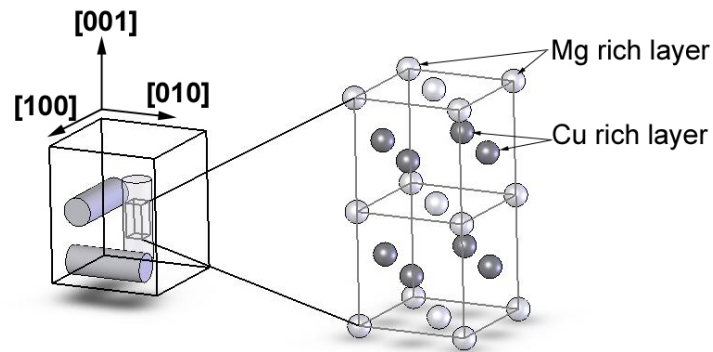


Figure 2-10 – Scheme of the GPB zones morphology and crystal structure (adapted from [46]).

Additionally, the S' phase has been shown to grow with a lath-type morphology [45]. Besides, precipitation investigations of Al-Cu-Mg alloy with artificial aging prior to the formation of stable S phase indicated the presence of a metastable phase named as GPB-II zone. It was observed the lath-type morphology for the detectable GPB-II zones are fully coherent with the matrix, using high-resolution transmission electron microscopy (HRTEM) analysis. It has been assumed that after 4 hours of aging at 180°C , some of the GPB zones grow to larger sizes and are identified as GPB-II zones. The HRTEM observations and diffraction analysis implied that the crystal structure of the GPB-II zones is distinctly different from that of GPB zones, having an orthorhombic lattice as the S phase and its precursors [46].

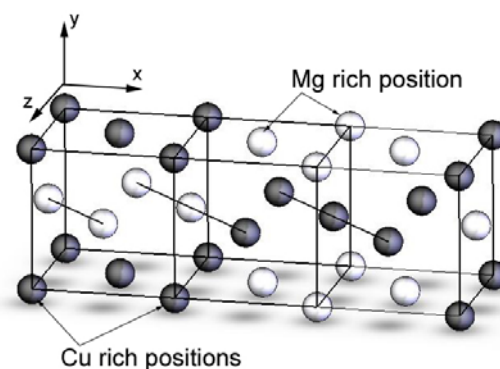
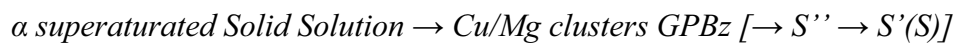


Figure 2-11 – Crystal structure of the GPB-II zones [46].

Fundamental investigations on the precipitation hardening and precipitation sequence of Al-Mg-Cu alloys has been carried out by Ratchev *et al.* [45]. It was shown that S'' phase can be formed heterogeneously on dislocation loops and helices, and a new mechanism of precipitation hardening due to this S'' was proposed. The precipitation of S'' on dislocations is the

predominant cause of strengthening during the initial stage of precipitation hardening. GPB zones (Cu/Mg clusters) also appear in the initial stage, but their contribution to hardness was shown to be smaller than that of the S'' precipitates. The usual precipitation sequence for the studied alloy was split in two parts since no link was observed between clusters and S'' phase formation in the early aging stage. The clusters form uniformly in the aluminium matrix, while S'' phase forms heterogeneously on dislocation helices and later transforms to the S' phase. On the other hand, at late aging stages S'' phase also precipitates uniformly in the matrix and transforms further to S' . The proposed precipitation sequence during aging at 180°C was [45]:



As no difference between the S' and S phase was detected, the last stage ($S' \rightarrow S$) of the sequence was dropped. Furthermore, it was reported [45] that by introducing pre-deformation, the clusters (GPBz) formation is inhibited, due to the annihilation of the quenched-in vacancies, then a precipitation hardening effect can be observed with baking. This was related to the hardening contribution of S'' phase precipitating on dislocations.

2.6.1 FSW of 2xxx alloys

The effects of the energy input produced during FSW on the resulting microstructure and mechanical properties, discussed in section 2.5.1, have also to be considered here for the 2xxx alloys, since overaging and dissolution of second phase particles can take place. A number of studies have been undertaken to characterize the effects of the FSW process on the resulting microstructure evolution and the mechanical properties of aluminium 2xxx series joints [48-54]. Investigations concerning process parameters evaluation were done by Ying Li *et al.* [48], which examined the flow pattern developed in the dissimilar FSW of 2024 to 6061. Three different tool rotating speeds were used: 400, 800 and 1200 rpm and their stir zones were analysed. At 400 rpm the contrast variation with deformation and dynamic recrystallization associated with the FSW process could be visualised by metallographic contrast in light microscopy. Therefore, the same weld zone at 1200 rpm tool rotation speed, where the apparent increase in FSW turbulence occurs, has effectively destroyed the regular flow zone features. Benavides *et al.* [49] compared the residual grain sizes and microstructures in 2024 Al friction stir welded specimens at temperatures of 30°C and -30°C. The maximum temperature measured in the low-temperature FSW specimen was about half of that in the room-temperature FSW specimen, where the maximum temperature in the weld zone was 330°C (0.6 T_M). The microhardness results have

shown the narrowing of the weld zone and a reduction of the HAZ at low temperatures (-30°C welded specimen) as well a declination of the weld efficiency represented by a tunnel defect. Investigations of 2219-O and 2219-T6 FSW joints from Chen *et al.* [50] indicated that the base material condition has a significant effect on weld morphologies, weld defects and mechanical properties of joints. In the 2219-O, no discernible interface was observed between SZ and TMAZ, and weld defects are liable to form in the lower part of the weld. However, in the 2219-T6, there is visible interface between the SZ and the TMAZ, and the defects are liable to form in the upper part of the weld. The strength of 2219-O joints was 100%, while that of 2219-T6 joints was only up to 82%. In addition, the two types of joints presented different fracture locations.

Investigations in 1mm thick 2024-T3 aluminium alloy have been recently carried out by Shukla *et al.* [51], evaluating the effects of the FSW process parameters on the microstructure and mechanical properties. The hardness profiles across the weld indicated a soft region in the HAZ adjacent to the TMAZ, a hardness peak in the HAZ, and a second hardness minimum in the HAZ. The changes in hardness were attributed to the presence and coarsening of *S* phase, the formation of GPB II zones, and the dissolution of GPB zones, respectively. The hardness minima at the TMAZ/HAZ boundary, percentage elongation and the tensile strength of the welds were showed to increase with the decrease in heat input. Jones *et al.* [52] by using transmission electron microscopy (TEM) to explain the correlation between the weld microstructures and microhardness, found that the HAZ on the retreating side of a friction stir welded AA2024-T351 aluminium alloy contains two distinct hardness minima on either side of a maximum out of the stir zone. The explanation of the inner hardness minimum close to the TMAZ was the coarsening and overaging of the *S* phase (Al_2CuMg) occurring during the thermal cycle. The outer hardness minimum was thought to be due to dissolution of the very fine *S* phase, occurring towards the outer edge of HAZ. The hardness maximum between these two minima was seen to be due to the presence of very fine *S* phase precipitates, and is likely to be a result of optimum aging conditions being achieved.

Recent investigations of AA2024 from Genevois and co-workers [53] reported precipitation and mechanical behavior for the T351 and T6 tempers. For the weld in T351, the initial precipitation is composed entirely of GPB zones. In the HAZ, the increase of temperature induces the dissolution of GPB zones and the latter are replaced by fine *S'*(*S*) precipitates. These particles grow with higher temperature, producing a hardness fall in the region HAZ/TMAZ. In the TMAZ, the *S'*(*S*) fraction is maximal, leading to a minimum in hardness due to the precipitates coarsening. Throughout the stir zone, the highest temperature results in a smaller

fraction of coarse $S'(S)$ precipitates, and consequently, a higher level of available solute. For the weld T6 temper, the precipitation microstructure is similar to the weld in T351 temper, from the weld line to the high temperature HAZ. In the base material and HAZ close to the base material, the 2024 T6 weld is harder than the 2024 T351, because the main precipitates are fine $S'(S)$. The main contribution to the strengthening is controlled by the size and volume fraction of $S'(S)$ precipitates. Tensile testing normal to the welding direction showed fracture in the TMAZ/SZ boundary. Strain localization is more pronounced in the 2024 T6 weld than in the 2024 T351 due to the higher strength differences between base material and TMAZ. Additionally, the effect of the microstructure heterogeneity on the global and local tensile properties of FSW joints in AA2024 (T351 and T6 tempers) was also investigated by Genevois *et al.* [54]. It was verified that the tensile properties of the various regions of the 2024 T351 and 2024 T6 welds were very heterogeneous and essentially controlled by the state of precipitation. The 2024 T6 base material was stronger than the 2024 T351 alloy, leading to more pronounced strain localisation during transverse tensile tests and a lower overall ductility.

Considering the effects of the FSW process on the above mentioned 2xxx naturally aged alloys, where the alloy strength is initially assured by the GPB zones, the indications of softening in the HAZ and mainly in the TMAZ region are unpleasant, but can be controlled by the energy input generated during welding. The strength deterioration at these zones is essentially attributed to formation and coarsening of S' precipitates, and the dissolution of GPB zones. There is still a lack of understanding, particularly concerning the influence of the FSW energy input on the resulting micro and substructure evolution and their relation to mechanical properties. *The systematic study of the micro and substructure evolution along the different weld zones of FSW 2xxx naturally aged joints, in relation to energy input, is needed to understand the metallurgical transformations and consequently to minimize the softening effect produced by the FSW process, thereby improving the joint performance.*

3. OBJECTIVES

When using FSW to join precipitation-strengthening alloys such as AA2024 T351, AA6013 T6 and Al-Mg-Sc alloys, several phenomena occur mainly regarding overaging and dissolution of precipitates, which are crucial in order to assure the material strength and subsequent quality of the joint. Therefore, an optimized control of the FSW process parameters through *knowledge, based on the selection of the energy input supplied to the joint*, is expected to improve the resulting microstructure and mechanical behaviour. In this work, it is intended to establish the interrelation between process and joint performance, through process assessment and monitoring, and by further mechanical investigation into the macro, micro and substructural analysis of the welded joints.

The global objective of the present work is to *explain the metallurgical transformations* resulting from the FSW process on AA2024-T351, AA6013-T6 and Al-Mg-Sc plates joined using different welding parameters, with the purpose of *establishing the influence of the plastic flow and thermal cycle, produced during the process, on the microstructure, stability of the precipitates and related mechanical properties*. Additionally, the appropriated methodology has been developed to substantiate the properties of the joints, based on the understanding of the micro and substructural evolution resulting from the previous heat treatment conditions and the welding parameters used to produce the joints.

Moreover, specific objectives have also been defined as follows:

- To establish relationships between the characteristics of the different weld zones and the thermal cycle, resulting from the different welding parameters, involving basically the understanding of the structural evolution between the different Al alloys.
- To generate, compile and correlate data from mechanical tests, including microhardness, transverse tensile testing and microflat tensile testing. The mechanical testing program includes the base material investigation for comparative purposes.
- To generate knowledge from process data such as thermal cycle and microstructural evolution, to be used to validate further modelling and simulations.
- To develop a methodology to determine the structural properties/welding parameters relationships of AA2024 T351, AA6013 T6 and Al-Mg-Sc alloys joined by an FSW process.

4. EXPERIMENTAL PROCEDURE

4.1 Overview of the Methodology

The experimental investigation follows the methodology described in the flow chart presented in Figure 4-1.

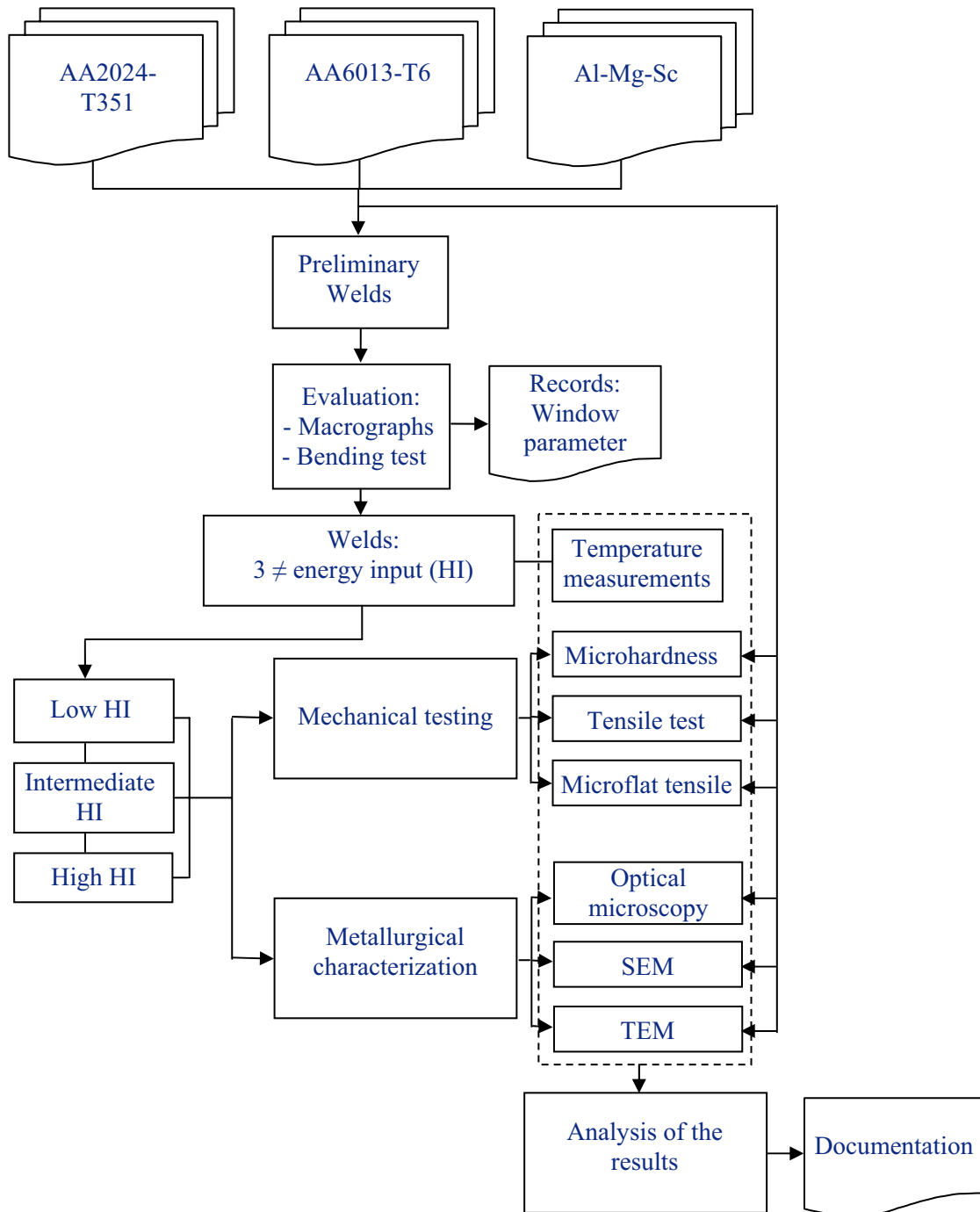


Figure 4-1 - Flow chart describing the overall work program.

The following Al alloys have been selected for this work: AA2024 T351, AA6013 T6 and Al-Mg-Sc. Preliminary welds were performed within the scope of the cooperation project with Airbus ENFASIS, comprising a wide parameter matrix of FSW joints, which were subsequently evaluated in terms of macrograph and bending test, in order to establish an optimized FSW parameter matrix to produce non-defective and good-quality joints. The information about the development of the optimized parameter matrix can be found in the unpublished final report of the ENFASIS project.

Based on the optimized FSW parameter matrix, butt joints of the selected aluminium alloys were produced with 3 different FSW energy inputs, which were named low HI, intermediate HI and hot HI (HI = Heat Input). Temperature measurements were carried out during welding using thermocouples in the workpiece and backing bar. Samples for mechanical testing and microstructure characterization were produced from the different base material alloys and joints as well as the different energy inputs. The mechanical testing included microhardness profiles, flat tensile tests and microflat tensile tests, in order to determine the global and local tensile properties across the base material and different FSW zones of the joint. The metallurgical characterization was performed in terms of optical microscopy and scanning electron microscopy (SEM), in order to observe the effects of the weld on the macro and microstructural aspects of the materials. The substructural aspects of the materials, such as precipitation and dislocation features, were investigated using transmission electron microscopy (TEM). Therefore, an evaluation of the mechanical testing and metallurgical characterization was accomplished comparing the results from the base material alloys and weldments with different energy inputs, and a correlation between process energy inputs, structural features and mechanical properties has been established as well as a precipitation evolution model proposed. The documentation of the work has been done by the present PhD. thesis and additional papers for scientific journals.

4.2 Materials and Heat Treatment

The aluminium alloys under investigation in this work were 4mm thick plates of:

- **AA2024 heat treated to T351.** The condition T351 included solution heat treatment and stress relieved by stretching. This is equivalent to T4 condition and is usually applied to 2024 plate and rolled bars.
- **AA6013 artificially aged to T6.** The heat treatment to T6 included artificial ageing during 4 hours at 190°C and air-cooling. This treatment produces a fully heat-treated condition (maximum strength).

- **Al-Mg-Sc** (Weld joints were followed by post-weld heat treatment (PWHT), being aged 2 hours at 325°C)

These aluminium alloys are designed specially for aerospace applications. Further information on the aluminium alloys investigated in this work is given in items 2.4 to 2.6 of Chapter 2. The chemical composition of the base materials are presented in Table 4-1.

Table 4-1- Chemical composition of the aluminium alloys base material [(%) weight]

Alloy	Si	Mg	Cu	Mn	Fe	Zn	Cr	Ti	Sc	Al
AA2024	0.19	1.24	3.94	0.55	0.234	0.221	0.009	0.024	-	93.6
AA6013	0.699	1.07	0.783	0.357	0.215	0.034	0.028	0.016	-	96.8
AlMgSc	0.06	4.3	0.024	0.08	0.12	0.007	0.009	0.018	0.27	94

4.3 Friction Stir Welding Process

The plates of AA2024 T351, AA6013 T6 and Al-Mg-Sc were friction stir welded using a Neos Tricept 805 robotic system with five axis and a CNC Siemens Sinumeric 840D controller, located at GKSS Research Center GmbH, Geesthacht - Germany. The Tricept 805 robot is equipped with a force control unit, to ensure reproducibility and consistency of the friction stir welds. Figure 4-2 presents the robotic system used to perform the welds with considerably quality and reproducibility, mainly due to the coupled gauge systems and mechanisms of process control. A similar butt joint configuration was used to produce all the friction stir welds.

One of the aspects exerting great influence on the final weld seam produced is the FSW tool, which according to size and geometry (added to other FSW parameters) will produce a characteristic material flow. Coupled to the robot spindle, the FSW tool is responsible for the material stirring and forging during the welding process. Unique tool geometry was chosen to perform the welds for the different aluminium alloys in this work. The FSW tool used comprises a 15 mm diameter concave shoulder and a 5 mm diameter conical threaded pin with three flats, both made of high-speed steel. The FSW tool used to produce all the joints for this work is shown in the images of Figure 4-3. The image of the concave shoulder, presented in Figure 4-3 (a), shows details of the surface that produces most of the heat and the forging pressure (clear part) with a hole in the center where the tool pin of Figure 4-3 (b) is fixed.



Figure 4-2 - Neos Tricept 805 Robot system used to produce the joints by FSW, with the ability to perform welds of up to 45kN axial load.

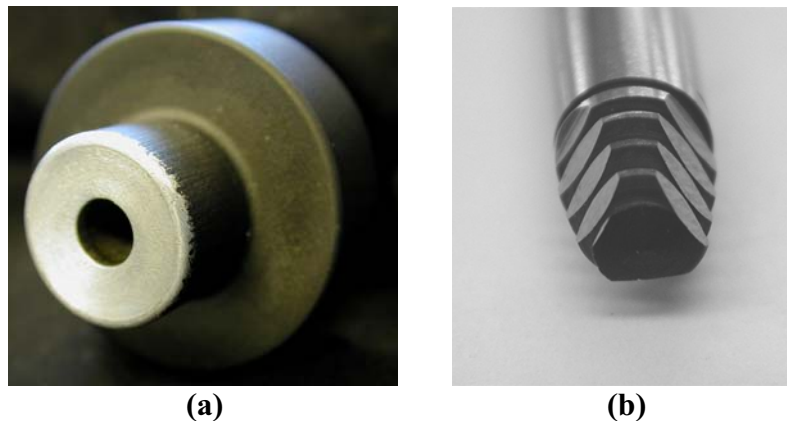


Figure 4-3 – FSW tool used to produce the joints. (a) Concave shoulder and (b) threaded 3 flats pin, shown separately.

As mentioned in section 3.1, based on the optimized matrix of parameters, all friction stir welds for a given alloy were produced, when possible, using a unique down force in conjunction with 3 levels of energy inputs, in order to produce samples with particular parameter combinations; named high HI, intermediate HI and low HI conditions. FSW studies have demonstrated that weld travel speed is the primary factor in controlling heat input during processing [7,55,56,57]. It was envisaged that the energy input could be much better manipulated through varying weld travel speeds than by any variation in rotation speed or axial load exerted on the FSW tool. An important and unknown factor, however, is to what extent an aluminium alloy can be induced to flow by means of the FSW process, varying essentially the weld pitch (tool rotation/weld travel speed) without disruption of the aluminium plastic flow and the

degradation of mechanical properties. The ability to maintain a constant tool rotation speed and a variable weld travel speed allows one to estimate the effects of aluminium plastic flow and the resulting mechanical properties as a function of the number of tool rotations per mm of weld length, hereafter defined as weld pitch (WP). The three different welding parameters selected are described with their respective terminologies in Table 4-2.

Table 4-2 – Terminology and FSW parameters employed.

Material	Terminology	FSW parameters		
		Rotation speed (rpm)	Welding speed (mm/min)	Axial load (kN)
AA2024-T351	WP8 (high HI)	800	100	12
	WP4 (inter. HI)	800	200	12
	WP2 (low HI)	800	400	12
AA6013-T6	WP4 (high HI)	900	225	12
	WP2 (inter. HI)	900	450	12.5
	WP1.33 (low HI)	900	675	13
Al-Mg-Sc	WP4 (high HI)	700	175	10
	WP2 (inter. HI)	700	350	10.5
	WP1.33 (low HI)	700	525	10.5
AA2024-T351, AA6013-T6, Al-Mg-Sc	BM	Base Material		

In terminology, WP (Weld Pitch) is a relation rotation (rpm) / welding speed (mm/min)

It has to be remarked that WP is an “energy input equivalent” (rotation/mm) and not exactly the energy input produced during the process. The energy input can be correlated with WP as demonstrated in the diagram of Figure 4-4. In this case, the energy input has been calculated for the selected alloys according to the welding parameters presented above in Table 4-2. The heat generated (q) was determined based on equation 2, using a frictional coefficient $\mu = 0.2$ and the friction interface considered was related to the shoulder radius. For the determination of the energy input, the heat generated was related to the transverse welding speed (q/v), regardless of the efficiency of the spindle (motor) of the FSW machine. According to the chart of Figure 4-4, the highest energy energy inputs were used to join the AA2024 T351 alloy while lower energy inputs were enough to join the AA6013 T6 and especially Al-Mg-Sc alloy.

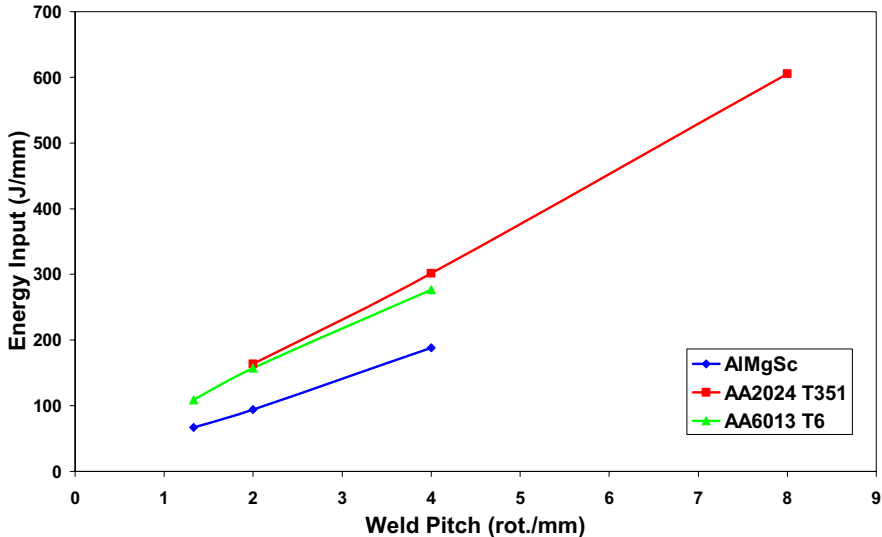


Figure 4-4 – Correlation between WP and calculated energy input considering the FSW parameters used to join Al-Mg-Sc, AA2024 T351 and AA6013 T6 alloys.

4.4 Temperature Measurements

Temperature measurements were performed during FSW for the different aluminium alloys and the respective WP’s. The temperature values were helpful to quantify and correlate the three levels of energy inputs in this study for the all different aluminium alloys. The measurements were carried out using a computerized signal processing system. The equipment consists of a data acquisition system with an external amplifier and integrated AD-converter. The equipment can evaluate signals from up to 32 channels using an aquisition rate of 333 kHz. The software Labview performs the evaluation in real time. Thermocouples type k (nickel-chrome / nickel-aluminium) with 0.5 mm diameter were used, placed in the plate material and in the backing bar for the temperature measurements. The thermocouples were fixed in different positions along the plates and the backing bar. The layout of the thermocouples’ positioning was the same for all alloys investigated.

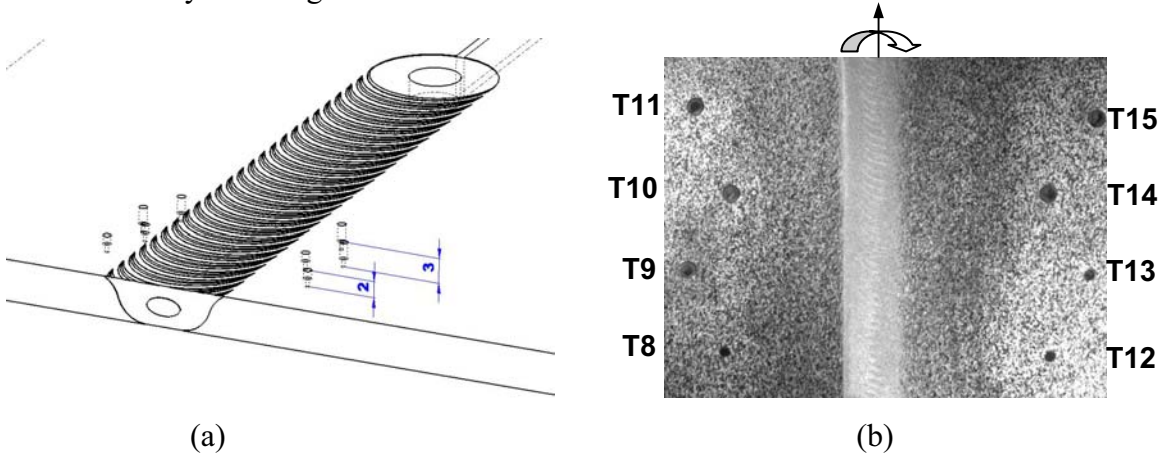


Figure 4-5 – Scheme of the FSW joint in (a) and top surface macrograph in (b) showing the position of the thermocouples for the temperature measurements in the workpiece.

For the insertion of the thermocouples in the aluminium plates, 0.5 mm diameter holes were drilled in the top surface of the material at 10 mm and 12.5 mm from the center line of the butt joints with 2 mm (half plate thickness) and 3 mm depths, separated by 5 mm from one other (in the welding direction), as illustrated in the schematics and macrograph in Figure 4-5. Additionally, 1 mm diameter holes were drilled in the top surface, over the previous holes with 1 mm and 2 mm depths respectively, in order to facilitate locating the thermocouples, as can be observed by the different diameters of the holes in the macro of Figure 4-5 (b). The same location of the thermocouples was applied for both retreating and advancing side. Consequently, the temperature was monitored with 4 thermocouples on each side of the weld seam.

Thermo-channels for 7 thermocouples (T1-T7) were machined about 0.5 mm under the surface of the backing plate. The thermocouples were mounted in the channels in different positions, in order to obtain the temperature profiles in different weld zones under the FSW tool. Following the welding direction, the thermocouples were placed 10, 5 and 2.5 mm away from the weld centre on the retreating side, one on the weld center line, and at 2.5, 5 and 10 mm away from the weld centre on the advancing side (see Figure 4-6). The thermocouples were properly fixed in the backing bar so that the influence of external factors would be minimized in the temperature measurements.

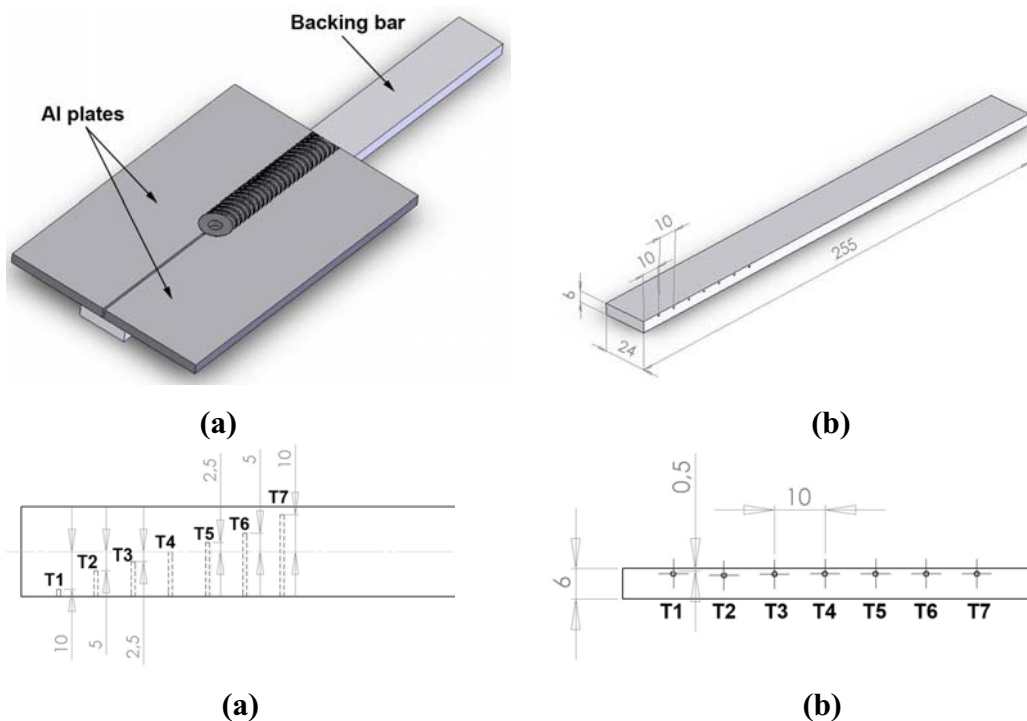


Figure 4-6 – Schematics of the the temperature measurements in the backing bar showing the location of the thermocouples (distance in mm). (a) Assembly of backing bar and weld plates, (b) backing bar, (c) top view and (d) side view.

4.5 Mechanical Testing

Mechanical tests were carried out in the friction stir welded joints as well as in the base material, in order to determine the mechanical properties and to correlate these with the micro and substructural characteristics along the joints. The testing methods used to investigate the mechanical properties included microhardness profiles, transverse tensile testing and microflat tensile testing, all performed at room temperature. The testing methods are described in the following sections.

4.5.1 Microhardness

Microhardness tests following the ASTM E384-99 standard [58], were performed across the joint section previously polished, transverse to the weld seam, using a Shimadzu-HMV-200 machine with a computer controlled displacement and indentation, coupled with the software Duramin for Windows NT to analyse the data results. The tests were accomplished using conventional Vickers indenter for hardness measurements and using a 1.96 N (0.2 kg) load for an indent period of 10 seconds. The measurements were conducted at the mid-thickness of each work-piece across the welded joint, along the base material and FSW zones, maintaining 0.5 mm spaces between each indentation.

4.5.2 Tensile Test

Static tensile tests were performed using flat tensile specimens extracted by spark erosion transverse to the plate rolling direction for the parent material and for the friction stir welded material. The specimens were machined according to the Standard DIN – EN 895 [59] for transverse flat tensile test specimens, as shown in Figure 4-7. The specimen centre was located exactly in the middle of the welded joint (see Figure 4-7). The flat tensile test results were given as an average of three tested specimens for each FSW energy input in the AA20224 T351, AA6013 T6 and Al-Mg-Sc joints and the respective base materials. The testing conditions used were a maximum load of 50 kN and the testing speed was 0.5 mm/min to an $l_0 = 60$ mm. The tests were carried out at room temperature in a screw-driven tensile testing machine model 1484 from ZWICK.

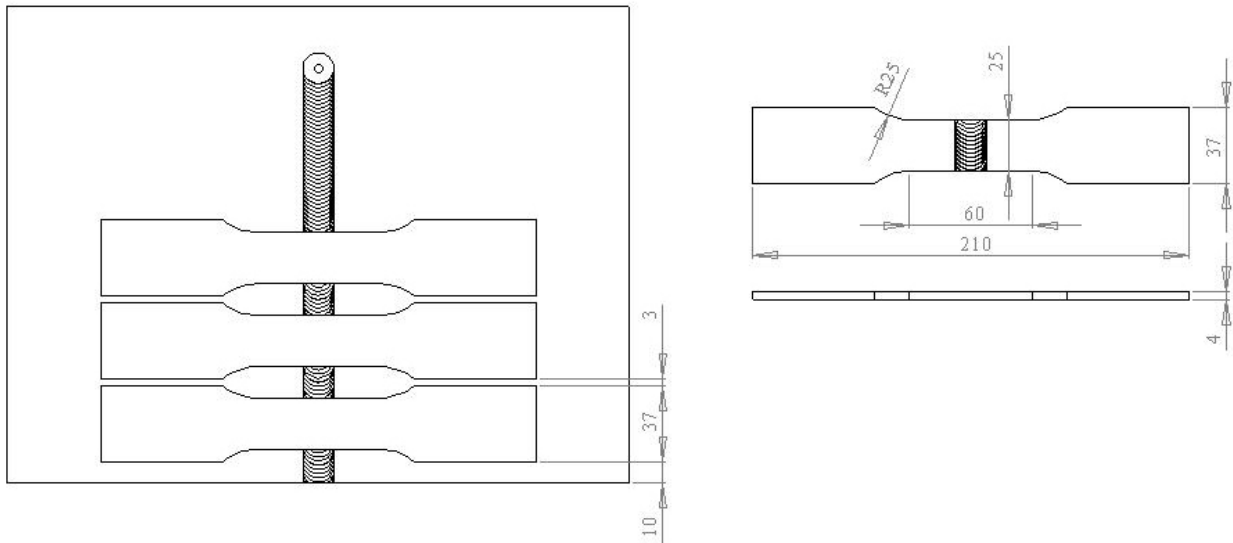


Figure 4-7 – Geometry of the flat tensile specimens used to evaluate the tensile properties of the FSW joints and base material (dimensions in mm)

4.5.3 Microflat Tensile Test

Microflat tensile test specimens with 0.5 mm thickness were precision extracted by spark erosion from the friction stir welded plates, located along the welded joint. Figure 4-8 presents the position parallel to the weld joint, where the microflat tensile specimens were obtained from the different friction stir weld zones and base material. This test enables a detailed characterization, revealing the local tensile properties along the different weld zones of the joint, compared to the base material [60]. Microflat tensile tests were performed using an INSTRON screw-driven machine model 1195. A maximum load of 1 kN with a speed of testing of 0.2 mm/min were the machine parameters for the different aluminium alloys. The tests were monitored by a FOEPS 50 mm laser extensometer, coupled with a data system to record the displacement. White stripes were painted in the surface of the specimen in order to produce an l_0 of 8 mm, making elongation measurement possible by the laser gauge system. The values measured were registered and analysed using LQ/CFG 1.8 software. The microflat tensile specimens were produced with the dimensions presented in Figure 4-9. Contrary to the conventional tensile tests of the base material, the microflat tensile specimens of the base material were obtained in the rolling direction of the plates.

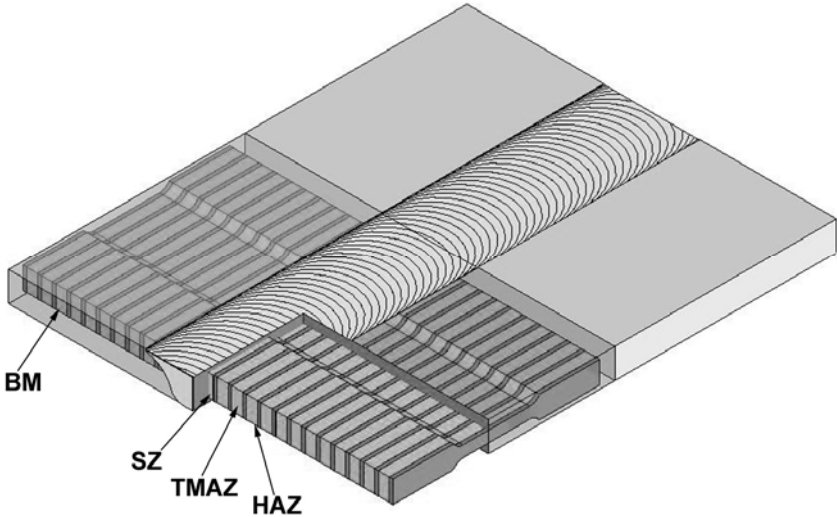


Figure 4-8 - Schematic illustration of the microflat specimens obtained. Weld joint representation with the specimen’s disposition along the weld joint, indicating the corresponding weld zone and base material.

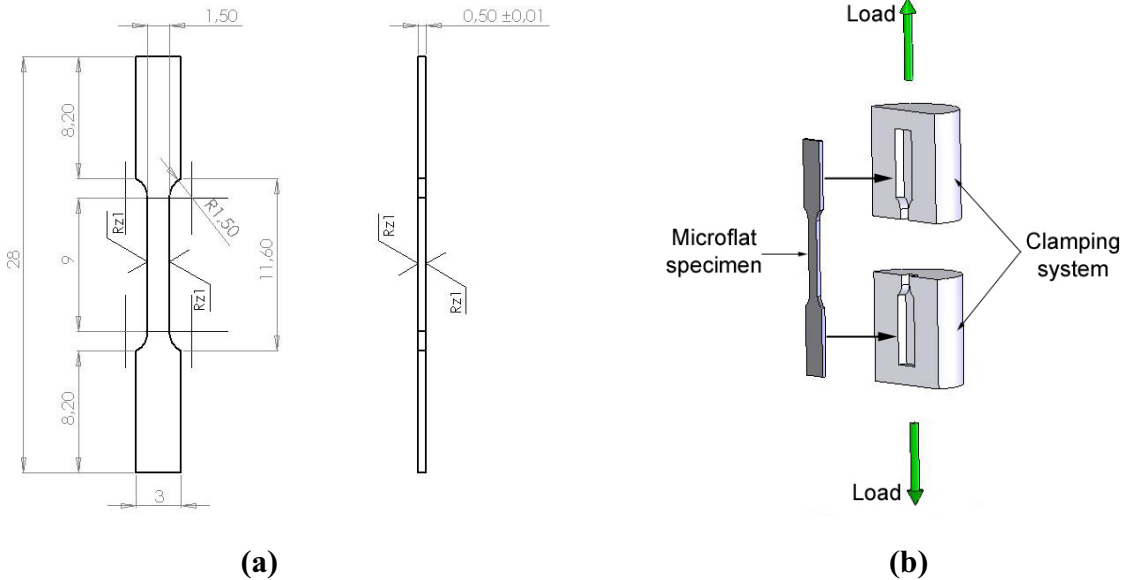


Figure 4-9 – Geometry of the microflat tensile specimens used to investigate the local tensile properties for the FSW process (dimensions in mm) (a), and scheme of the clamping system (b).

4.6 Metallurgical Characterization

A detailed metallurgical characterization was devised in order to understand the effects of the thermo-cycle and deformation produced by the FSW process on the aluminium alloys studied, correlating them with the mechanical testing. The complete metallurgical assessment was performed using Optical Microscopy (OM), Scanning Electron Microscopy (SEM) and Transmission Electron Microscopy (TEM).

4.6.1 Macrostructure Characterization

All the welded joints were carefully evaluated in order to reveal the macrostructure and verify the presence of defects or other effects resulting from the solid-state welding process. The samples were cut perpendicularly to the welded seam and prepared according to standard metallographic procedures, following ASTM E3-95 [61] and ASTM E340-95 standards [62]. Samples were ground and polished on a Buehler Motopol 2000 mechanical grinding and polishing automatic machine, using grinding papers (320/500/800/1200/2400) for 1 minute in each step at 300 rpm with water, and later polished using cloth Struers Mol-Tuch with a 3 μm diamond suspension for 4 minutes with Struers lubricant red at 150 rpm. The finishing step was carried out in a cloth Struers Chem-Tuch with an OP-S 0.05 μm SiO_2 alkaline solution for 4 minutes at 150 rpm with water dripping. After the metallographic preparation, samples were etched using: Kroll reagent (2% HF, 8% HNO_3 and H_2O balance) for the AA2024-T351 and Al-Mg-Sc alloys, and Flick reagent (i.e. 10 ml HF, 15 ml HCl and 90 ml H_2O) for the AA6013-T6 alloy.

The macrostructure investigation was carried out by producing images from the weld region features using an optical microscope Olympus MPG 3 with a CCD camera adapted, which was subsequently also used for the microstructural characterization in polarized light mode.

4.6.2 Microstructure Characterization

A microstructure characterization was carried out to investigate the microstructure evolution within the joints (i.e. grain size, morphology), resulting from the FSW process, as well as a base material microstructure evaluation of the different aluminium alloys.

Fundamentally, the metallographic procedures that were used for the microstructural investigation were the same as those used to prepare samples for macrostructural characterization. However, all the samples for OM investigation under polarized light were electrolytic anodized using Barker reagent (i.e. 5 ml fluoroboric acid in 200 ml water) in order to

disclose the grain structures. Images were taken approximately at half thickness of the transverse section of the welded joints, i.e. evidencing the weld centre for the stir zone, beside the stir zone bordering the TMAZ (interface region recrystallized/unrecrystallized grains) and HAZ (non deformed grains). The grain structure from the base material, which was unaltered by the process, was also evidenced for comparison purposes.

The microstructural analyses using SEM were conducted using a ZEISS model DSM 962 in BSE (Back Scattered Electrons) mode, in order to observe microstructural aspects that require higher magnification, such as particular grain structures and dispersoids. The samples preparation was similar to that previously described for macrostructural characterization, but the samples were not etched and a conductive mounting resin (DemoTec 70) was used, in order to obtain a suitable electric contact between the sample (cathode) and the SEM sample holder (anode).

4.6.3 Substructure characterization

The substructure features, particularly those related to precipitation phenomena and dislocation structures, were investigated by TEM. The preparation of thin foils for the TEM investigation began by cutting discs of 2.3 mm diameter from the head of the microflat tensile specimens in different weld zones along the welded joint and base material, as illustrated in Figure 4-10, for the different weld energy inputs of all aluminium alloys investigated. There was no plastic deformation associated with the area where the samples were extracted (head of the microflat specimen), retaining the previous material characteristics, even after the tests. It occurs because the geometry of the clamping system allows only the applied load to act directly over the internal radius (both sides) of the microflat tensile specimen, instead of the usual clamping system using grips (see Figure 4-9, Figure 4-11). The samples were later polished using jet electro-polishing Struers Tenupol-3 by the twin-jet method, in a solution of 15 ml nitric acid, 50 ml perchloric and 935 ml methanol at -30°C until producing a very small hole, generally in the center of the disc. The electrolytic polishing parameters selected were 18 V and 0.05 A. Schematics of the microflat tensile specimen, with the position of the TEM sample and electrolytic polishing are shown in Figure 4-11.

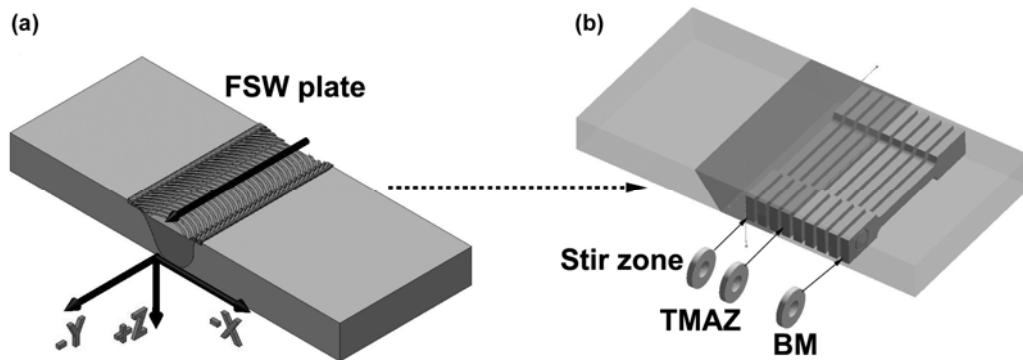


Figure 4-10 – Schematic illustration of the friction stir welded plate and the disposition of TEM specimens obtained from the microflat tensile specimens, located in different weld zones and base material.

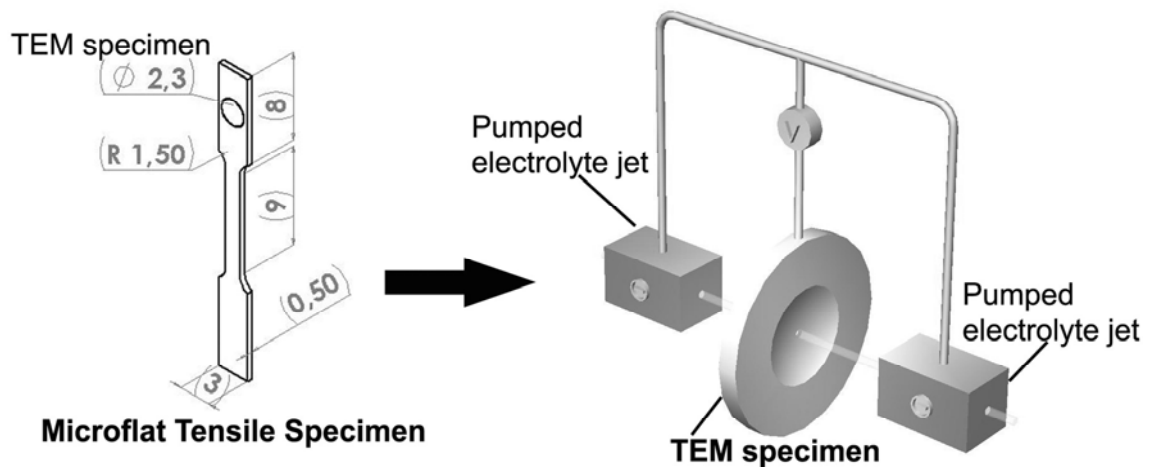


Figure 4-11 - Schematic illustration of the TEM sample extraction from a microflat tensile specimen and its electropolishing.

To produce the micrographs and diffraction patterns presented in this work, a Philips CM 20 transmission electron microscope (TEM) working with an accelerating voltage of 200 kV was used, coupled with a scanning transmission electron microscope (STEM) bright-field/dark-field detector, using a double-tilt holder stage. The chemical elements present in the second-phase particles were determined using an Energy Dispersive Spectrometer (EDS) equipped with an Si (Li) detector.

Dislocation and precipitate evolution were investigated along the transverse section of the welded joints and respective base materials, as shown in the illustration in Figure 4-10. Some microstructural aspects as grain structures and second phase particles were also observed in TEM, mainly for the Al-Mg-Sc alloy. Bright as well as dark-field images were generally used to verify the morphology, size and disposition of dispersoids and strengthening precipitates across the aluminium matrix. The diffraction patterns were produced in order to identify the precipitates presence and orientation relative to the aluminium matrix [63].

4.6.4 Image Processing

Image analyses were performed directly on images obtained from TEM (essentially for the Al-Mg-Sc alloy), in order to estimate quantitative precipitation results, providing statistically significant data, such as precipitate average diameter, amount of precipitates, morphologies, as well as the volume fraction of precipitates. A minimum of 500 precipitates were analyzed for each weld zone and each FSW condition. TEM images were then imported into Leica QWin software [64]. Occasionally it was necessary to reduce the total information content of an image to a few pertinent measurements. The advantage of this approach is that information was discarded in a controlled manner and it made images easier to analyse with irrelevant details removed. An illustration of the image processing carried out on the TEM micrographs is shown in Figure 4-12, where the measurements of amounts of precipitates, precipitate diameters and grain areas are represented. A prior calibration of the software was carried out according to the scale of each TEM micrograph. The precipitate counting and precipitate area calculations were done automatically by the software and displayed in a worksheet, simultaneously with the precipitate diameter measurements, which were done manually. The volume fraction of precipitates was estimated in terms of precipitates per area of the micrograph, and then extended to the volume, assuming that its precipitation characteristics do not vary significantly along the material volume. The distribution of precipitates was given in terms of A/A_0 , where A is relative to the area occupied by the precipitates in the micrograph, and A_0 is the overall area of the micrograph. The precipitate distribution was estimated for the stir zone and TMAZ of different energy inputs, and the corresponding base material, for comparison. Thus images in a magnification range from 50K to 200K were measured.

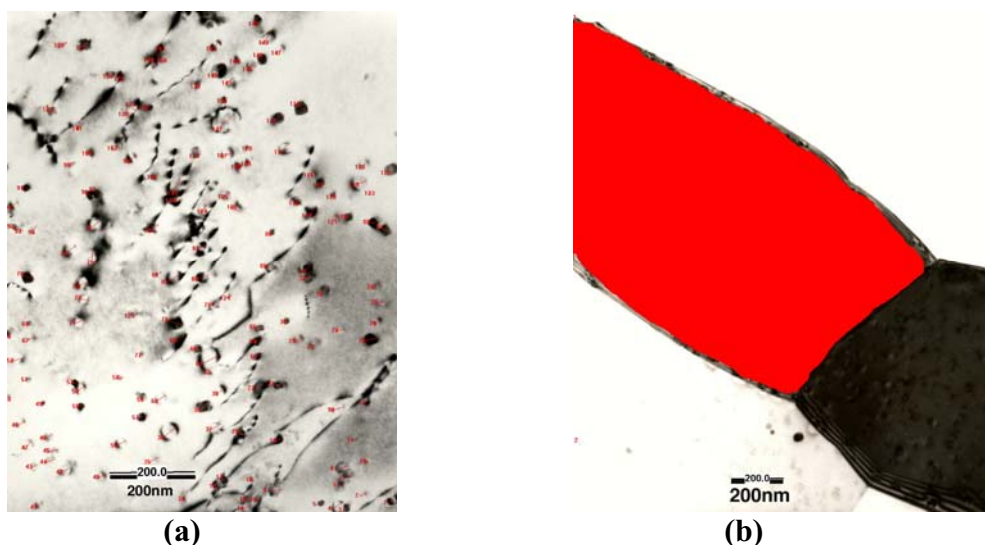


Figure 4-12 – Illustration of the measurements performed on TEM images using Leica QWin software. (a) Determination of precipitate average size and population, (b) grain area.

5. RESULTS AND DISCUSSION

In this chapter, the results of the work described in chapter 3 are presented and discussed systematically, in order to provide the necessary understanding on the FSW process of the 3 different aluminium alloys. In section 5.1, the results of the work in terms of temperature measurements, mechanical and metallurgical characterization of the Al-Mg-Sc FSW joints are presented and discussed. The same investigations on the AA2024 T351 FSW joints are presented in section 5.2 and, subsequently, the investigations on the AA6013 T6 FSW joints are presented in section 5.3.

5.1 Characterization of the Al-Mg-Sc Friction Stir Welded Joints

5.1.1 Thermal history during FSW Process

The temperature measurements carried out in-situ, during the FSW of the Al-Mg-Sc joints, were obtained through thermocouples placed in the aluminium plates and in the backing bar, which registered the thermal cycle applied for each welding condition. As mentioned in section 4.4, the thermocouples T1 to T7 were placed in the backing bar, while thermocouples T8 to T15 were placed in the Al-Mg-Sc plates for all FSW conditions. It was attempted to measure the thermal cycles taking place at the SZ and HAZ/TMAZ interface. Thus, in this work, temperature measurements obtained from the backing bar (very close to the stir zone) were assumed as an approach of the temperatures in the SZ and the temperature measurements obtained at the workpiece (Al-Mg-Sc plates) were assumed as an approach of the temperatures in the HAZ/TMAZ interface, since the measurements were close to this region. It is still necessary to consider that peak temperature variations for thermocouples placed at the same distance on both sides of the weld can sometimes be positioned at different distances and depths as a consequence of the plastic stirring, which can drift the weld centre. Inaccuracies associated with the drilling of the holes for the thermocouples fixing has also to be considered. Minor differences in the maximum temperature in the backing bar can be attributed to misplacement of the plates. A possible shift of the weld centre line can also be considered, but may not be significant. Therefore, the resulting thermal cycle for each region was determined in terms of “average thermal cycle”, essentially considering the maximum temperature values obtained in the backing bar for the SZ and in the workpiece for the HAZ/TMAZ. The thermal history measured for the Al-Mg-Sc joints in WP1.33, WP2 and WP4 conditions are shown in Table 5-1.

Table 5-1 – Thermal history of Al-Mg-Sc FSW joints using WP1.33, WP2 and WP4, low intermediate and high HI, respectively.

Energy input	WP1.33		WP2		WP4	
	HAZ/TMAZ	SZ	HAZ/TMAZ	SZ	HAZ/TMAZ	SZ
Max. temp.	250°C	295°C	276°C	309°C	327°C	372°C
Heating rate	36.6° C/s	106° C/s	30.7°C/s	55.8°C/s	12.4°C/s	26.3°C/s
Cooling rate	2.85°C/s	3.14°C/s	3 °C/s	3.32°C/s	2.8°C/s	2.4°C/s
Dwell time	6 s	2.5 s	8 s	5 s	24s	13s

The maximum temperature in the *backing bar* (SZ - 295°C) of the WP1.33 joint (low HI), was measured in T3 and T5 thermocouples placed 2.5 mm from the joint line. T3 and T5 registered 2.5 seconds to reach maximum temperature at 2.5 mm from the joint line and the weld cooling down to 50°C took about 78 seconds (cooling rate of 3.14°C/s). The maximum temperature in the *workpiece* (TMAZ - 250°C) was measured at 10 mm from the joint line on the advancing side (T10). For the thermocouple T10, it took around 6 seconds to reach maximum temperature and the weld cooling, from the maximum peak temperature down to 50°C, being about 70 seconds (cooling rate of 2.85°C/s). It has to be remembered that the thermocouples were positioned close to, but not in, the core of the heat input where the highest temperature occurs. The low HI condition is expected to produce less influence on the mechanical and microstructural aspects, due to the lower temperature and faster thermo-cycles involved (i.e. high heating and cooling rates).

The thermal history obtained in the WP2 condition (intermediate HI) shows the maximum temperatures in the *backing bar* (SZ - 309°C) placed 2.5 mm from the joint line (T3 and T5). These thermocouples registered around 5 seconds to reach maximum temperature and the weld cooling down to 50°C took about 78 seconds (cooling rate of 3.32°C/s). The maximum temperature was achieved in the *workpiece* (TMAZ - 276°C) at 10 mm distant of the joint line in the advancing side (T10). The thermocouple T10 took about 8 seconds to reach maximum temperature and the weld cooling down to 50°C took about 75 seconds (cooling rate of 3°C/s).

The WP4, the most critical energy input condition (high HI) showed the maximum temperatures in the *backing bar* (SZ - 372°C) at 2.5 mm from the joint line (T3 and T5). Thermocouples T3 and T5 showed 11 and 13 seconds, respectively, to reach maximum temperature and the weld cooling down to 50°C took about 114 seconds for both T3 and T5 thermocouples (cooling rate of 2.4°C/s). Thermocouples placed in the *workpiece* showed the maximum temperature (TMAZ - 327°C) at 10 mm distant of the joint line, in the advancing side

(T8 and T10). In this region, thermocouples T8 and T10 took respectively, around 21 and 24 seconds to reach peak temperature in the advancing side and approximately 112 s (T8) and 114 s (T10) to cool down to 50°C (cooling rate of 2.8°C/s).

The thermal cycles obtained for the SZ closest region are given for the different FSW energy inputs in the diagram in Figure 5-1, in terms of backing bar temperature measurements, whilst the thermal cycles obtained for the HAZ/TMAZ interface closest region (workpiece) of all FSW energy inputs are presented in Figure 5-2.

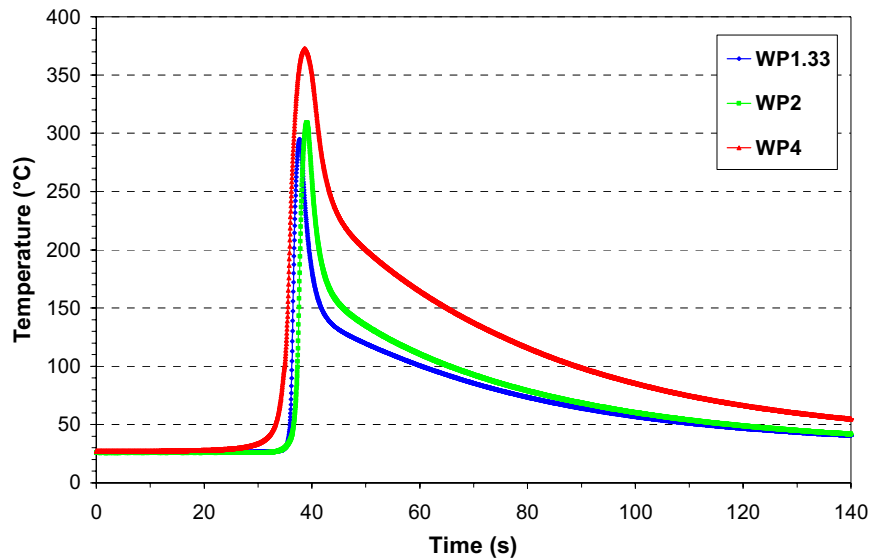


Figure 5-1 - Thermal cycles obtained close to the SZ during FSW of Al-Mg-Sc joints, produced applying WP1.33, WP2 and WP4. Average thermal cycles measured from thermocouples fixed in the backing bar.

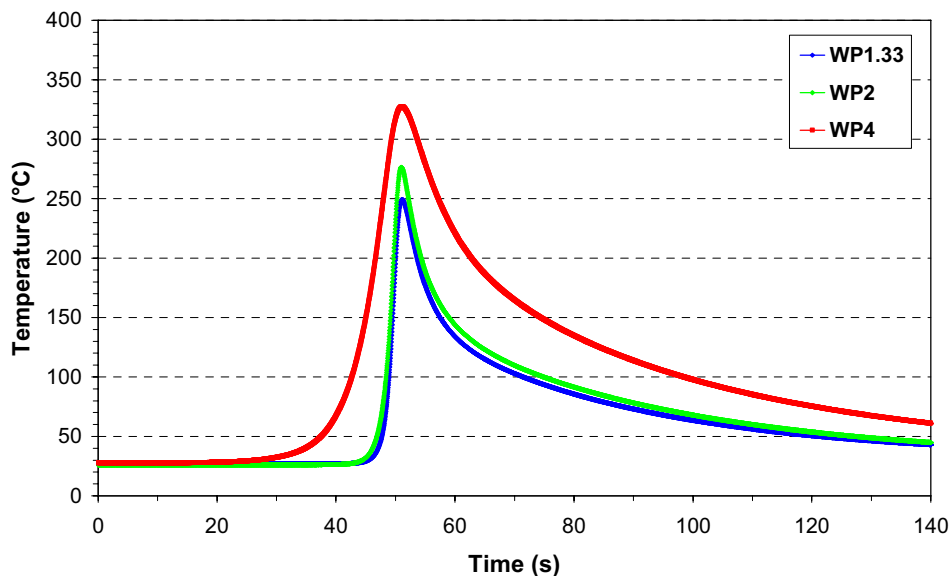


Figure 5-2 - Thermal cycles obtained close to the HAZ/TMAZ during FSW of Al-Mg-Sc joints, produced applying WP1.33, WP2 and WP4. Average thermal cycles measured from thermocouples fixed in the workpiece.

The increase in the temperature values obtained using the thermocouples agrees with the increase in the heat input produced by the variation of the FSW parameters. A decrease of the heating rate was clearly verified using intermediate HI in comparison with low HI, but the cooling rate does not significantly change. If compared to the low HI joint, the delay in the heat-up to peak temperature of the WP2 joint, associated with an inferior welding speed, could be linked to the higher peak temperatures and consequently more homogeneous stirring. A significant variation of mechanical and metallurgical behaviour would not be expected, since no large variations of the peak temperatures and cooling rates occurred. Furthermore, the high stability of the compounds present in the Al-Mg-Sc alloy would not be likely to be susceptible to slight variations in the thermo-cycle [20]. For the WP4 weld condition, the increase in the peak temperature values obtained using the thermocouples also agrees with the increase in the heat input produced by the variation of the FSW parameters, as well as with experiments reported in the literature [57]. Once again, it verified a reduction of the heating rate, followed by an increase in cooling time, but no significant variation of the cooling rate. The heating rate can be directly associated to the variation in welding speed, and also relative to the higher peak temperatures overcome and homogeneous stirring. For this FSW condition, a variation of mechanical and metallurgical behaviour could be expected, since the peak temperatures and thermo-cycles increase reasonably, in comparison with cold and intermediate parameters. However, the high stability of the compounds present in the Al-Mg-Sc alloy could prevail at these peak temperature and thermo-cycles, proving of little consequence for the mechanical and metallurgical properties or even retaining the original properties of the base material [17,20].

5.1.2 Mechanical Characterization

5.1.2.1 Microhardness Test

Microhardness profiles were performed along the transversal cross section surface of the Al-Mg-Sc FSW joints for the three different conditions (WP's), after post-weld heat treatment at 325°C lasting 2 hours. Figure 5-3 presents the microhardness profile of the Al-Mg-Sc FSW joined using WP1.33, WP2 and WP4 energy inputs, across the base material and welded zones at mid thickness of the transversal weld seam section. The advancing side corresponds to the left-hand side of the diagram (from weld centre direction to -20 mm) and the correspondent retreating side on the right-hand side (from weld centre direction to 20 mm). The three different FSW conditions do not demonstrate significant hardness variations, in comparison with the base material, along the entire investigated section. Even the most differing weld energy inputs of the high HI (WP4) and low HI (WP1.33) do not present any extremely relevant hardness variations.

Comparing the different welding conditions, it remains possible to verify a slight hardness increase in the stir zone of the low HI (WP1.33). The dependence of the hardness on the Sc concentration has been measured by aging Al-0.1, 0.2 and 0.3 wt% scandium alloys at 300°C [20]. It was verified that, as the Sc concentration increases, the incubation time decreases and the value of peak hardness increases. The Al alloy investigated in the present work, containing 0.27 wt% Sc and aged 2 hours at 325°C, seems to agree well with the literature [20], indicating that the effect of incubation time decreasing took place during welding and even after PWHT, where consequently the base material characteristics were retained or even slightly increased in the SZ. In Figure 5-3 an average hardness value of 102 HV0.2 for the base material is shown, which is in agreement with the literature [65,66].

In FSW zones, the highest hardness value of about 110 HV0.2 was observed for the low HI (WP1.33), followed by 100 HV0.2 for both intermediate HI and high HI (WP2 and WP4 respectively). However, it is possible to observe that the three input energies do not show any great discrepancy in the hardness results across the welded zones, and the microstructure variations produced by the process would be expected to barely affect the initial hardness of the base material. The effect of the PWHT has also to be considered, since it could mask the effects of the thermal cycle produced during the welding process. Nevertheless, the PWHT required by the aeronautic industry, possibly due to creep forming applications, has been also investigated for FSW alloys before PWHT in unpublished work [67]. These investigations did not show any which has shown no hardness variation along the FSW zones for the low HI (WP1.33) and intermediate HI (WP2), but undermatching was observed in the SZ of the high HI (WP4) joint, with a hardness loss of 15-20%.

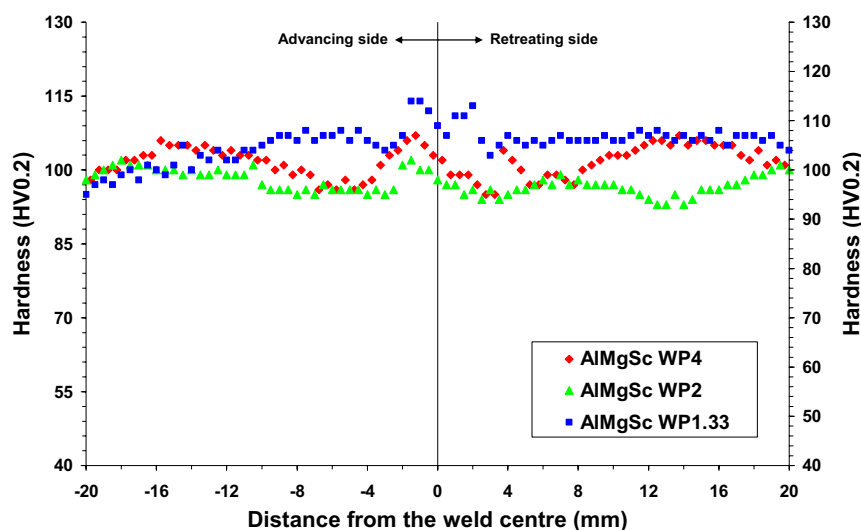


Figure 5-3 – Microhardness profile obtained in the mid thickness of the transverse section, across the BM and FSW zones of the Al-Mg-Sc joint, for the three energy inputs investigated.

5.1.2.2 Conventional Flat Tensile Test

Global tensile properties were determined by means of conventional flat transverse tensile specimens, tested at room temperature for the Al-Mg-Sc alloy base material and for the FSW joints using three different energy inputs. Thus, the specimens were extracted from the joined plates and base material in the same orientation, with the load position transverse to the weld seam, and consequently to the rolling direction as well. The results for base material and FSW joints are given as an average value of three tested specimens for each condition. Table 5-2 presents the tensile properties for the three studied weld conditions WP4 (high HI), WP2 (intermediate HI), WP1.33 (low HI) and respective base material (BM). The results are presented in terms of yield strength ($R_{p0.2}$), tensile strength (R_m) and elongation (A). The BM tensile properties are approximately in accordance with values presented in the literature [17], which were shown in Table 2-1 (chapter 2). Variations in the chemical composition and thermo-mechanical fabrication processing are responsible for small deviations of $R_{p0.2}$ and R_m found in the literature [17]. The general effect of Sc added to the presence of Mg can be expected to promote a small decrease of the elongation, but a sharp increase of the yield strength, even for small additions of Sc. The tensile properties and the structural stability depend on the size of Al_3Sc precipitates. The reduced difference in the lattice parameters permits it to preserve the coherence of Al_3Sc particles at higher temperatures and for longer exposures [17]. Figure 5-4 shows the global tensile behaviour of the FSW joints with energy inputs WP1.33, WP2 and WP4, as well as the BM tensile behaviour.

Table 5-2 – Tensile test results of Al-Mg-Sc FSW joints WP4, WP2 and WP1.33 followed by a comparison with the results from BM.

Al-Mg-Sc Condition	Measured values			Comparison with BM		
	$R_{p0.2}$ [MPa]	R_m [MPa]	A [%]	$R_{p0.2}$ [%]	R_m [%]	A [%]
WP4	253 ± 1	341 ± 1	6.4 ± 1	85	87	32
WP2	290.5 ± 6	382 ± 4	9.6 ± 1	97	97	48
WP1.33	287.5 ± 2	374.6 ± 3	8.9 ± 1	96	95	45
BM	298.3 ± 1	393.7 ± 2	20 ± 2	--	--	--

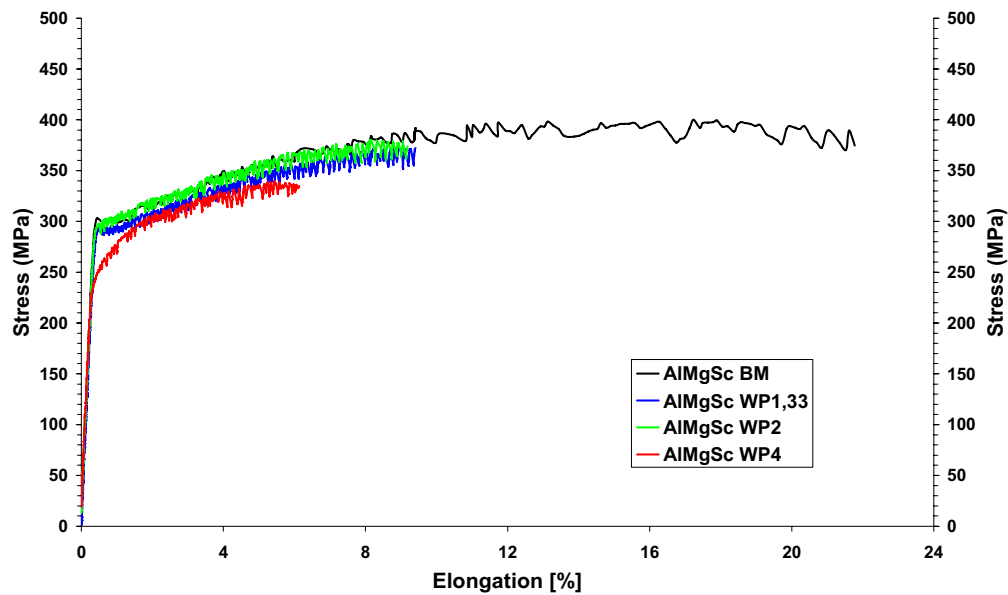


Figure 5-4 – Tensile behaviour of the Al-Mg-Sc FSW joints using energy inputs WP4, WP2 and WP1.33, in association with results from the BM.

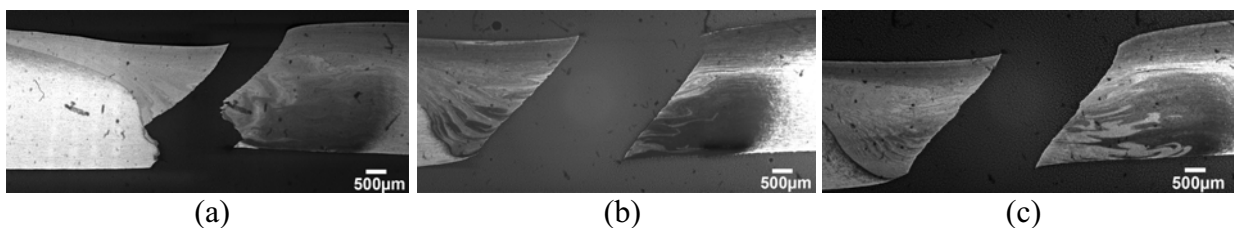


Figure 5-5 – Macrographs of the rupture location for the different parameter conditions: (a) low HI - WP1.33, (b) intermediate HI - WP2 and (c) high HI - WP4.

According to the results presented in Table 5-2, global tensile properties of friction stir welded Al-Mg-Sc joints demonstrate only a small decrease of the tensile and yield strength for the hot parameter condition (WP4). In comparison with the BM, a very significant decrease in elongation for all welding conditions was verified. The location where the tensile specimens broke during the tests is shown in detail for the different energy inputs in Figure 5-5. It can be seen that the necking region concentrates on the welded region and the fracture happens at 45° to the load axis. The exception is the low HI WP1.33, which presented a deviation in the fracture path, following the interface TMAZ/SZ close to the weld bottom (see Figure 5-5 (a)). This macrograph of the WP1.33 fractured specimen indicates the presence of weak consolidation flaw. Considering the microhardness results (no general undermatching), which show no loss of strength at the SZ, the failure can be explained by the different microstructure in the SZ and thinner cross section, resulting from the forging forces of the tool shoulder during welding. As observed, all the welded specimens broke in the SZ, and this zone is usually characterized by superplasticity behaviour with a microstructure of equiaxed grains, which generally increase the elongation. Thus, finer dimples in the fracture surface are expected to be found as a result of the

finer grain structure generated by the presence of Sc, allied to the thermomechanical process produced during FSW. Despite observing an indication of weak bond in the WP1.33 joint, the tensile properties of WP1.33 and WP2 are practically identical. The differences in strength (i.e. 3 and 8 MPa) could be considered within the error margins of tensile testing. However, all the energy inputs presented a good level of weld tensile properties, particularly the intermediate and cold welds with yield and tensile strength values of over 90% of the base material.

5.1.2.3 Microflat Tensile Test

Microflat tensile tests were carried out in order to establish the tensile properties profile along the base material and FSW zones for the Al-Mg-Sc alloy welds, joined with different energy inputs. The following diagrams represent the local tensile properties along the weld joint for the three different energy inputs (high HI, intermediate HI and low HI), correlating the yield strength ($R_{p0.2}$) behaviour in Figure 5-6, the tensile strength (R_m) behaviour in Figure 5-7 and the elongation in Figure 5-8. The zero value in the “x” axis corresponds to the weld centre and each point of the profile respectively describes the local tensile strength, yield strength and elongation. The advancing side is located in the left-hand-side (negative values in “x” axis) and the retreating side in the right-hand-side (positive values in “x” axis) of the graph.

Observing the microflat tensile results from FSW Al-Mg-Sc presented in Figure 5-6 to Figure 5-8, for the three energy inputs, it can generally be observed that there is almost no significant variation in tensile strength and yield strength ($\pm 10\%$) along the FSW zones, also in comparison with base material. Slight variations in the SZ and TMAZ were perceived, and it can be seen that for the high HI joint (WP4), tensile and yield strength tend to decrease in the friction stir welded region. Tensile strength tends to reduce slightly in the weld center for all energy inputs, showing the lowest values for the high HI specimens (see Figure 5-7). The small increase in tensile and yield strength of the intermediate HI (WP2), in comparison with high HI, shows a respectively inferior increase of elongation in the weld zones, as shown in Figure 5-8, but still the tensile properties values are close to the range of the base material values. The low HI (WP1.33) presented a small decrease in tensile strength in the welded region, but on the other hand, the yield strength showed a slight increase in the friction stir welded region (see Figure 5-6 and Figure 5-7). Elongation shows an increase in the welded zones, for all weld energy inputs. There is a clear tendency of a major increase in elongation in welded zones for the high HI condition, compared with intermediate HI and low HI conditions (Figure 5-8).

In the high HI condition (WP4), the yield strength values in the weld zones are about 231 MPa on average and in the base material the average values reached 256 MPa. The tensile

strength values for the same heat input condition, show values in the weld zones of 314 MPa, and in the base material an average of 344 MPa. In this way, weld zones demonstrate both yield and tensile strength values of around 92% of the base material values. Elongation average values of high HI condition reach approximately 22% in the very centre of the weld while base material values are about 14%. Compared with the high HI, the intermediate HI (WP2) shows an increase in yield and tensile strength in welded zones of over 95% of the base material values, which correspond to 246 MPa and 327 MPa, respectively. In this case, elongation values in the weld centre reached 19%. Low HI condition (WP1.33) presented yield strength values in the weld zones of about 252 MPa on average, sometimes reaching around 275 MPa in the SZ. The tensile strength values of this heat input condition showed average values of 328 MPa in weld zones representing, just as the intermediate HI condition, about 96% of the base material values. Elongation in the weld zones of the low HI condition does not show any excessive variation in comparison to BM. However, at some local points it was able to reach 18% in the middle of the SZ. Nevertheless, $R_{p0.2}$ and R_m , in all weld conditions, presented values over 90% of BM values, indicating a good welding performance.

It has to be emphasized that some comments above are based on marginal differences in results which might well be within the errors margins of the test procedure. *In practical terms, only minor deviations to the BM yield and tensile strength could be observed in the SZ.* On the other hand, elongation has shown to profit from the welding process, displaying significant increases at the SZ in comparison to the BM behaviour.

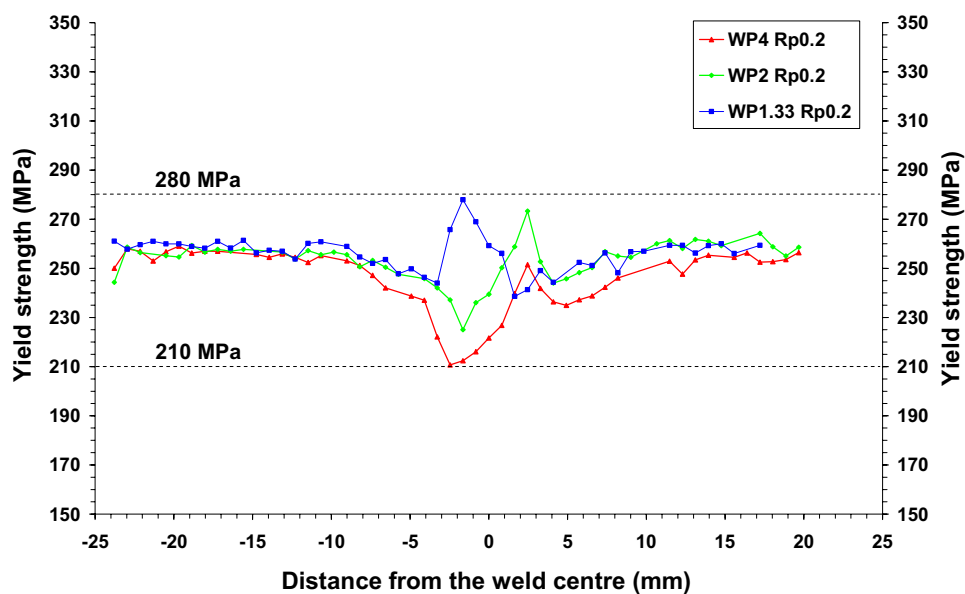


Figure 5-6 – Yield strength profiles from microflat tensile testing across the BM and FSW zones of the WP1.33 (low HI), WP2 (intermediate HI) and WP4 (high HI) parameters.

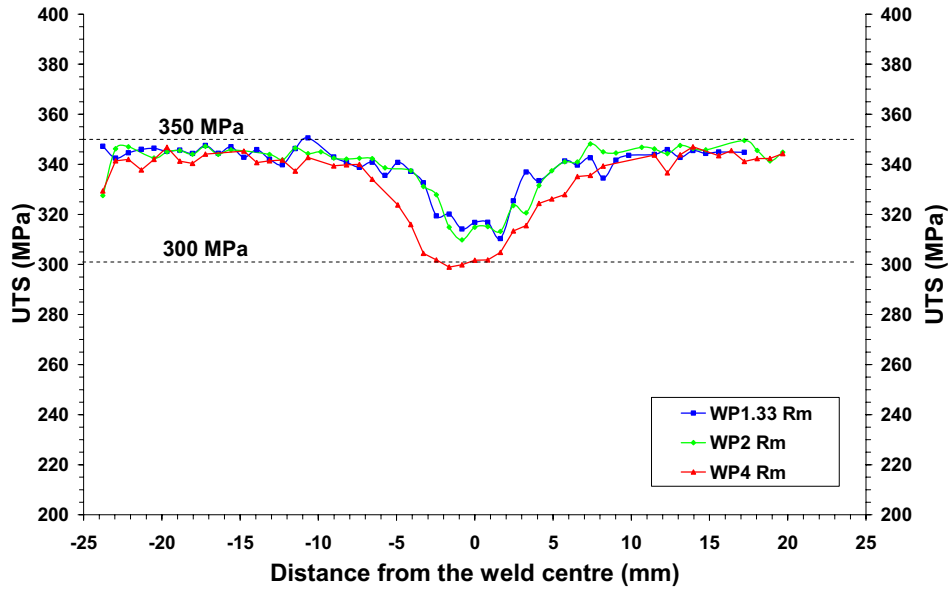


Figure 5-7 – Ultimate tensile strength (UTS) profiles from microflat tensile testing across the BM and FSW zones of the WP1.33 (low HI), WP2 (intermediate HI) and WP4 (high HI) parameters.

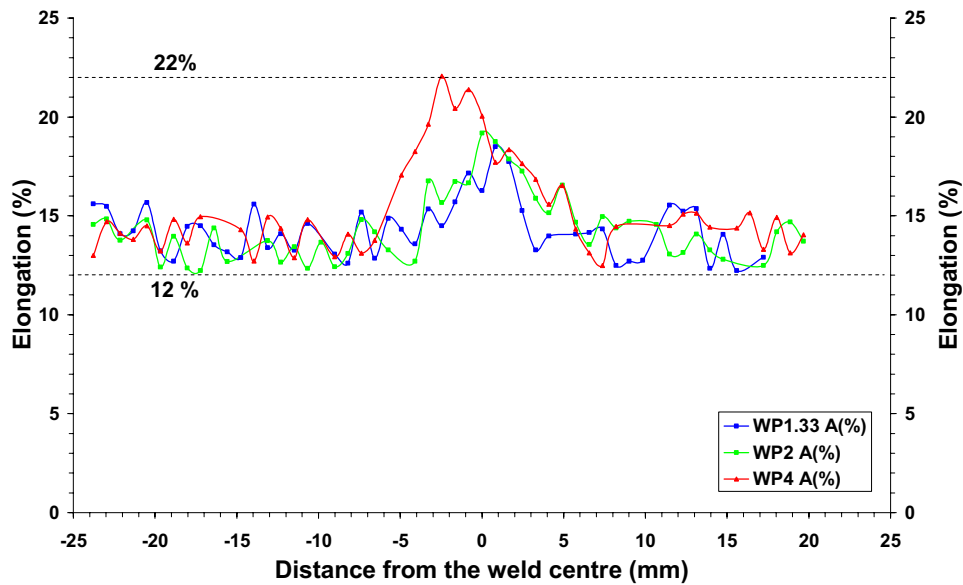


Figure 5-8 - Elongation profiles from microflat tensile testing across the BM and FSW zones of the WP1.33 (low HI), WP2 (intermediate HI) and WP4 (high HI) parameters.

The validity of the results can be evaluated by comparing the mechanical properties obtained by transverse flat tensile and microflat tensile tests, as shown representatively by plotting the tensile curves obtained from both testing techniques, Figure 5-9. The tensile test curves obtained for the BM through conventional flat tensile and microflat tensile tests showed a misfit which can be attributed to several reasons. One would be the specimen’s preparation (machining), which could introduce small superficial defects in the microflat specimen (local stress risers). It should be mentioned that the behaviour of the elongation, which theoretically

should increase for shorter “ l_0 ”, does not occur when comparing conventional tensile specimens with microflat tensile specimens, but it has to be considered that the latter has a shorter l_0 and also an inferior thickness (transverse section area). Moreover, the sampled volume in the microflat testing is substantially smaller. The tensile strength undermatching observed in Figure 5-7 would be responsible for the fracture in the SZ, observed previously in Figure 5-5. According to the literature [68], in materials with ductile behaviour it would be expected to act as a state-of-stress type “plane stress”, since the crack surface morphology was mostly approximately 45° in the conventional flat tensile and microflat tensile specimens. The dimensional difference between the specimens, such as thickness and respective transversal section area, could contribute to changes in the failure mechanisms and result in the difference between the curves of both the test techniques. Additionally, the local tensile properties obtained by microflat tensile tests showed a ductile behaviour in the weld centre (SZ), as also represented in Figure 5-9, with higher yield and tensile properties for the cold and intermediate parameters. Nevertheless, the suitability of the mechanical properties measured with microflat tensile specimens emerged from the established relationships between tensile strength and hardness, as well as by comparison with standardized test specimens [60].

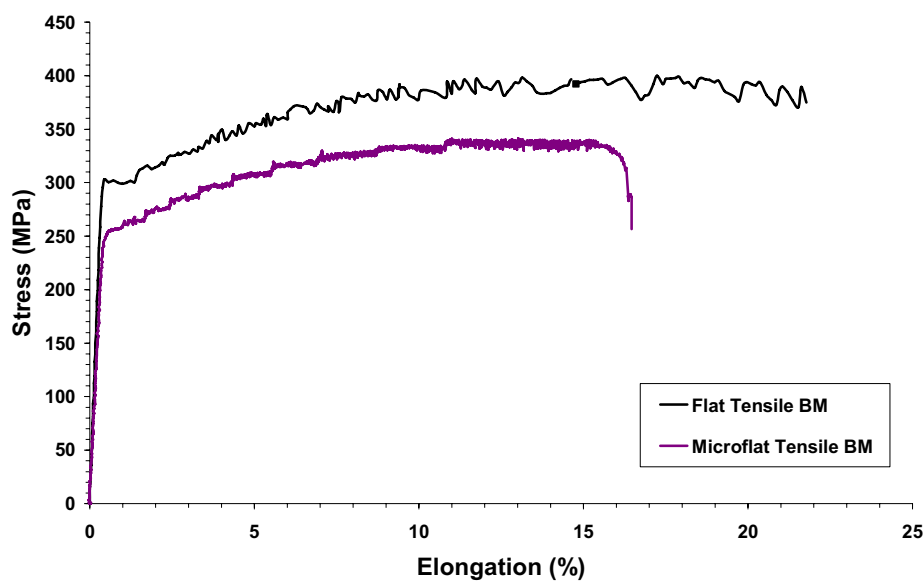


Figure 5-9 – Microflat tensile behaviour of the Al-Mg-Sc alloy BM in comparison with transverse flat tensile behaviour from BM.

5.1.3 Metallurgical Characterization

5.1.3.1 Macro and Microstructural Investigation

A typical FSW joint is commonly divided into zones (as previously described in section 2.3 of chapter 2), which are affected by different thermal cycles and degrees of deformation. The microstructure of the Al-Mg-Sc BM consists of deformed elongated grains, while the centre of the welds (SZ), which undergoes the highest amount of deformation and thermal cycle, is characterized by a fine equiaxed recrystallized grain structure. In contrast, surrounding the SZ, the recovered grains of the TMAZ, which presented a highly distorted structure, were characterized by a high degree of deformation and rotation of about 90° of the base material pancake grains.

Macro and micrographs in the Figure 5-10 show a typical joint segment, representative of the plane transverse to the weld travel direction of Al-Mg-Sc FSW joints (in this case represented by the low HI condition WP1.33). Here the geometry of the weld seam is easily revealed in the macrograph, as well as the plastic flow tendency in the stirred zone, indicating full penetration and no significant defects (this condition was characterized by an apparent consolidation flaw in the interface TMAZ/SZ of the advancing side, close to the bottom of the weld seam). The grain boundary details have not been properly revealed using optical microscopy, even using polarised light, as can be seen in the micrographs detailing the base material and interfaces of TMAZ and SZ (Figure 5-10 a and b). However, it was perfectly possible to distinguish the different grain morphologies, coming from the rolled BM in the missoriented grains in the TMAZ, surrounding the very fine recrystallized grains in the SZ. Such similar microstructural aspects of cold rolled BM have been reported in the literature for sheets annealed at high temperatures (300-400°C), demonstrating a completely non-recrystallized structure [69].

According to the FSW thermal cycle measurements, obtained in the present and previous studies [10], the HAZ experiences peak temperatures from 200°C (bottom) to 250°C (top) measured for the low HI joints, reaching from 300°C (bottom) to 350°C (top) in the high HI joints, which, especially for the high HI, would influence the strengthening features in most aluminium alloys. In contrast, very close to the SZ, the temperature is estimated to reach between 350 and 450°C and here, allied to deformation, a rotation of elongated and partially recrystallized grains around the SZ is produced. A large plastic deformation is introduced in the SZ during FSW and temperatures are expected to reach more than 500°C, giving place to a microstructure entirely recrystallized with grain size in the order of about 1µm. It was not possible to acquire

quantitative results about grain size using optical microscopy, due to the very refined structure formed in the SZ and the poor grain boundary contrast in all zones of the joint.

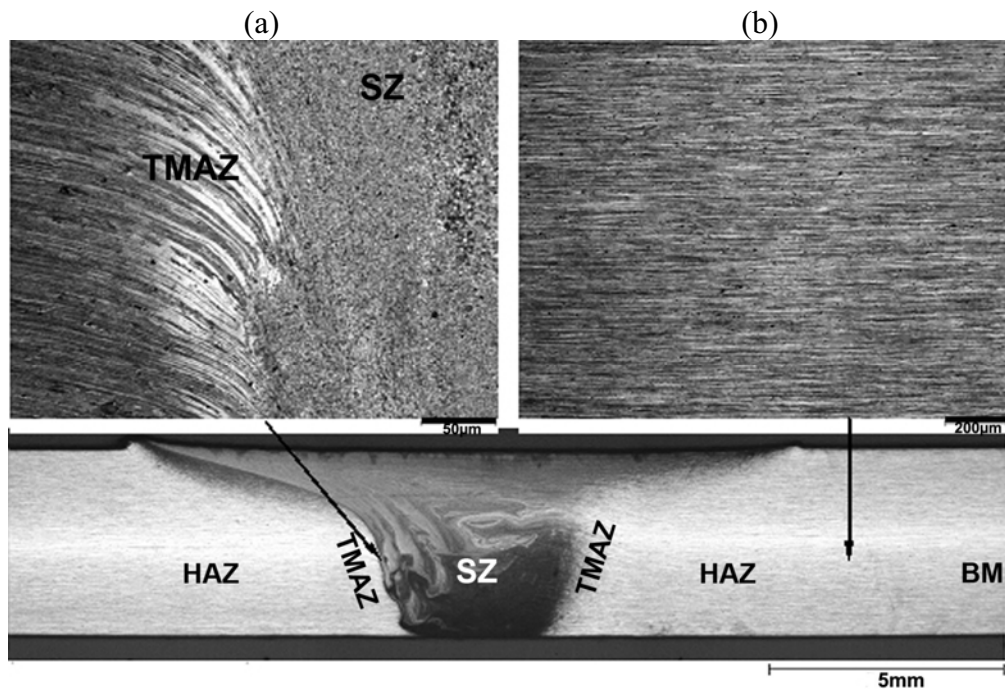


Figure 5-10 - Transversal section overview of the weld seam of the Al-Mg-Sc FSW joint by optical microscopy. (a) Detail of the microstructure interface, delimiting SZ and TMAZ/HAZ regions and in (b) the microstructure of the HAZ/BM.

Hence, SEM analyses were carried out, in order to observe the microstructural details and investigate the grain size variations produced during FSW. Figure 5-11 shows backscattered electron micrographs of the cross section of the Al-Mg-Sc FSW joints, illustrating the grain morphologies in the SZ for the three energy inputs, (a) high HI - WP4, (b) intermediate HI - WP2, (c) low HI - WP1.33 and (d) TMAZ, represented for high HI - WP4. As in the optical microscope observations, SEM images of these regions clearly reveal the flow structure contrast, giving little information about the grain structure. SEM micrographs from the SZ revealed a little better contrast of grain structure, allowing for a qualitative correlation of the different energy inputs. Analysis of the micrographs in Figure 5-11 (a), (b) and (c) shows a typical grain morphology resulting from dynamic recrystallization for the three FSW energy inputs, which present a very refined equiaxed grain structure. Furthermore, the grain size is considerably smaller for the cold parameter joint, when compared with hot and intermediate parameter joints. It possibly occurs due to the characteristic thermal cycle and respective peak temperatures taking place during the FSW using low HI, thereby increasing the degree of strain and decreasing diffusion along the grain boundaries, which hinders grain growth. This recrystallized microstructure is typically characterized by an increase in material ductility, which can be confirmed by the elongation

results in the SZ of the microflat tensile tests, in particular the high HI (WP4). Observing the results from microflat tensile profiles, in comparison with high HI (WP4), the decrease in elongation, allied to the slight increase in yield strength of the cold weld parameter (WP1.33), suggests it is contributed by the smaller grain size, resulting from the higher welding speed during FSW. Also it has to be noted that the hardness profile is not significantly influenced by the grain size variation in the SZ for the different energy inputs and if compared with BM, except for a slight increase of the hardness in the SZ of the low HI condition WP1.33. The twisted grains resulting from the thermal cycle and plastic flow in the TMAZ were evidenced, as shown in Figure 5-11 (d). In this zone, a microstructural gradient indicates a mixture of pancake grains, highly deformed and recovered, sometimes presenting localized recrystallized grains surrounding the SZ.

Additionally, coarse second-phase particles and dispersoids were evidenced in the SEM micrographs, which can be identified as the white coarse particles and the white fine particles spread along the aluminium matrix, respectively. The dispersoids were more easily observed in the TMAZ micrograph (Figure 5-11 d). Chemical elements present in the coarse particles were verified using EDS analysis directly on the particles. In general, the presence of Al, Mg, Mn and Si was observed in the coarse particles. This indicates the presence of different compounds such as Mg_2Al_3 , Mg_2Si and $(Fe, Mn)Al_6$ produced during the fabrication stages [70]. Furthermore, there is no reported interaction of scandium with manganese and the binary dispersoids would be Al_6Mn , forming independently of Sc [71].

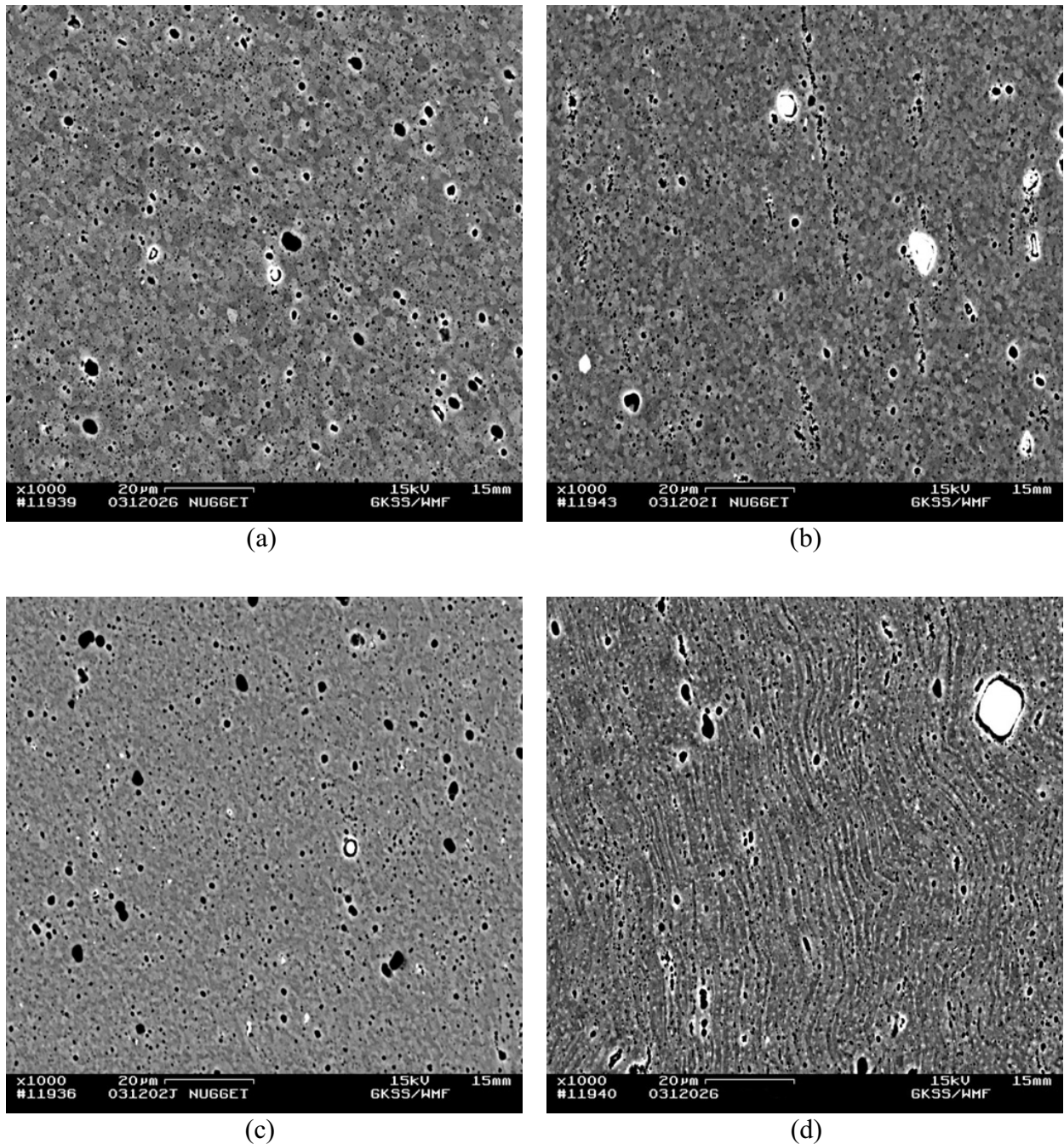


Figure 5-11 - SEM micrographs of the transversal sections of the Al-Mg-Sc FSW joints, showing equiaxed grains in the SZ of conditions: (a) high HI - WP4, (b) intermediate HI-WP2, (c) low HI - WP1.33 and (d) representing distorted microstructure from the TMAZ.

5.1.3.2 Substructural Investigation

Thin foils of the Al-Mg-Sc joints were prepared, according to the procedure described in section 3.4.3 for TEM investigation, in order to observe the grain morphology and its substructure in the FSW zones and base material. This technique allowed a deep analysis of the variation of the structural features in the friction stir welded joints. In this section, the investigation of the Al-Mg-Sc alloy joined with different energy inputs is presented in a logical

sequence, in order to provide a better understanding to the reader. Initially, the grain structure results across the FSW zones and BM is presented in order to reveal the grain structure evolution, previously difficult to observe in SEM and OM investigations. Subsequently, the deformed microstructure and the mechanisms of recrystallization and recovery are presented in terms of dislocation features. Next, the precipitation features are presented for the BM and FSW zones with further correlation of the mechanical testing results and thermal cycles produced for the different energy inputs applied. Finally, strengthening predictions are exploited, in order to understand the material strengthening attributed to the precipitation phenomenon.

Figure 5-12 shows micrographs representing the different grain structures observed in the BM, TMAZ and SZ of the Al-Mg-Sc joints. In the micrograph presented in Figure 5-12 (a), a fine pancake grain structure, as a result of the rolling process during the manufacture of the plates, is clearly observed for the Al-Mg-Sc alloy BM. The grain size refined by the Sc addition is significantly smaller than for the other studied aluminium alloys (see section 2.4). The TEM analysis established an average grain length of 2.6 μm and average width of 0.5 μm . The effect of scandium in BM grain refinement is to inhibit the recrystallization process during thermo-mechanical processing [17,70-73]. Figure 5-12 (b) shows a grain morphology combination, which characterizes the TMAZ. TEM investigation of this zone allows us to observe the detailed grain structure, which includes a pancake grain structure remaining from the BM, distorted and rotated, combined with some equiaxed grains originating from a mixture of recovered and partially recrystallized structure, resulting from the plastic flow and thermal cycle during FSW. The SZ of the Al-Mg-Sc joints was characterized by only a very fine equiaxed grain structure, as presented in Figure 5-12 (c). In this zone, dynamic recrystallization controls the resulting grain structure, having reached the highest temperatures and deformation levels during the FSW process. An average grain diameter in the SZ of the Al-Mg-Sc was established from TEM micrographs for the different FSW energy inputs, resulting in an average value of 2 μm for high HI (WP4), 1.4 μm for intermediate HI (WP2) and roughly 1 μm for the low HI (WP1.33). These results, indicating a smaller grain size for the low HI joint, agree with previous qualitative comparisons made in SEM micrographs. It is expected that the presence of stable Al-Sc precipitates would inhibit the motion of thermally activated subgrain boundaries under the elevated temperatures promoted during the FSW process, as occur in the SZ [74]. As mentioned in previous observations, the recrystallized grain structure supplies a superior elongation to the SZ without significantly affecting its tensile and hardness properties.

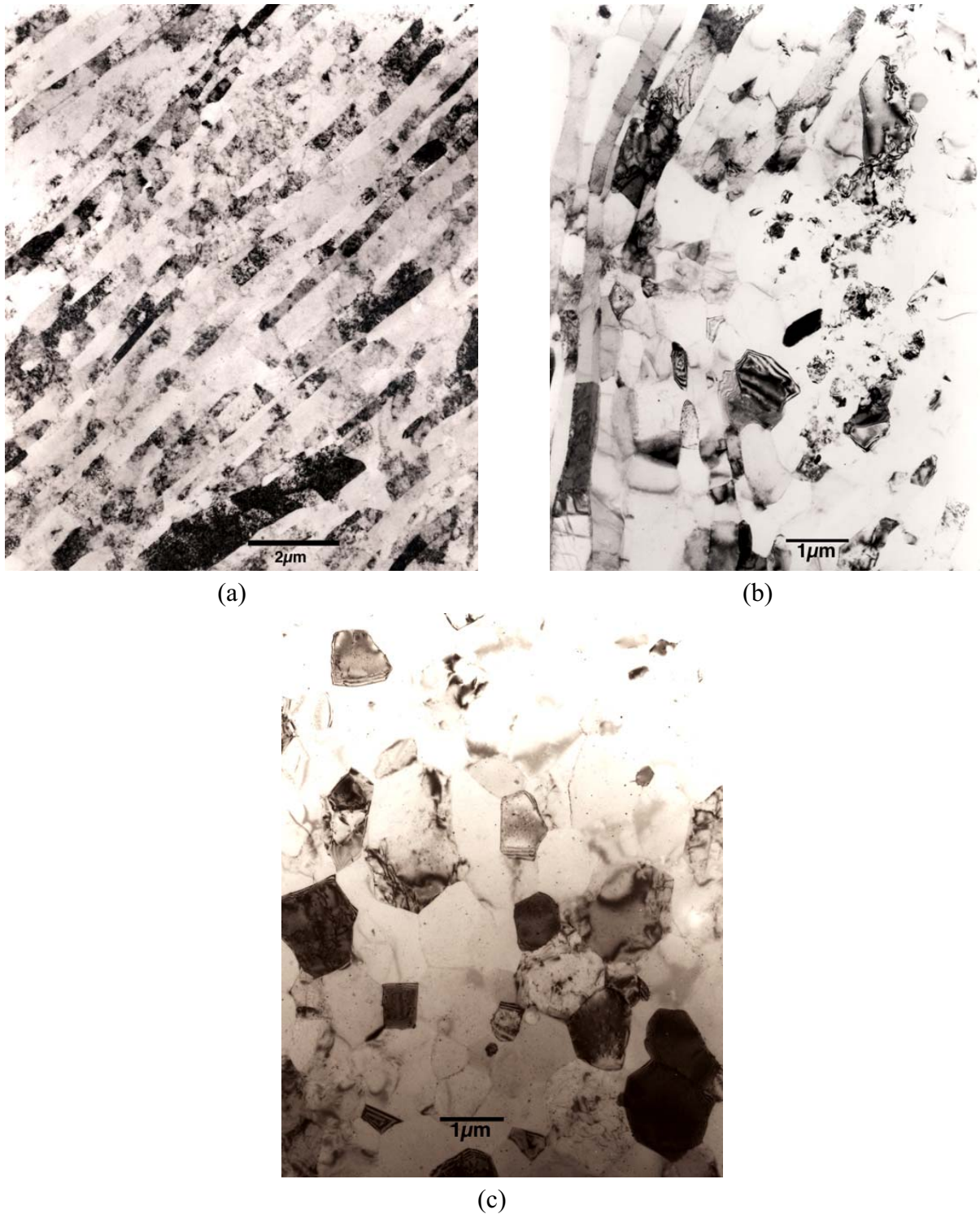


Figure 5-12 - Bright-field TEM micrographs of the grain structure present in the base material and different FSW regions of Al-Mg-Sc alloy. (a) BM, (b) TMAZ and (c) SZ.

In the Al-Mg-Sc FSW joints, a relevant dislocation density presenting singular aspects was verified along the base material and subsequent weld zones. The dislocation features of the different weld zones and base material of Al-Mg-Sc alloy are represented in the micrographs of Figure 5-13. The micrographs from TMAZ and SZ were chosen from high HI (WP4), as more

representative to illustrate the arrangement of dislocations, but bearing in mind that no notable variation in dislocation features were visually perceived from TEM examinations of the different energy inputs. However, the highest dislocation densities are expected to be introduced using lower energy input (WP1.33), since the resulting peak temperatures produced are lower, hindering the dislocation annihilation and rearrangement. It is important to note that no specific quantitative evaluation, in terms of dislocations, was performed in this work. Starting from BM, a considerable dislocation density was evidenced, in general showing no order at all, except some particular areas where dislocations presented groups, as indicated in Figure 5-13 (a). The dislocation pinning by second phase particles was also evidenced in the BM and weld zones, as indicated in Figure 5-13 (a). In the TMAZ, presented in Figure 5-13 (b), dislocation features show a similar character to the BM. However, the dislocations here indicate more interaction with one another and with second phase particles. The dislocation features most often found in TMAZ include dislocation pile-ups, forming subgrain boundaries, dislocation tangles (network structure) in some regions, and looping around second phase particles. Dislocation density was found at a lower level for grains in the SZ, as shown in Figure 5-13 (c). In terms of qualitative analysis, the major magnification of Figure 5-13 (c) should be noted, in comparison with TMAZ and BM. However, a pile-up of dislocations and interaction with second phase particles were evidenced, mainly for the hot weld condition, where the higher temperatures favour dislocation mobility. It has to be considered, that even being in the SZ, where deformation during FSW is highest, the elevated temperatures and dynamic recrystallization effects in the SZ usually result in a final microstructure presenting inferior dislocation density levels compared to the BM and recovered zones [10]. Such an effect is to be expected, because of the dislocations annihilation resulting from the recrystallization process and the atoms diffusion, is helped by the high peak temperature in this zone. However, in FSW, a continuous recrystallization process (dynamic) occurred, accompanied by incessant deformation, introducing and constantly increasing the dislocation density at the same time as new grains, free of deformation, are formed.

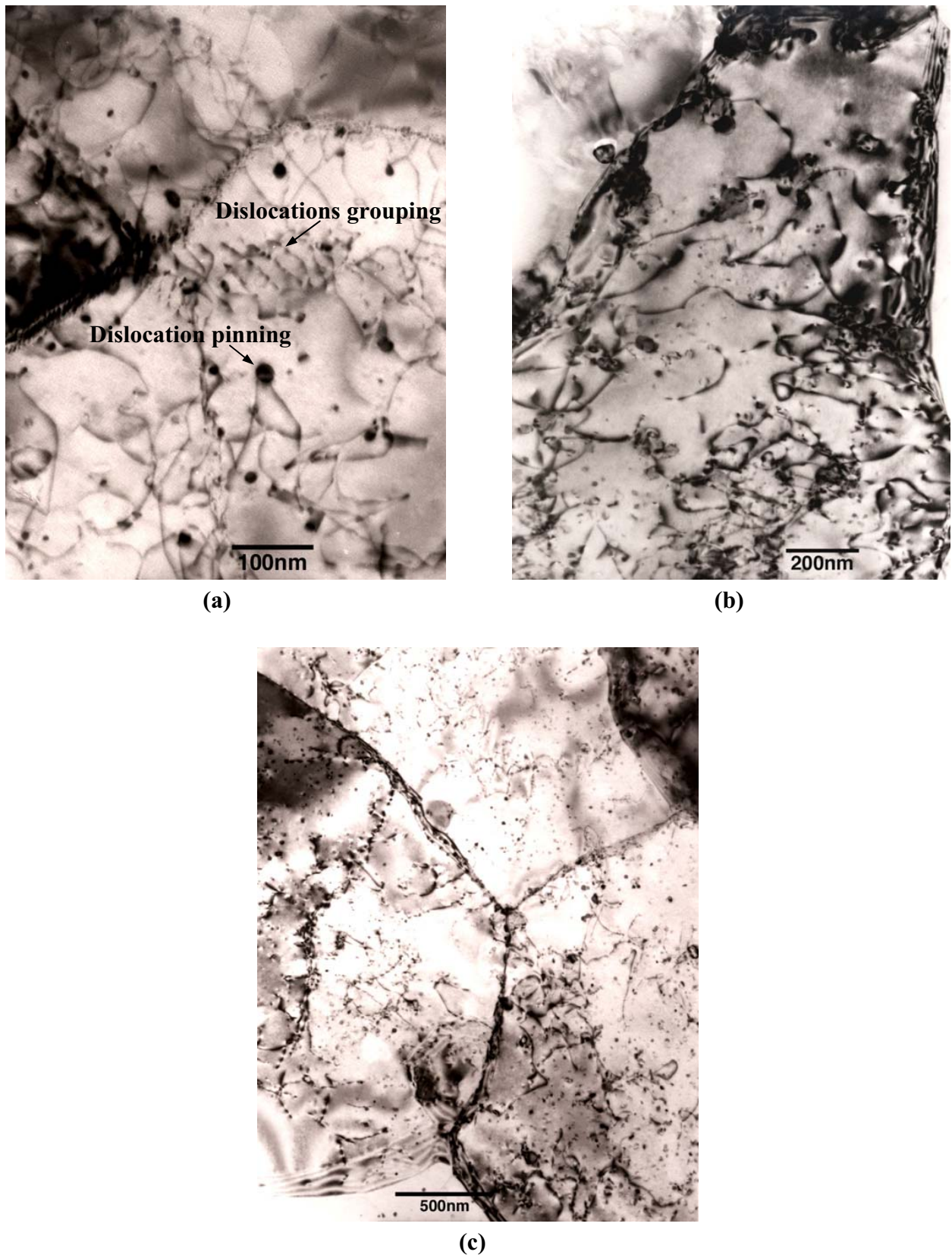


Figure 5-13 - Bright-field micrographs from Al-Mg-Sc alloy, showing typical dislocation features in (a) BM in $[\bar{1}11]_{Al}$ ($g = 202$), (b) TMAZ in $[001]_{Al}$ ($g = 200$) and (c) SZ close to $[011]_{Al}$ zone axis.

Yet certain particular substructural features were encountered for the different weld zones and parameters. Figure 5-14 (a) shows a bright field micrograph of BM, showing pancake shaped grains characterized by contrast of parallel bands crossing the grain in transverse direction, as indicated by the arrows, which could be associated with stacking faults. The high stacking fault energy, which is typical in Al alloys, promotes dislocation climb and cross-slip occurrence, which is characteristic of the dynamic recovery phenomenon [70]. The presence of dislocation walls, providing evidence of the initial stages of subgrain formation, was found for all the weld zones and base material as a product of recovery stages, in particular in the TMAZ, as illustrated by the micrograph of Figure 5-14 (b).

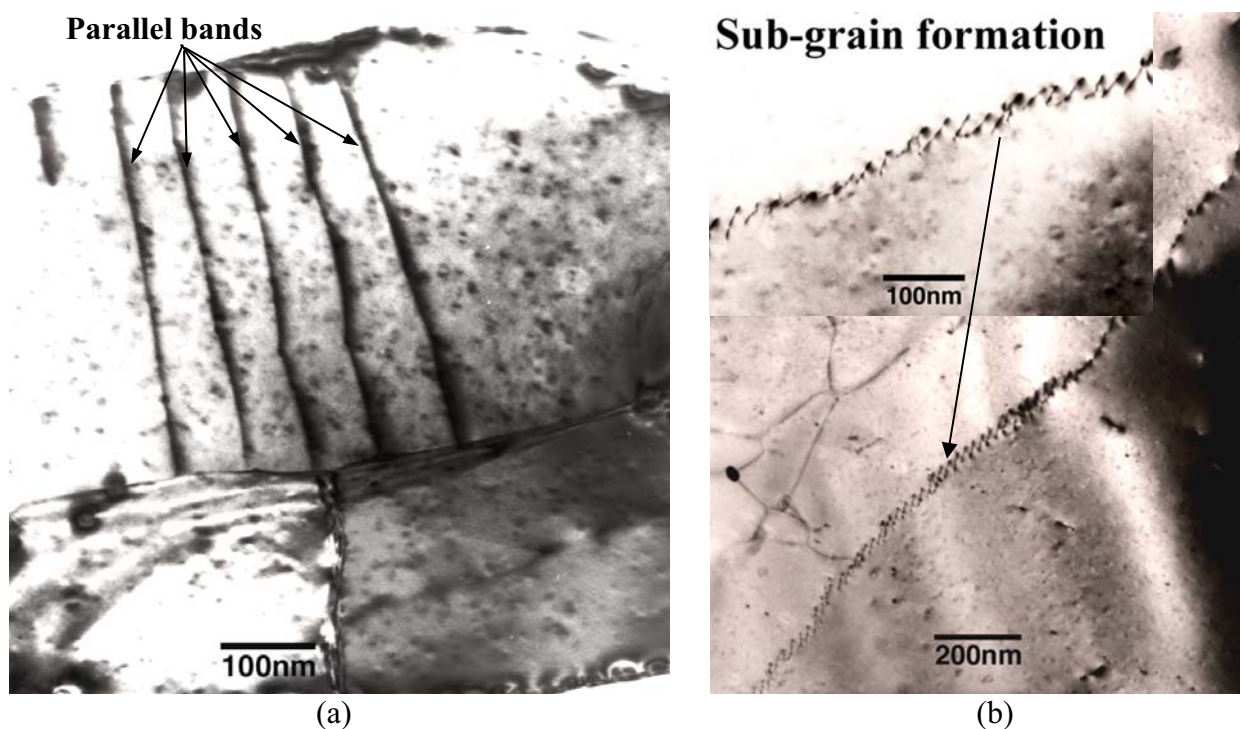


Figure 5-14 - Bright field micrographs of Al-Mg-Sc alloy showing particular substructural aspects. (a) Parallel bands in BM pancake grain, and (b) initial stages of sub-grain formation in TMAZ of WP4 condition.

A high density of nearly spherical, most likely Al_3Sc precipitates, was evidenced for all weld zones and the BM for all the FSW input parameters studied. The main precipitation characteristics are presented in Figure 5-15. Figure 5-15 (a) shows round type precipitates in nanometer scale, disposed along α -Al elongated BM grain, in conjunction with scarcely any dislocations in contrast. The presence of Al_3Sc precipitates was confirmed by selected area diffraction pattern (SADP) analysis. The superlattice spots, due to the presence of Al_3Sc ordered precipitates in [001] zone axis of BM, indicate that an orientation relationship exists with a cubic α -Al matrix, as shown in Figure 5-15 (b). From these observations can be assumed that

precipitates are coherent with an Al matrix, if the size of precipitates and lattice constant mismatch with the matrix are not too large, as is the case with Al_3Sc . As previously reported in chapter 2, the intermetallic Al_3Sc precipitates were found to be of the same FCC crystalline lattice as $\alpha\text{-Al}$, with a lattice parameter of 0.4106 nm, differing only 1.3% from the Al matrix [17,76,77]. EDS scans of precipitate chemistry were taken when the TEM beam was focused directly on a precipitate. The presence of Sc-rich particles was verified by EDS analysis, as can be seen in the peaks of the diagram presented in Figure 5-15 (c). The data presented in this diagram is representative of the results from scans on many precipitates.

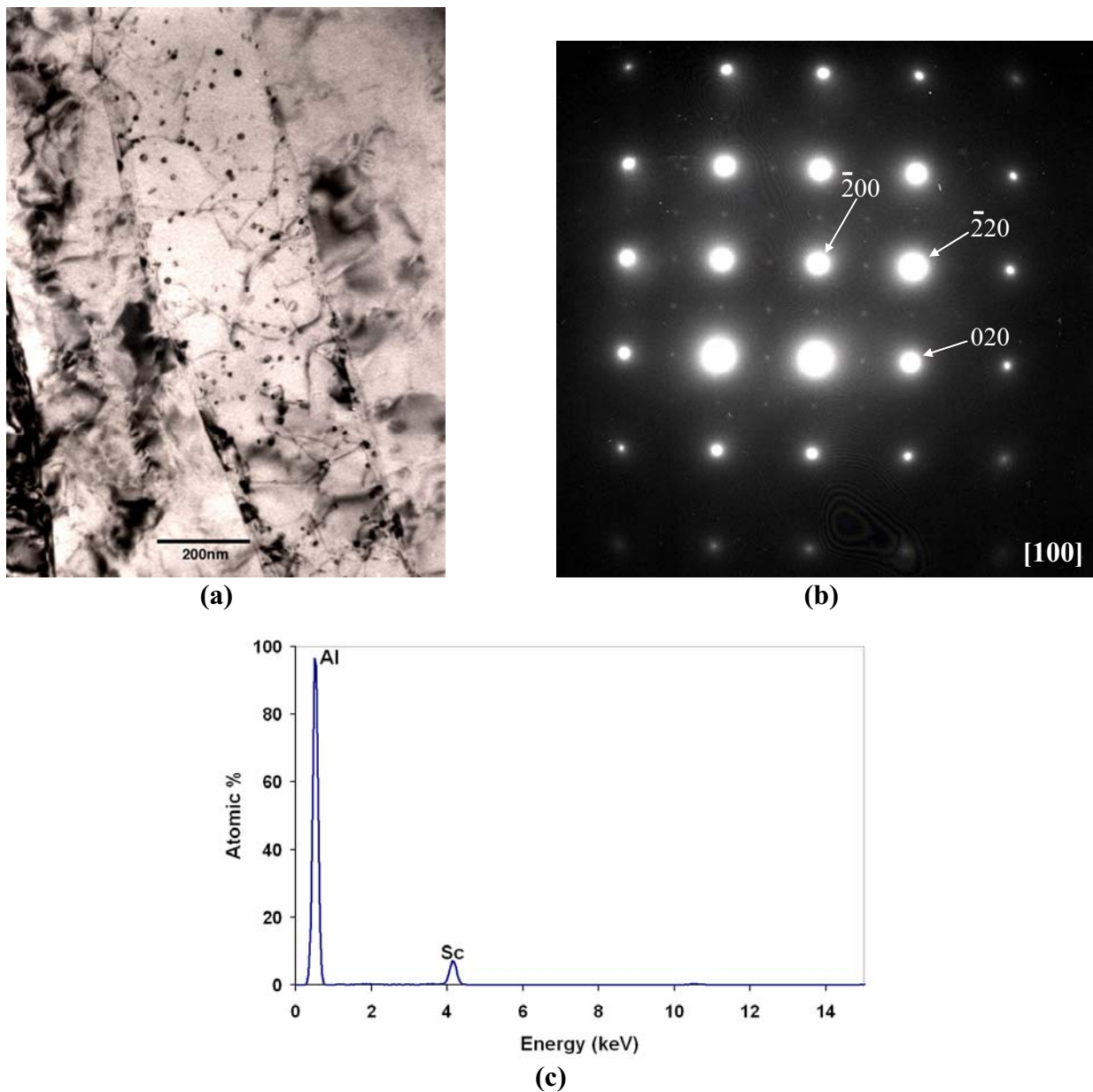


Figure 5-15 - TEM analysis presenting precipitate features in the BM. (a) Micrograph showing precipitates appearance and distribution along pancake grains. (b) SADP in $[001]_{\text{Al}}$ zone axis. (c) EDS peaks from precipitates presented in the micrograph.

Sc rich precipitates presenting apparently similar size and morphology were also observed in TEM analysis of the SZ for the three FSW energy inputs, as represented in Figure 5-16. In the micrograph of Figure 5-16 (a), dislocations ordered and pinned by the precipitates were found, which infers an effective role of the Al_3Sc precipitates in order to inhibit recrystallization and also acting as precipitate strengthener. According to Seidman and co-workers [20], coherency strain (Ashby-Brown contrast) in bright-field TEM image is one of the indications that precipitates are coherent with the $\alpha\text{-Al}$ matrix. The strain-field contrast (SFC), due to the coherent interfaces is also evidenced in the present work for most of the bright field micrographs and it was characterized by a lack of contrast, usually crossing the precipitate center, as can be seen better in some precipitates indicated by the arrows as “Ppt_{SFC}” in Figure 5-16 (a). Some authors also refer to this phenomenon as coffee-bean-like stress contrast of coherency [18,78,79]. Marquis and Seidman [18] reported loss of coherency by precipitates over 40 nm diameter, which are typically characterized by interfacial dislocations around the coarse precipitate. Similar contrast of dislocations is evidenced here, in some cases as presented by indication of Ppt[⊥] in Figure 5-16 (a). SADP spots in the [011] zone axis, presented in Figure 5-16 (b), also evidenced the presence of Al_3Sc precipitates, showing good order relation with Al matrix, which agrees with investigations by Blake *et al.* [76], who verified parallel orientation relationship for rod-type primary Al_3Sc precipitates with $\alpha\text{-Al}$ in the [011] direction. Moreover, Kendig *et al.* [80] reported that the presence of non-primary particles precipitated from supersaturated solid solution was confirmed for superlattice spots of ordered $\text{Al}(\text{ScZr})$ precipitates in the [011] zone axis, having a cube-on-cube orientation relationship with an $\alpha\text{-Al}$ matrix. Additionally, a good relation of coherency between second phase particles and $\alpha\text{-Al}$ matrix was also encountered in these studies of Al-Mg-Sc-Zr alloys. According to their [80] estimation of precipitate average size diameter and precipitates disposition from TEM micrographs and strengthening predictions, it indicated a significant enhancement of strength due $\text{Al}_3(\text{Sc,Zr})$ precipitates.

Scandium peaks were also verified in EDS analysis of these precipitates in the SZ, as shown in Figure 5-16 (c). Such investigations show a high stability of Al_3Sc particles, which even under the highest thermo-cycle (WP4) remained present, dispersed in the $\alpha\text{-Al}$ matrix apparently without severe coarsening and dissolution effects. However, studies of Huneau *et al.* [81] suggest that the original Al_3Sc particles might have been dissolved during FSW and nucleated again just after recrystallization, due to the low solubility of Sc in Al. Arguments of such nature are not sustained by the results found in the present work, when considering the

precipitate morphology and disposition features, allied to short time at peak temperatures, to dissolve the very stable Al_3Sc precipitates.

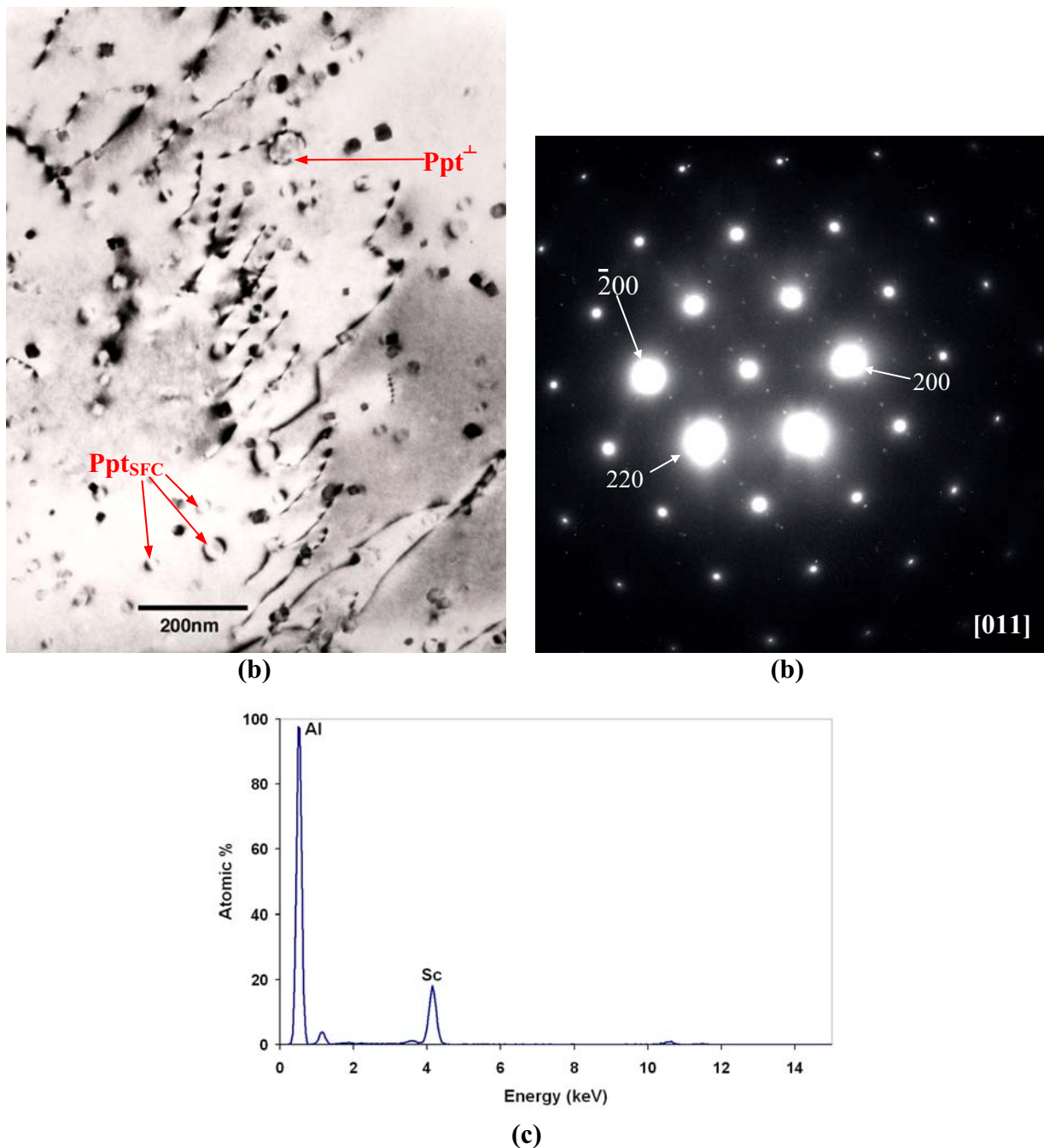


Figure 5-16 - TEM analysis presenting precipitate features in the SZ. (a) Micrograph showing precipitate characteristics and interactions with dislocations in equiaxed grain. (b) SADP in $[011]_{\text{Al}}$ zone axis. (c) EDS peaks from precipitates presented in the micrograph.

The Orowan's dispersion hardening (discussed in section 2.4), is suggested to be taking place because of the dislocations looping around the precipitates, which was frequently observed, particularly for high HI and intermediate HI joints, in the TMAZ. The apparent Orowan's

mechanism in the TMAZ of an Al-Mg-Sc joint welded with parameter set WP4 is presented in Figure 5-17, indicating the dislocation motion through the Burgers vector.

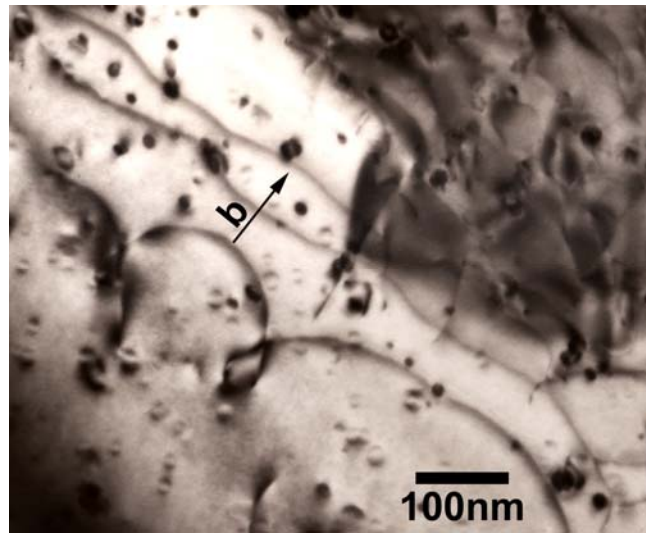


Figure 5-17– Orowan’s mechanism occurring in TMAZ of hot parameter (WP4 joint), in $[011]_{Al}$ zone axis, $g = 200$.

As mentioned before, precipitates containing Sc were found across the BM, HAZ, TMAZ and SZ for the three different energy inputs. Hence, precipitation features in the BM and the different FSW zones are represented by the micrographs shown in Figure 5-18. The micrographs obtained from the FSW zones were selected from high HI (WP4) condition, which are considered the most critical in terms of high peak temperature and slow cooling rates, as observed in the thermal cycle measurements, with consequent influence on the precipitation features. The mostly round type Al_3Sc precipitates were encountered in the elongated structure of grains and subgrains of BM, as showed in Figure 5-18 (a). High contrast of Al_3Sc precipitates with the same characteristics was also encountered, often almost fully covering the recovered grain structure of the TMAZ, as showed in Figure 5-18 (b). These precipitates were also observed in the equiaxed recrystallized grain structure of the SZ, showing no significant variation in size, morphology and distribution, as illustrated in Figure 5-18 (c). It should be considered that even the high temperature levels attained in TMAZ ($\geq 327^\circ C$) and SZ ($\geq 372^\circ C$) were not enough to dissolve or to coarsen the very stable Al_3Sc precipitates. The results from TEM analysis of Al-Mg-Sc joints across BM and FSW zones reported a high density of thin precipitates, randomly distributed along the α -Al matrix, which implies great performance in terms of precipitation strengthening. Such performance can be easily verified in the mechanical testing results presented in section 4.1.2, where no significant undermatching was found in hardness and microflat tensile profiles, accompanied by high quality global yield and tensile strength.

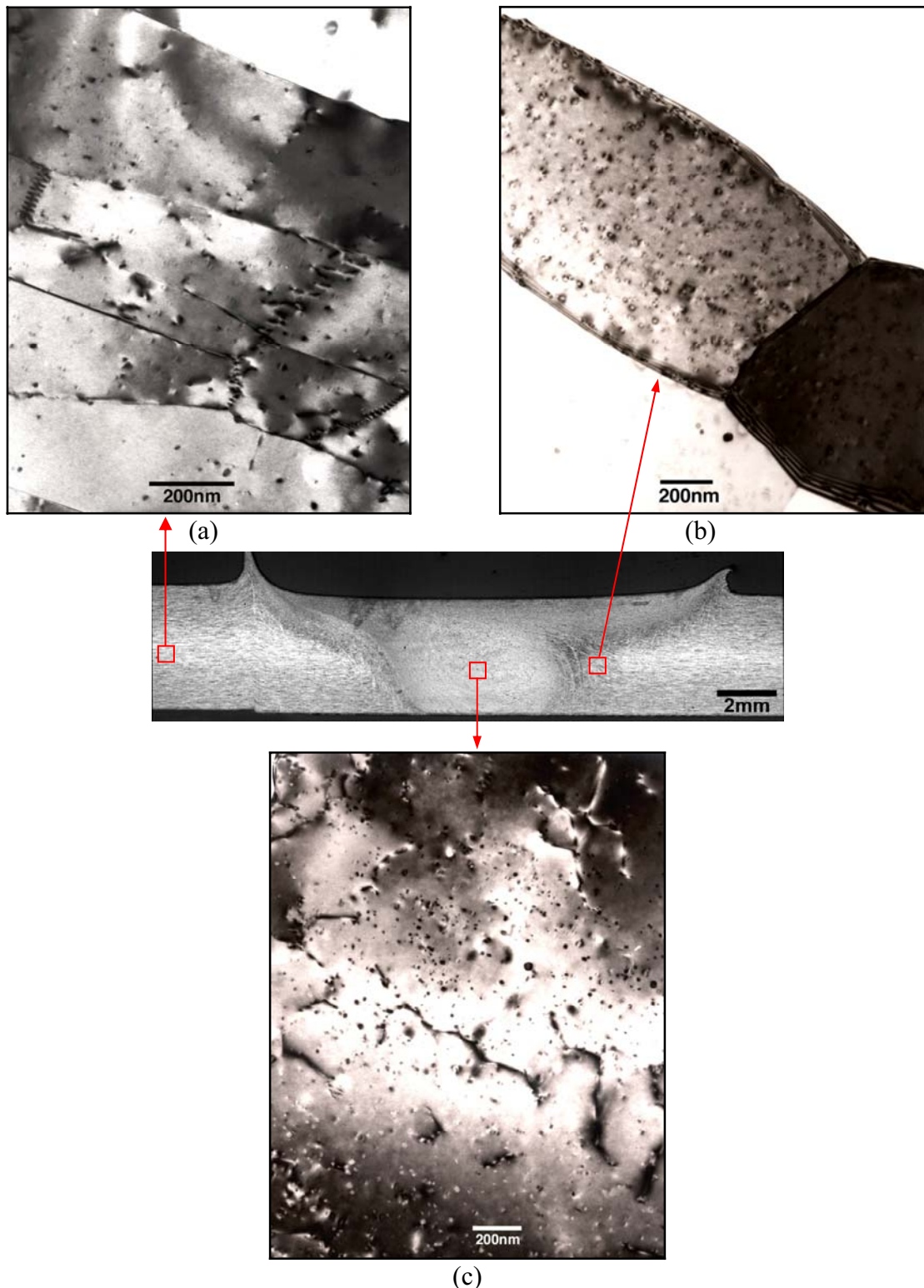


Figure 5-18 - TEM bright-field micrographs, representing Al_3Sc precipitates in different FSW zones and BM indicated in the macrograph of a Al-Mg-Sc joint. (a) BM, (b) TMAZ and (c) SZ.

In order to understand the effects of the FSW input parameters on the resulting microstructure and their corresponding influence on mechanical properties of the Al-Mg-Sc joints, some aspects have to be considered. Evaluating the microhardness profile of Figure 5-3, it

was verified that even microstructural variation (evidenced by different microscopy analysis techniques) produced by high deformation and thermal cycle levels does not have significant influence on the hardness values. The presence of Al_3Sc precipitates confirmed by TEM analysis in all FSW zones, showing no significant variation in size, morphology and distribution, indicates that precipitation hardening is controlling the mechanical behaviour of the Al-Mg-Sc FSW joints. The results found in microflat tensile tests (Figure 5-6 to Figure 5-8), where local tensile properties from different weld zones and BM were obtained, also agree with this conclusion. In this case, a significant variation of elongation was found for samples from the SZ. However, this behaviour was attributed to the equiaxed grain microstructure, resulting from the FSW process, which increases ductility and is characteristic of superplasticity resulting from the recrystallization phenomenon. It is also noted that the increase in ductility can be controlled by means of welding process parameters. Analysing SEM micrographs of the low HI condition (Figure 5-11) and values of grain size, previously determined from TEM micrographs, it can be assumed that the smaller equiaxed grain size in the SZ reduces the superplasticity effect from recrystallization.

Even so, analysing microflat tensile profiles, in terms of yield and tensile strength, the slight variations found along the FSW zones also demonstrated changes according to the weld energy input. Knowing that hardness and microflat tensile profiles from Al-Mg-Sc joints demonstrate a great dependence on the precipitate size and distribution and a low dependence on the grain and dislocation structures, an evaluation study focused on the distribution and size of Al_3Sc precipitates was carried out, in order to establish a better understanding of the minor mechanical property variations detected in the hardness and microflat tensile tests. To this end, average size and distribution of Al_3Sc precipitates were estimated from direct measurements on TEM negatives. Figure 5-19 shows the precipitate size range, related to their respective distribution for Al-Mg-Sc FSW joints in TMAZ and SZ of the three studied weld energy inputs, in comparison with values measured in BM.

Evaluating Al_3Sc precipitate aspects from BM, the presence of a large population of precipitates was observed, in a range from 6 to 21 nm diameter, especially a major proportion of precipitates with a diameter range between 9 and 15 nm. In general, the weld zones presented relative minor variations in Al_3Sc precipitates size and population. Compared to the BM, the hot weld condition (WP4) exhibited an increase in size for the major amount of precipitates to a range of 12-18 nm in TMAZ and SZ, as demonstrated in Figure 5-19. In this case, the higher temperatures and slower cooling rates produced by the low weld speed seems to affect the

precipitates from both weld zones in similar proportion. The intermediate HI (WP2) condition was less affected by the thermal cycles produced during the FSW process, presenting a major amount of precipitates in a size range of 9-15 nm for TMAZ and SZ. Apart from distribution values, where precipitate size concentrates more in a range of 9-15 nm in the BM, it is possible to confirm that temperature effects produced using intermediate HI produce almost no influence on precipitate size across all FSW zones. For the low HI (WP1.33) condition, it also verified that there is no precipitate coarsening due to the thermal cycles. The major amount of precipitates was found in a size range of 6-15 nm for TMAZ and between 9-15 nm for SZ. The lower energy weld input tends to produce no influence on precipitate coarsening, even in the SZ, where peak temperatures are higher.

As mentioned earlier, several researchers [16,17,18,20] have studied Sc added alloys and reported the high stability of supersaturated solid solutions and coherent precipitates formed from its decomposition. Studies by Marquis [18] reported the very stable behaviour of Al_3Sc precipitates with respect to coarsening, even for long aging times. It was described that Al_3Sc precipitates, with sizes in a range of 4-10 nm from Al-0.5 wt% Sc alloy aged above 400°C, results in coarsening of precipitates, which tends to lose coherency when their size exceeds about 20-30 nm. It also agrees with studies from Milman and co-workers [77], which showed precipitates with sizes from 3 to 15 nm produce a very strong hardening effect, also growing and losing coherency at temperatures over 400°C. During the FSW process, the critical temperatures are attained in the SZ, and temperatures very close to this zone were measured as being around 372°C, as is the case of the high HI (WP4) condition. In the SZ, temperatures can be expected up to 200°C higher than these (over 550°C). The high peak temperatures in the SZ and practically no variation in the precipitates size and distribution imply that the thermal cycle was too fast (about 10 s above 250°C measured in the plate joints and about 5 s above 300°C measured in the backing plate, see Figure 5-22 and Figure 5-23) to provoke any instability in the Al_3Sc precipitates. It is still important to emphasize that the cooling rates where the temperatures were measured would be different to the SZ, where thermal conductivity and heat input were changed, mainly due to the structural changes and position, in relation to the core of the material heating during FSW, respectively. It shows that thermal cycles were not sufficient to produce a significant precipitate dissolution and coarsening effect, contrary to the studies by Huneau [81]. The low solubility of Sc in Al is suggested here to be responsible for the insignificant size variation of the Al_3Sc precipitates, therefore with all the Sc content precipitated as Al_3Sc , the low Sc solute α -Al matrix cannot contribute directly to precipitate coarsening. These considerations

lead me to believe that Al_3Sc precipitates, which remain in a size range of 6-18 nm (the great majority) are primarily responsible in ensuring the strengthening of the FSW zones in the studied Al-4.3wt% Mg-0.27wt% Sc alloy.

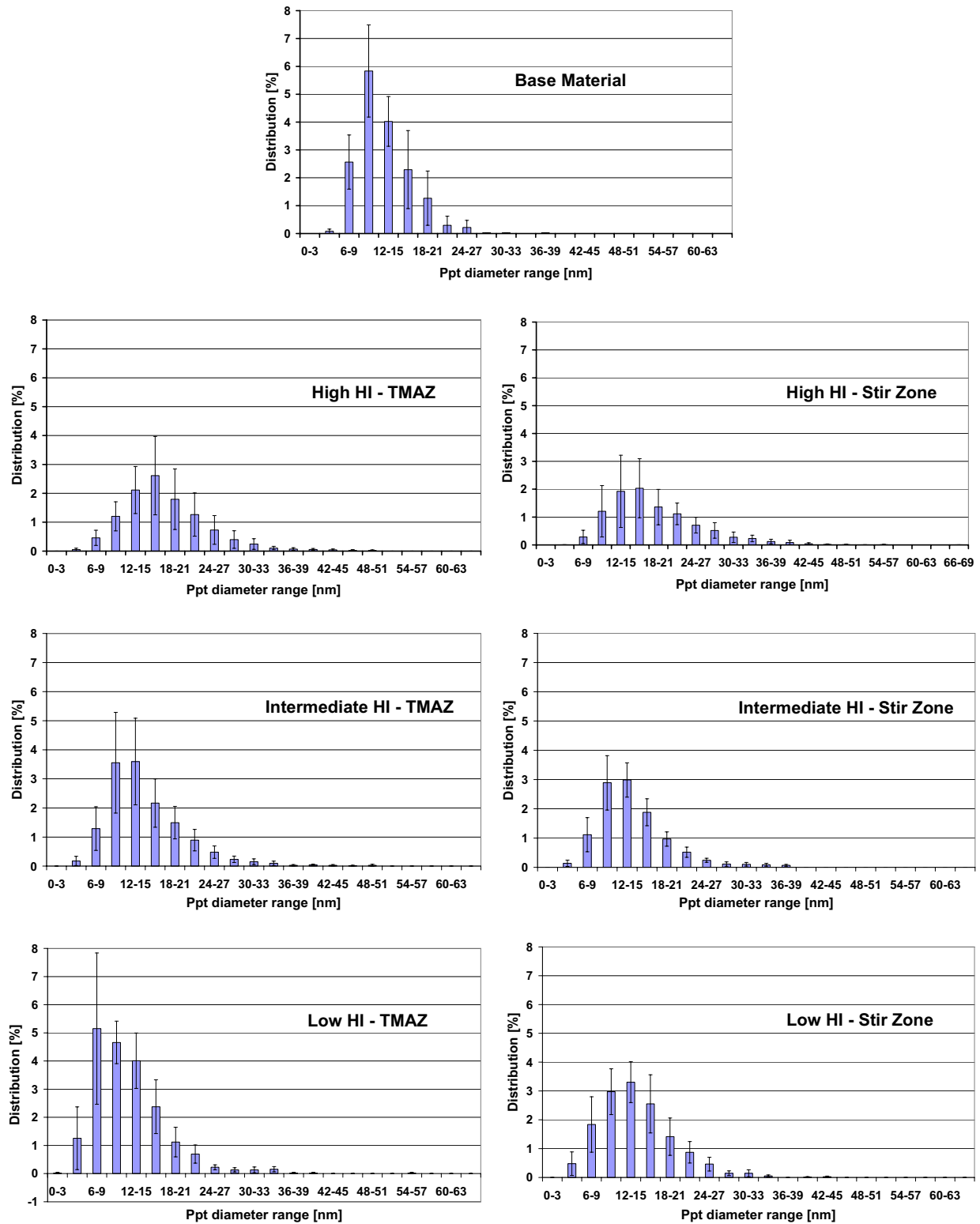


Figure 5-19 - Precipitate (Ppt) size and distribution of the Al-Mg-Sc FSW joints using three different input parameters (high HI - WP4, intermediate HI - WP2 and low HI - WP1.33) along TMAZ, SZ and BM.

The influence of the thermal cycles on the Al_3Sc stability is represented by the graphs in Figure 5-20 for the SZ and TMAZ. It can be observed that even the highest thermal cycle in the SZ is far away from dissolution temperature, but the coarsening temperature has shown to be reached. However, no detectable variation of the precipitate size and distribution suggests that the thermal cycle (WP4) is too fast for significant coarsening of Al_3Sc precipitates to occur. In the TMAZ, all welding conditions have shown to be below the coarsening temperature, indicating stability of the Al_3Sc precipitates in these temperature fields.

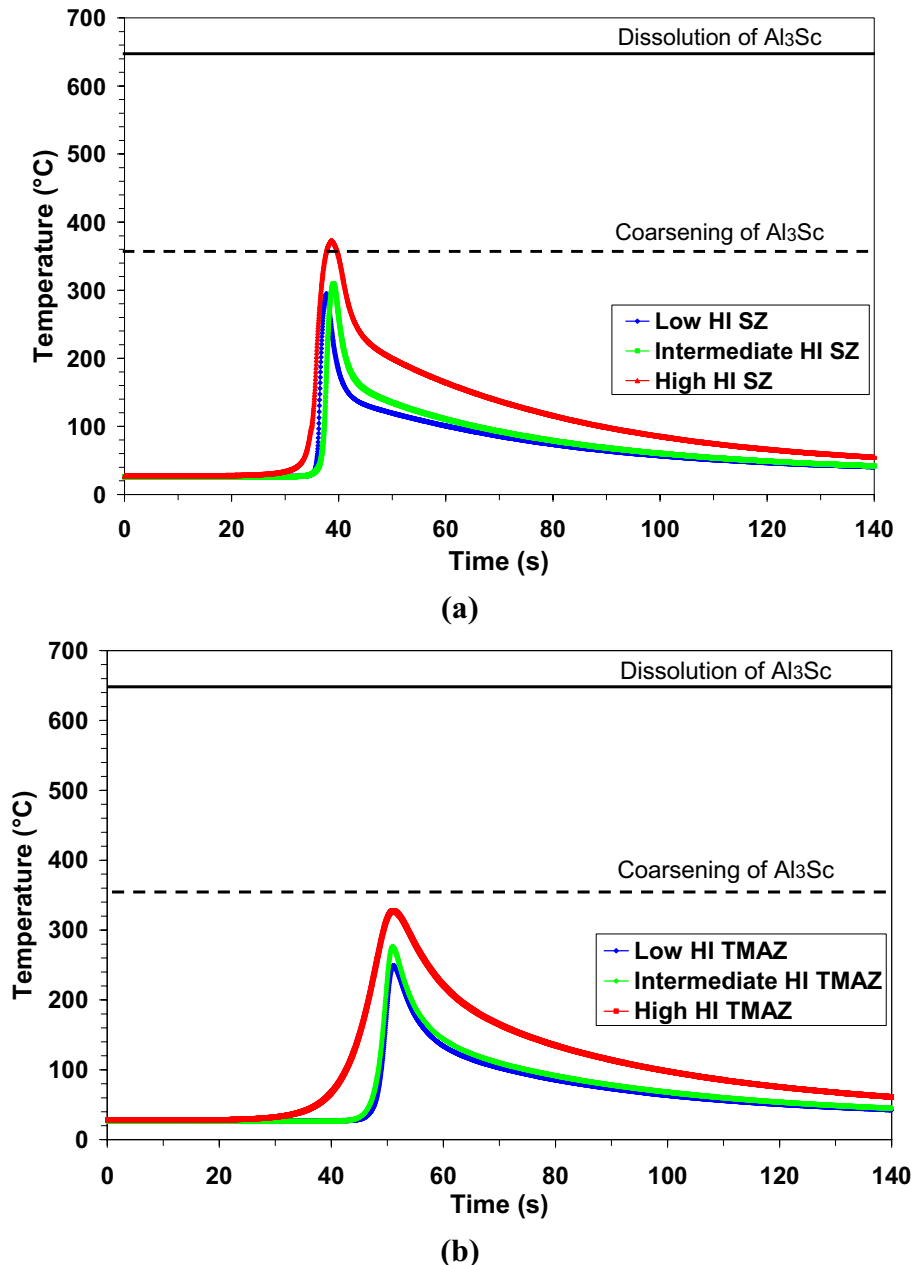


Figure 5-20 – Correlation between precipitation stability and thermal cycles obtained in (a) SZ and (b) TMAZ of Al-Mg-Sc joints.

5.1.3.3 Analogy of Al-Mg-Sc FSW joints / strengthening predictions

The contributions of microstructural features in Al-Mg-Sc alloys can be basically classified in three different ways: Solid Solution, Grain Boundary and Precipitate Strengthening. The solid solution strengthening is assumed here as being basically produced by Mg that is present in 4.3wt% in this alloy. It is known that Mg can also be present as Mg_2Al_3 particles, but EDS analysis showed the presence of scarcely coarse particles presenting Mg peaks, which according to size and distribution would not contribute to the alloy strengthening. However it is believed that the majority of Mg content remained in solution, even in weld zones. As commented before in section 2.4, Sc has very low solubility in Al (about 0.05% at 500°C) and due to the temperatures attained in the PWHT and FSW process, the amount of Sc in solution in Al-Mg-Sc joints is expected to be very low, producing no significant contribution to the alloy strengthening by solid solution [80].

The grain boundary strengthening contribution in this case can be estimated using the Hall-Petch model (section 2.4, equation 7), which considers the intrinsic resistance of the lattice to dislocation motion added to the dependence of the grain size. This contribution was not estimated here, because it was not possible to obtain accurate grain size values from TEM, SEM and optical microscopy analysis. In the case of optical microscopy, recrystallized grains in SZ were too small and in the SEM backscattered images, the grain boundary was not sufficiently revealed to generate any reliable results. In the TEM micrographs, the grain structure was revealed, as shown in Figure 5-12, but the number of grains was insufficient to generate accurate quantitative results. However, equiaxed grains with an average size of 2 μm were evidenced for the high HI condition and an average grain size about 1 μm for the low HI condition, which indicates a very fine grain structure and so capable of producing a significant contribution to strengthening.

The strengthening contribution attributed to fine Al_3Sc precipitates is expected to act through two different strengthening mechanisms: APB-anti-phase boundary (particle shearing) or the Orowan (dislocation looping) mechanism, previously discussed in section 2.4. These strengthening mechanisms consider the resistance to dislocation motion produced by the material due the presence of fine precipitates. In Al-Mg-Sc alloy, fine Al_3Sc precipitates are characterized by an ordered structure, and the APB mechanism describes the resistance of these precipitates to dislocation motion by formation of an anti-phase boundary, which results from shearing of these precipitates. The determination of dislocation motion by looping of dislocations around the precipitate, given by the Orowan model, is also applicable in this case and it scarcely depends on inter-particle spacing. For small-sized precipitates, the shearing of precipitates by dislocations is

energetically more favourable than looping around the precipitates. However, as the precipitate size increases, shearing becomes difficult and it results in increased strengthening promoted by the precipitates. Upon reaching a critical precipitate size, the easiest way for a dislocation movement during interaction with a precipitate is looping around the precipitate. For a fixed volume fraction of precipitates, if precipitate size increases, the strengthening tends to decrease, but the looping around the precipitate becomes easier. It is worth noting that the optimum precipitate size in terms of alloy strengthening is found at the transition from the shearing to the looping mechanism [20,80]. Kendig and Miracle [80] reported precipitate sizes for optimum strengthening for 1.5, 2.5 and 3.5% volumetric fractions as between 20 and 25 nm, as illustrated for the region close to the peaks, where the curves intersect in the diagram of Figure 5-21. It agrees with studies by Marquis *et al* [18], who describes that precipitates remain coherent in a diameter field of 20-30 nm, and, as previously mentioned, the coherency loss is detected by the presence of interfacial dislocations, when the precipitate diameter reaches about 40 nm. Other authors suggest that Al_3Sc precipitates cause very strong hardening in a size range from 3 to 15 nm diameter and tend to coarsen slowly with increasing temperature [20,74,77].

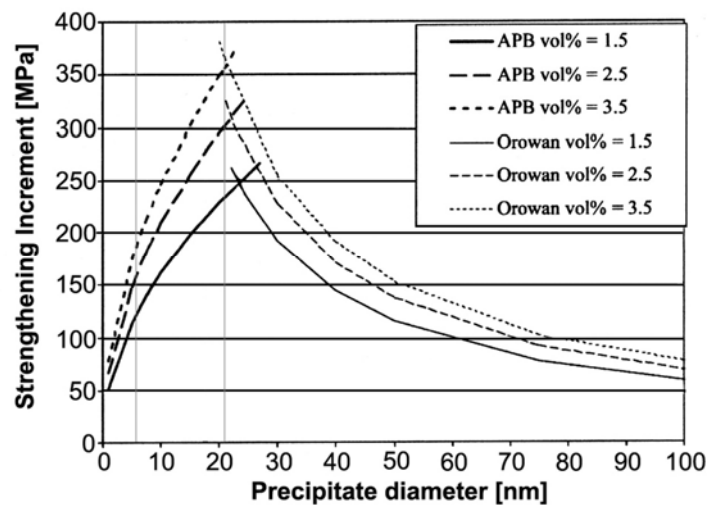


Figure 5-21 – APB and Orowan strengthening mechanisms due to resistance to dislocation movement, predicted for 1.5, 2.5 and 3.5% volume fraction [80].

Volume fraction was also estimated in this work, from measurements of the area fraction of Al_3Sc precipitates directly from TEM micrographs. The measured volume fraction for base material and welded zones of the three studied weld input parameters were found in a range from 3 to 4.5%. The highest volumetric fraction values were found in welded zones, showing no significant changes from high HI to low HI joints, but decreasing in the BM. By observing values of Al_3Sc precipitate size, illustrated in the diagrams of Figure 2-1, it can be seen that the majority of precipitate sizes are in the range 6-21 nm diameter for base material and all different weld input parameters. According to the predicted diagram of Figure 5-21, for the alloy Al-0.27%wt

Sc investigated, it was established that they are in a range (indicated by lines in the diagram of Figure 5-21) where the APB mechanism is the main contribution responsible for strengthening. Precipitates coarser than the critical size were also evidenced in the diagrams of Figure 5-19, hence indicating that Orowan mechanism is also acting, but at a minor level, as verified by the TEM analysis (Figure 5-17). From the considerations mentioned above, it can be affirmed that even with both strengthening mechanisms acting, for the size range of precipitates found here, the precipitate shearing mechanism is predominantly responsible for the material strengthening.

5.2 Characterization of the AA2024 T351 Friction Stir Welded Joints

5.2.1 Thermal history during FSW Process

Temperature measurements were carried out in-situ during the FSW of the AA2024 T351 joints, using the same procedure applied for Al-Mg-Sc joints, as described in section 3.3. The assumptions regarding the approach of the thermal cycles in the HAZ/TMAZ interface and SZ, as mentioned in section 4.1.1, were also assumed for the AA2024 T351 joints, as well as considerations associated with the accuracy of the temperature measurements. The thermal history measured for the AA2024 T351 joints in WP2, WP4 and WP8 conditions are shown in Table 5-3.

Table 5-3 – Thermal history of AA2024 T351 FSW joints using WP2, WP4 and WP8, low HI, intermediate HI and high HI, respectively.

Energy input	WP2		WP4		WP8	
Weld zone	HAZ/TMAZ	SZ	HAZ/TMAZ	SZ	HAZ/TMAZ	SZ
Max. temp.	284°C	315°C	318°C	365°C	362°C	412°C
Heating rate	42.3° C/s	95° C/s	16°C/s	25.8°C/s	7°C/s	9.1°C/s
Cooling rate	3.5°C/s	3.7°C/s	3.2 °C/s	3.25°C/s	2.3°C/s	2.6°C/s
Dwell time	6 s	3 s	18 s	13 s	47 s	42 s

In the WP2 condition (low HI), the maximum temperature verified in the *backing bar* (SZ - 315°C) was measured at 2.5 mm from the joint line (retreating and advancing sides) for T3 and T5 thermocouples. T3 and T5 registered 3 seconds to reach maximum temperature and the weld cooling down to 50°C took about 85 seconds (cooling rate of 3.7°C/s). The maximum temperature attained in the *workpiece* (TMAZ - 284°C) was at 10 mm distant of the joint line, on the advancing side (T8 and T10). In the workpiece, it took about 6 seconds to reach maximum temperature and about 81 seconds for the weld cooling down to 50°C (cooling rate of 3,5°C/s). For AA2024 T351, lower temperature and faster thermo-cycles are involved (i.e. high heating and cooling rates), so are expected to exert less influence on the mechanical and microstructural aspects.

The thermal profiles obtained for the AA2024 T351 joint in WP4 condition (intermediate HI) registered maximum temperatures in the *backing bar* (SZ - 365°C) at 2.5 mm from the joint line (advancing side) for thermocouple T5. It took 13 seconds to reach its maximum temperature and the weld cooling down to 50°C took about 112 seconds (cooling rate of 3.25°C/s). The thermocouple placed in the *workpiece* (TMAZ - 318°C) showed maximum temperature at 10 mm

distant of the joint line on the retreating side (T8). It took around 18 seconds to reach its maximum temperature and about 100 seconds (cooling rate of 3.2°C/s) to cool down to 50°C .

In WP8, the critical energy input condition (high HI) of the AA2024 joints, the peak temperature was verified in the *backing bar* (SZ - 412°C) at 2.5 mm from the joint line (advancing side) in thermocouple T5. It took 42 seconds to reach maximum temperature in the region at 2.5 mm from the joint line, while the weld cooling down to 50°C took about 155 seconds (cooling rate of 2.6°C/s). In the *workpiece* (TMAZ - 362°C), the maximum temperature was measured at 10 mm distant from the joint line on the advancing side (T8). It took around 47 seconds to reach peak temperature and about 153 seconds to cool down to 50°C (cooling rate of 2.3°C/s).

Thermal cycles obtained in the SZ closest region of the AA2024 T351 joints are shown for the different FSW energy inputs in the diagram of Figure 5-22 in terms of backing bar temperature measurements, whilst the thermal cycles obtained for the HAZ/TMAZ interface closest region of all FSW energy inputs are presented in Figure 5-23.

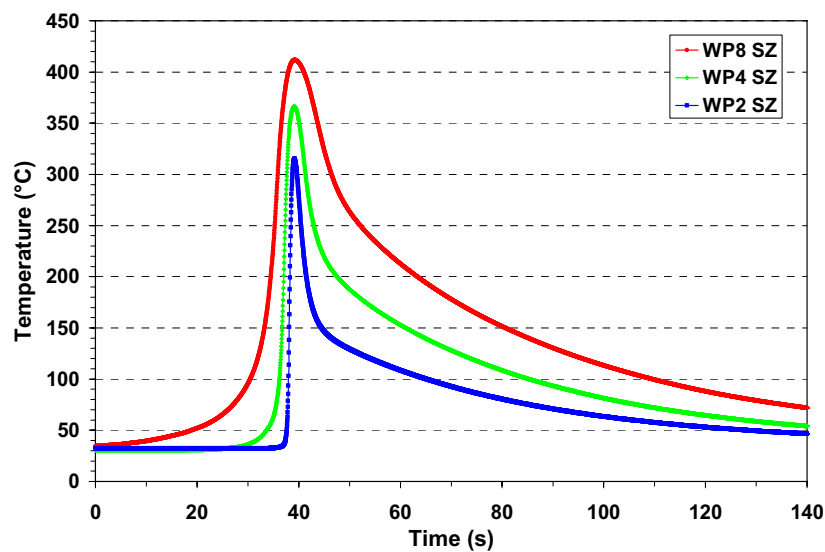


Figure 5-22 - Thermal cycles obtained close to the SZ during FSW of AA2024 T351 joints produced applying WP2, WP4 and WP8. Average thermal cycles measured from thermocouples fixed in the backing bar.

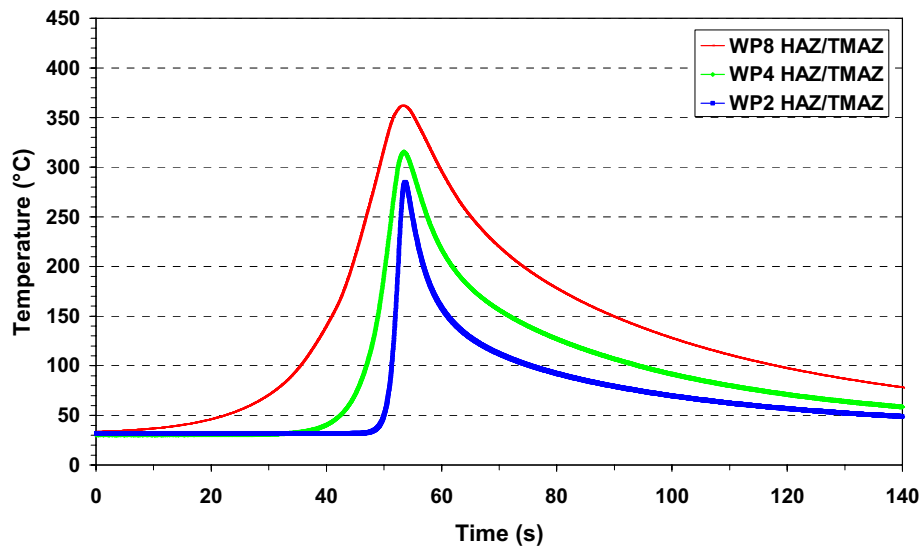


Figure 5-23 - Thermal cycles obtained close to the HAZ/TMAZ during FSW of AA2024 T351 joints produced applying WP2, WP4 and WP8. Average thermal cycles measured from thermocouples fixed in the workpiece.

A decrease of the heating rate was observed using intermediate HI, in comparison with low HI, but the cooling rate does not significantly change. Increasing the welding speed has been shown to control the heating rate. For this alloy, a variation in mechanical and metallurgical behaviour is to be expected, since an increase of peak temperatures was verified for the different welding conditions. However, the high strength AA2024 T351 alloy would not be affected by small variations in the thermal cycle, but this age-hardened alloy can be considered more susceptible to precipitate coarsening and dissolution, in comparison with the Al-Mg-Sc alloy. A further reduction of the heating rate was observed using high HI, followed by a decrease of the cooling rate. The heating rate was again associated with the increase of the welding speed and the higher peak temperatures attained. Welding the AA2024 T351 alloy using such high energy input and consequent peak temperatures will strongly influence the mechanical and metallurgical behaviour, once the strengthening S phase precipitates and GPB zones present in the BM coarsen and dissolve across the FSW zones. The temperature measurements obtained in this work closely fits with previous peak temperature values suggested for the AA2024 alloy. The literature reports a temperature range of 250 to 350°C for the HAZ, increasing to 350 to 450°C in the TMAZ and attaining 500°C in the SZ [53]. In the present work, the thermocouples measurements in the weld plates (10 mm away from the joint center) indicated a range of 284 to 362°C from low HI to high HI, which would represent the peak temperatures in the HAZ. The peak temperatures obtained through thermocouples in the backing bar attained 315°C (low HI) and 412°C (high HI), respectively, and so are reasonable to estimate the peak temperatures expected to be attained in the SZ during FSW.

5.2.2 Mechanical Characterization

5.2.2.1 Microhardness Test

Microhardness profiles were obtained along the transversal cross-section surface of the AA2024 joints FSW for the three different conditions, according to the procedure presented in section 3.4.1. Figure 5-24 presents the microhardness profiles of the AA2024 T351 joints produced with high HI (WP8), intermediate HI (WP4) and low HI (WP2). The advancing side corresponds to the left-hand side of the diagram (from weld centre direction to -14 mm) and the retreating side corresponds to the right-hand side (from weld centre direction to 14 mm). The typical “W” shape is only clearly seen in the high HI (WP8), which points out a minimum hardness in TMAZ, presenting values of 111 HV0.2 and, increasing somewhat in the SZ to about 127 HV0.2. The minimum hardness values tend to increase with an increase in the weld travel speed, presenting 120 HV0.2 for the intermediate HI (WP4) and attaining a value of about 126HV for the low HI (WP2) specimen. Evaluating the results in Figure 5-24, it can be seen there is a small hardness loss in the welded zones of low HI and intermediate HI joints when compared with average hardness values from the BM (145 HV0.2). Hardness values in the SZ also increase as the welding travel speed increases, but to a lesser degree than observed in the TMAZ, keeping the hardness values to a very small range for the three different energy inputs.

The results of the present work confirm those reported in previous studies in which the hardness minimum is located in the TMAZ, close to the SZ of the AA2024 FSW joints [51,53,55,82]. Furthermore, an outer hardness minimum has been observed, mostly showing hardness values close to the SZ hardness values [51,82]. It was proposed that the second minimum in the HAZ was related to *S* phase coarsening and GPB zones dissolution [55]. The hardness minima in TMAZ and HAZ were more pronounced in the higher heat input welds [51] and these results agree with hardness results observed in the present work. Hardness profiles did not show a clear second hardness minimum, even for the highest energy input (WP8), but the measured value is pronounced for the high HI in the TMAZ, presenting undermatching of more than 30 HV0.2, in comparison to the BM values. It is important to note that the minimum hardness values found in the TMAZ are approximately equivalent for both sides of the FSW joints (advancing and retreating sides). Such symmetry could be attributed to the geometry of the FSW tool, which combined with the FSW parameters for a given Al-alloy, result in a more homogeneous plastic flow and temperature distribution. For AA2024 alloy, the hardness profile greatly depends on the precipitation distribution and only slightly on the grain and dislocation

structure. Thus, in this work, special attention is paid to the precipitates evolution using TEM and is presented later on.

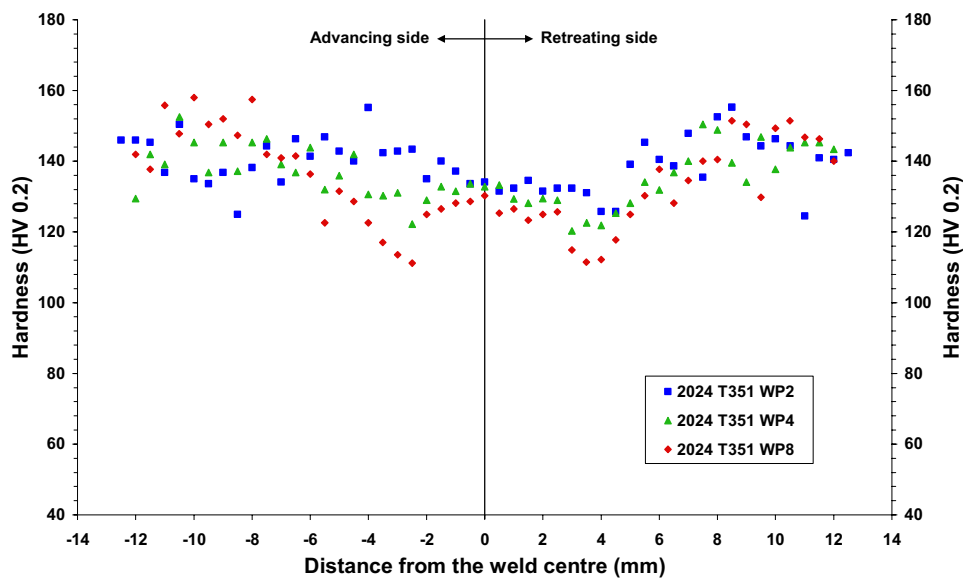


Figure 5-24 - Microhardness profiles obtained in the mid thickness of the transverse section, across the BM and FSW zones of the AA2024-T351 joint for the three energy inputs investigated.

5.2.2.2 Transverse Flat Tensile Test

Tensile properties were determined at room temperature for the AA2024 T351 alloy BM and for the FSW joints transverse to the joint, for the three different energy inputs. Table 5-4 presents the tensile properties for the three weld conditions studied: WP8 (high HI), WP4 (intermediate HI), WP2 (low HI) and the respective BM. Results are presented in terms of yield strength ($R_{p0.2}$), tensile strength (R_m) and elongation (A). The results presented in Table 5-4 show a trend of tensile properties improvement with increasing welding speed. Therefore, the low HI (WP2) presented the best performance, attaining yield and tensile strength values superior to 97% of the BM values. Allied to this, the low HI joints presented reasonable elongation values, reaching roughly 70% of the BM values. The good tensile behaviour observed in the low HI joints is better illustrated in Figure 5-25, in comparison with the intermediate HI, high HI and the respective BM tensile properties. In Table 5-4, the global tensile properties of AA2024 T351 FSW joints demonstrates a decrease of the tensile and yield strength for the high HI (WP8), but it remains around 90% of the BM tensile properties. In relation to BM, a significant decrease in elongation for the three FSW conditions was verified.

The general trend to an increase in UTS and percentage elongation with decreasing heat input was also observed by Shukla *et al.* [51] and it was followed by an increase of $R_{p0.2}$. The

authors reported [51] that for high heat input welds fracture almost always occurred near to the TMAZ/HAZ boundary, apparently in the region of hardness minima. In the present work, a similar behaviour was observed for the three different energy inputs, as shown in Figure 5-26. Failure of the tensile specimens always occurred on the retreating side at 45°, and the fracture region can be indicated as in the TMAZ/HAZ region. There is still a tendency to approximation of the fracture to the SZ, for lower energy inputs. Such an occurrence can be explained in terms of higher stress concentration, due to the higher strain rate, in conjunction with a lower thermo-cycle in the TMAZ close to the SZ in low HI joints. Moreover, the precipitate coalescence and GPB zones dissolution promoted by the higher thermal cycle of the high HI joint can reach a wider region of precipitate coarsening, extending the softening region through to the HAZ in opposite direction to the SZ.

Table 5-4 – Tensile test results of AA2024 T351 weld joints WP 8, 4 and 2 followed of comparison with results from base material.

AA2024 T351	Measured values			Comparison with BM		
Condition	Rp _{0.2} [MPa]	Rm [MPa]	A [%]	Rp _{0.2} [%]	Rm [%]	A [%]
WP8	301.2 ± 3	421.4 ± 4	6 ± 1	90	88	31
WP4	315.4 ± 2	448.1 ± 3	9 ± 1	95	94	48
WP2	328.2 ± 8	465.5 ± 1	13 ± 2	98	97	69
Base Material	333.4 ± 2	478 ± 1	19 ± 2	--	--	--

Thin plates (1 mm thick) of AA2024 T3 have shown a distinct tensile behaviour, according to the FSW parameters [55], which varied with a rotation speed range of 1800 to 2200 rpm and a transverse speed range from 50 to 450 mm/min. It has been found that for welds produced at lower transverse rates, failures occur in the HAZ, just outside the TMAZ on the retreating side, while for welds produced at lower tool rotation speeds and with higher transverse rates, failures occur mainly in the SZ. Moreover, studies [55] have reported that in welds produced at higher tool rotation speeds and higher transverse rates, failures occur on the advancing side. It is worthy of note that in the present work plate thickness was about 4mm, and by applying a rotation speed of 800 rpm and a transverse speed range from 100 to 400 mm/min, all the conditions presented failure on the retreating side (see Figure 5-26). Thus, the failure location seems to be directly dependent on the energy input, and the rupture in the TMAZ/HAZ retreating side region, has generally shown to be linked to high input energy, extending to a certain range.

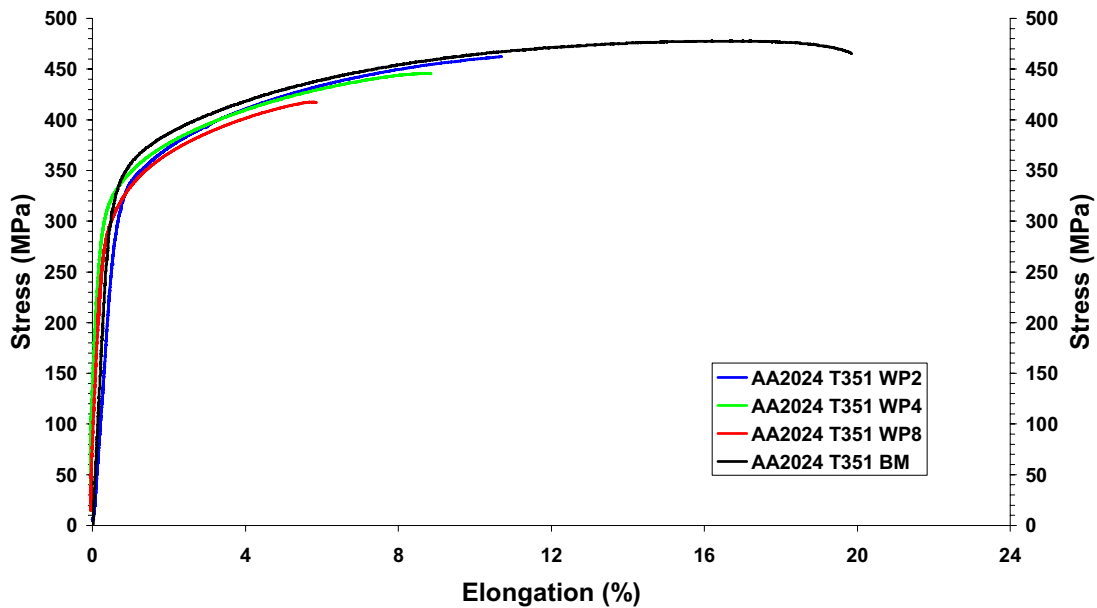


Figure 5-25 – Tensile behaviour of the AA2024 T351 FSW joints, using energy inputs WP2, WP4 and WP8 in association with results from the BM.

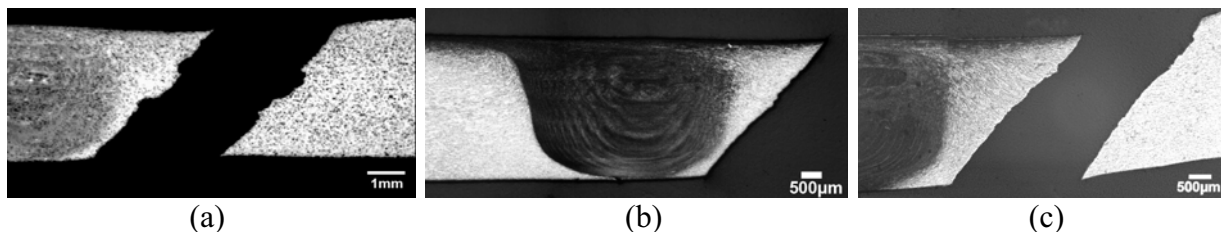


Figure 5-26 - Macrographs of the rupture location for the different parameter conditions: (a) low HI - WP2, (b) intermediate HI - WP4 and (c) high HI - WP8.

5.2.2.3 Microflat Tensile Test

Microflat tensile tests were performed for the AA2024 T351 alloy joined using different energy inputs, in order to establish a local tensile properties profile along the BM and FSW zones, as described in section 3.4.3. Just as with the Al-Mg-Sc joints, local tensile properties from AA2024 T351 joints are presented in terms of yield strength ($R_{p0.2}$) behaviour in Figure 5-27, tensile strength (R_m) behaviour in Figure 5-28 and elongation in Figure 5-29 for the three different energy inputs (low HI, intermediate HI and high HI).

The microflat tensile profiles from AA2024 T351 joints demonstrated a good performance, particularly with the low HI (WP2) condition, which presented minor deterioration of the yield strength particularly in TMAZ and HAZ close to TMAZ (see Figure 5-27). The yield strength values in the SZ were slightly restored to approximately the BM values. The tensile specimens failed at a hardness minima location, which corresponds to the TMAZ/HAZ, retreating side region. The fact that failure occurred in the retreating side of the transverse tensile

test (Figure 5-26) was attributed mainly to the low local tensile strength (Figure 5-28) in conjunction with high microstructural gradient (heterogeneity) resulting from the plastic flow. The intermediate HI and high HI (WP4 and WP8, respectively), presented higher deterioration of the tensile properties in TMAZ and HAZ, especially for the high HI condition.

Comparing the microflat profiles for the three energy inputs (Figure 5-27), a similar behaviour of the $R_{p0.2}$ profiles can be observed, with different levels of deterioration in relation to the BM $R_{p0.2}$ (≈ 320 MPa). The $R_{p0.2}$ minimum, found to be in TMAZ, was less influenced by the thermal cycle and plastic flow resulting from low HI, which presented an $R_{p0.2}$ minimum of about 255 MPa, while the intermediate HI presented an $R_{p0.2}$ minimum of about 235 MPa and high HI presented an $R_{p0.2}$ minimum of about 222 MPa. The $R_{p0.2}$ values in the SZ have shown to be near to the BM $R_{p0.2}$ values for the low HI joint, presenting around 300 MPa. The $R_{p0.2}$ values in the SZ were lower with an increase in energy input, presenting values around 292 MPa for the intermediate HI joints and 275 MPa for the high HI joints. The R_m profiles observed for intermediate HI and high HI also follow a similar pattern, presenting R_m minimum in the TMAZ with values of about 372 MPa and 357 MPa (Figure 5-28), respectively. The influence of a higher peak temperature on the deterioration of R_m was evident, in comparison with BM average values of the R_m (≈ 410 MPa). The R_m values in the SZ have also shown as the yield strength, values near to the BM R_m values for the high HI joint (402 MPa), roughly the same BM R_m values for the intermediate HI joint (≈ 410 MPa) and also similar values for the low HI joint (≈ 405 MPa). Such behaviour indicates that tensile properties are significantly restored in the SZ for all energy inputs investigated. Elongation profiles have shown to follow approximately the $R_{p0.2}$ and R_m tendency, increasing A with the increase of $R_{p0.2}$ and R_m , and decreasing A with a respective decrease in $R_{p0.2}$ and R_m (see Figure 5-29).

For such an alloy, the FSW tool geometry used to produce the welds also generates a balanced material flow and the critical material softening area (TMAZ) has shown to be nearly equivalent in the retreating and advancing sides. The material softening in the critical FSW region (TMAZ) can be represented by 87% and 70% of the R_m and $R_{p0.2}$ of the BM for the high HI joint, 91% and 74% of the R_m and $R_{p0.2}$ of the BM for the intermediate HI joint and about 100% and 80% of the R_m and $R_{p0.2}$ of the BM for the low HI joint, respectively. The good performance of the low HI joint is evidenced by the microflat tensile results and has shown a good relation to those for transverse flat tensile tests and microhardness.

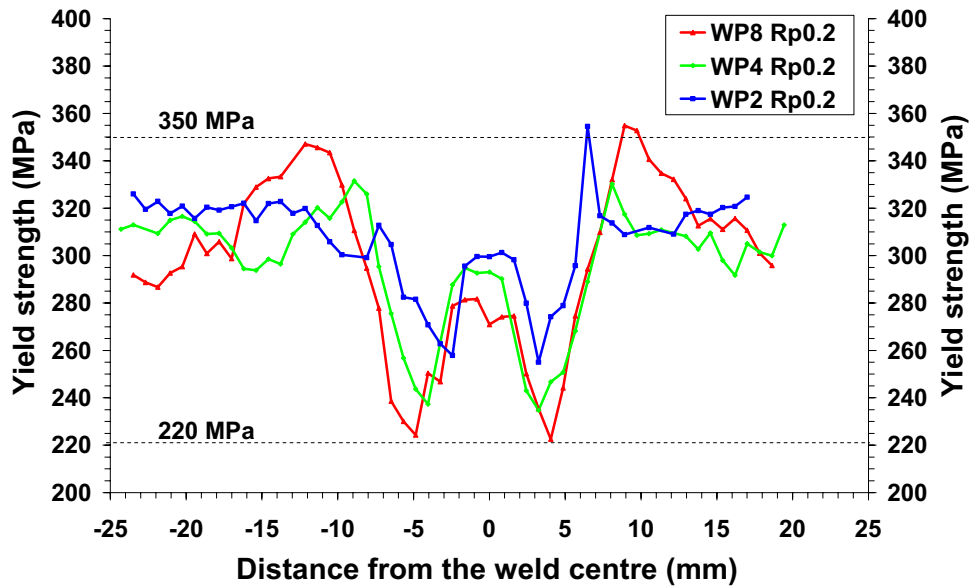


Figure 5-27 – Yield strength profiles from microflat tensile testing across the BM and FSW zones of the WP2 (low HI), WP4 (intermediate HI) and WP8 (high HI) parameters.

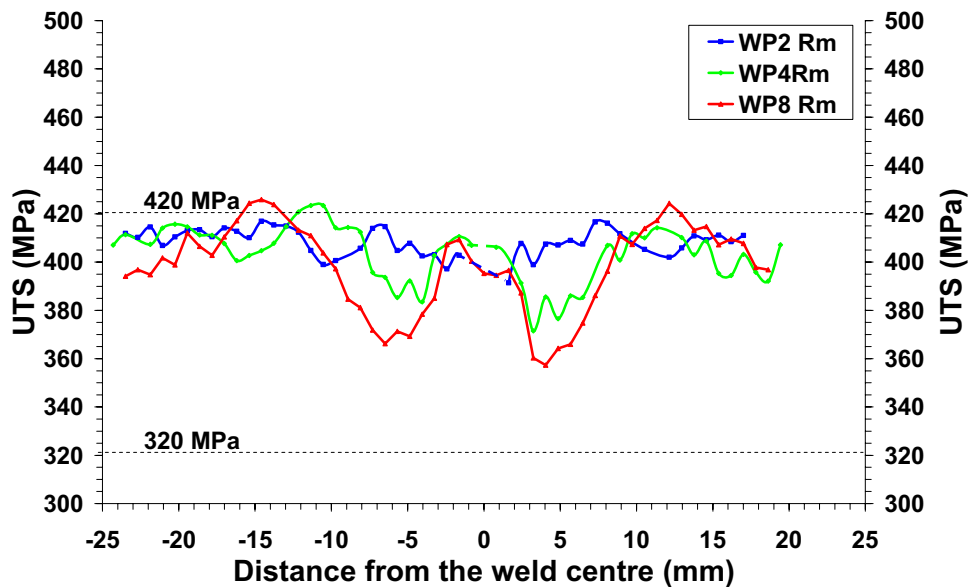


Figure 5-28 – Ultimate tensile strength (UTS) profiles from microflat tensile testing across the BM and FSW zones of the WP2 (low HI), WP4 (intermediate HI) and WP8 (high HI) parameters.

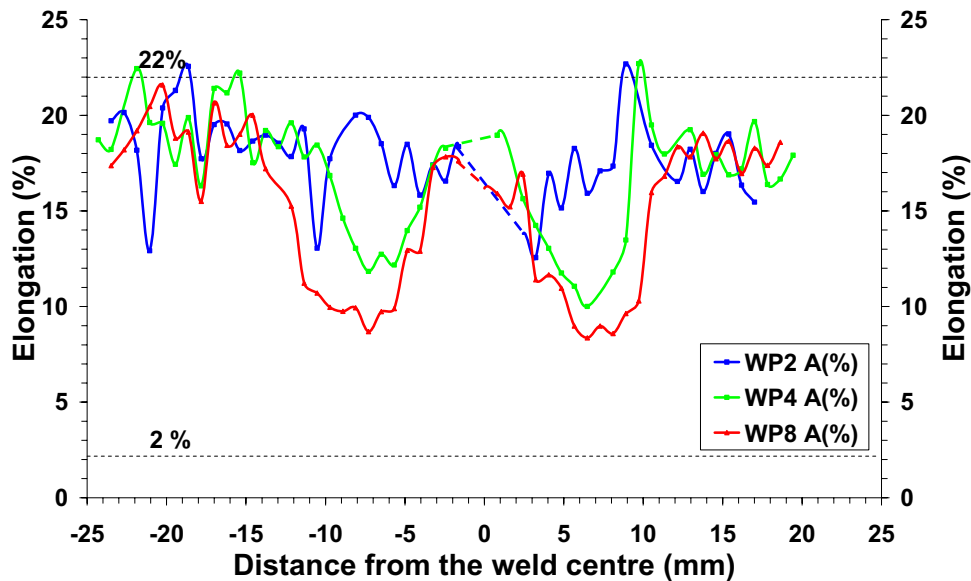


Figure 5-29 - Elongation profiles from microflat tensile testing across the BM and FSW zones of the WP2 (low HI), WP4 (intermediate HI) and WP8 (high HI) parameters.

The different tensile testing results were also compared through mechanical properties obtained by conventional flat tensile and microflat tensile results for AA2024 alloy, as showed representatively by the the tensile curves obtained through both testing techniques in Figure 5-30. The tensile curves obtained for the AA2024 T351 BM through conventional flat tensile and microflat tensile tests showed a misfit, similar to the characteristics presented for the Al-Mg-Sc alloy. The same reasons suggested previously for the Al-Mg-Sc alloy joints, regarding the gap between the microflat tensile curves and the flat tensile curves, were here assumed for the AA2024 T351 alloy joints. Just as with Al-Mg-Sc, the microflat tensile results for the AA2024 T351 BM and joints also showed lower R_m and $R_{p0.2}$ values than the BM flat tensile tests. In this case, microflat investigations of the joints have shown the highest $R_{p0.2}$ for the low HI, the highest R_m for the intermediate HI and highest A for the high HI joint. The maximum values presented for microflat tensile specimens from the SZ were close to, but still below, the microflat tensile values obtained from the BM. Ductile behaviour was observed for the local tensile properties, obtained by microflat tensile tests in the weld centre, where a clear yield extension was observed for the three FSW energy inputs.

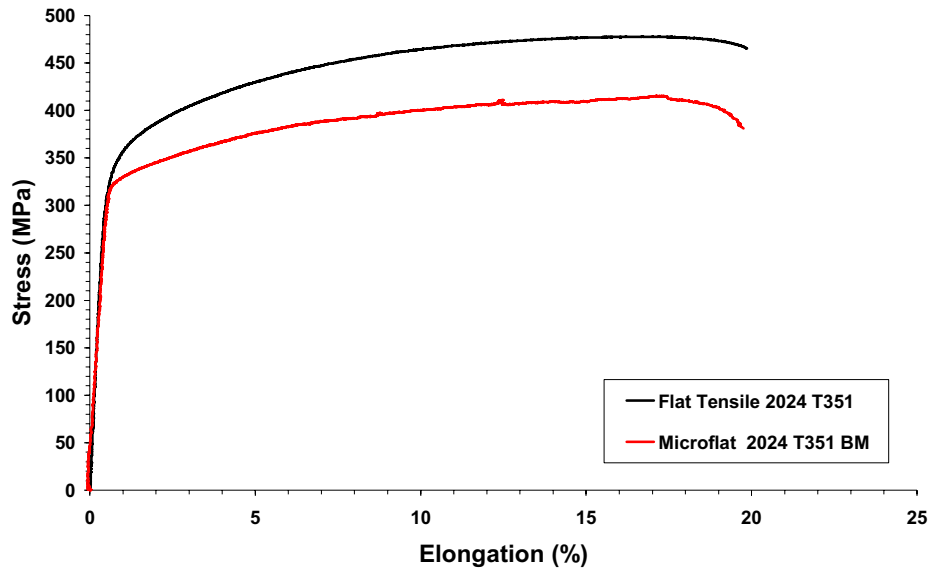


Figure 5-30 - Microflat tensile behaviour of the AA2024 T351 alloy BM in comparison with transverse flat tensile behaviour from BM.

5.2.3 Metallurgical Characterization

5.2.3.1 Macro and Microstructural Investigation

Global microstructural features of the FSW joint and its respective zones were previously described in section 2.3. Similar to the previously investigated alloys, the microstructure of the AA2024 T351 BM was characterized by deformed elongated pancake shaped grains, followed by the HAZ where no visible microstructural variation was observed and highly distorted structure presenting a high degree of deformation and grain rotation of about 90° right in the interface with the weld centre (TMAZ). The SZ, where the highest degree of deformation and the highest temperatures take place, was characterized by fine equiaxed recrystallized grain structure.

Figure 5-31 shows macro and micrographs of the plane transverse to the weld seam representative of the AA2024 T351 FSW joint welded with parameter set WP2 (low HI). Such an alloy and parameters combination showed the typical onion-rings structure in the SZ. All the energy inputs presented satisfactory weld characteristics, as full penetration and absence of defects, varying in some aspects of the joint geometry, due to the distinct plastic flow. It was observed that high input energy, i.e. WP8, tends to produce a wider recrystallized area in the SZ close to top side of the joint and the resulting onion rings were thinner and more homogeneous compared to those for intermediate and cold parameters. This is mainly due to the higher peak temperatures taking place in the hot parameter joint, which facilitate the material flow. Intermediate HI and low HI joints showed a warped and wider spaced onion ring structure (see Figure 5-31). Grain boundary details were well revealed using optical microscopy under

polarised light, as shown in the micrographs detailing the HAZ and interfaces of TMAZ and SZ (Figure 5-31 a and b). The microstructure of the AA2024 T351 alloy presented a high degree of deformation imposed on the grains in the TMAZ. This effect is illustrated in detail in Figure 5-31 (a) and (b), for the interfaces TMAZ/SZ on the advancing and retreating sides. The microstructural gradient is visibly wider on the retreating side, essentially as a result of the material flow direction.

The FSW thermal cycle measurements obtained from thermocouples indicated peak temperatures from 315°C (bottom) to 284°C (mid-thickness) measured for the low HI joints, being able to reach from 412°C (bottom) to 362°C (mid-thickness) for the high HI joints. It can be assumed that peak temperatures in the HAZ were equivalent to the temperatures measured in the weld plates in a range of 284 – 362°C, from low HI to high HI. In contrast, very close to the SZ (measurements in the backing bar), the temperature was observed to reach a range of 315-412°C from low HI to high HI joints, which was expected to be approximately the TMAZ peak temperatures, where a rotation of elongated and partially recrystallized grains around the SZ were produced. The highest plastic deformation was introduced in the SZ during FSW and temperatures are expected to reach more than 500°C, giving place to an entirely recrystallized microstructure with grain size in the order of about 4 μm [10]. However, in the present work, the temperatures measured in the workpiece were associated to the HAZ/TMAZ and the temperatures obtained in the backing bar were associated to the SZ, since it was the closest region where temperature has been measured. Such peak temperatures have shown to reflect directly on the resulting microstructure of the AA2024 T351 FSW joints, mainly by the critical softening produced in TMAZ of the high HI joint, extended to a lesser degree to the adjacent HAZ and recrystallized SZ identified in the hardness and tensile tests (see section 4.2.2). The softening effect is expected to be less affected by the grain structure and more controlled by the strengthening second phase particle dissolution and coarsening caused by the FSW process, where, for this alloy, the strengthening is extremely dependent on the stability and distribution of the GPB zones and precursors of *S* phase.

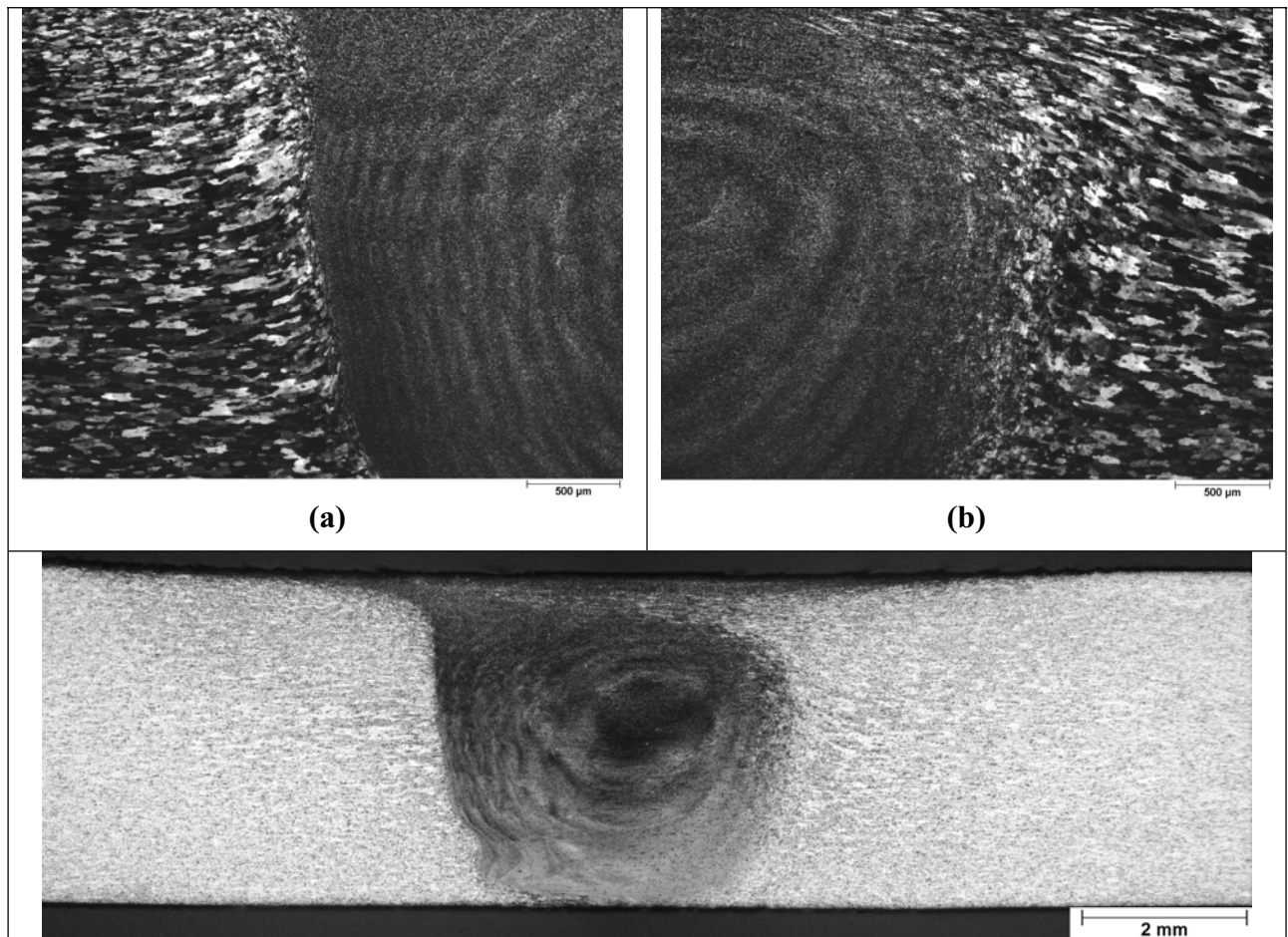


Figure 5-31 - Transversal section overview of the weld seam of the AA2024 T351 FSW joint by optical microscopy. (a) Detail of the microstructure interface delimiting SZ and TMAZ/HAZ in the advancing side and in (b) the retreating side.

SEM analyses of the AA2024 T351 were performed to observe the microstructural details particularly those related to the recovered and recrystallized grain structure produced during FSW. Figure 5-32 shows backscattered electron micrographs of the SZ of the AA2024 T351 FSW joints for the three energy inputs, (a) high HI WP8, (b) intermediate HI WP4, (c) low HI WP2 and (d) TMAZ, represented for low HI. The recrystallized grain structure in the SZ was better elucidated through SEM, and the fine grain structure has shown to change, according to the input energy applied. These micrographs presented a trend similar to the Al-Mg-Sc joints, since the SZ of the AA2024 T351 joints also presented coarser grain size for the higher FSW input energy (i.e. high HI WP8). High weld travel speed resulted in inferior peak temperature and consequently the reduction in grain size, as can be clearly observed for the low HI joint (WP2), shown in Figure 5-32 (c). The distortion of grains at the interface (TMAZ) with the SZ generated by the plastic flow is demonstrated in Figure 5-32 (d), where a 90° rotation of the elongated grains from the BM can be seen. This zone presented a microstructural gradient with a mixture of

pancake grains, highly deformed and recovered, also presenting particular localized recrystallization cores surrounding the SZ.

The recrystallized grain structure in the SZ can contribute to strengthening and toughness simultaneously, and such a contribution would be expected to be inversely proportional to the grain size, i.e. the finer the grain size the higher its contribution in strengthening. The mechanical tests showed just such a tendency, as previously presented in the hardness and microflat tensile profiles (see Figure 5-24, Figure 5-27 and Figure 5-28), where the higher energy input resulted in an extended softening effect in the SZ. Considering the microflat tensile results, the recrystallized equiaxed microstructure has shown to increase the material ductility, which can be verified in terms of the elongation results in the SZ in Figure 5-29 (WP8), and tends to decrease for lower heat input (WP2). The coarser SZ grain size observed for the high HI joint has the ability to absorb a higher density of dislocations during testing, increasing the elongation and consequently the ductility of the joint. Moreover, hardness results did not show any relevant variation in the SZ range for the three energy inputs, except for a very slight decrease in the high HI joint. However, re-precipitation of GPB zones can also be expected in the SZ after FSW [55] and, depending on distribution, this would be the prime factor to consider in terms of strengthening contribution. TEM investigations of the substructural aspects of second phase particles are presented and discussed in a later section.

The presence of coarse second phase particles and dispersoids was verified during SEM observations. Such particles and dispersoids are recognized by their coarse white reflections and the thin white dots in Figure 5-32. EDS analyses positioned over the coarse second phase particles indicated for one particle the presence of Fe, Mn, Si and Al, suggesting the presence of $\text{Al}_{12}(\text{Fe},\text{Mn})_3\text{Si}$ and for another particle the presence of Cu, Fe and Al, which suggests the formation of Al_7CuFe and $\text{Al}_6(\text{Fe},\text{Cu})$. These kinds of particle are generally very stable and do not dissolve at high temperatures, mainly due to the low solubility of Fe and Mn in the α -Al matrix. Furthermore, such particles are incoherent with the matrix, producing no strengthening contribution to the alloy [55]. Dispersoids observed along the weld zones were attributed to Mn-rich particles, which are typical of the AA2024 T351 alloy and can be suggested as being $\text{Al}_{20}\text{Cu}_2\text{Mn}_3$ particles [51,55]. The presence of the Ω phase (Al_2Cu), usually as plate-like particles is also expected.

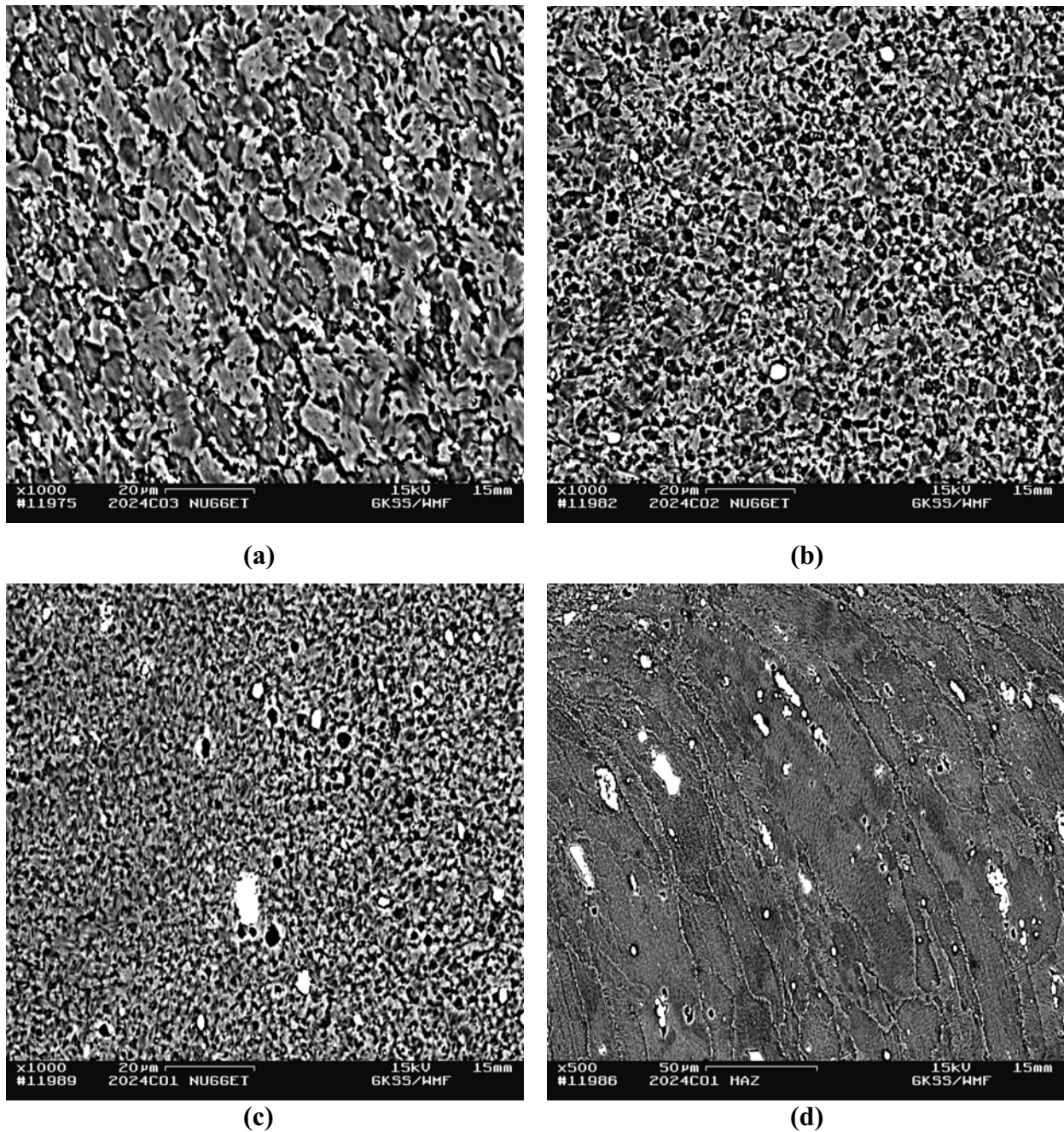


Figure 5-32 - SEM micrographs of the transversal sections of the AA2024 T351 FSW joints, showing equiaxed grains in the SZ of conditions: (a) WP8, (b) WP4, (c) WP2 and (d) representing distorted microstructure from TMAZ (WP2).

5.2.3.2 Substructural Investigation

The AA2024 T351 FSW joints were investigated using TEM by means of thin foils, prepared according to the procedure described in section 3.4.3, fundamentally in order to observe the presence of second phase particles and precipitates evolution in the FSW zones and BM. In this section, the results are presented systematically according to the region of the investigated joints. Initially, the features observed in the BM substructure are presented and discussed, and subsequently, the substructure evolution in the SZ and TMAZ for the different energy inputs is

presented and correlated with the previous BM features. Furthermore, the deformation and thermal cycle resulting from FSW are associated with the resulting precipitate evolution in the welded region and correlated with the mechanical testing results.

Base Material: Figure 5-33 shows micrographs with the presence of preferentially oriented dispersoids and small *S* phase precipitates observed in the BM of the AA2024 T351 joints followed by the respective EDS peaks, indicating the chemical elements present in such particles. In Figure 5-33 (a), the expected Mn-rich dispersoids, presenting lengths in a range of 200-260 nm and widths in a range of 50-100 nm, were observed with a typically elongated (rod and bar type) morphology and oriented in the same direction, most likely caused by the rolling process during fabrication. Furthermore, *S* phase precipitates presenting sizes of 15-20 nm with round morphology were also observed, as shown in Figure 5-33 (b). According to size, distribution and interaction with dislocations, it was suggested that such particles are predominantly *S''* precipitates, precursors of the stable *S* phase (Al_2CuMg). As reported earlier in section 2.6, the *S''* precipitates can be formed heterogeneously on dislocation loops and helices and it is the predominant cause of strengthening during the initial stage of precipitation hardening, producing even an higher contribution in strengthening than the GPB zones (Cu/Mg clusters) [45]. The GPB zones were not observed in conventional TEM micrographs, and also the diffused streaks detected in the diffraction pattern were not assumed to be valid to characterize the presence of GPB zones. The chemical composition of the dispersoids was analysed as shown in Figure 5-33 (c), showing the presence of Al, Cu and Mn. In agreement with prior studies [51], it was indicated that the presence of $\text{Al}_{20}\text{Cu}_2\text{Mn}_3$ particles, which are not coherent with an α -Al matrix, do not producing a significant strengthening effect, but are able to act as nucleation sites for new grains during thermo-mechanical processing. Careful EDS analysis of the small *S''* precipitates indicated the presence of Al, Cu and Mg, suggesting the same chemical composition of the stable *S* phase, as shown in Figure 5-33 (d). The EDS results presented in these diagrams (Figure 5-33 c and d) are representative of the results from scans on many dispersoids and precipitates presented in the respective micrographs (Figure 5-33 a and b).

Furthermore, the presence of Ω (Al_2Cu) dispersoids in the BM of the AA2024-T351 is also expected to be evidenced, presenting a diverse morphology, coarse and incoherent with α -Al matrix. Such dispersoids are formed as plates on the $\{111\}$ planes with a hexagonal structure and can also contribute to some strengthening [55]. The presence of Ω type dispersoids has been attributed to a slow cooling effect and the crystallographic relationships between dispersoids and α -Al matrix indicate that they formed during material cooling to room temperature [82]. As

mentioned previously, BM constituent particles presenting Fe and Mn are very stable and do not dissolve, even at high peak temperatures. However, particles like Mg_2Si , Al_2Cu and Al_2CuMg are soluble. Thus Ω (Al_2Cu) dispersoids did not produce the main contribution in BM strengthening, but their dissolution during FSW can increase the solute (in this case Cu) concentration in the weld zones, increasing the aging response.

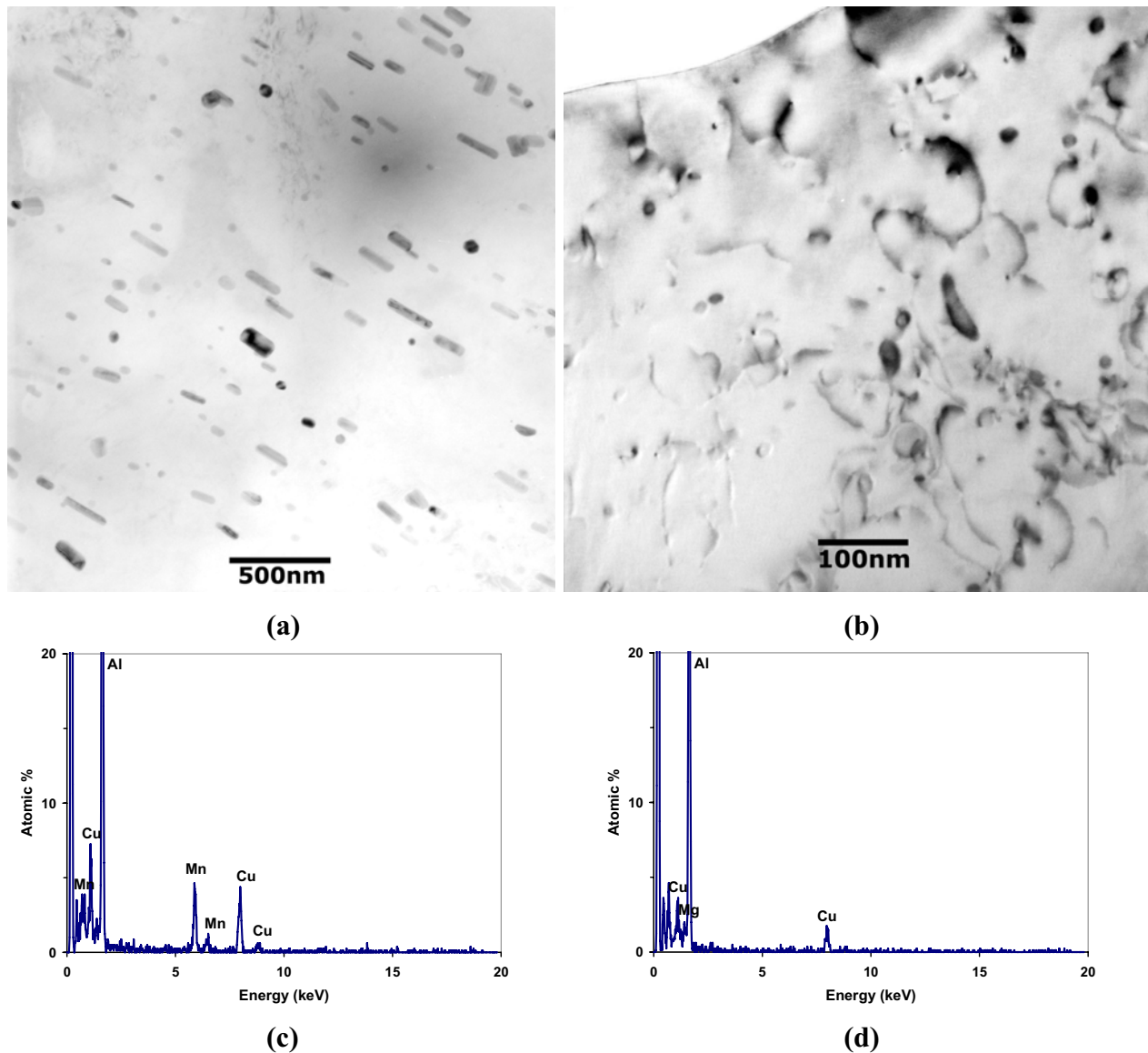


Figure 5-33 – Precipitation in the base material of AA2024-T351 alloy. (a) Nearly oriented dispersoids, (b) S phase thin strengthening precipitates with respective (c) EDS peaks of dispersoids and (d) EDS peaks of small S phase precipitates.

Stir Zone: The SZ of FSW AA2024-T351 joints presented equiaxed grains with predominantly round type precipitate morphology, as can be observed in the bright-field micrographs of Figure 5-34 for the low HI (WP2), intermediate HI (WP4) and the hot HI (WP8). The low HI condition presented round type precipitates with somewhat inferior size, when compared with the other energy inputs (average diameter about 80 nm). Figure 5-34 (a) shows

helical dislocation interaction with particles inside the dynamically recrystallized grain. Helical dislocation structures were observed in the SZ, generally in a low dislocation density grain, and have been suggested to be generated during cooling to room temperature [36,82]. The round type precipitates presented particularly for this low energy input, possess an apparent coherency contrast, at least for some orientation directions in relation to the α -Al matrix, as observed in Figure 5-34 (b). It is assumed that due to the low peak temperatures occurring for the low HI (WP2), less stable GPB zones dissolve in the SZ while previously more stable S'' and S' precipitates grow to form the stable S phase, while still retaining some coherency relation with the matrix. Such indication of coherency was concluded from the strain contrast, similar to those observed for Al-Mg-Sc precipitates (see 4.1.3.2). It has been reported that the high temperature experienced in the SZ results in a smaller fraction of coarse $S'(S)$ and a higher level of available solute, which consequently would produce nucleation of GPB zones, leading to a greater hardness [53]. It must be pointed out that the suggested re-precipitation of GPB zones in the SZ after FSW did not attain the full precipitation condition, in order to match the BM formation of GPB zones, which would result in a partial strengthening effect. The higher energy inputs of WP4 and WP8 parameters showed coarse dispersoids randomly dispersed across the α -Al matrix of the equiaxed grains in the SZ, as presented in Figure 5-34 (a) and (b), differing from the ordered dispersoids previously observed in the BM (Figure 5-33 a) and presenting a chaotic arrangement of its second phase particles in the SZ after FSW. These second phase particles are attributed to coarse S phase resulting from the FSW thermal cycle, in this case incoherent with the α -Al matrix due to the higher peak temperatures attained for such weld conditions, and also stable second phase particles, i.e. Mn-rich dispersoids. The last constituent phase, previously referred to as $\text{Al}_{20}\text{Cu}_2\text{Mn}_3$ particles and Fe-containing particles, which exhibited a mainly rod and bar type in BM, were broken up by the stirring action of the FSW tool and coarsened to spherical or block shapes, produced by the thermo-mechanical cycles imposed on the SZ. These assumptions are in accord with previous studies regarding FSW of aluminium alloys, including AA2024 FSW joints [36].

The strengthening effect in the SZ of the AA2024 T351 joints can be clearly observed in the hardness profiles and microflat tensile profiles (mainly $R_{p0,2}$), presented in sections 4.2.2.1 and 4.2.2.3, where the softening effect produced by the $S'(S)$ phase coarsening was substantially restored by the formation of GPB zones after the FSW thermal cycle, which was found to reach up to 412°C very close to SZ (WP8). In the case of WP2, the slightly superior contribution to the strengthening, observed in hardness and specially in $R_{p0,2}$ profiles, was attributed to smaller grain

size, contributing to hardening through the well-known Hall-Petch relationship, and the presence of the partially coherent S' phase found in such a weld condition (see Figure 5-34 b). The elongation sink observed in the SZ with intermediate HI and low HI conditions was not possible to explain by means of substructural changes. The presence of particles with apparent coherency contrast in the SZ of WP2 could contribute to alloy strengthening, but without producing deterioration of the magnitudes observed to the tensile strength and elongation (Figure 5-28 and Figure 5-29).

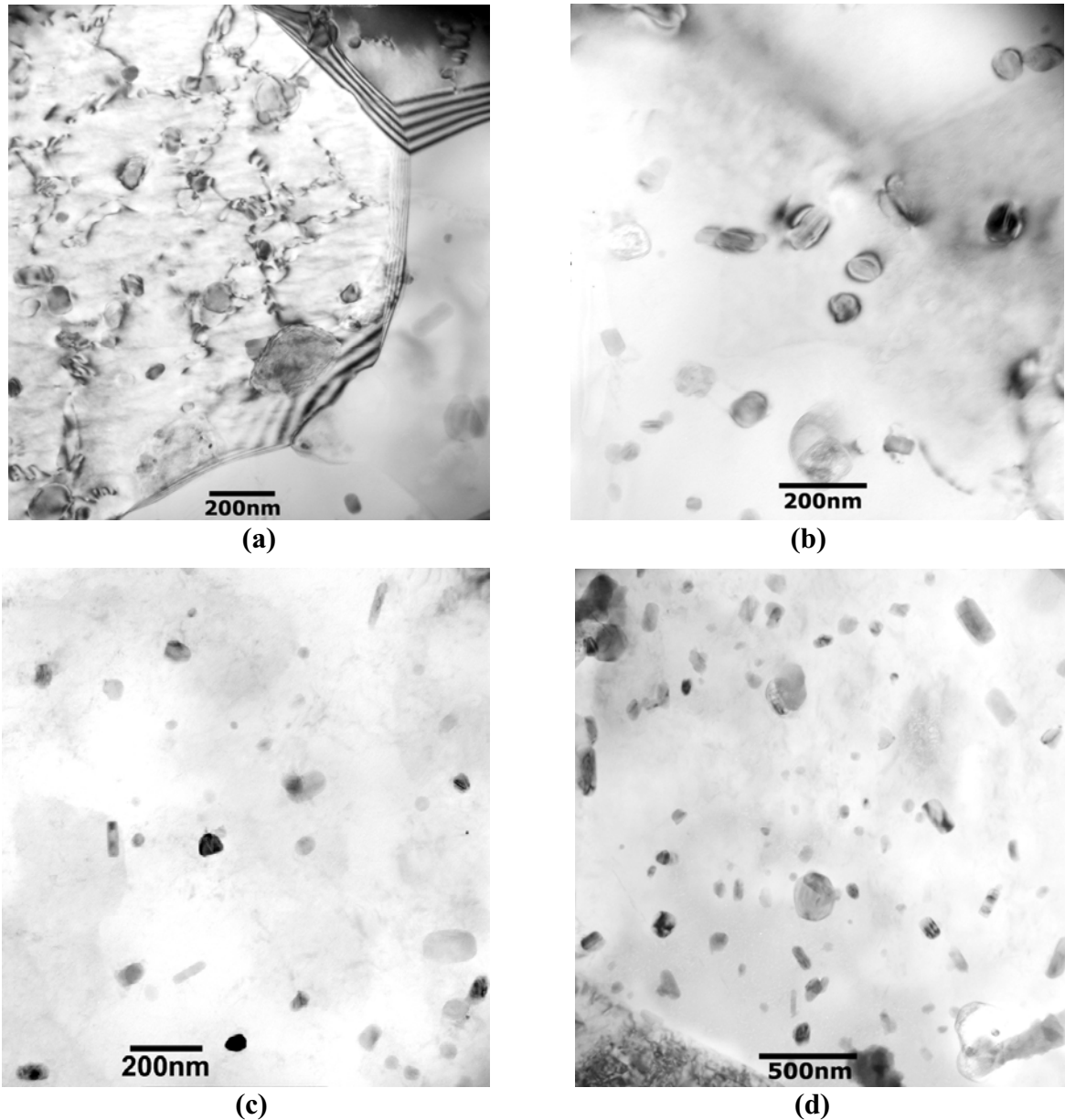


Figure 5-34 – Precipitation in the SZ of FSW AA2024-T351 joints. (a) and (b) are coarse round particles and round type precipitates with coherency contrast in the equiaxed grains (WP2); (c) and (d) are dispersoids with different morphologies, randomly distributed in intermediate HI (WP4) and high HI (WP8) conditions, respectively.

Thermomechanical Affected Zone: The precipitation phenomena in the TMAZ of AA2024 T351 are evident in the micrographs of Figure 5-35 for the low HI (WP2), intermediate HI (WP4) and high HI (WP8) conditions. In this region basically elongated precipitates were observed, preferentially oriented along the matrix for the different parameter sets, varying to some extent in the precipitate average size and morphology. TEM observations in the $[001]_{Al}$ zone axis revealed the presence of coarse, rod-type precipitates in the TMAZ of WP2 with an average size of 95 nm long and 15 nm wide, as shown in Figure 5-35 (a). In Figure 5-35 (b), bright-field TEM observations also evidenced the presence of rod-type precipitates for the intermediate HI (WP4) condition. Such preferentially orientated precipitates are suggested to originate from the initially fine S'' precipitates, which become increasingly coarse, due to the large strain and high peak temperature experienced in the TMAZ. However, the intermediate HI and high HI presented lath-type precipitates, while the low HI predominantly rod-type precipitates. The lath-type precipitates found in the TMAZ of intermediate HI and high HI joints are shown in Figure 5-35 (c) and (d). Lath-type precipitates were usually oriented, but in a different direction when compared to the rod-type precipitates, as found in the low HI joint. The lath-type precipitates in the TMAZ for WP4 presented an average size of about 68 nm long and 28 nm wide, while the precipitates in the same weld zone of the high HI joint presented average size of 94 nm long and 30 nm wide. Coarser and principally wider, lath-type precipitates are induced by the higher energy input, this is the precipitate coalescence favoured by high diffusion in grain boundaries, and the high energy of subgrain boundaries and dislocations. Furthermore, the precipitation in the TMAZ can also be induced by stable dispersoids [53]. Detailed studies of precipitate distribution were not conducted for this alloy in this work. However, according to direct observations in the TMAZ TEM micrographs, it can be suggested that an increase in the energy input resulted in an increase in the size and a decrease in the density of the S' precipitates, which for higher energy inputs tend to form predominantly lath-type precipitates.

Alloy strengthening is heavily dependent on the precipitation aspects of the AA2024 T351 alloy, and mechanical evaluations have shown that the TMAZ is the critical region for material softening of the different FSW joints (see section 4.2.2). The coarsening effect promoted by the FSW thermal cycle on the initially fine S'' and S' precipitates as well as the GPB zones dissolution are the main reasons for the hardness and explains the $R_{p0.2}$ fall observed in the hardness and microflat profiles, especially for the high energy input (see Figure 5-24 and Figure 5-27). It has been reported that at the HAZ/TMAZ boundary and extended through the TMAZ, the S' precipitate fraction is maximal and the GPB zones fraction is minimal [53]. Even high

density of S' precipitates is not sufficient to preserve the original BM strength, because these precipitates grow during welding, losing their coherency relation with the α -Al matrix. Moreover, GPB zones, which are mainly responsible for the material strengthening, are expected to dissolve and the thermal cycle imposed on the TMAZ (with peak temperatures over 362°C) was not sufficient to produce desirable GPB zone formation after welding. It is still possible to mention that for the minimum values of hardness, yield and tensile strength observed in the mechanical testing profiles, the coarse lath-type precipitates, more widely spaced as a result of the highest peak temperatures, contributed to attaining the critical deterioration of the properties in the TMAZ of the joints produced with higher energy inputs.

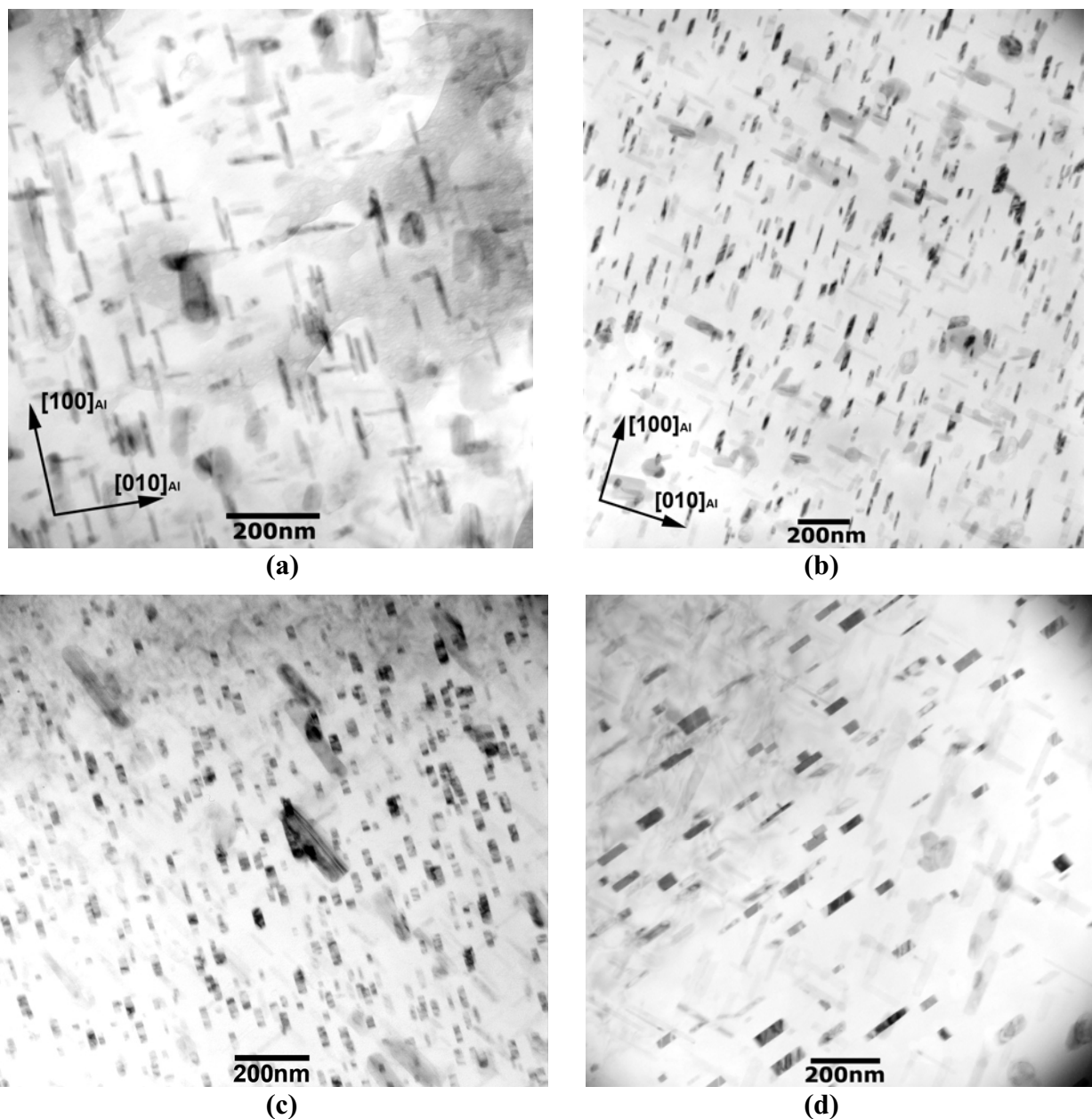


Figure 5-35 – Precipitation in the TMAZ of FSW AA2024-T351 joints. (a) Low HI WP2; (b) and (c) Intermediate HI WP4 and (d) high HI WP8.

High peak temperatures experienced in the TMAZ are expected to advance the less stable strengthening precipitates to the solution heat-treatment temperature, thus re-precipitating preferentially along grain boundaries, subgrain boundaries and dislocation cores during cooling. Such a phenomenon has also been reported for η precipitates in Al-Zn-Mg-Cu FSW alloys [36]. Figure 5-36 (a) shows heterogeneous precipitation of rod-type precipitates in TMAZ of the intermediate HI joint (WP4) with the respective SADP in [011] zone axis (Figure 5-36 b) presenting faint streaks relative to the high-contrast lath particles observed in this micrograph. This particular random distribution is attributed to re-precipitation of S' precipitates on dislocation cores and dispersoids that act as nucleation sites for the S phase precipitates. Such a precipitation feature is largely expected, since the TMAZ is affected by a high degree of deformation followed by recovery and stable dispersoids that remain there during FSW.

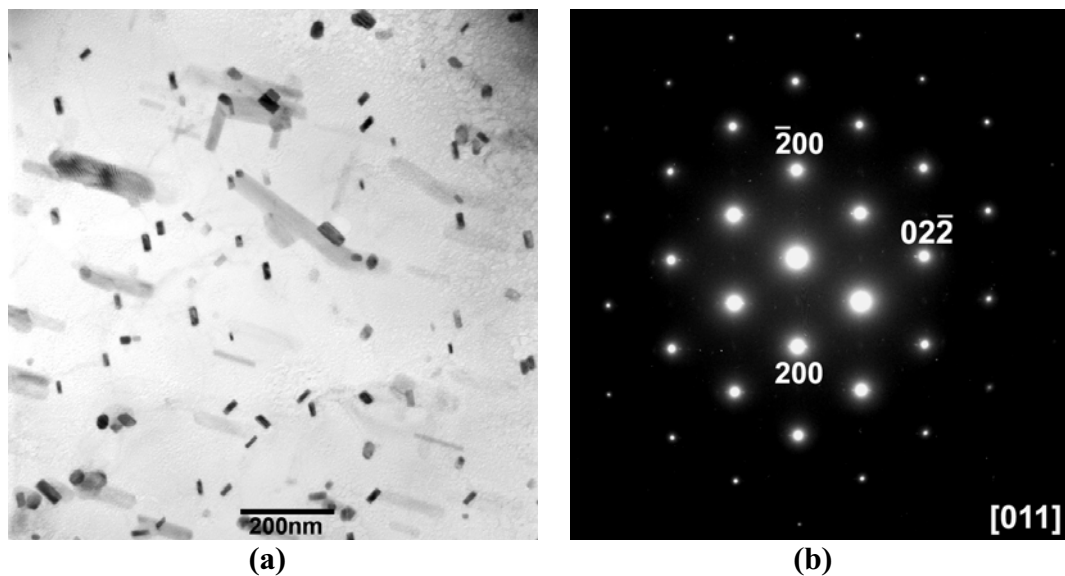


Figure 5-36 – Particular precipitation feature in TMAZ. (a) Bright field micrograph of heterogeneous nucleation sites for S' precipitates and (b) SADP showing the respective precipitate reflections in $[011]_{Al}$ zone axis.

Further investigation of the TMAZ showed the presence of precipitate free zones (PFZ), as shown in Figure 5-37. The PFZs were observed to form mainly alongside the grain boundaries, being featured by two layers free of precipitates adjacent to the grain boundary and coarsening of precipitates in the grain boundary. The precipitate nucleation and coarsening is favoured by the high diffusion in the grain boundary. Therefore, the high diffusion in the grain boundaries attract solute atoms dissolved in the α -Al, due to the peak temperatures during FSW, producing coarsened particles in the grain boundaries and an impoverishment of the adjacent matrix. This results in a precipitate-free layer surrounding the grain boundary, due to the non-existence of solute in this region. The PFZs occurrence was verified for the intermediate HI (WP4) and high

HI (WP8) joints, where the thermal cycle during FSW was higher, as shown by the bright-field TEM micrographs in Figure 5-37 (a) and (b), respectively. The presence of PFZ has been reported as an indication of overaged microstructure [82], and it was suggested that the lath-type and rod-type intragranular precipitates observed here in TMAZ are coarsened S' precipitates. The extra coarsened intergranular precipitates still preserved some elongated morphology, but according to size and location, were classified as incoherent dispersoids and so can promote intergranular weakness of the material.

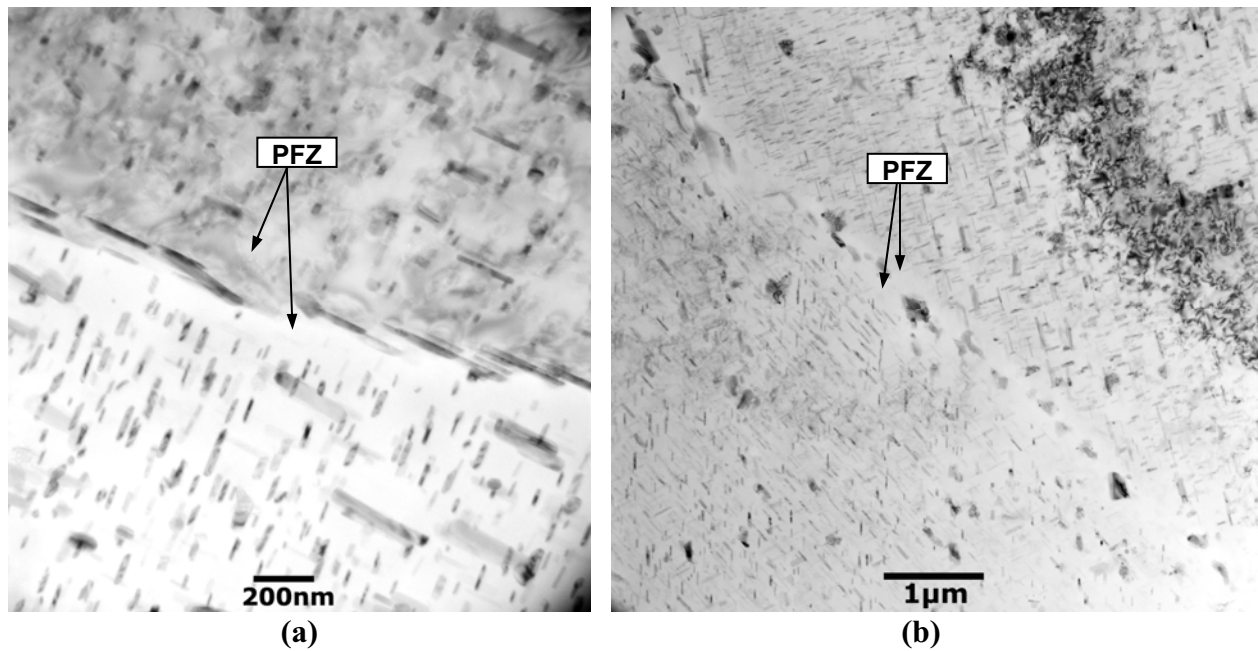


Figure 5-37 – PFZ and precipitate coarsening along the grain boundaries of TMAZ in (a) intermediate HI WP4 and (b) high HI WP8 of the AA2024-T351 joints.

Another cause of PFZs can be attributed to the vacancies sinking close to interfaces, i.e. grain boundaries and dislocations. Since the vacancies have a high diffusivity, it is difficult to avoid losing vacancies in the vicinity of grain boundaries and interfaces, which has important effects on the precipitation during ageing. Close to the boundary, the vacancy concentration will be the equilibrium value for the ageing temperature, while away from the boundary it will be that for the solution treatment temperature. During ageing, the solute concentration within the zone adjacent to the grain boundary is largely unchanged, but no precipitation occurs. The reason for this is that a critical vacancy supersaturation must be exceeded for nucleation to occur. In this case, the PFZ width can be determined by the vacancy concentration and, at low temperatures, when the driving force for precipitation is high, the critical vacancy supersaturation is lower and so narrower PFZs are formed. High cooling rates will also produce narrow PFZs by reducing the width of the vacancy concentration profile [83]. Narrower PFZs are expected to avoid

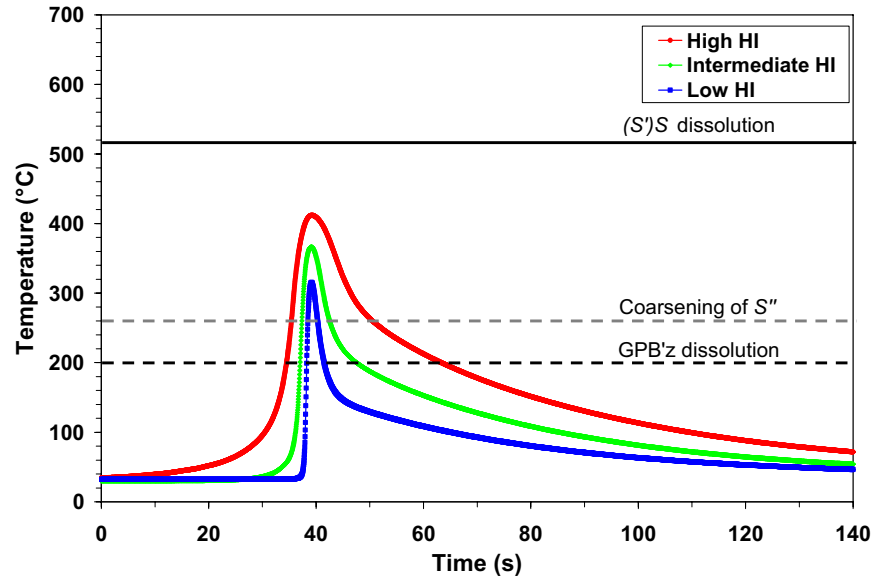
undesirable degradation of material properties that would be credited to such a microstructural feature.

5.2.3.3 Substructural evolution

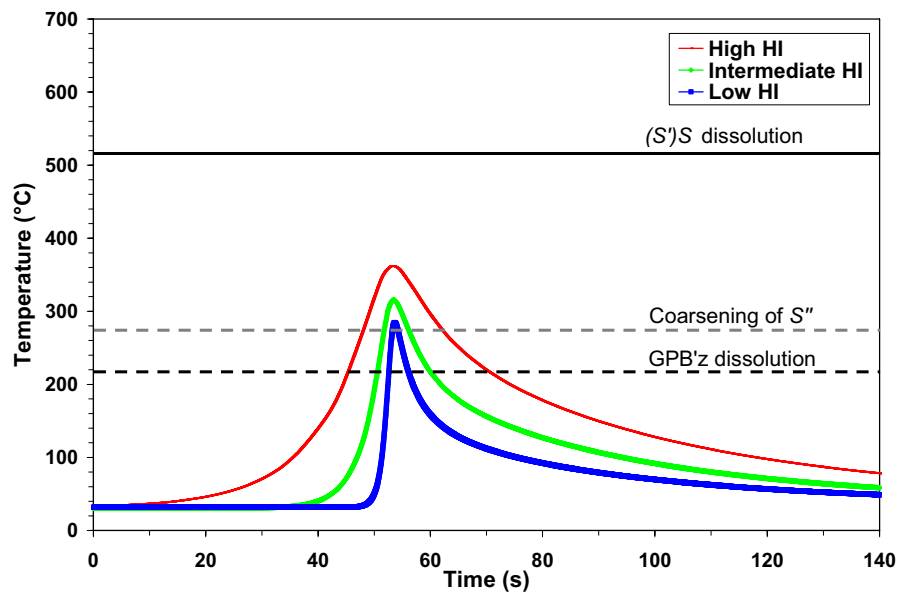
Thermal cycles generated during the FSW have shown significant influence on the original micro and substructural features of the AA2024 T351 alloy, which was also verified through the properties variation observed in mechanical testing results. According to the peak temperatures involved and results from TEM investigations, a precipitation evolution sequence for each weld condition has been proposed for the different weld zones (TMAZ and SZ). The model proposed is described as follows:

TMAZ			
BM	WP2	$S'' + S'$ (rod-type) \rightarrow	S' (rod-type)
S'' (15-20nm) +	WP4	$S'' + S'$ (rod-type) \rightarrow	S' (rod) + S' (lath)
GPB zones \rightarrow	WP8	$S'' + S'$ (rod-type) \rightarrow	S' (lath-type)
SZ			
BM	WP2	$S'' + S'$ (rod-type) \rightarrow	$S' \rightarrow S$ (round) +GPB reprecipitation
S'' (15-20nm) +	WP4	$S'' + S'$ (rod-type) \rightarrow	$S' \rightarrow$ GPB reprecipitation + dispersoids
GPB zones \rightarrow	WP8	$S'' + S'$ (rod-type) \rightarrow	$S' \rightarrow$ GPB reprecipitation + dispersoids

Schematics of the thermal cycles in relation to precipitate stability are shown in Figure 5-38 for the SZ and TMAZ. According to the proposed precipitation sequence during FSW, a good relation with the scheme of Figure 5-38 can be observed. In the SZ, the peak temperatures are expected to dissolve GPB zones and coarse S'' for all the energy inputs investigated. However, GPB zones are expected to re-precipitate during cooling, since mechanical testing results indicate such behaviour. The minor peak temperature in the TMAZ indicate the dissolution of GPB zones in order to form coarse S' precipitates, thus, the poor solute matrix is not able to reproduce such re-precipitation of GPB zones on cooling, which is more significant for the high HI (WP8) condition.



(a)



(b)

Figure 5-38 – Correlation between precipitation stability and thermal cycles obtained in (a) SZ and (b) TMAZ of AA2024 T351 joints.

5.3 Characterization of the AA6013 T6 Friction Stir Welded Joints

5.3.1 Thermal history during FSW Process

Thermal cycles generated during FSW of the AA6013 T6 joints were measured using the same routine applied for Al-Mg-Sc and AA2024 T351 joints, as described in section 3.3. The same considerations concerning the temperature measurements close to the HAZ/TMAZ interface and SZ described in section 4.1.1 are also assumed here for the AA6013 T6 joints. The thermal history observed for the AA6013 T6 joints in WP1.33, WP2 and WP4 conditions are presented in Table 5-5.

Table 5-5 – Thermal history of AA6013 T6 FSW joints using WP1.33, WP2 and WP4, low HI, intermediate HI and high HI, respectively.

Energy input	WP1.33		WP2		WP4	
Weld zone	HAZ/TMAZ	SZ	HAZ/TMAZ	SZ	HAZ/TMAZ	SZ
Max. temp.	265°C	315°C	295°C	337°C	350°C	396°C
Heating rate	78.3°C/s	285°C/s	44.2°C/s	102.3°C/s	16°C/s	28.2°C/s
Cooling rate	4.9°C/s	5°C/s	3.1°C/s	3.4°C/s	3.3°C/s	3.7°C/s
Dwell time	3 s	1 s	6 s	3 s	20 s	13 s

The peak temperature measured for the AA6013 T6 joint for the WP1.33 condition (low HI) in the *backing bar* (SZ - 315°C) at 2.5 mm from the joint line (retreating side) for thermocouple T3. Taking about 1 second to reach maximum temperature, the weld cooling down to 50°C took about 62 seconds (cooling rate of 5°C/s). Thermocouples placed in the *workpiece* (TMAZ - 265°C) showed the maximum temperature at 10 mm distant from the joint line, in the advancing side (T8 and T10). It took about 3 seconds to reach maximum temperature and the weld cooling down to 50°C took about 54 seconds (cooling rate of 4.9°C/s).

For the WP2 condition (intermediate HI) the peak temperatures in the *backing bar* (SZ - 337°C) were measured at 2.5 mm from the joint line (retreating side) for thermocouple T3. It took 3 seconds to reach maximum temperature and the weld cooling down to 50°C took about 98 seconds (cooling rate of 3.4°C/s). The thermocouples placed in the *workpiece* (TMAZ - 295°C) showed the maximum temperatures at 10 mm distant from the joint line in the advancing and retreating sides (T10 and T14). This region took 6 seconds to reach maximum temperature and the weld cooling down to 50°C took about 95 seconds (cooling rate of 3.1°C/s).

The high HI (WP4) showed peak temperature in the *backing bar* (SZ - 396°C) at 2.5 mm from the joint line (advancing side, T5). It took 13 seconds to reach maximum temperature and the weld cooling down to 50°C took about 107 seconds (cooling rate of 3.7°C/s). Thermocouples

placed in the *workpiece* (TMAZ - 350°C) showed maximum temperatures at 10 mm distant from the joint line in the advancing side (T8). It took around 20 seconds to reach peak temperature and the weld cooling down to 50°C took about 104 seconds (cooling rate of 3.3°C/s).

Thermal cycles obtained for the SZ closest region are plotted for the different FSW energy inputs in the diagram of Figure 5-39 in terms of backing bar temperature measurements, whereas the thermal cycles obtained for the HAZ/TMAZ interface closest region (*workpiece*) of all FSW energy inputs are presented in Figure 5-40.

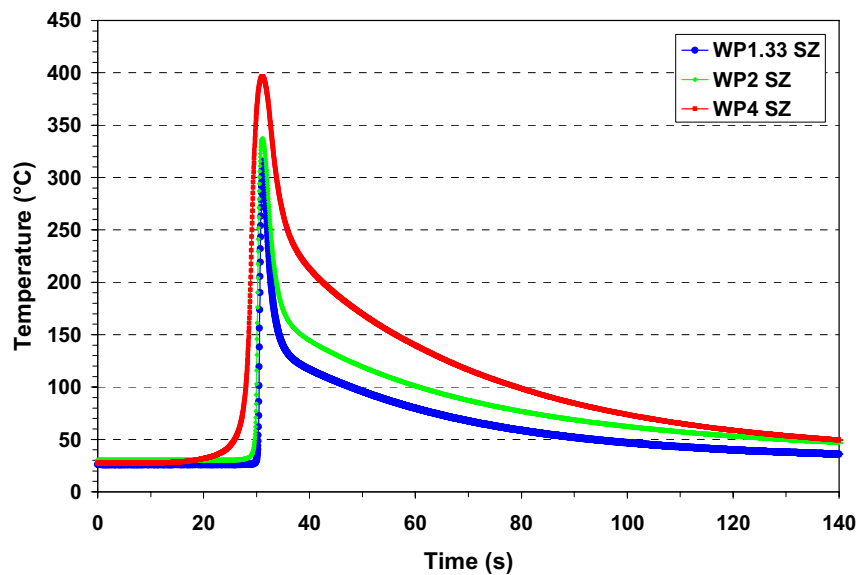


Figure 5-39 - Thermal cycles obtained close to the SZ during FSW of AA6013 T6 joints produced applying WP1.33, WP2 and WP4. Average thermal cycles measured from thermocouples fixed in the backing bar.

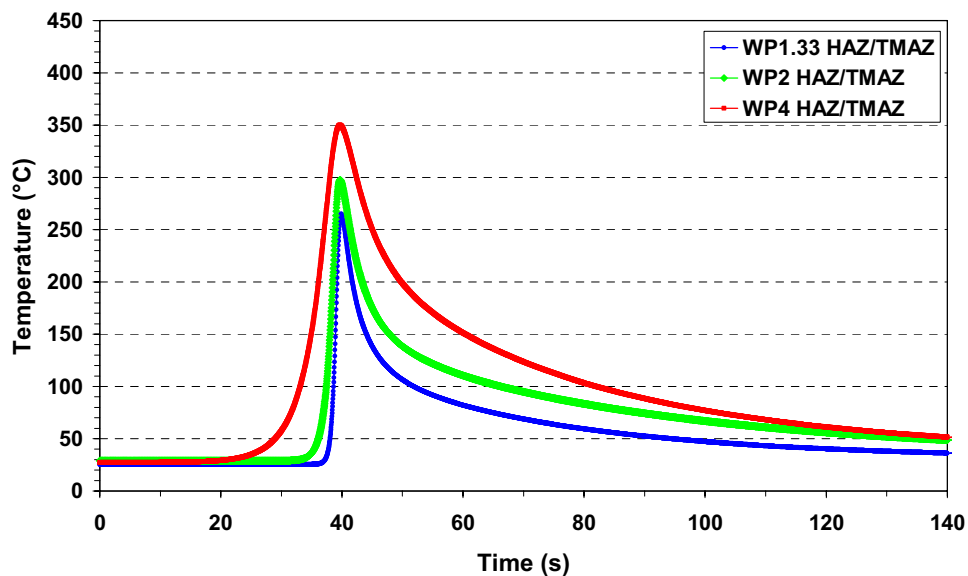


Figure 5-40 - Thermal cycles obtained close to the HAZ/TMAZ during FSW of AA6013 T6 joints produced applying WP1.33, WP2 and WP4. Average thermal cycles measured from thermocouples fixed in the workpiece.

For AA6013 T6, lower peak temperatures and the faster thermal cycles involved (i.e. high heating and cooling rates) are expected to have less influence on mechanical and microstructural features of this alloy, mainly due to the low stability of Mg-Si strengthening precipitates at temperatures over 200°C [41]. As expected, peak temperature values have been shown to increase with the increment of the heat input, produced by the decrease of the transverse welding speed, thereby producing an extended thermal cycle. The decrease of the heating rate and also decrease of the cooling rate using the low HI was verified. The dwell time was observed to increase using high HI, but the cooling rate does not show a significant variation. The age hardening AA6013 T6 alloy has a high disposition to precipitate coarsening and dissolution and, thus, great dependence on the thermal cycle generated during FSW. A severe deterioration of mechanical and metallurgical behaviour is expected for this alloy, since an increase of peak temperatures was verified in comparison with low HI condition. It indicates that the strengthening β phase precipitates and GP zones present in the BM are inclined to coarsen and dissolve across the FSW zones.

Thermal cycles obtained in this work can be considered realistic and accord with previous peak temperature values suggested for AA6013 alloy and similar 6xxx series alloys. Sato *et al.* [35], simulated FSW thermal cycles of an AA6063 alloy with different peak temperatures, and indicated that regions 0 to 8.5, 10, 12.5 and 15 mm away from the joint line undergo temperatures higher than 402°C, 353°C and 302°C, and lower than 201°C, respectively. He concluded that all precipitates were dissolved when the temperature was above 400°C and that the minimum hardness occurred at a position where the peak temperature had been around 350°C. According to estimations using ThermoCalc [30] software, it has been reported that an AA6022 alloy present certain equilibrium range temperatures for the precipitates and θ (Al_2Cu), Q and Si would be the equilibrium precipitates below 320°C. Between 320°C and 460°C, Q and Si would remain as the equilibrium precipitates. Furthermore, β phase would become one of the equilibrium precipitates between 460°C and 530°C, even considering 0.91 wt % Cu alloy. In addition, maximum temperatures near to the top surface and centre of the weld zone were reported to be around 425°C for an AA6061 alloy plate [84]. Thus, considering the lower thermal cycle provided by the WP1.33 joint, the peak temperatures attained very close to the SZ (315°C in the backing bar) would still present Cu precipitates, even if coarsened or partially dissolved. In the case of intermediate HI (WP2) and particularly high HI (WP4), which attain 337°C and 396°C, respectively, these are expected to present Q precipitates and large Si particles in the

HAZ/TMAZ region. In the SZ, strengthening precipitates dissolution is expected, and the formation of coarse β phase would take place.

5.3.2 Mechanical Characterization

5.3.2.1 Microhardness Test

As in the case of Al-Mg-Sc and AA2024 T351 joints, microhardness profiles were determined along the transversal cross section surface of the AA6013 T6 FSW joints for the three different conditions, following the procedure described in section 3.4.1. Figure 5-41 shows the microhardness profiles at mid thickness, transverse to the weld direction of AA6013 T6 of similar FSW joints produced with high HI (WP4), intermediate HI (WP2) and low HI (WP1.33) conditions. The advancing side corresponds to the left-hand side of the diagram (from weld centre direction to -20 mm) and the retreating side corresponds to the right-hand side (from weld centre direction to 20 mm). Hardness values in the BM were shown to be about 150 HV0.2 on average. For this alloy, material softening in comparison with BM is easily observed from start to finish of the FSW zones, resulting from the weld thermal cycle. The softening is observed within about 4 to 10 mm of both sides of the joint line. The high HI (WP4), which points out a minimum hardness in TMAZ/HAZ region, presented values of 75 HV0.2 (retreating side) at 4 mm away from the weld centre and, slightly increasing in the SZ (joint line) to about 93 HV0.2. Less material softening and greater hardness closer to the joint line were observed for faster weld travel speeds, as can be seen in the profiles of the intermediate HI (WP2) and low HI (WP1.33). Hardness minima can be observed of approximately 85 HV0.2 at around 2 mm for the intermediate HI (WP2) and for the low HI joint (WP1.33). It is also possible to observe slight variations between advancing and retreating sides. The minimum hardness values found here were more prominent in the case of higher energy input welds and correspond to the measurements from the retreating side of the weld. Hardness values in the SZ slightly increase, in comparison with TMAZ/HAZ minimum hardness, attaining an average of 95 HV0.2. However, hardness values in the SZ were practically unaltered with the increase of the welding travel speed, indicating that peak temperatures are affecting the hardening precipitates in a similar way for the different FSW energy inputs.

The softening in the 6xxx series BM has been widely reported, mainly for artificially aged alloys, which are easily influenced by effects such as thermal cycle resulting from the FSW process. The microhardness results obtained in this investigation are in agreement with the literature. FSW AA6013 T6 sheet, investigated by Heiz *et al.* [85] showed a BM hardness of about 140 HV, falling to about 110 HV on the center line of the weld and attaining a 95 HV

minimum hardness at about 10 mm away from the joint line. Murr *et al.* [84] reported a BM softening of a 6061 FSW alloy in T6 condition, which presented a variation in hardness of 60 HV, from 110 HV in the BM to 50 HV in the supposed HAZ region. Investigations of FSW 6063 T5 joints by Sato and co-workers [35] also reported extensive material softening in the weld zones. It was shown that the minimum hardness was located around 10 mm away from the weld center and the softening extends to about 15 mm. In addition, investigations of Svensson *et al.* [56] for a 6082 FSW alloy showed material softening from 110 HV to a minimum hardness of 60-65 HV at 8 mm from the weld center, on each side of the weld, but between 70-75 HV in the SZ. In most of the cases, BM softening in the SZ has been associated with precipitate dissolution and, across the TMAZ and HAZ, it has been attributed to precipitate overaging. The fact is that the gain in hardness resulting from artificial aging, basically by the formation of GP zones and fine coherent precipitates, is shown to deteriorate during FSW. Moreover, the smaller distance of the minimum hardness and softening extent from the joint line in relation to the above mentioned investigations can be attributed essentially to the FSW tool dimensions, and is also influenced by the tool geometry and FSW parameters.

As in the case of AA2024 alloy, the hardness profile of the AA6013 T6 significantly depends on the precipitate characteristics and only slightly on the grain and dislocation structure. Even when generating lower temperatures during FSW, in comparison with AA2024, the optimized precipitate condition of AA6013 T6 is expected to be severely affected due to its inferior stability at the high temperatures experienced during FSW. Considering such aspects, investigations of precipitates evolution using TEM were carried out and are presented in section 4.3.3.2.

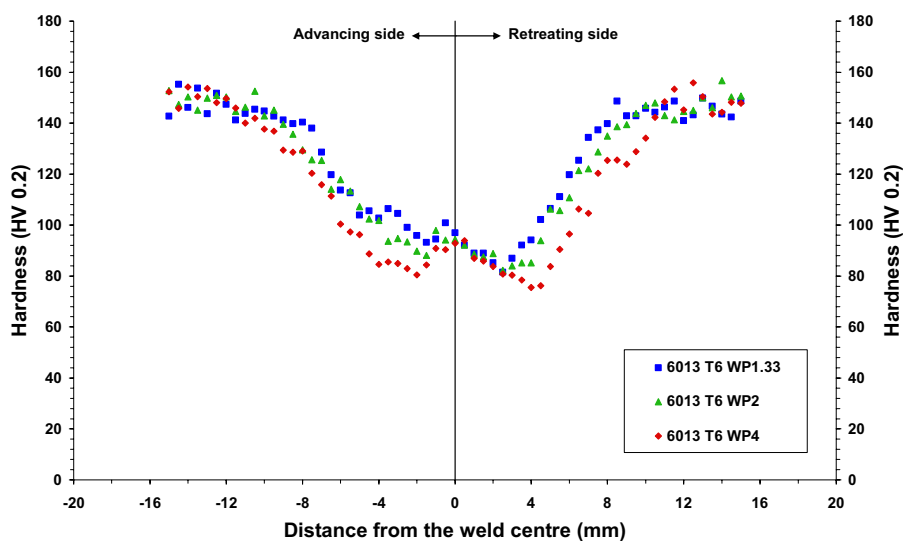


Figure 5-41 - Microhardness profile obtained in the mid thickness across the base material and welded zones of the AA6013-T6 joint for all the welding parameters investigated.

5.3.2.2 Transverse Flat Tensile Test

Transverse flat tensile specimens were tested in order to determine the tensile properties at room temperature for the AA6013 T6 alloy BM and for the FSW joints, for the three different energy inputs applied. Following the same procedure used earlier, specimens were obtained from the butt joined plates and BM along the same direction, with the testing load position transverse to the welding direction and rolling direction (see Figure 4-7). The tensile properties for the three weld conditions studied, WP4 (high HI), WP2 (intermediate HI), WP1.33 (low HI) and the respective BM are shown in Table 5-6. The trend to yield and tensile strength improvement, by means of energy input decrease, can be clearly observed in Table 5-6. FSW low HI (WP1.33) joint showed the highest performance, achieving yield and strength values superior to 94% and tensile strength of about 82% of the BM values. However, elongation values obtained for the low HI joint show that it decreases abruptly to around 10% of the BM elongation. The intermediate HI and high HI joints showed inferior values of yield and tensile strength, but remained in the range 82-88% for yield strength and 74-78% of the BM tensile properties. A drastic decrease in the elongation was observed for all three FSW conditions, reaching a maximum value of 12% of the BM elongation values for the intermediate HI. Such elongation results can be explained by large undermatching, resulting mainly from the softening of the HAZ/TMAZ region. Strain concentration takes place in the relatively thin low strength region, under loading resulting in tri-axiality and hence reduced elongation. The tensile behaviour obtained for the AA6013 T6 alloy and its FSW joints can be better demonstrated in Figure 5-42 for material joined using low HI, intermediate HI and high HI in comparison with the respective BM tensile properties. The effect of the high peak temperature on the global tensile properties was noticeable and the best performance was observed for the lowest heat input welds. However, the ductility performance of the joints was severely affected by a similar proportion.

Table 5-6 – Tensile test results of AA6013 T6 weld joints WP1.33, WP2 and WP4 followed of comparison with results from BM.

AA2024 T351	Measured values			Comparison with BM		
Condition	Rp _{0.2} [MPa]	Rm [MPa]	A [%]	Rp _{0.2} [%]	Rm [%]	A [%]
WP4	197.2 ± 2	266.5 ± 1	2.6 ± 1	82	75	10
WP2	210.3 ± 2	281.3 ± 1	3.1 ± 1	88	78	12
WP1.33	226.5 ± 3	292.8 ± 3	2.5 ± 2	95	82	10
Base Material	240 ± 9	358 ± 9	26 ± 1	--	--	--

Figure 5-43 shows the failure location of the tested tensile specimens for different welding conditions. It was possible to observe that failure took place as a 45 deg shear fracture

followed by necking for all three FSW conditions. However, the failure location has shown that moved towards the SZ for higher welding transverse speed (WP1.33) while the opposite occurred for the inferior welding transverse speed, which moved towards the HAZ. Hence, it can be assumed that for the low HI (WP1.33) joint, the fracture location occurred in the TMAZ/SZ, crossing TMAZ up to the top and SZ down to the bottom; for the intermediate HI (WP2) joint fracture location occurred essentially across the TMAZ; and for the high HI (WP4), fracture location was close to the interface TMAZ/HAZ. It is important to remark that fracture occurred in the retreating side for all three welding conditions. The shift in failure location is basically attributed to the stretching of the temperature gradient with increasing energy inputs. In this way, critical temperature fields (leading to metallurgical reactions which result in softening) are shifted towards the BM and away from SZ. Such observations are quite in accordance with previous investigations involving tensile properties of FSW artificially aged alloys [56,85]. Similar behaviour was reported for a friction stir welded 6013 T6 alloy, when compared to the BM, specimens tested transversally to the weld exhibited reduced strength and ductility, although failure always occurred on the advancing side [85]. In addition, it was reported for a friction stir welded 6082 alloy that fracture never occurred close to the original joint line, but mostly close to the line where the shoulder of the tool had touched the top side of the weld, and considering a 45° fracture, at the bottom side of the weld the fracture surface was closer to the SZ, but still displaced 7mm from it. Such a behaviour can be attributed to wider extents of the softening region that can be generated by high input energies, FSW tool dimensions and geometries. In this investigation, the failure locations actually accorded well with the microhardness profiles, presenting the fracture location approximately at the point of hardness minima, and shifting slightly towards the SZ or HAZ, according to the softening extent resulting from the FSW process. Such behaviour was also comparable to previous results for the AA2024 T351 joints and the suggested metallurgical phenomenon to understand such features can also be assumed for AA6013 T6 alloy.

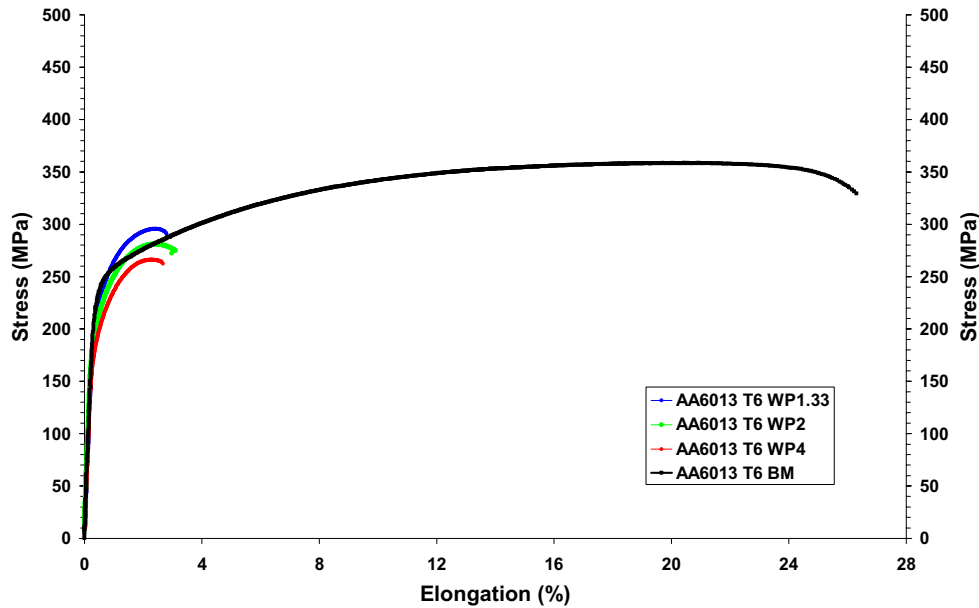


Figure 5-42 – Tensile behaviour of the AA6013 T6 FSW joints for energy inputs WP1.33, WP2 and WP4 in association with results from the base material.

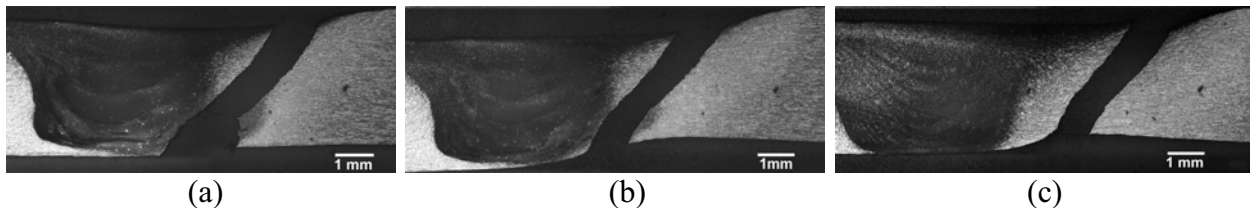


Figure 5-43 - Macrographs of the rupture location for the different parameter conditions: (a) cold WP1.33, (b) intermediate WP2 and (c) hot WP4.

5.3.2.3 Microflat Tensile Test

Microflat tensile tests were carried out for the AA6013 T6 alloy welded using different energy inputs, in order to determine the local yield strength, tensile strength and elongation across the BM and FSW zones. Specimens were obtained from the transverse section of the weld as described in section 3.4.3. The microflat tensile profiles for the AA6013 T6 joints are shown in terms of yield strength ($R_{p0.2}$) behaviour in Figure 5-44, tensile strength (R_m) behaviour in Figure 5-45 and elongation in Figure 5-46 for the three different energy inputs (high HI, intermediate HI and low HI).

The softening effect previously observed in the microhardness profiles, were visibly observed for the microflat tensile profiles performed on the AA6013 T6 joints for the three different energy inputs investigated. It indicated changes to the softening magnitude according to the weld transverse speed varied by only a very small fraction, indicating a slightly higher yield and tensile strength for the lower energy input applied during joining. FSW energy inputs

produced a material softening that varies from 8 mm from the joint line (zero distance in the diagrams) on both sides (advancing and retreating sides) for the low HI (WP1.33), extending to 12 mm on each side for the high HI (WP4) joint. Particularly for the high HI (WP4) joint, the yield and tensile strength indicate minimum strength values at approximately 4 mm distant from the joint line, which would be close to the TMAZ/HAZ interface, while yield and tensile strength minimums for intermediate HI (WP2) and low HI (WP1.33) joints are somewhat closer to the joint line. The yield and tensile strength levels in the SZ are slightly higher, except for the yield strength of the low HI (WP1.33) joint, which presents no substantial variation of values from TMAZ (advancing side) to TMAZ (retreating side) between 2.5 - 3 mm away from the joint line on both sides (see Figure 5-44). Such critical softening locations agree with previous microhardness measurements and the failure locations shown for global tensile tests was essentially found to be in the TMAZ, where R_m , $R_{p0.2}$ and hardness minima were also determined. The failures occurred on the retreating side and this is associated to the slightly lower local tensile properties than the advancing side (see Figure 5-45). Furthermore it could be also associated with the higher microstructural gradient (heterogeneity) resulting from the plastic flow, in comparison with the advancing side, and to a slightly superior thermal cycle theoretically undergone in this region, mainly for intermediate HI and low HI joints, since temperature measurements in the backing bar indicated such.

Microflat profiles for the three energy inputs show similar behaviour of the $R_{p0.2}$ profiles (see Figure 5-44) with significant levels of deterioration in relation to the BM $R_{p0.2}$ (≈ 325 MPa). As expected, the $R_{p0.2}$ was less influenced by the thermal cycle and plastic flow resulting from low HI (WP1.33), which presented an average $R_{p0.2}$ minimum of about 182 MPa across the TMAZ and SZ, while intermediate HI (WP2) presented an $R_{p0.2}$ minimum of about 164 MPa across TMAZ and SZ, and high HI (WP4) presented an $R_{p0.2}$ minimum of about 145 MPa in the TMAZ and approximately 170 MPa in the SZ. All the $R_{p0.2}$ values in the TMAZ and SZ are far away from the BM $R_{p0.2}$ values. R_m profiles obtained for low HI, intermediate HI and high HI conditions followed a similar pattern (see Figure 5-45), showing R_m minima in the TMAZ with values of about 260 MPa, 237 MPa and 234 MPa, respectively. The effect of the high peak temperature in deteriorating the R_m was evident, in comparison with BM average values of the R_m (≈ 350 MPa). The R_m values in the SZ show an increase, but remain below the BM R_m values, presenting roughly 280 MPa for the three different energy inputs. Yield and tensile strength obtained through microflat tensile tests were considerably different from the results obtained from transverse flat tensile tests and this was basically attributed to the different testing

directions (see Figure 4-7 and Figure 4-8). It has to be considered the typical anisotropic behaviour caused by the pancake grain structure present in such aluminium rolled plates.

Elongation basically shows an increase in the welded region, attaining maximum values in the SZ for all weld energy inputs (see Figure 5-46). The higher elongation in the weld zones can be related to the superplasticity of equiaxed recrystallized grains in SZ and recovered grains in TMAZ and HAZ. The dislocations annihilation and accommodation, allied to precipitate coarsening and dissolution, promoted by the high peak temperatures, tend to support the matrix ductility increment. Generally, material softening in the critical FSW region, which were mostly found to be in the TMAZ, were characterized by 67% and 45% of the R_m and $R_{p0.2}$ of the BM for the high HI joint (WP4), 68% and 50% of the R_m and $R_{p0.2}$ of the BM for the intermediate HI joint (WP2) and about 74% and 56% of the R_m and $R_{p0.2}$ of the BM for the low HI joint (WP1.33). A better performance of the low HI was evident. However, the microflat tensile results showed considerable undermatching of the joints in terms of yield and tensile strength. These results are in accordance with microhardness profiles previously shown. Nevertheless, transverse flat tensile results showed a joint efficiency able to reach over 94% of the BM yield strength and about 82% of the BM tensile strength.

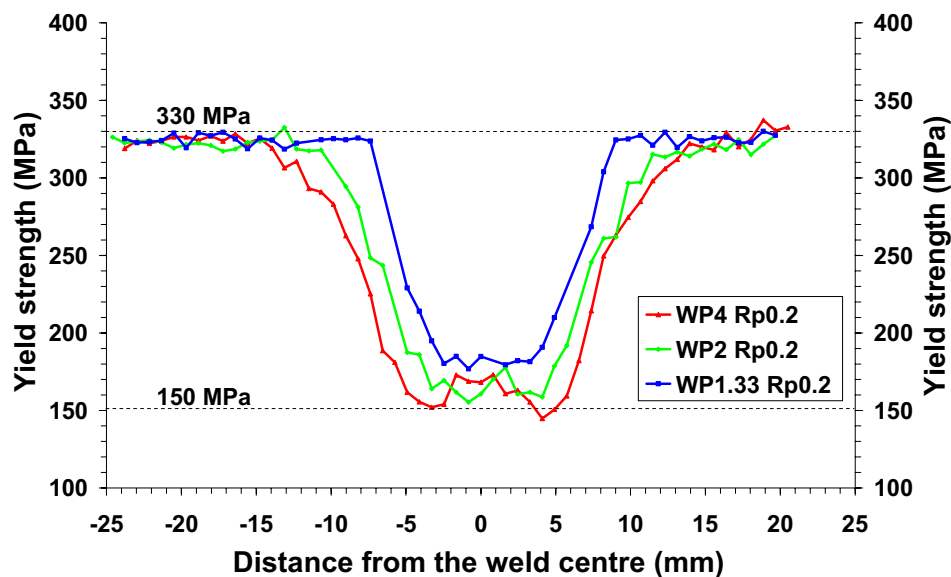


Figure 5-44 – Yield strength profiles from microflat tensile testing across the BM and FSW zones of the WP1.33 (low HI), WP2 (intermediate HI) and WP4 (high HI) joints.

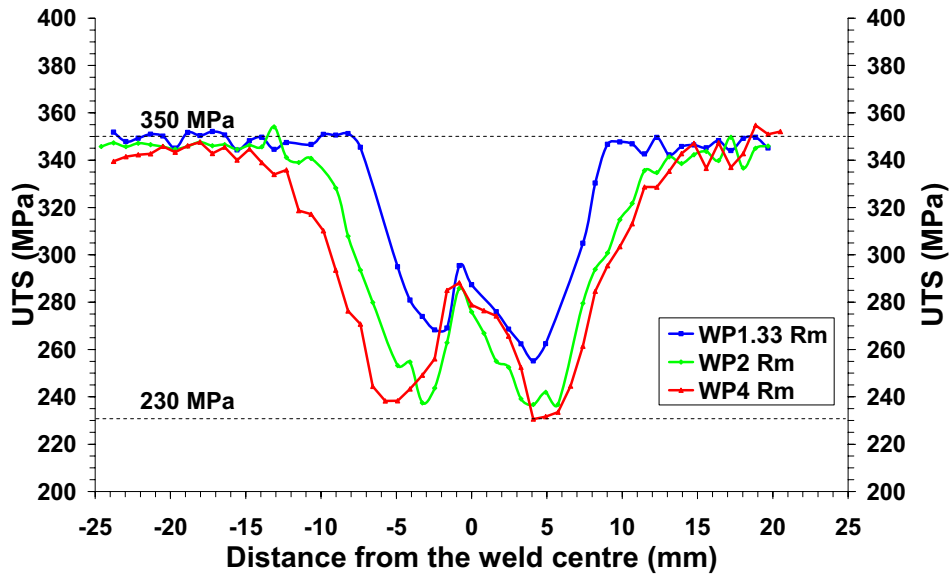


Figure 5-45 – Ultimate tensile strength (UTS) profiles from microflat tensile testing across the BM and FSW zones of the WP1.33 (low HI), WP2 (intermediate HI) and WP4 (high HI) joints.

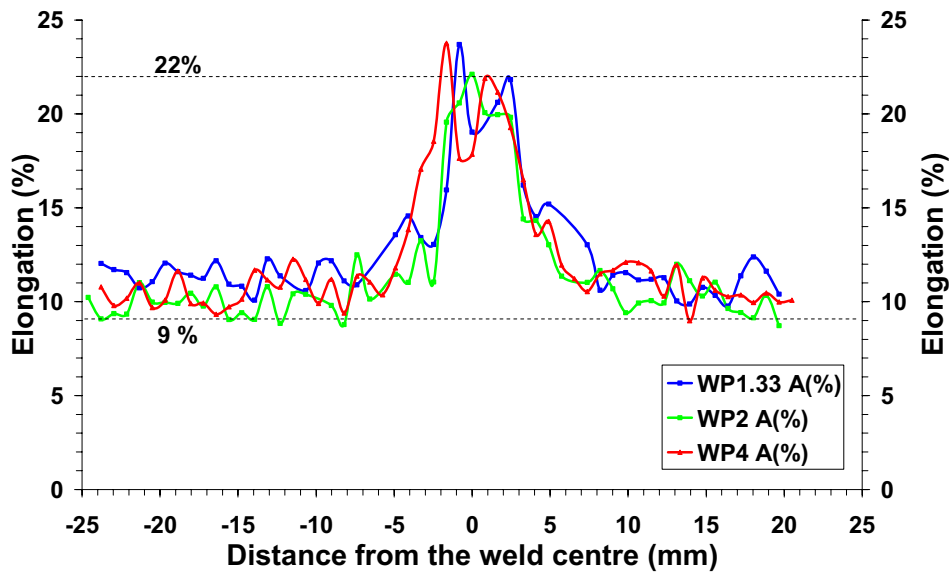


Figure 5-46 - Elongation profiles from microflat tensile testing across the BM and FSW zones of the WP1.33 (low HI), WP2 (intermediate HI) and WP4 (high HI) joints.

5.3.3 Metallurgical Characterization

5.3.3.1 Macro and Microstructural Investigation

As for the previously investigated aluminium alloys, the FSW resulting microstructure of the AA6013 T6 joints show well defined HAZ, TMAZ (with grain rotation) and SZ (equiaxed recrystallized grain structure). Figure 5-47 shows the transverse section of the AA6013 T6 FSW joint. The macrograph (intermediate HI - WP2) reveals the weld seam geometry, showing also a plastic flow trend in the SZ for a full penetration weld with no presence of defects. A similar

microstructure observed in the optical microscopy investigations for the different weld conditions was the reason for only representative micrographs at such magnifications. However, particular aspects, such as the geometry and penetration depth of the SZ, were observed to vary on a small scale. Nevertheless, since no effects on the joint performance were revealed in the mechanical testing results, further investigations into these aspects were not considered pertinent. For this alloy, an onion rings structure in the SZ was not as evident as those observed for the AA2024 T351 joints. Onion rings are clearly seen in the AA6013 T6 joined using high HI (WP4). It was observed that high input energy, i.e. WP4, tends to produce a slightly wider recrystallized area in the SZ, close to the top side of the joint, and consequently a wider TMAZ and HAZ. This is the consequence of the higher thermal cycle taking place in the high HI (WP4) joint, which assists material flow and deformation. The grain structure was evidenced using an optical microscope under polarized light, detailing the interface HAZ/TMAZ/SZ as presented in Figure 5-47 (a) and (b) for the advancing and retreating sides, respectively. Microstructure of the AA6013 T6 alloy showed a high level of deformation absorbed by the grains in TMAZ. The retreating side was characterized by a wider interface between SZ and TMAZ, presenting a microstructural gradient with a mixture of recrystallized and visibly recovered grains, due to the plastic flow of the material. Particularly for joints of this alloy, a grain size heterogeneity in the SZ was verified, which can be seen better in the micrograph of Figure 5-47 (c). These recrystallized grains tend to produce a coarser grain size, preferentially following the plastic flow lines of the SZ. This particularity can also be observed in the center region of the SZ as presented in Figure 5-47 (d). Such a phenomenon makes it difficult to determine the average grains size of the equiaxed grains in the SZ.

According to the thermo-cycle measurements during FSW, peak temperatures reached from 315°C (bottom) to 265°C (middle) for low HI, and from 396°C (bottom) to 350°C (middle) with the high HI joints. It is reasonable to assume that peak temperature in the HAZ was equivalent to the temperatures measured in the weld plates, with a range of 265 – 350°C, from low HI to high HI. Close to the SZ (measurements in the backing bar), the temperature was observed to reach a range between 315-396°C from low HI to high HI joints, which is expected to be a good approximation of the TMAZ peak temperatures, where the pancake grains around the SZ were observed to rotate following this interface. Similarly to the AA2024 T351 FSW joints, AA6013 T6 alloy is expected to reach more than 500°C in the SZ during FSW, producing a microstructure entirely recrystallized, with grain size able to reach an order of about 3 μm , as reported by Olea *et al.* for a AA6056 alloy, friction stir welded in condition T6 [43]. However,

earlier studies concerning grain size in the SZ of AA6013 joints reported variations between 8-15 μm [22]. At any rate, a considerable grain size variation across the SZ was observed (see Figure 5-47 c and d). The peak temperatures are shown to affect directly the resulting microstructure of the AA6013 T6 FSW joints, mostly by the critical softening produced across the welded zones for the three different FSW parameters, which were showed by the microhardness, microflat and flat tensile tests (see section 4.2.2). For a 6xxx alloy, the softening effect is less affected by the grain structure and more affected by the strengthening second phase particles, dissolution and coarsening tendency from FSW process and for this alloy, the strengthening is extremely dependent of the stability and distribution of the GP zones and precursors of β and Q phase.

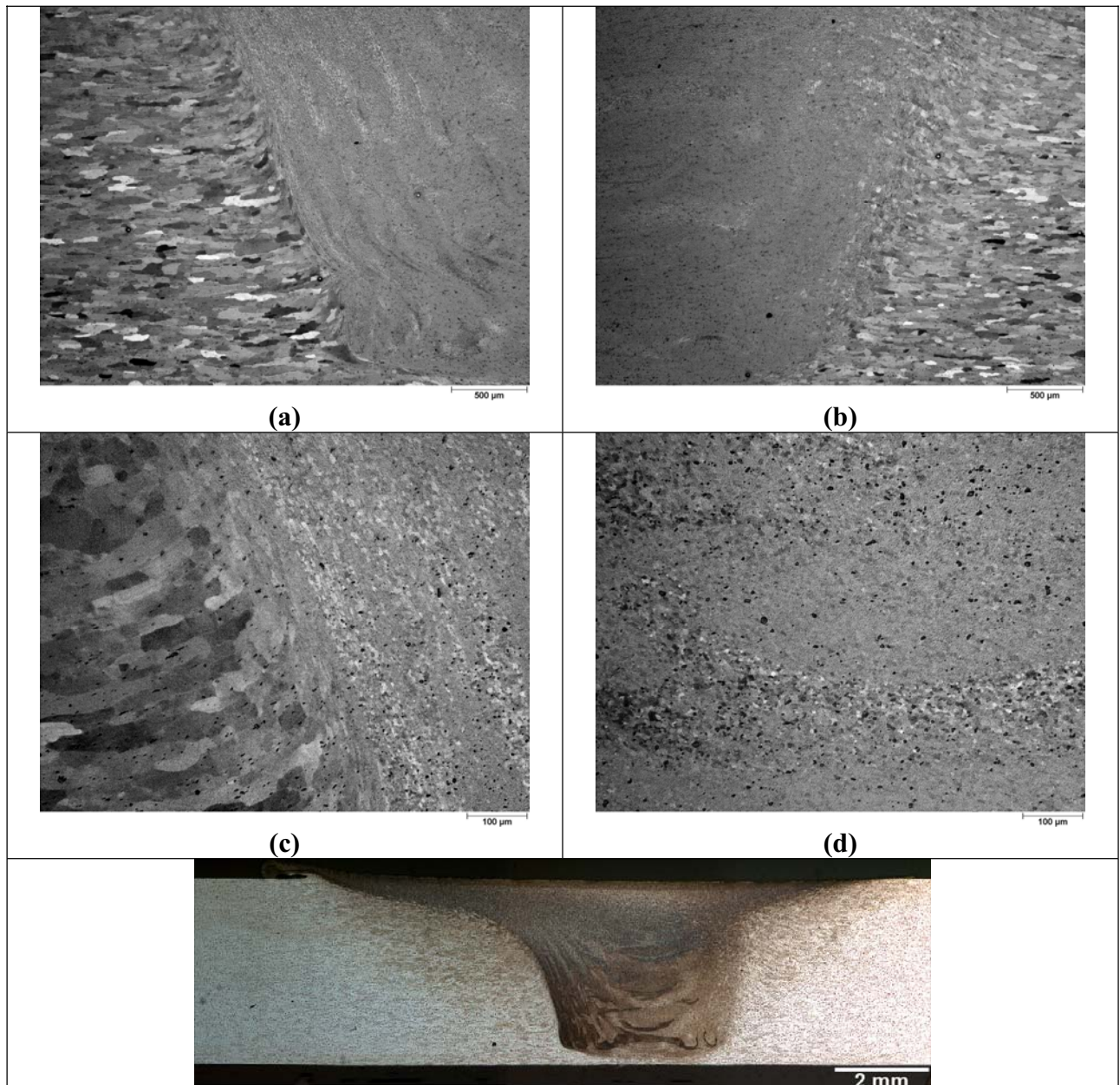


Figure 5-47 - Overview of the transverse section of the AA6013 T6 FSW joint by optical microscopy. (a) HAZ/TMAZ/SZ interface on the advancing side, (b) retreating side, (c) detail of the grain structure in TMAZ/SZ, and (d) SZ.

SEM analyses of the AA6013 T6 joints were carried out to investigate the microstructural details, predominantly those related to the recovered and recrystallized grain structure produced during FSW. Figure 5-48 shows backscattered electron micrographs along the cross section of the AA6013 T6 joints, welded with three energy inputs, (a) SZ of the high HI WP8, (b) SZ of the intermediate HI WP4, (c) SZ of the low HI WP2 and (d) TMAZ, represented for low HI WP2. Thin recrystallized grain structure in the SZ was better observed using SEM, and grain size measurements were shown to be independent from energy input. Contrary to the previous alloys, the SZ of the AA6013 T6 joints presented an apparently coarser grain size for the intermediate HI (WP2), while a similar grain size was found for low HI and high HI joints (WP1.33 and WP4, respectively). Such an aspect can be better understood considering the grain size gradient observed by optical microscopy analysis (see Figure 5-47 c and d), where grain size coarsening was observed along the material flow lines. However, considering the lower peak temperature resulting from the high weld travel speed of the low HI (WP1.33) a smaller average grain size for this condition should have been expected. Grain morphology variation at the interface TMAZ/SZ is showed in Figure 5-48 (d), where it is possible to observe the small recrystallized grains surrounded by recovered pancake grains. The TMAZ presented a similar grain structure for the different energy inputs and is illustrated by the low HI (WP2) micrograph as representative for all welding conditions.

The effect of the recrystallized grains in the SZ in terms of high ductility was clearly documented by the microflat tensile profiles, where the elongation increased considerably in the weld centre, followed by a decrease of the yield strength (see Figure 5-44 and Figure 5-46). However, the global tensile properties, represented by flat tensile tests of the joint, showed a decrease of ductility in comparison with the BM results, reaching a maximum of 12% of the BM elongation, but attaining good levels of yield strength, from 80 - 95% of the BM values (see Figure 5-42). The effect of the grain structure on ductility shows it is nearly the same for the different weld conditions, presenting a slightly worse result for the highest thermal cycle (WP4). A global degeneration of joint ductility is not usually attributed to the grain structure, but to the precipitation characteristics of the material across the welded region. The location where joints usually fail (TMAZ) is highly affected by deformation and thermal cycle, and results in a complex microstructural arrangement, composed of elongated recovered grains, elongated grains twisted and fine equiaxed grains in particular regions. Added to the effect of thermal cycle on precipitation features, the complex grain structure and the stress concentration resulting from the

FSW process, even at a lower level are expected to contribute to the properties deterioration i.e. low ductility.

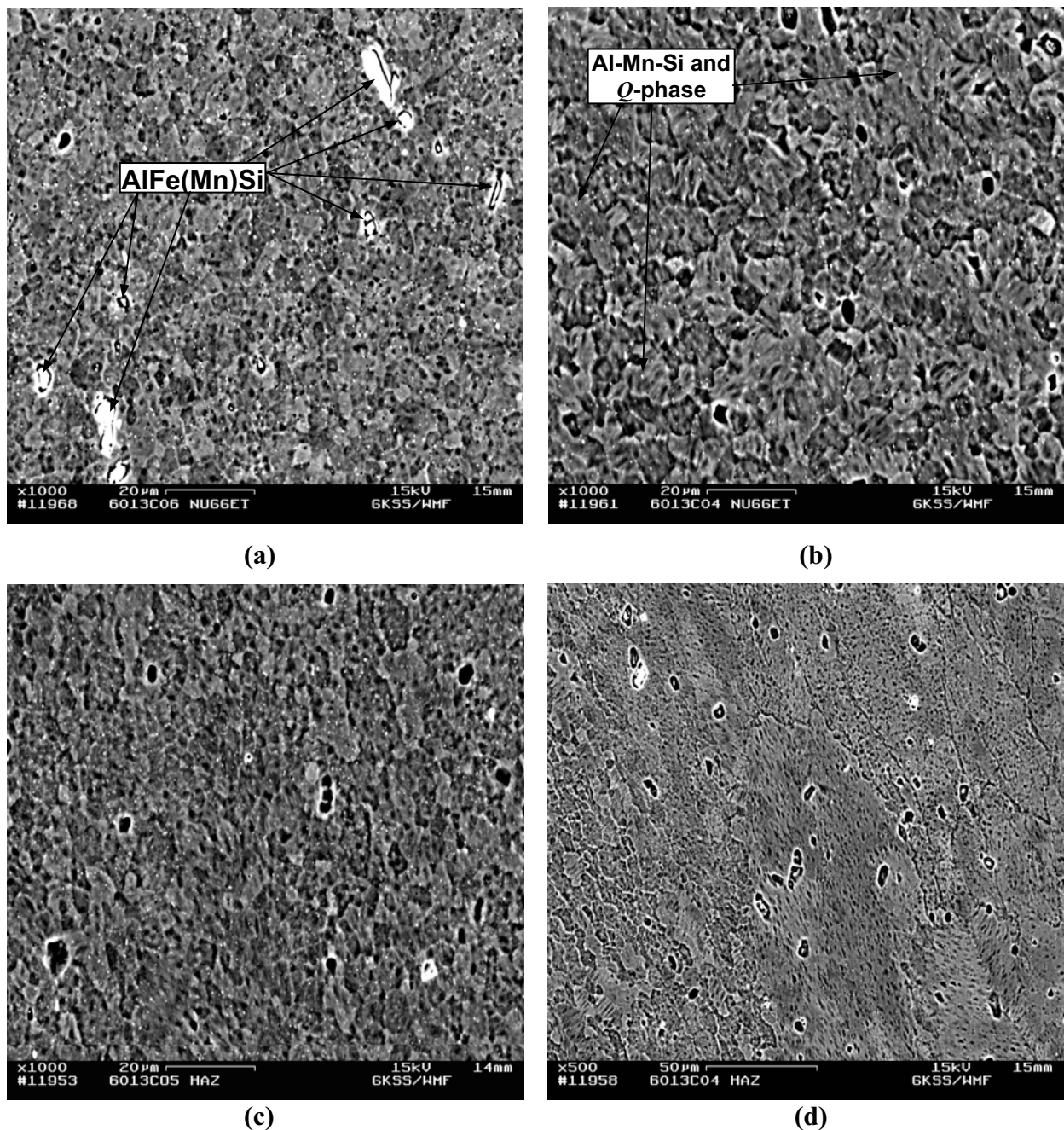


Figure 5-48 - SEM micrographs of the transverse sections of the AA6013 T6 FSW joints, showing equiaxed grains in the stir zone of conditions: (a) WP4, (b) WP2, (c) WP1.33 and (d) representing the interface between SZ and TMAZ.

Analysis of coarse second phase particles and dispersoids were also observed on the SEM. As in the case of Al-Mg-Sc and AA2024 T351, coarse particles and dispersoids were recognized in the AA6013 T6 by means of white coarse reflections and the white thin dots in Figure 5-48. Qualitative results from EDS analyses, positioned at most of the inclusions indicated

peaks of Fe, Mn, Si, Cu and Al, suggesting the presence of intermetallic particles type AlFe(Mn)Si and to a lesser extent dispersoids containing of Mn, Si, Mg, Cu and Al, indicating stable β -phase (Mg_2Si) and/or Q -phase (Al-Mg-Si-Cu). Investigations from Svensson *et al.* [56] also reported the presence of different second phase particles along the weld zones, where the coarser particles (1-5 μm) were referred to as AlFe(Mn)Si or the stable β Mg_2Si phase, both with elongated shape. Particles with sizes between 100-150 nm were identified as Al-Mn-Si dispersoids. Such particles are very stable and do not dissolve at the FSW peak temperatures, mainly due to the low solubility of Fe and Mn in the α -Al matrix. In addition, these particles are incoherent with the matrix, and even dispersoids produce no significant strengthening to the material. In order to investigate the strengthening precipitates, TEM investigations were performed across the BM and weld zones as presented and discussed in a later section.

5.3.3.2 Substructural Investigation

FSW joints of AA6013 T6 were investigated using TEM thin foils prepared according to the procedure described in section 3.4.3, essentially in order to explore the presence of second phase particles and precipitates evolution in the FSW zones and BM under the different welding conditions.

Base Material: The AA6013-T6 alloy presented a high density of needle-type precipitates, which are suggested as being basically composed of metastable β'' precipitates, precursor of stable β (Mg_2Si) phase, as showed in Figure 5-49. The size of the needle-type precipitates was found to be in a range of 20-70 nm length and 2-5 nm width. These precipitates were preferentially oriented along the aluminium matrix, being formed as a result of the artificial aging (heat treatment to T6 condition). Moreover, these precipitates are characterized by a high coherency relation with the α -Al matrix, which produce the highest condition of material strengthening for such alloy. Figure 5-49 (a) shows a bright-field (BF) image of the α -Al matrix, presenting a high density of needle-type precipitates (β'') with relatively low image contrast of the needle precipitates, which were crossing each other approximately at transverse orientation (relation of about 90°). In Figure 5-49 (b), the same characteristic was observed, but the precipitates showed a different relation of orientation, which was above 100° between each other, due to the crystallographic direction of analysis. The weak contrast of the needle precipitates is attributed mainly to the conditions of specimen preparation. The SADP in Figure 5-49 (c) for the direction $[011]_{\text{Al}}$ showed no clear streaks that would be expected for the needle precipitates reflections. GP zones were also expected to be present, but no evidence of such clusters was confirmed through diffraction patterns. According to the literature, needle-type precipitates have

shown the best image contrast at different directions i.e. studies of Heinz *et al.* [22] that have shown evidence of needle-type precipitates in a 6013 T6 along $[100]_{Al}$ and $[010]_{Al}$ presenting respective streaks in the SADP, which indicate the presence of precipitates along these directions. Investigations of Sato *et al.* [35] have also shown a high density of needle-type precipitates of about 40 nm length in the BM of a 6063 T5, oriented along the $[100]$ direction of the matrix. Furthermore, a recent study of Olea *et al.* [43] has shown the presence of needle-type precipitates for a 6056 T6 alloy, with different orientations and several streaks along $[233]_{Al}$. A number of detailed investigations on 6xxx series were also dedicated to the precipitation features of artificial aged alloys [26, 30,84,86,88], which conform with the precipitation behaviour of AA6013 T6 BM found in the present work.

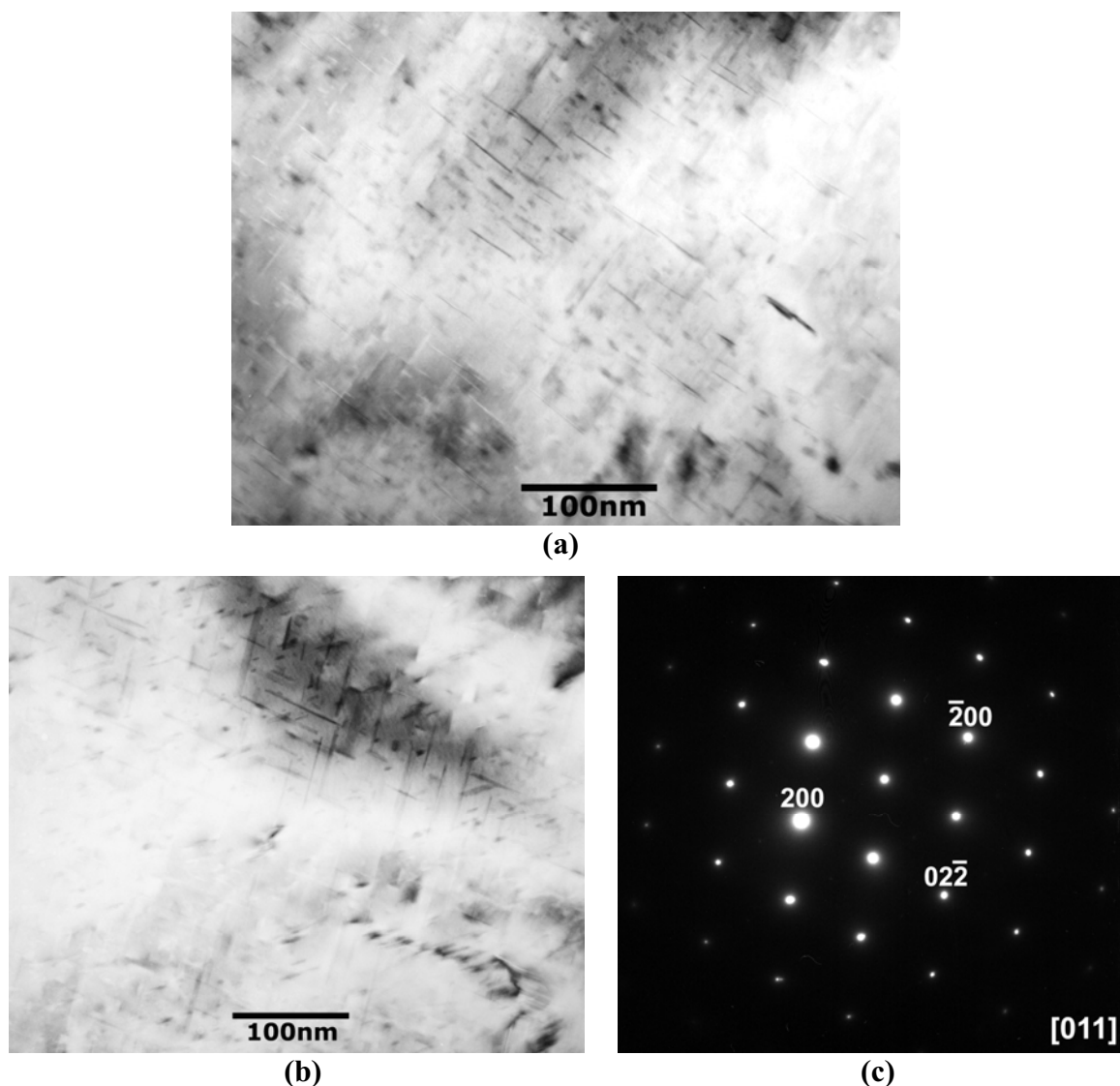


Figure 5-49 – Precipitation in AA6013-T6 alloy (BM). (a) and (b) Needle-type precipitates (β'') Preferentially oriented in a Widmanstätten structure, (c) SADP along the $[011]_{Al}$ zone axis.

It is known that mechanical properties of AA6013 T6 alloy greatly depend on the density of needle-type precipitate and only slightly on the density of rod-type and lath-type precipitates [35]. Hence, a precipitation condition as found here for the BM would be the ideal substructural condition to attain the highest contribution in strengthening. Such aspects were confirmed by the mechanical testing performed in this work, which always showed superior hardness and tensile properties for the BM, independent of the energy input used to produce the joints.

Stir Zone: In the SZ of the AA6013-T6 joints, the needle-type precipitates completely disappear along the microstructure for the three different energy inputs. The precipitation in the equiaxed grains, typically derived from recrystallization, is shown in Figure 5-50 for the high HI (WP4), intermediate HI (WP2) and low HI (WP1.33) joints. Coarse precipitates have been observed with mostly round morphology among dislocations, indicating dissolution of the strengthening needle-type precipitates (β'') previously present in the BM, due to the high peak temperatures generated during FSW. Figure 5-50 (a) shows the presence of second phase particles inside a dynamically recrystallized grain with high dislocation contrast in the SZ of the high joint, which according to the EDS peaks presented in Figure 5-50 (b) corresponds to typical Al-Mn-Si dispersoids, according with information reported in previous investigations [56]. Such particles were usually over 140 nm size. The SZ generally presented low dislocation density grains, since recrystallization is responsible for the dislocations annihilation. However, the effects of dynamic recrystallization can result in dislocation structures remaining after cooling, since strain is introduced simultaneously. The SZ of joints produced with intermediate HI (WP2) is shown in Figure 5-50 (c). It shows recrystallized grain interfaces with scarce coarse second phase particles between 50-90 nm, in addition to dispersoids and a low density of dislocations in contrast. The respective SADP along the $[112]_{Al}$ shown in Figure 5-50 (d) denotes the presence of additional phase, through diffuse streaks in the diffraction pattern. Likewise, in Figure 5-50 (e), round-type precipitates measuring 20-60 nm were observed, randomly spread in equiaxed grains of the SZ for the low HI joint. Dispersoids were observed for this condition as well. Low dislocation density can also be observed along the recrystallized grains. Additional faint reflections in $[011]_{Al}$ zone axis was observed, as shown in Figure 5-50 (f), indicating the presence of these round-type precipitates.

Round-type precipitates are smaller than dispersoids, mainly for the intermediate HI and low HI joints. Even assuming the size and some relation of coherency with the α -Al matrix, low precipitate distribution across the microstructure suggests no satisfactory contribution to hardening. It was observed that lower peak temperatures attained during FSW were not able to

dissolve completely the needle-type precipitates, but were able to produce some isolated particle coarsening, resulting in a different morphology (mostly round-type). Another possibility would be the fracture of coarse second phase particles and dispersoids, resulting from the higher weld transverse speed and its respective lower temperature, producing small particles randomly dispersed along the grains. The effect of the thermal cycle on precipitates evolution in the SZ during FSW has been reported by Sato *et al.* [35] for a 6063 alloy in T5 condition. In their investigation, no precipitates were detected in the SZ and precipitate dissolution during welding was reported. Moreover, the slightly higher hardness in the SZ compared with TMAZ was attributed to the refined recrystallized microstructure, which is in agreement with some verifications made in the present work. Svensson *et al.* [56] reported for a friction stir welded joint in AA6082 alloy that fine needle-type precipitates observed in the HAZ and supposed these to nucleate on dispersoids, were observed to disappear in the SZ and no other small precipitate was seen. Additionally, friction stir welded 6013 in different heat treatment conditions investigated by Heinz *et al.* [22] showed that in SZ of T6 sheets, strengthening precipitates dissolve completely during FSW, and in T4 sheets the SZ is also free of precipitates, although, after PWHT, precipitates were found in this region. A similar effect was observed by Olea *et al.* [43] for AA6056 FSW joints that reported the GP zones and β'' precipitates dissolution in the SZ after welding in T4 and T6 conditions, while a particular precipitation feature was observed in the SZ of the PWHT condition. It was reported that equiaxed grains were fully filled with very thin precipitates of about 2-10 nm distributed in the α -Al matrix. Such precipitates are associated with GP zones and/or end-on sections of β'' precipitates (precursor of stable β phase). Thus, the SZ of the FSW AA6013 T6 investigated in this work could be considered as a solute rich region that if subjected to heat treatment after welding (artificial aging) would produce the precipitation of strengthening β'' , regardless the energy input used to perform the joint.

The softening effect in the SZ of the AA6013 T6 joints was clearly observed through the microhardness profiles and microflat tensile profiles, presented in sections 4.3.2.1 and 4.3.2.3. A softening effect, produced essentially by the dissolution of β'' precipitates, was shown for the three energy inputs, which was not compensated by microstructural changes and round type precipitates remained. The latter was only observed in the intermediate HI (WP2) and low HI (WP1.33) joints. However, strength levels in the SZ did not show significant variations in the microhardness and microflat tensile profiles between the different energy inputs. In addition, the global tensile properties showed to increase for lower energy inputs (WP2 and WP1.33), but in

this case, precipitates dissolution and microstructural changes were not the main focus of attention, since the tests showed fracture usually occurred outside the SZ.

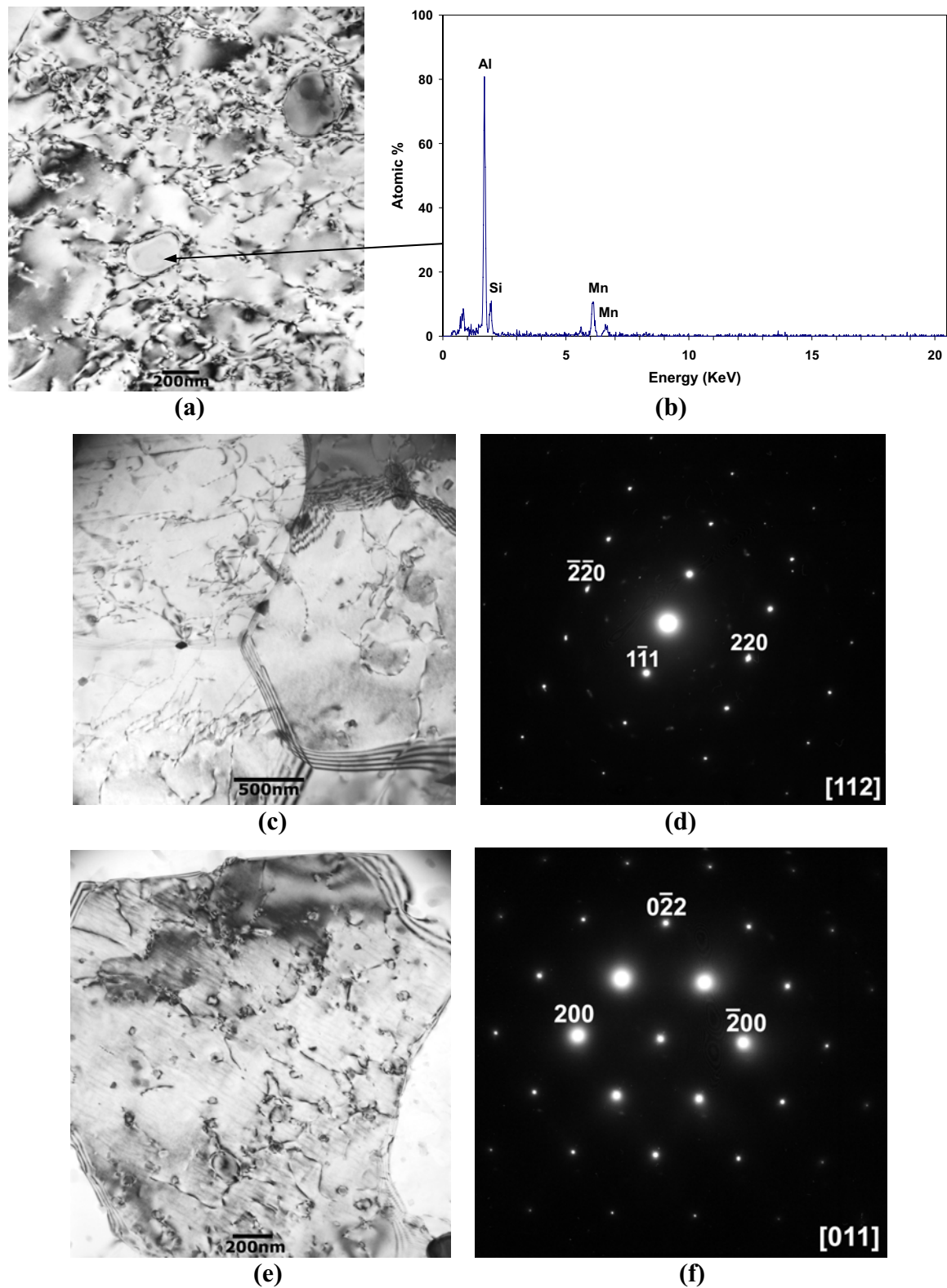


Figure 5-50 - Precipitation in the SZ of FSW AA6013-T6 joints. (a) High HI (WP4) and (b) EDS analysis of dispersoid; (c) Intermediate HI (WP2) close to $[112]_{Al}$ and (d) respective SADP; (e) low HI (WP1.33) in $[011]_{Al}$ and (f) respective SADP.

The small round type precipitates observed in the SZ of intermediate HI and low HI joints were also analysed using EDS, coupled to the TEM. Figure 5-51 (a) shows recrystallized grains of the SZ (WP1.33) presenting the small round-type precipitates (20-60 nm size). Figure 5-51 (b) shows the respective EDS peaks, indicating the presence of Cu and Si in addition to Al. Such verifications suggest the formation of Q phase in the SZ during FSW. The formation of a quaternary phase Q containing Al, Cu, Mg, and Si has been previously reported, forming as an equilibrium phase in 6xxx alloys [26-28]. For such alloys, a precipitation sequence has been proposed as α (SSS) \rightarrow GP zones \rightarrow needle-type β'' \rightarrow lath-type Q' \rightarrow Q + Si. It was concluded that Cu induces the formation of Q and its precursor metastable phases theoretically produce a beneficial effect on the kinetics of artificial aging [30,89]. Nevertheless, the presence of Mg was not clearly verified here by the EDS analysis, in order to affirm the presence of Q phase. However, it was indicated that the round-type precipitates presenting Cu peaks are possibly the stable Q phase and presented such a morphology due to the high peak temperatures generated in the SZ during FSW. Furthermore, for the high HI (WP4), it seems that the temperature peak in the SZ was too high and so the solvus temperature for Q phase was reached and dissolution was completed.

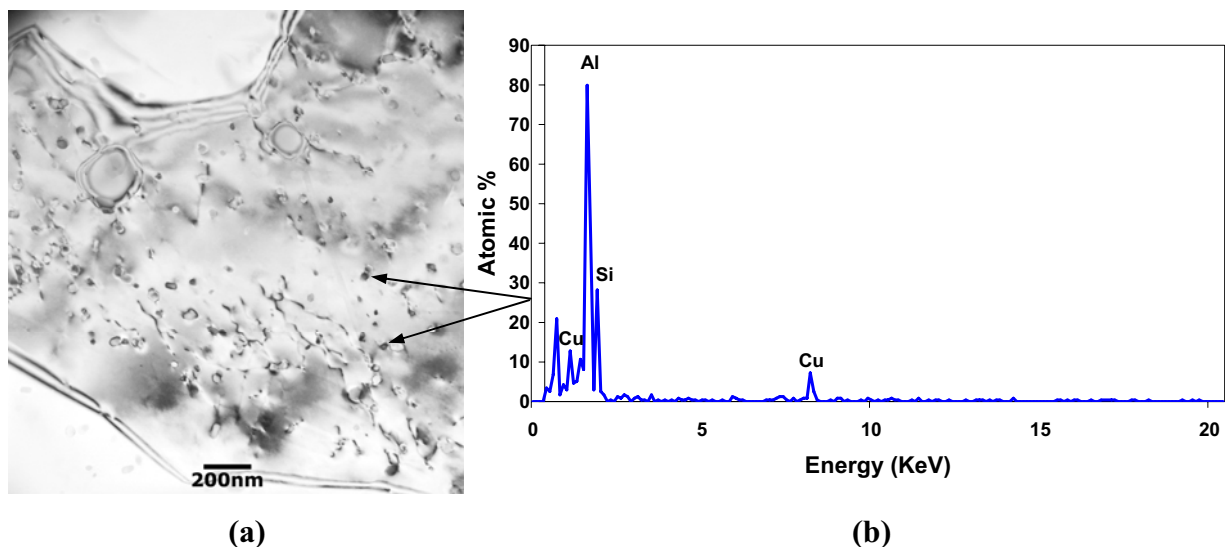


Figure 5-51 – Precipitation of Q -phase in the SZ of FSW AA6013-T6 joint. (a) BF micrograph of the precipitates; (b) EDS analysis indicating Cu peaks.

Thermomechanical Affected Zone: Precipitates evolution in the TMAZ of AA6013 T6 is evidenced in Figure 5-52 for the low HI (WP1.33), intermediate HI (WP2) and high HI (WP4) joints. TMAZ shows different precipitation aspects, according to the weld energy input employed. The precipitates characteristics for the three different welding parameters resulted in a coarsening effect of the needle type β'' previously observed in the BM, during FSW. Figure 5-52

(a) shows a bright field micrograph evidencing lath-type precipitates preferentially oriented in the TMAZ of the high HI (WP4) joint, which would be associated with Q' precipitates, the precursor of Q phase. The respective SADP is shown in $[001]_{Al}$ zone axis is presented in Figure 5-52 (b). For the intermediate parameter (WP2), low contrast of lath-type precipitates along $[011]_{Al}$ zone axis in conjunction with dispersoids in TMAZ was observed, as shown in the BF micrograph of Figure 5-52 (c). The respective SADP, presenting faint streaks in association with BM spots is shown in Figure 5-52 (d). In the TMAZ of the low HI (WP1.33) joint, precipitates with different morphology were revealed, as shown in the BF micrographs of Figure 5-52 (e). Such precipitates were suggested to be rod-type precipitates β' , since no contrast of lath-type precipitates was found along $[001]_{Al}$ zone axis, in order to associate these particles to an end-on section of Q' lath-type precipitates. Another indication was the distribution of precipitates, showing a trend to form parallel lines of precipitates, which differ from the lath-type precipitates observed before in joints produced with higher energy input. Figure 5-52 (f) shows SADP in $[001]_{Al}$ zone axis, corresponding to the area depicted in the micrograph of the low HI joint.

Lath-type precipitates found mainly in the TMAZ of high HI and intermediate HI joints were dispersed following the same orientation observed for the β'' precipitates in the BM, but presenting larger size and interparticle spacing. In the TMAZ of high HI (WP4) joint, lath-type precipitates presented an average size of about 146 nm length and 30 nm width, while the precipitates in the same weld zone of the intermediate HI joint (WP2) presented an average size of 115 nm length and 15 nm width. The precipitate coarsening effect, resulting from the high HI (WP4), is clearly seen; mostly due to the highest peak temperature attained, in comparison with intermediate HI (WP2) joint. The precipitates found in TMAZ of low HI (WP1.33) joint, here associated with rod-type precipitates β' , presented an average size of 30 nm length and about 10 nm width. It is important to point out that precipitate size observed for the low HI joint approaches the end-on section of the lath-type precipitates, observed for intermediate HI and high HI joints. Another possibility to be considered would be re-precipitation of dislocation structures and dispersoid sites, producing different dispersion characteristics in comparison with intermediate HI and high HI. Direct TEM investigations in the TMAZ indicated that the higher energy input resulted in an increase in size and a decrease in the density of the Q' and/or β' precipitates, which for higher energy inputs tend to form predominantly lath-type precipitates Q' with higher interparticle spacing. However, both precipitates (Q' and β') are supposed to be partially coherent and incoherent with the α -Al matrix, which significantly reduces the strengthening effect.

For the precipitation hardening AA6013 T6 alloy, strengthening is also fundamentally dependent on the precipitation characteristics, and the mechanical assessment has shown TMAZ to be the critical region for the different FSW joints in terms of softening (see section 4.3.2). The effects of precipitate coarsening, promoted by the FSW thermal cycle on the initially fine β'' precipitates in addition to the GP zones dissolution, are mainly responsible for the hardness and the fall in yield strength, observed in the microhardness and microflat profiles, which was evidenced in the high HI joint (see Figure 5-41 and Figure 5-44). Heinz *et al.* [22] reported an overaging effect in the HAZ of AA6013 T6 FSW joints, where lath-type precipitates were observed along $[001]_{Al}$ zone axis with about 280 nm length. In their work [22], the zone suggested as being HAZ represented the weakest part of the welded material and, contrary to results found in this work, always presented fractures on the advancing side of the transverse tensile specimens. Low density of rod-type precipitates were observed in the hardness minimum zone (TMAZ or very close to this zone) of 6063 T5 FSW joint by Sato *et al.* [35] and it was accompanied by a loss of solute from the matrix. As previously mentioned, literature also suggests that precipitates β' nucleated on the dispersoids in the HAZ of AA6082 FSW alloy [56], although, Olea *et al.* [43] showed the presence of lath-type precipitates between 60-90 nm in length and 10 nm width in the TMAZ for AA6065 T6 FSW joints. Rod-type precipitates were also evidenced in the TMAZ for PWHT joints with size between 37-60 nm length and 9 nm width [43]. Such investigations agree well with results obtained in the present work, however these indicate precipitate overaging allied to hardness minimum in the TMAZ. Moreover, GP zones, which are also expected to provide the material strengthening in conjunction with precipitates β'' , indicated a full dissolution in the TMAZ of AA6013 T6 joints and the thermal cycle experienced was not able to promote the formation of GP zones on cooling. Comparing the different energy inputs, it is feasible to observe for the lowest hardness, yield and tensile strengths, that in fact coarser lath-type precipitates, wider spaced as a result of the higher peak temperature, cause a decrease in mechanical properties in the TMAZ (i.e. high HI joint WP4).

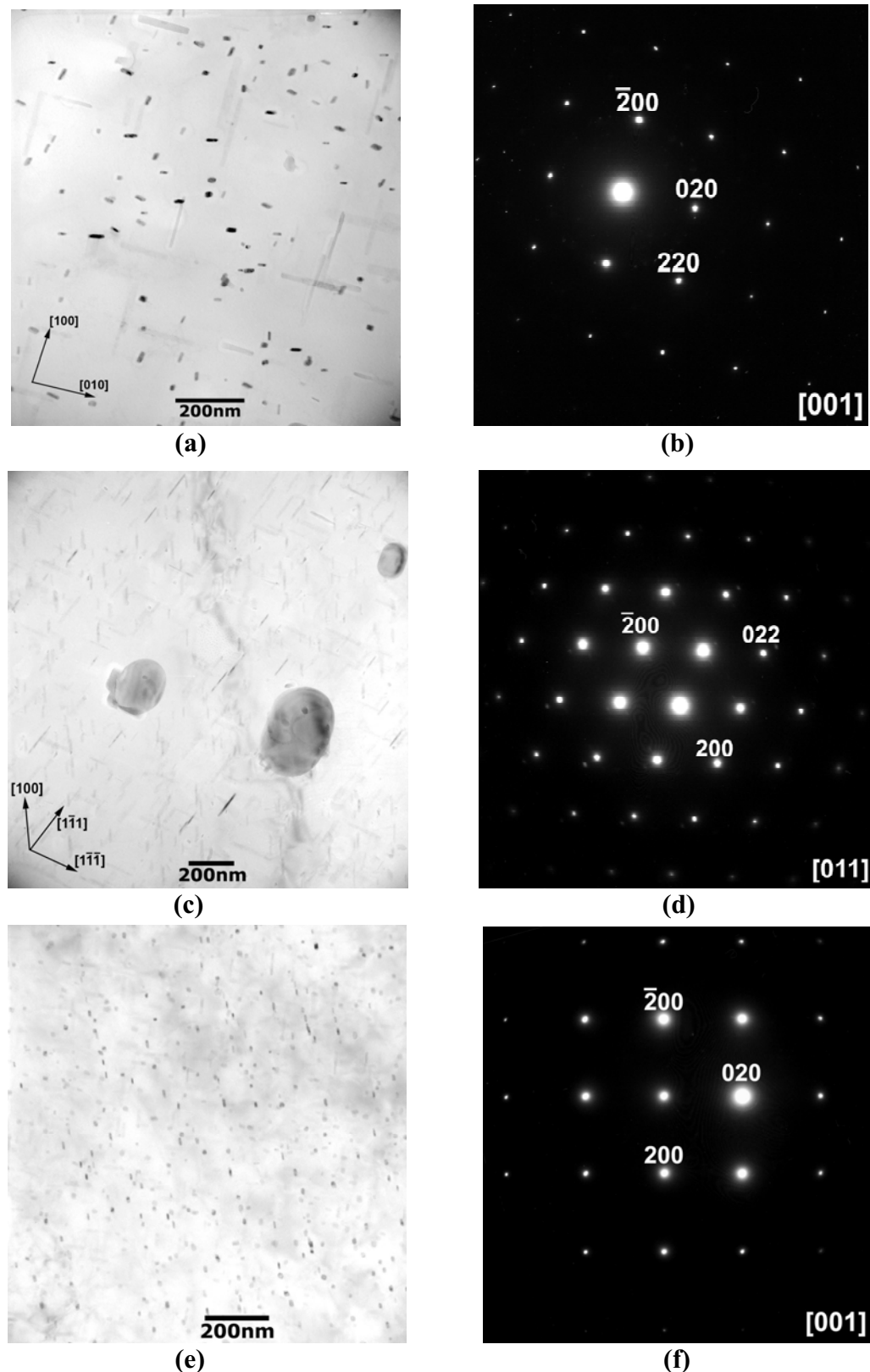


Figure 5-52 - Precipitation in the TMAZ of FSW AA6013-T6 joints. (a) high HI (WP4) and (b) SADP along $[001]_{Al}$ zone axis; (c) Intermediate HI (WP2) in $[011]_{Al}$ zone axis and (d) respective SADP; (e) low HI (WP1.33) in $[001]_{Al}$ zone axis and (f) respective SADP.

EDS analysis was performed directly on the lath-type precipitates observed in the TMAZ of intermediate HI and high HI joints. Figure 5-53 (a) shows a BF micrograph for the high HI

joint (WP4) presenting the lath-type precipitates with the average sizes mentioned before (146 nm length and 30 nm width) in a deformed grain of the TMAZ. Figure 5-53 (b) shows the respective EDS peaks indicating discrete presence of Cu beyond Al. As previously suggested for the SZ, these observations also suggest the formation of quaternary phase Q (Al-Mg-Si-Cu) in the TMAZ during FSW. According to the morphology, size and disposition of the precipitates, it is assumed there is a formation of Q' precipitates, the precursors of the Q -phase, in the TMAZ after FSW, for WP2 and WP4 parameters. Such implications are in accordance with previous investigations of precipitate overaging for this alloy series [26,30,43,88]. Considering the precipitation sequence mentioned before for such quaternary alloy: α (SSS) \rightarrow GP zones \rightarrow needle-type β'' \rightarrow lath-type Q' \rightarrow Q + Si, the lath-type precipitates Q' would form from needle-type β'' previously present in the BM, assuming the same orientation characteristics, but changing morphology. Again, the presence of Mg and Si was not verified in this work by the EDS analysis, but according to general aspects and correlations with the literature, in addition to the Cu peaks observed, the lath-type precipitates were associated directly with Q' precipitates. Furthermore, coarser precipitates and larger interparticle spacing for higher energy input was observed, which can be compared in Figure 5-52 (a) and (c) for WP4 and WP2 parameters, respectively.

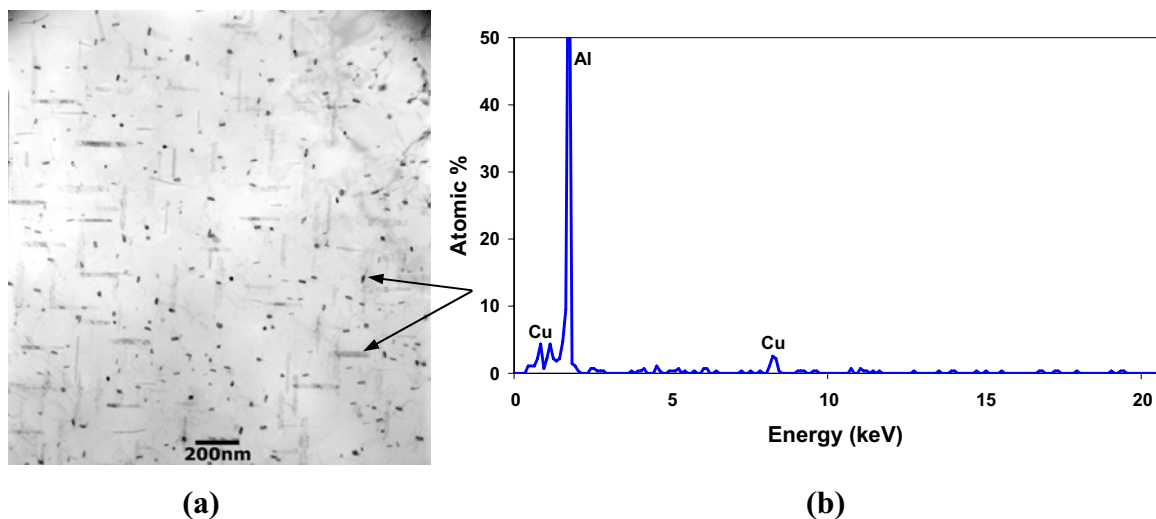


Figure 5-53 – Precipitation of Q -phase in the TMAZ of FSW AA6013-T6 joint. (a) bright field micrograph of the precipitates; (c) EDS analysis, indicating Cu peaks.

Figure 5-54 shows a detailed investigation of the grain boundary region in TMAZ of AA6013 T6 joints, indicating the presence of precipitate free zones (PFZ). PFZs adjacent to the grain boundaries and typical coarse grain boundary phases were also observed along the interfaces. As previously mentioned, particle coarsening is favoured by an intense diffusion in the grain boundary. In this alloy, this type of substructural feature was only verified for the high HI

(WP4) joint, as a consequence of the higher thermal cycle during FSW, in comparison with TMAZ of the different energy inputs. A TMAZ α -Al matrix covered by coarsened lath-type precipitates can be also observed alongside the PFZs as shown in Figure 5-54 (a) and (b). The presence of PFZs would be assimilated as an indication of overaged microstructure, which is detrimental to the performance of the FSW joint. It has been reported that properties such as the hardness and tensile strength of FSW joints would only increase if given a homogenization post-weld heat treatment [43,90]. In that case, the overaged intergranular lath-type precipitates and other incoherent or low coherency relational particles would go into solution and re-precipitate as strengthening needle type β'' and GP zones. Moreover, on-line cooling would be an alternative, to diminish the dissolution and coarsening effect of the strengthening precipitates, thus decreasing the softening effect from the original BM mechanical properties.

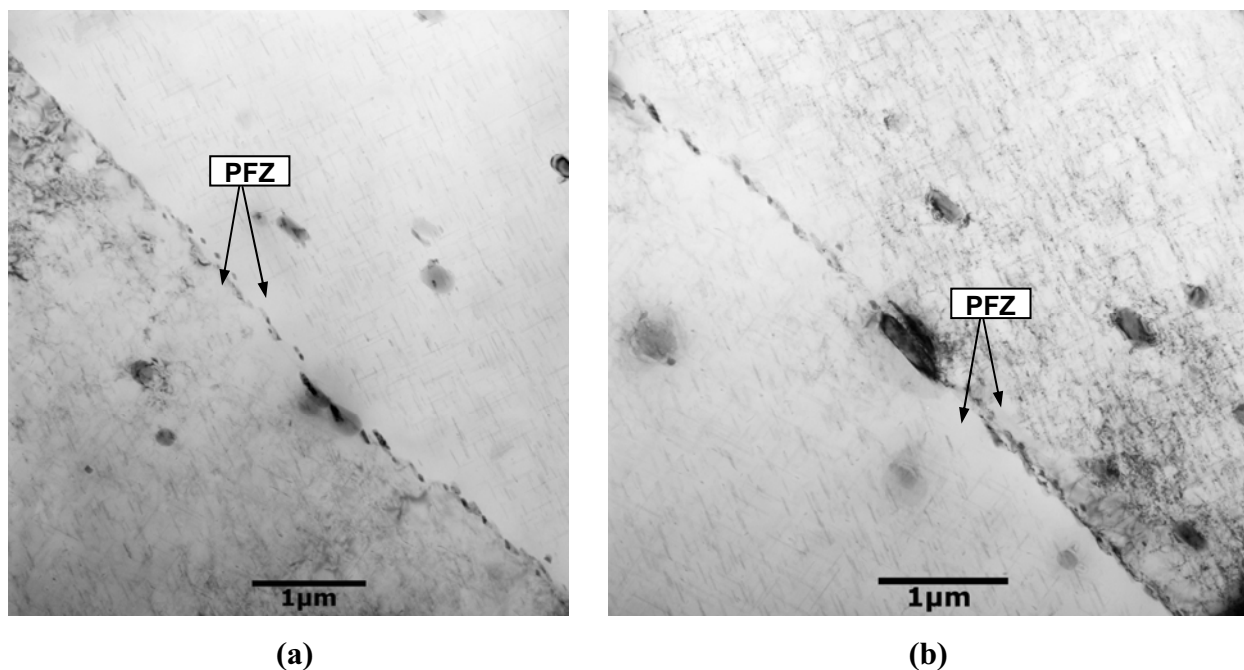


Figure 5-54 - PFZ and precipitate coarsening along the grain boundaries of TMAZ in high HI (WP4) of the AA6013-T6 joints in (a) and (b) at slightly higher magnification.

5.3.3.3 Substructural evolution

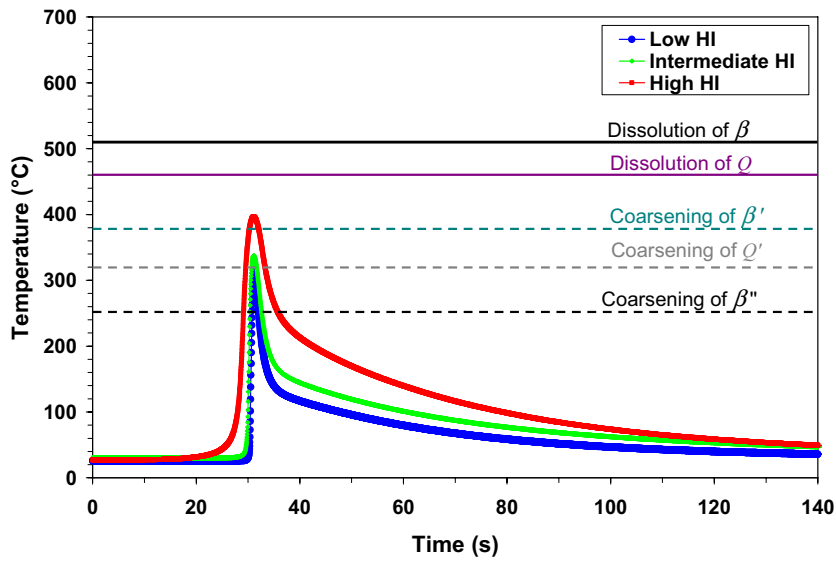
The thermal cycles involved during the FSW have shown to exert significant influence on the original micro and substructure of the AA6013 T6 alloy, which was also verified by the undermatching observed in the mechanical properties. The effects of the thermal cycle produced during FSW can be observed in Figure 5-55. According to the peak temperatures involved and the results from the TEM investigations, a precipitate evolution sequence is proposed for each weld condition, in the different weld zones (TMAZ and SZ). The model proposed is described below:

TMAZ

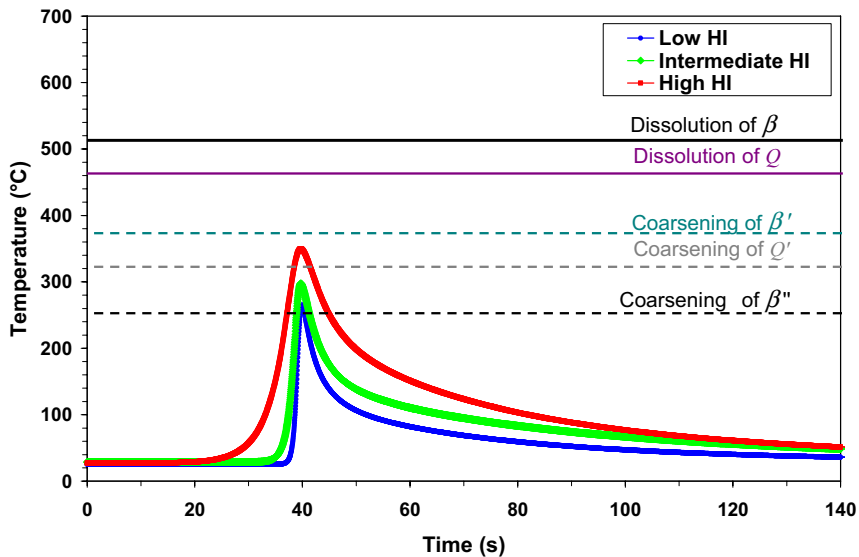
BM	WP1.33	$\beta'' + \beta'$ (rod-type) \rightarrow	β' (rod-type)
β'' (needle) \rightarrow	WP2	$\beta'' + \beta'$ (rod-type) \rightarrow	β' (rod) + Q' (lath)
	WP4	$\beta'' + \beta'$ (rod-type) \rightarrow	β' (rod) + Q' (lath) \rightarrow Q' (lath-type)

SZ

BM	WP1.33	β' (rod) + Q' (lath) \rightarrow	Q phase + AlMnSi
β'' (needle) \rightarrow	WP2	β' (rod) + Q' (lath) \rightarrow	Q phase + AlMnSi
	WP4	β' (rod) + Q' (lath) \rightarrow	Q phase + AlMnSi \rightarrow AlMnSi particles



(a)



(b)

Figure 5-55 – Correlation between precipitation evolution and thermal cycles obtained in (a) SZ and (b) TMAZ of AA6013 T6 joints.

The precipitation sequence during FSW proposed above indicates a good relation to the graph in Figure 5-55. In the SZ, the high temperatures are expected to coarsen the original precipitates (β'), resulting in coarse Q phase (WP1.33 and WP2) or even dissolve them (WP4). In the TMAZ, the coarsening of the original precipitates (β') is evident for the different welding conditions. However, low HI condition would follow the precipitation sequence similar to a ternary alloy (Al-Mg-Si), resulting in formation of β' precipitates, while higher temperatures would form the Q phase (Q' lath-type).

6. SUMMARY

The different Al alloys presented satisfactory weld characteristics for all energy inputs investigated, including full penetration, absence of significant defects and satisfactory mechanical properties of the joints. The three Al alloys studied presented definite FSW zones, characterized by the formation of fine equiaxed grains in the SZ, the result of dynamic recrystallization, and recovered grains, occasionally partially recrystallized in the TMAZ. Most of the precipitates in each region of the different alloys investigated were strongly dependent on the local thermal mechanical cycle experienced during FSW.

1. The Al-Mg-Sc did not show significant hardness variation for the three different FSW conditions in comparison with the BM, along the whole investigated section. Transverse flat tensile results showed a loss in tensile (R_m) and yield strength ($R_{p0.2}$) for the high HI condition. High performance was observed for intermediate HI (WP2) and low HI (WP1.33) joints, with R_m and $R_{p0.2}$ over 95% of the BM values. Elongation was close to 50% of the BM values. Fracture of the specimen always occurred at the SZ. Local mechanical properties, obtained from the microflat tensile profiles across the different FSW zones, showed values of R_m and $R_{p0.2}$ above 90% of BM values for all welding conditions. A slight decrease in R_m and $R_{p0.2}$ of the high HI joint, mainly in the SZ, has been observed. Microstructural changes result in a slight decrease of R_m and a slight increase of $R_{p0.2}$ in the SZ of the low HI joint. Superplasticity effects were evidenced during microflat testing and a tendency of higher elongation values for higher weld energy input could be observed. Results suggest that plastic deformation and thermal cycles during FSW and post weld heat treatment (PWHT) have not substantially influenced the material strength.

The fine pancake grain structure from BM showed an average length of about 2.6 μm and width about 0.5 μm , indicating an effective contribution of Sc in inhibiting recrystallization phenomena and so generating a fine BM grain structure. Finer grain size in the SZ of low input energy (WP1.33) was observed, increasing gradually for intermediate HI and high HI conditions, presenting average values estimated from TEM micrographs in the range 1-2 μm . Therefore, according to local elongation results in the weld zones, it is suggested that an increase in ductility could be controlled by process parameters.

TEM investigations showed a number of dislocation features, including grouping to form subgrain boundaries, dislocation tangles and looping around second phase particles, especially in the TMAZ for all welding conditions. Pile-up of dislocations and interaction with precipitates

were evidenced mainly for high HI joints, where the highest temperatures attained favoured dislocation movements. In general, the dislocation density was lower for grains in the SZ.

In Al-Mg-Sc joints, a high distribution of Al_3Sc precipitates with spherical morphology was evidenced, randomly dispersed along the BM and FSW zones for the three energy inputs investigated. No great variation in size and distribution of Al_3Sc precipitates along the BM and welded zones was observed. SADP presented superlattice spots due to the presence of Al_3Sc ordered precipitates in [001] zone axis, indicating a coherency relation between Al_3Sc precipitates and the FCC aluminium matrix. Strain field contrast (coffee-bean-like) due to coherent interfaces also evidenced such an effect for BM and weld zones of the different FSW conditions. The precipitates control the mechanical properties, preserving a high level of the BM mechanical behaviour along the different weld zones, regardless of the welding condition.

2. The AA2024 T351 joints showed a degradation of microhardness and tensile properties in the TMAZ and HAZ, and a trend to higher degradation with increasing energy input, from low HI (WP2) to intermediate HI (WP4) and high HI (WP8) joints. Flat tensile test specimens showed up to 97.4 % R_m and 98.4% $R_{p0.2}$ of the BM and fracture always occurred on the TMAZ retreating side (hardness minimum). The mechanical properties showed to be optimized when utilizing high weld transverse speed (i.e. low HI joint - WP2).

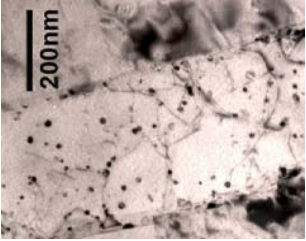
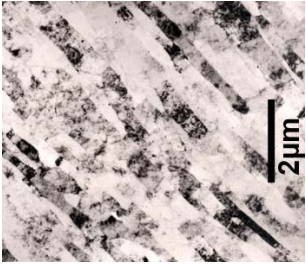
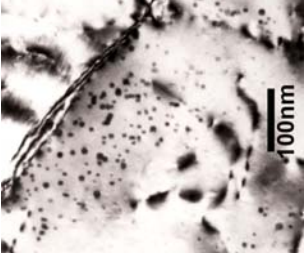
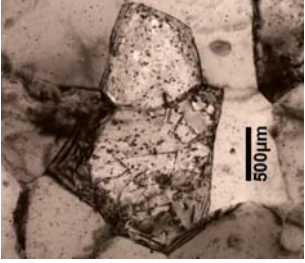
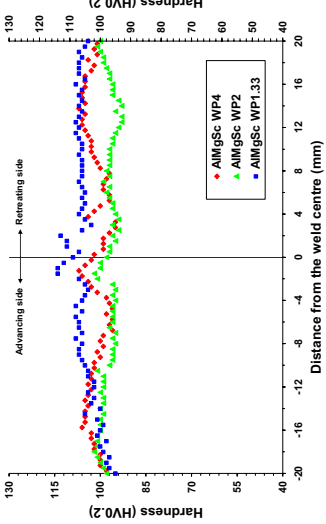
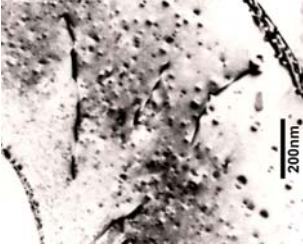
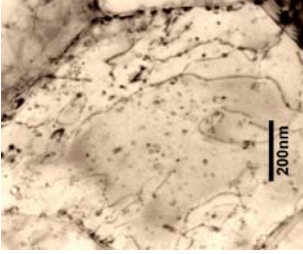

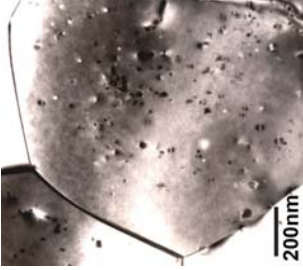
The AA2024-T351 joints presented strengthening S'' precipitates (Al_2CuMg) in the BM, but no evidence of GPB zones could be found. FSW leads to the formation of scarcely coarse S -phase (≈ 80 nm) for the low HI (WP2) joint and the dissolution of S'' and GPB zones in the SZ for all energy inputs, leaving basically dispersoids for the intermediate HI (WP4) and high HI (WP8) joints. The peak temperatures in the SZ promoted a resulting solute rich matrix, which is expected to form GPB zones during cooling. Overaging occurred in the TMAZ and S' precipitates were observed, presenting predominantly rod-type morphology (95 nm long and 15 nm wide) for the low HI (WP2), a mixture of rod-type and lath-type precipitates (68 nm long and 28 nm wide) for intermediate HI (WP4) and essentially lath-type precipitates (94 nm long and 30 nm wide) for high HI (WP8). Different energy inputs in the TMAZ show they affect the precipitate morphology, size and distribution, which reflects directly on the mechanical properties. The rod-type precipitates observed in the TMAZ indicated it was less affected by the thermal cycle, retaining the strengthening effect, which reduces the hardness minimum in this region. Rod-type precipitates in the TMAZ and round-type S -phase in conjunction with GPB zones in the SZ assured the best performance of the low HI joint (WP2). Moreover, PFZs in the

TMAZ of intermediate HI and high HI joints, evidenced adjacent to the grain boundaries, indicate the occurrence of overaging.

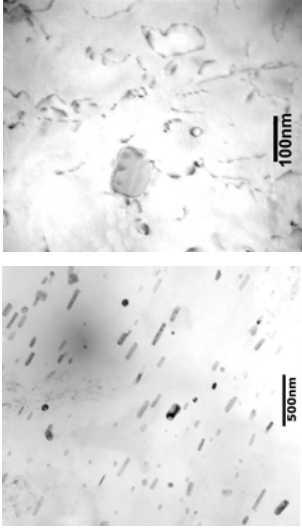




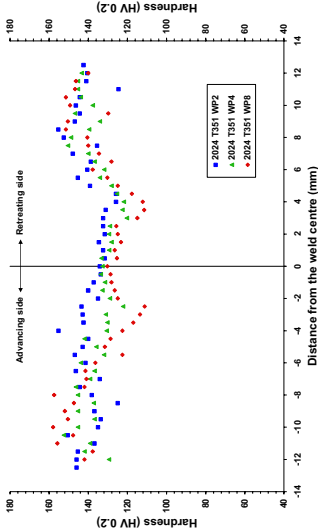
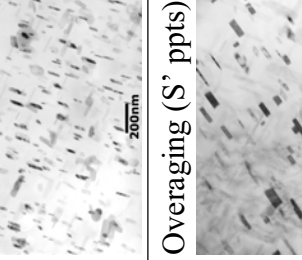

3. The AA6013 T6 joints showed significant degradation of microhardness and tensile properties all along the weld, for all FSW input energies to comparable extents. Deterioration of mechanical properties was greater for the high HI (WP4). Flat tensile results showed up to 81.8 % Rm and 94.4% Rp_{0.2} of the BM for the low HI (WP1.33) and fracture always occurred on the TMAZ retreating side (hardness minimum). Elongation was very low, about 10% of the BM. Similarly to the AA2024 joints, the AA6013 FSW joints showed a trend of Rm and Rp_{0.2} improvement with the increase in FSW transversal speed.

In the AA6013-T6 alloy, strengthening needle-type precipitates β'' resulting from artificial aging were observed. The needle-type precipitates were fully dissolved in the SZ after FSW for the three energy inputs utilized. Scarcely stable Q - phase formation along the equiaxed grains of SZ was evidenced with sizes of 20-60 nm for the low HI (WP1.33) joint and 50-90 nm for the intermediate HI (WP2) joint. The high HI (WP4) joint showed only Al-Mn-Si dispersoids over 140 nm, which were also observed for all energy inputs. The TMAZ was characterized by precipitate coarsening, forming rod-type precipitates with average size of 30 nm length and 10 nm width in the low HI (WP1.33) and Q' precipitates, which grow and acquire essentially the lath-type morphology with an average size of 94 nm length and 30 nm width in the intermediate HI (WP2) and high HI (WP4) joints. These precipitates are generally semi-coherent and/or non-coherent with the α -Al matrix. The particular precipitate morphology in the TMAZ of low HI (WP1.33) has been associated with the formation of ternary β' precipitates. For this alloy, overaging extended across all weld zones for the different energy inputs.

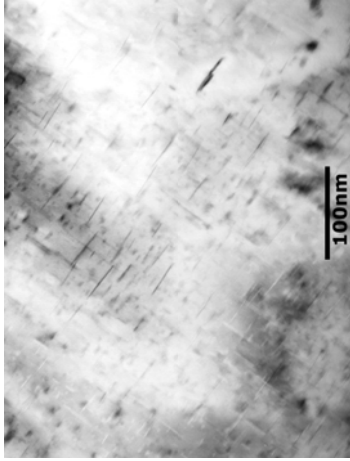
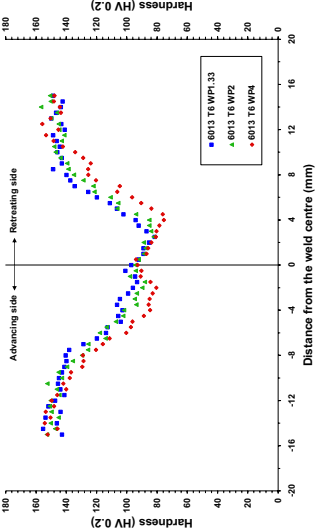
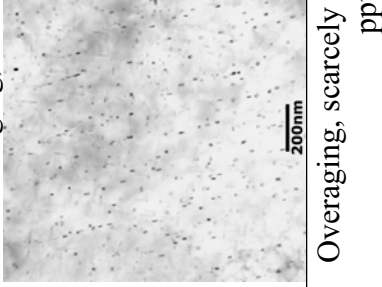
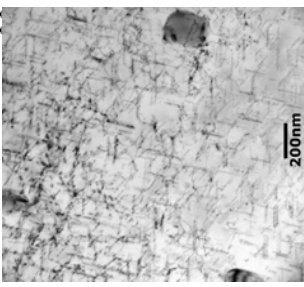
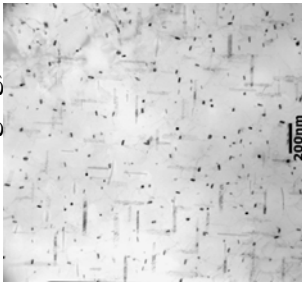
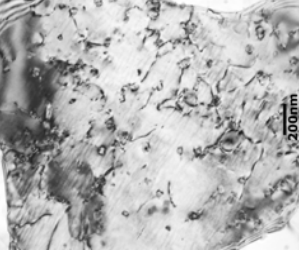
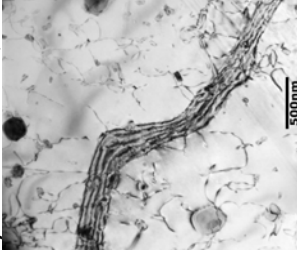
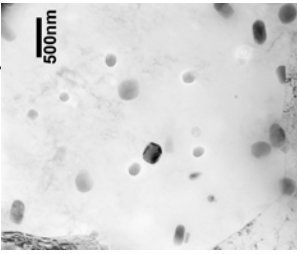
Al-Mg-Sc Joints

BM	Joint	TMAZ	SZ
<p>High density of spherical Al₃Sc ppts with size between 6-21 nm, and highest distribution between 9-15 nm.</p>  	<p>WP1.33 700 rpm, 525 mm/min</p>	<p>High density of spherical Al₃Sc ppts Highest distribution of ppts between: 6-15 nm</p> 	<p>High density of spherical Al₃Sc ppts Highest distribution of ppts between: 9-15 nm</p> 
<p>Microhardness behaviour:</p>  <p>Flat tensile behaviour [% of the BM]: WP1.33: Rp_{0.2} = 96, Rm = 95, A = 45 WP2: Rp_{0.2} = 97, Rm = 97, A = 48 WP4: Rp_{0.2} = 85, Rm = 87, A = 32</p>	<p>WP2 700 rpm, 350 mm/min</p>	<p>High density of spherical Al₃Sc ppts Highest distribution of ppts between: 9-15 nm</p> 	<p>High density of spherical Al₃Sc ppts Highest distribution of ppts between: 9-15 nm</p> 
	<p>WP4 700 rpm, 175 mm/min</p>	<p>High density of spherical Al₃Sc ppts Highest distribution of ppts between: 12-18 nm</p> 	<p>High density of spherical Al₃Sc ppts Highest distribution of ppts between: 12-18 nm</p> 

AA2024 T351 Joints

BM	Joint	TMAZ	SZ
<ul style="list-style-type: none"> • Oriented Mn-rich dispersoids (200-260nm length, 50-100 nm width) • Low density of S'' ppts with round morphology (15-20 nm diameter) • GPB zones (suggested) 	<p>WP2 800 rpm, 400 mm/min</p>	<p>Overaging (S' ppts) and GPB dissolution</p>  <p>Predominantly rod-type ppts with average size: 95 nm length 15 nm width</p>	<p>Dissolution of S'' ppts, GPB'z formation</p>  <ul style="list-style-type: none"> • Coarse round type ppt's with average size: 80 nm • Re-precipitation of GPB zones on cooling (suggested)
<p>WP4 800 rpm, 200 mm/min</p>	<p>Overaging (S' ppts) and GPB dissolution</p>  <p>Rod-type + lath-type ppts with average size: 68 nm length 28 nm width</p>	<p>Dissolution of S'' ppts, GPB'z formation</p>  <ul style="list-style-type: none"> • Dispersoids randomly dispersed • Re-precipitation of GPB zones on cooling (suggested) 	
<p>Microhardness behaviour:</p>  <p>Flat tensile behaviour [% of the BM]: WP2: Rp_{0.2} = 98, Rm = 97, A = 69 WP4: Rp_{0.2} = 95, Rm = 94, A = 48 WP8: Rp_{0.2} = 90, Rm = 88, A = 31</p>	<p>WP8 800 rpm, 100 mm/min</p>	<p>Overaging (S' ppts) and GPB dissolution</p>  <p>Predominantly lath-type ppts with average size: 94 nm length 30 nm width</p>	<p>Dissolution of S'' ppts, GPB'z formation</p>  <ul style="list-style-type: none"> • Dispersoids randomly dispersed • Re-precipitation of GPB zones on cooling (suggested)

AA6013 T6 Joints

BM	Joint	TMAZ	SZ
<p>High density of needle type β'' ppts preferentially oriented with size of: (20-70 nm length, 2-5 nm width)</p>  <p>Microhardness behaviour:</p>  <p>Flat tensile behaviour [% of the BM]: WP1.33: Rp_{0.2} = 95, Rm = 82, A = 10 WP2: Rp_{0.2} = 88, Rm = 78, A = 12 WP4: Rp_{0.2} = 82, Rm = 75, A = 10</p>	<p>WP1.33 900 rpm, 675 mm/min</p> <p>WP2 900 rpm, 450 mm/min</p> <p>WP4 900 rpm, 225 mm/min</p>	<p>Overaging, formation of β' ppts</p>  <p>Predominantly rod-type ppts with average size: 30 nm length 10 nm width</p> <p>Overaging, scarcely β' ppts</p>  <p>Predominantly lath-type ppts with average size: 94 nm length 30 nm width</p> <p>Overaging, formation of Q' ppts</p>  <p>Predominantly lath-type ppts with average size: 94 nm length 30 nm width High interparticle spacing.</p>	<p>β'' dissolution, stable Q-phase formation</p> <ul style="list-style-type: none"> • Coarse round-type ppt's (20-60 nm size). • Al-Mn-Si dispersoids randomly dispersed, over 140nm size.  <p>β'' dissolution, stable Q-phase formation</p> <ul style="list-style-type: none"> • Coarse round-type ppts (50-90 nm size) • Al-Mn-Si dispersoids randomly dispersed, over 140nm size.  <p>β'' dissolution</p> <ul style="list-style-type: none"> • Al-Mn-Si dispersoids randomly dispersed, over 140nm size. 

7. CONCLUSIONS

The metallurgical and mechanical properties of the base material and welded zones of friction stir welded Al-Mg-Sc, AA2024 T351 and AA6013 T6 alloys, joined using different energy inputs, were investigated. The results obtained from these investigations lead to the following conclusions:

1. The proposed methodology has been successfully used to explain the metallurgical transformations resulting from FSW of the different precipitation hardening Al alloys.

I. Al-Mg-Sc

2. In the Al-Mg-Sc alloy, a high distribution of Al_3Sc precipitates with spherical morphology was observed along the TMAZ, SZ and BM for all energy inputs investigated. The reduced coarsening effect in the TMAZ and SZ is attributed to the low scandium solubility in aluminium in addition to low diffusion coefficients and fast thermal cycle during FSW.

3. The temperatures attained during the FSW process of Al-Mg-Sc alloy were not sufficient to promote solute diffusion in order to produce dissolution and significant coarsening of the very stable Al_3Sc precipitates. Precipitates have been shown to control the mechanical properties and they retained a good stability level along the different weld zones for all the weld energy inputs investigated.

4. Predictions of strengthening based on the established values of volume fraction and precipitate diameter, indicate that the APB mechanism (precipitate shearing) is mainly responsible for the strengthening contribution of Al_3Sc in Al-Mg-Sc alloys friction stir welded.

5. There is a wide operating window for the production of satisfactory joints concerning the mechanical properties (tensile and hardness properties) of friction stir welded Al-Mg-Sc joints. The precipitation stability indicates that Al-Mg-Sc is a robust alloy for FSW applications, showing a wide range of process parameters to be exploited in order to produce high quality joints with the highest process efficiency.

II. AA2024 T351

6. In AA2024 T351 alloy, precipitate overaging in the TMAZ and dissolution in the SZ was observed to different degrees, depending on the energy input. The peak temperatures during FSW produced the highest deterioration of mechanical properties in the TMAZ, due to the coarsening of the original S'' (Al_2CuMg) precipitates previously present in the BM, which lose coherency with the Al matrix and their consequent strengthening effect is lost. The low amount of solute

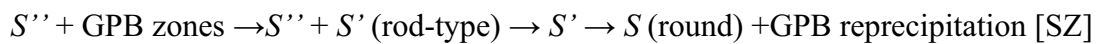
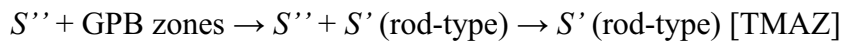
dissolved in the Al matrix is not able to produce additional natural aging in the TMAZ after FSW, resulting in inferior mechanical properties.

7. The improvement of mechanical properties in the SZ of AA2024 T351 joints was associated to re-precipitation of GPB zones during cooling, after FSW.

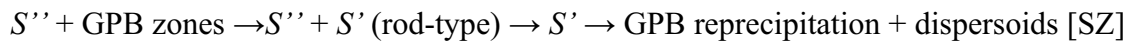
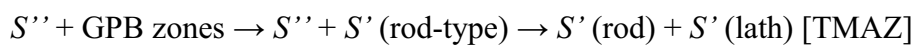
8. The joint tensile strength and hardness of AA2024 T351 alloy was optimized using low energy input (i.e. low HI), which reduces the deterioration of the mechanical properties in the TMAZ due to the lower precipitate coarsening effect and the presence of S' precipitates with a predominantly rod-type morphology.

9. The following precipitation evolution has been proposed for the TMAZ and SZ of AA2024 T351 joints:

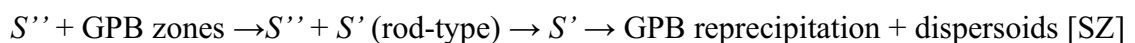
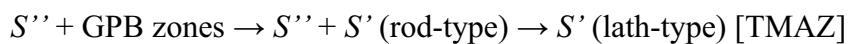
- Low HI:



- Intermediate HI:



- High HI:



III. AA6013 T6

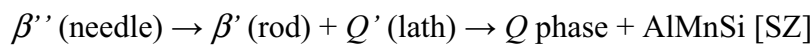
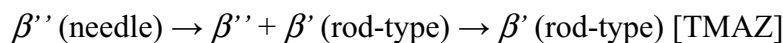
10. In AA6013 T6, the original β'' precipitates from artificial aging show low stability under FSW thermal cycles, resulting in precipitate overaging in the TMAZ, dissolution and formation of stable Q phase in the SZ. The resulting precipitation characteristics produced considerable softening of the alloy along the TMAZ and SZ for all FSW conditions.

11. The most inferior mechanical properties of the AA6013 T6 joints were observed in the TMAZ (see microhardness and microflat tensile tests) and this is attributed to the microstructural heterogeneity and the presence of coarsened precipitates. Higher peak temperatures (intermediate and high HI) form metastable quaternary Q' (lath-type) in the TMAZ. Coarsened rod-type and lath-type precipitates have no great influence on alloy strengthening.

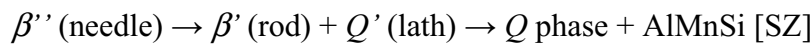
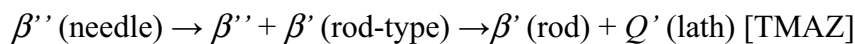
12. The window of weld parameters used in the present work significantly affected the resulting precipitation conditions and consequently the mechanical properties, mainly due to the thermal cycles generated. The performance of the AA6013 T6 joints can be improved by PWHT or using on-line cooling during FSW, to limit the dissolution and coarsening effect of the strengthening precipitates.

13. The following precipitation evolution has been proposed for the TMAZ and SZ of AA6013 T6 joints:

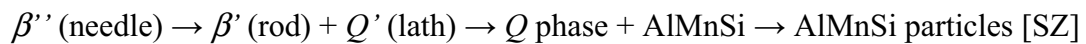
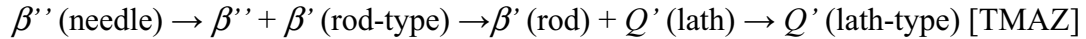
- Low HI:



- Intermediate HI:



- High HI:



14. In AA6013 T6, the effect of the peak temperature on the dissolution and coarsening of strengthening precipitates could also be minimized by process parameters, i.e. higher rotation speed and faster transverse welding speed could decrease the size of the welding zones, hence changing the heat generation and decreasing the extent of the area affected by the heat.

8. REFERENCES

- [1] Nakazato, R. Z., Codaro, E. N., Horovistiz, A. L., Hein, L. R. O., *A Metallurgical Study of Aluminium Alloys used as Aircraft Components*. Practical Metallography., v. 38, n. 2, p. 74-87, 2001.
- [2] Alfed - Aluminium Federation, <http://www.alfed.org.uk/welding>. Accessed on June 2005.
- [3] Strombeck, A. von, Santos, J. F. dos, Torste, F., Laureano, P., Koçak, M., *1st International Symposium on Friction Stir Welding*, Thousands Oaks, CA, June 1999.
- [4] Dawes, C., Thomas, W., *TWI Bulletin 6*, p. 124-27, 1995.
- [5] R. S. Mishra, Z. Y. Ma, *Friction stir welding and processing*. Materials Science and Engineering R, 50, pp. 1-78, 2005.
- [6] Olea, C.A.W., Roldo, L., dos Santos, J.F., Strohaecker, T.R. Friction Stir Welding of Precipitate Hardenable Aluminium Alloys: A Review. IIW – Welding in the World, Vol. 50, N° 11/12, p. 78-87, 2006.
- [7] Y.J. Chao, X. Qi and W. Tang, *Heat Transfer in Friction Stir Welding – Experimental and Numerical Studies*. Journal of Manufacturing Science and Engineering, V. 125, pp. 138-145, 2003.
- [8] Y.J. Chao and X. Qi, *Thermal and Thermo-Mechanical Modeling of Friction Stir Welding of Aluminium Alloy 6061-T6*. Journal of Materials Processing & Manufacturing Science, V. 7, pp. 215-233, 1998.
- [9] Kh. A.A. Hassan, A.F. Norman, D.A. Price and P.B. Prangnell, “*Stability of nugget zone grain structures in high strength Al-alloy friction stir welds during solution treatment*”. Acta Materialia, vol. 51, pp. 1923-1936, 2003.
- [10] C. Genevois, A. Deschamps, A. Denquin and B. Doisneau-cottignies, “*Quantitative investigation of precipitation and mechanical behaviour for AA2024 friction stir welds*”. Acta Materialia, vol. 53, pp. 2447-2458, 2005.
- [11] C.J. Dawes: *An Introduction to friction stir welding and its development*. Welding and Metal Fabrication, vol. 63, no.1, pp.13-14, 16, Jan. 1995.
- [12] C.J. Dawes, R. Woodward and C. Leroy, *Friction Stir Welding*. Training in Aluminium Application Technologies - TALAT Lecture 4410, TWI, 1999.
- [13] Kallee S W, Nicholas E D, Thomas W M: '*Friction stir welding - invention, innovations and applications*', INALCO 2001, 8th International Conference on Joints in Aluminium, Munich, Germany, 28-30 March 2001.
- [14] Welding & Joining Technology. TWI – The Welding Institute (accessed in 11/2006) http://www.twi.co.uk/j32k/unprotected/band_1/fswintro.html
- [15] P. Threadgill, *Friction Stir Welding in aluminium alloys – preliminary microstructural assessment*. TWI Bulletin, March-April, 1997.
- [16] K. Venkateswarlu, L.C. Pathak, A.K. Ray, G. Das, P.K. Verma, M. Kumar and R.N. Ghosh, “*Microstructure, tensile strength and wear behaviour of Al-Sc alloy*”. Materials Science and Engineering A, 383, pp. 374-380, 2004.
- [17] L.S. Toropova, D.G. Eskin, M.L. Kharakterova and T.V. Dobatkina, “*Advanced Aluminum Alloys Containing Scandium – Structure and Properties*”. Gordon and Breach Science Publishers, 1998.

- [18] **E.A. Marquis and D.N. Seidman**, “Nanoscale structural evolution of Al_3Sc precipitates in $Al(Sc)$ alloys”. *Acta Materialia*, vol. 49, pp. 1909-1919, 2001.
- [19] **G. E. Dieter (GED)**, “*Mechanical Metallurgy*,” McGraw-Hill, Inc., NY (1976).
- [20] **D.N. Seidman, E.A. Marquis and D.C. Dunand**, “Precipitation strengthening at ambient and elevated temperatures of heat-treatable $Al(Sc)$ alloys”. *Acta Materialia*, 50, pp. 4021-4035, 2002.
- [21] **Murayama M., Hono K., Miao W. F., Laughlin D. E.**, “The Effect of Cu Additions on the Precipitation Kinetics in an $Al-Mg-Si$ Alloy with Excess Si”, *Metallurgical and Materials Transactions A*, 2001, Vol. 32A, pp. 239-246.
- [22] **B. Heinz and B. Skrotzki**, “Characterization of a Friction-Stir-Welded Aluminum Alloy 6013”, *Metallurgical and Materials Transactions B*, vol 33, June 2002, 489-498.
- [23] **Engler O., Hirsch J.**, “Texture control by thermomechanical processing of AA6xxx $Al-Mg-Si$ sheet alloys for automotive applications – a review”, *Materials Science & Engineering A336*, 2002, pp. 249-262.
- [24] **Alubook** - Secretariat for Aluminium and Environment, <http://www.alu-info.dk>. Accessed on June 2004.
- [25] **M. Vivas, P. Lours, C. Levallant, A. Couret, M.J. Casanove and A. Coujou**, “Transmission Electron Microscopy Study of Precipitate Morphology and Precipitate Overcoming Process in Aluminium Alloy 6056 T6”, *Mater. Sci. Eng.A*, Volumes 234-236, 1997, 664-667.
- [26] **D.J. Chakrabarti, B-K. Cheong and D.E. Laughlin**, *Precipitation in Al-Mg-Si-Cu alloys and the role of the Q phase and its precursors*. *Automotive Alloys II*, Proc. TMS Annual Meeting in San Antonio, TX, Feb. 1998, ed. Subodh K. Das, TMS, Warrendale, pp. 27-44, 1998.
- [27] **K. Matsuda, Y. Uetani, T. Sato and S. Ikeno**: “Metastable Phases In an $Al-Mg-Si$ Alloy Containing Copper”, *Metall. Mater. Trans. A*, vol. 32A, 2001, 1293-99.
- [28] **A. Denquin, D. Allehau, M. Campagnac and G. Lapasset**: “Microstructural Evolution and Strength Mismatch within a Friction Stir Welded 6056 Aluminium Alloy”, 3rd Int. Symp. on Friction Stir Welding, Kobe, Japan, 2001.
- [29] **Miao W.F., Laughlin D.E.** “Precipitation Hardening in Aluminium Alloy 6022”, *Scripta Materialia*, Vol. 40, No. 7, pp. 873-878, 1999.
- [30] **Miao W.F., Laughlin D.E.** “Effects of Cu Content and Preaging on Precipitation Characteristics in Aluminum Alloy 6022”, *Metallurgical and Materials Transactions A*, V. 31A, Feb. 2000, pp. 361-371.
- [31] **Blanc C., Mankowski G.**, “Susceptibility to Pitting Corrosion of 6056 Aluminium Alloy”, *Corrosion Science*, 1997, Vol. 39, N° 5, pp. 949-959.
- [32] **Edwards G. A., Stiller K., Dunlop G. I., Couper M. J.**, “The Precipitation Sequence in $Al-Mg-Si$ Alloys”, *Acta mater*, 1998, Vol. 46, No. 11, pp. 3893-3904.
- [33] **Dwight J.**, “*Aluminium Design and Construction*”, Edited by E & FN SPON, London and New York, 1999, pp. 63-68.
- [34] **ASM Handbook**: “*Heat Treating*”, 1991, Vol. 4, pp. 489-498 and 845-865.

- [35] **Sato Y. S., Kokawa H., Enomoto M., Jogan S.**, “*Microstructural Evolution of 6063 Aluminum during Friction-Stir Welding*”, Metallurgical and Materials Transactions A, Vol. 30A, pp. 2429-2437, 1999.
- [36] **J.-Q. Su, T. W. Nelson, R. Mishra and M. Mahoney**, *Microstructural investigation of friction stir welded 7050-T651 aluminium*. Acta Materialia, 51, 713-729, 2003.
- [37] **Scialpi, A., De Filippis, L.A.C., Cavaliere, P.**, *Influence of shoulder geometry on microstructure and mechanical properties of friction stir welded 6082 aluminium alloy*, Materials and Design, Vol. 28, pp. 1124-1129, 2006.
- [38] **Fujii, H., Cui, L., Maeda, M., Nogi, K.**, *Effect of tool shape on mechanical properties and microstructure of friction stir welded aluminium alloys*. Materials Science and Engineering A, 419, p. 25–31, 2006.
- [39] **Murr L. E., Liu G., McClure J. C.**, “*Dynamic Recrystallization in Friction-Stir Welding of Aluminium Alloy 1100*”, Journal of Materials Science Letters 16, pp. 1801-1803, 1997.
- [40] **Humphreys, F. J., Harthely, M.**, *Recrystallization and Related Annealing Phenomena*, 2nd Edition, Elsevier, UK, 2004.
- [41] **Liu G., Murr L.E., Niou C-S., McClure J. C., Vega F. R.** “*Microstructural Aspects of the Friction-Stir Welding of 6061- T6 Aluminum*”, Scripta Materialia, 1997, Vol. 37, N^o 3, pp. 355-361.
- [42] **Lienert, T. J., Grylls, R. J.**, *CRP - Coop. Res. Program summary report SR0018*, EWI WeldNet, 2000.
- [43] **C.A.W. Olea, L. Roldo, J.F. dos Santos and T.R. Strohaecker**, *A sub-structural analysis of friction stir welded joints in an AA6056 Al-alloy in T4 and T6 temper conditions*. Materials Science and Engineering A, 454-455, pp. 52-62, 2007.
- [44] **Chao Y. J., Qi X.**, “*Heat Transfer and Thermo-Mechanical Analysis of Friction Stir Joining of AA6061-T6 Plates*”, 1st International Symposium on Friction Stir Welding – Proceedings, USA, 1999.
- [45] **P. Ratchev, B. Verlinden, P. De Smet and P. Van Houtte**, *Precipitation hardening of an Al-2.2wt% Mg-0.6wt% Cu alloy*. Acta Materialia, vol. 46, No. 10, pp. 3523-3533, 1998.
- [46] **L. Kovarik, P.I. Gouma, C. Kisielowski, A.A. Court and M.J. Mills**, *A HRTEM study of metastable phase formation in Al-Mg-Cu alloys during artificial aging*. Acta Materialia, 52, pp. 2509-2520, 2004.
- [47] **S. P. Ringer, T. Sakurai, I. J. Polmear**, *Origins of hardening in aged Al-Cu-Mg-(Ag) alloys*. Acta Mater., 45, pp. 3731-3744, 1997.
- [48] **Ying Li, Murr L. E., McClure J. C.**, “*Solid-State Flow Visualization in the Friction- Stir Welding of 2024 Al to 6061 Al*”, Scripta Materialia, 1999, Vol. 40, N^o 9, pp. 1041-1046.
- [49] **Benavides S., Li Y., Murr L. E., Brown D., McClure J. C.**, “*Low-Temperature Friction-Stir Welding of 2024 Aluminum*”, Scripta Materialia, 1999, Vol. 41, N^o 8, pp. 809-815.
- [50] **Chen, Y., Liu, H., Feng, J.**, *Friction stir welding characteristics of different heat-treated-state 2219 aluminium alloy plates*. Materials Science and Engineering A, 420, p. 21–25, 2006.
- [51] **A.K. Shukla and W.A. Baeslack III**, *Process-Property Relationships and Microstructure evolution in Friction Stir Welded Thin Sheet 2024-T3 Aluminium Alloy*. 7th International Conference on Trends in Welding Research, Georgia-USA, pp. 16-20, 2005.

- [52] Jones, M. J., Heurtier., P., Desrayaud, C., Montheillet, F., Allehauux, D., Driver, J. H., *Correlation between microstructure and microhardness in a friction stir welded 2024 aluminium alloy*. Scripta Materialia, v. 52, p. 693-697, 2005.
- [53] C. Genevois, A. Deschamps, A. Denquin, B. Doisneau-Cottignies, *Quantitative investigation of precipitation and mechanical behaviour for AA2024 friction stir welds*. Acta Materialia, v. 53, 2447-2458, 2005.
- [54] Genevois, C., Deschamps, A., Vacher, P., *Comparative study on local and global mechanical properties of 2024 T351, 2024 T6 and 5251 O friction stir welds*. Materials Science and Engineering A, 415, 162–170, 2006.
- [55] A.K. Shukla and W.A. Baeslack III, *Effect of process conditions on microstructure evolution and mechanical properties of friction stir welded thin sheet 2024-T3*. 6th International Symposium on Friction Stir Welding, Montreal-Canada, October, 2006.
- [56] L.-E. Svensson, L. Karlsson, H. Larsson, B. Karlsson, M. Fazzini, J. Karlsson., *Microstructure and mechanical properties of friction stir welded aluminium alloys with special reference to AA5083 and AA6082*. Science and Technology of Welding and Joining, V. 5, No. 5, pp. 285-296, 2000.
- [57] Reynolds A.P., Tang W., “*Alloy, tool geometry, and process parameter effect on friction stir weld energies and resultant FSW joint properties*”, TMS, Indianapolis Indiana, Nov., pp. 15-23., 2001.
- [58] ASTM 384-99 “*Standard Test Method for Microindentation Hardness Materials*”, Annual Book of ASTM Standards Vol 03.03 (ASTM, Philadelphia, 2000), pp. 406-429.
- [59] DIN EN 895 “*Destructive Tests on Welds in Metallic Materials – Transverse Tensile Test*” (CEN – European Committee for Standardization), Brussels, pp. 199-205, 1995.
- [60] Von E. Klausnitzer, “*Entwicklung eines Verfahrens zur Entnahme und Prüfung von Mikro-Flachzugproben aus der Wärmeeinflußzone von Schweißverbindungen*“, Materialprüf. 18, N° 11, pp. 411-416, November, 1976.
- [61] ASTM E 3-95 “*Standard Practice for Preparation of Metallographic Specimens*”, Annual Book of ASTM Standards Vol. 03.03, (ASTM, Philadelphia, 2000, pp. 1-8.
- [62] ASTM E 340-95 “*Standard Test Method for Macroetching Metals and Alloys*”, Annual Book of ASTM Standards Vol. 03.03, (ASTM, Philadelphia, 2000, pp. 385-395.
- [63] Edington J. W., “*Practical Electron Microscopy in Materials Science*”, Techbooks, 1991.
- [64] Leica QWin User Guide – *Image Processing and Analysis System*, vols. 1 and 2. Leica Imaging Systems Ltda., 1996.
- [65] K. Yu, W. Li, S. Li and J. Zhao, “*Mechanical properties and microstructure of aluminium alloy 2618 with Al₃(Sc, Zr) phases*”. Materials Science and Engineering A, 368, pp. 88-93, 2004.
- [66] K.T. Park, D.Y. Hwang, Y.K. Lee, Y.K. Kim and D.H. Shin, “*High strain rate superplasticity of submicrometer grained 5083 Al alloy containing scandium fabricated by severe plastic deformation*”. Materials Science and Engineering A, 341, pp. 273-281, 2003.
- [67] ENFASIS – **Final Report**. GKSS confidential document, W/FT/015.03.
- [68] ASM Handbook: “*Fatigue and Fracture*”, Vol. 19, pp. 489-498 and 371-392, 1996.
- [69] Yu.A. Filatov, V.I Yelagin, V.V. Zakharov, “*New Al-Mg-Sc alloys*”, Materials Science and Engineering A, 280, pp. 97-101, 2000.

- [70] **S. Lathabai, P.G. Lloyd**, “*The effect of scandium on the microstructure, mechanical properties and weldability of a cast Al-Mg alloy*”. *Acta Materialia*, 50, pp. 4275-4292, 2002.
- [71] **H.G. Paris, T. H. Sanders Jr., Y. W. Riddle**, “*Assesment of Scandium Additions in Aluminium Alloy Design*”. *Proceedings of ICAA-6*, Vol. 1, pp. 499-504, 1998.
- [72] **T. D. Rostova, V.G. Davydov, V. I. Yelagin and V. V Zakharov**, “*Effect of Scandium on Recrystallization of Aluminum and its Alloys*”. *Materials Science Forum*, Vols. 331-337, pp. 793-798, 2000.
- [73] **V.G. Davydov, T. D. Rostova, V. V Zakharov, Yu. A. Filatov and V. I. Yelagin**, “*Scientific principles of making an alloying addition of scandium to aluminium alloys*”. *Materials Science and Engineering A*, 280, pp. 30-36, 2000.
- [74] **Y. W. Riddle and T. H. Sanders Jr.**, “*Recrystallization Performance of AA7050 Varied with Sc and Zr*”. *Materials Science Forum*, Vols. 331-337, pp. 799-804, 2000.
- [75] **Ø. Frigaard, Ø. Grong, J. Hjelen, S. Gulbrandsen-Dahl and O.T. Midling**, “*Characterization of subgrain structure in FSW Al alloys using SEM-EBSD technique*”. 1st International FSW Symposium, oct., 1999.vol. 30, pp. 2429-2437, 1999.
- [76] **N. Blake, M. A. Hopkins**, “*Constitution and age hardening of Al-Sc alloys*”. *Journal of Materials Science*, 20, pp. 2861-2867, 1985.
- [77] **Yu.V. Milman, D.V. Lotsko and O.I. Sirko**, “*Sc Effect of Improving Mechanical Properties in Aluminium Alloys*” *Materials Science Forum*, vols. 331-337, pp. 1107-1112, Switzerland 2000.
- [78] **B. Lenczowski, T. Hack, D. Wieser, G. Tempus, G. Fischer, J. Becker, K. Folkers, R. Braun and G. Lütjering**, “*AlMgSc Alloys for Transportation Technology*”. *Materials Science Forum*, vols. 331-337, pp. 957-964, 2000.
- [79] **Z. Yin, Q. Pan, Y. Zahng and F. Jiang**, “*Effect of minor Sc and Zr on the microstructure and mechanical properties of Al-Mg based alloys*”. *Materials Science and Engineering*, A280, pp. 151-155, 2000.
- [80] **K.L. Kendig and D.B. Miracle**, “*Strengthening mechanisms of an Al-Mg-Sc-Zr alloy*”. *Acta Materialia*, 50, pp. 4165-4175, 2002.
- [81] **B. Huneau, X. Sauvage, S. Marya and A. Poitou**, “*Microstructure evolution during friction stir welding of commercial aluminium alloys*”. *FSW and Processing III - TMS*, pp. 253-260, 2005.
- [82] **M.J. Jones, P. Heurtier, C. Desrayaud, F. Montheillet, D. Allehaux and J.H. Driver**, “*Correlation between microstructure and microhardness in a friction stir welded 2024 aluminium alloy*”. *Scripta Materialia*, 52, pp. 693-697, 2005.
- [83] **Porter D. A., Easterling K.E.** “*Phase Transformations in Metals and Alloys*”, Van Nostrand Reinhold, 1981.
- [84] **L. E. Murr, G. Liu and J. C. McClure**, “*A TEM study of precipitation and related microstructures in friction-stir-welded 6061 aluminium*”. *Journal of Materials Science*, 33, pp. 1243-1251, 1998.
- [85] **Heinz B., Skrotzki B.** “*Characterization of a Friction-Stir-Welded Aluminum Alloy 6013*”, *Metallurgical and Materials Transactions B*, V. 33B, pp. 489-498, June, 2002.

- [86] **Laughlin D.E., Miao W.F.** “*The Effects of Cu and Mn Content and Processing on Precipitation Hardening Behaviour in Al-Mg-Si-Cu Alloy 6022*”, <http://neon.mems.cmu.edu/Laughlin/paper5/p5-1.html>. June 2002.
- [87] **D.J. Chakrabarti and D.E. Laughlin**, *Phase relations and Precipitation in Al-Mg-Si alloys with Cu additions*. Progress in Materials Science 49, pp. 389-410, 2004.
- [88] **F. Delmas, M.J. Casanove, P. Lours, A. Couret, A. Coujou.** *Quantitative TEM study of the precipitation microstructure in aluminium alloy Al(MgSiCu) 6056 T6*. Materials Science and Engineering A, 373, pp. 80-89, 2004.
- [89] **Miao W.F., Laughlin D.E.** *Precipitation hardening in aluminum alloy 6022*. Scripta Materialia, 40, pp. 873-878, Feb., 1999.
- [90] **C.S. Paglia, K.V. Jata and R.G. Buchheit**, *A cast 7050 FSW with scandium: microstructure, corrosion and environmental assisted cracking*. Materials Science and Engineering A, 2006 (doi: 10.1016/j.msea.2006.03.065).

LIST OF FIGURES

Figure 2-1 – Friction stir welding principle.	5
Figure 2-2 – Yield-strength variation along the different FSW zones [8].	7
Figure 2-3 – Schematics of the heat distribution along the interface tool shoulder and workpiece adapted from [8].	8
Figure 2-4- Surface aspect of the FSW joint in Al 6xxx series alloy, macrograph of the weld transversal section and microhardness profile typicals, respectively from top to bottom.	10
Figure 2-5 – Micrographs showing the interface TMAZ/SZ of 2024 T351 alloy joint in detail. (a) Advancing side and (b) retreating side.	11
Figure 2-6 – Al-Mg-Sc system from Al - 17% Mg to Al - 1% Sc [adapted from 17].	12
Figure 2-7 – Effect of scandium addition on recrystallization temperatures [17]	13
Figure 2-8 – Orowan’s mechanism of dispersion hardening [19].	14
Figure 2-9 – Schematic illustration of the precipitation sequence during FSW [35].	20
Figure 2-10 – Scheme of the GPB zones morphology and crystal structure (adapted from [46]).	22
Figure 2-11 – Crystal structure of the GPB-II zones [46].	22
Figure 3-1 - Flow chart describing the overall work program.	27
Figure 3-2 - Neos Tricept 805 Robot system used to produce the joints by FSW, with the ability to perform welds of up to 45kN axial load.	30
Figure 3-3 – FSW tool used to produce the joints. (a) Concave shoulder and (b) threaded 3 flats pin, shown separately.	30
Figure 3-4 – Correlation between WP and calculated energy input considering the FSW parameters used to join Al-Mg-Sc, AA2024 T351 and AA6013 T6 alloys.	32
Figure 3-5 – Scheme of the FSW joint in (a) and top surface macrograph in (b) showing the position of the thermocouples for the temperature measurements in the workpiece.	32
Figure 3-6 – Schematics of the the temperature measurements in the backing bar showing the location of the thermocouples (distance in mm). (a) Assembly of backing bar and weld plates, (b) backing bar, (c) top view and (d) side view.	33
Figure 3-7 – Geometry of the flat tensile specimens used to evaluate the tensile properties of the FSW joints and base material (dimensions in mm).	35
Figure 3-8 - Schematic illustration of the microflat specimens obtained. Weld joint representation with the specimen’s disposition along the weld joint, indicating the corresponding weld zone and base material.	36

Figure 3-9 – Geometry of the microflat tensile specimens used to investigate the local tensile properties for the FSW process (dimensions in mm) (a), and scheme of the clamping system (b).36

Figure 3-10 – Schematic illustration of the friction stir welded plate and the disposition of TEM specimens obtained from the microflat tensile specimens, located in different weld zones and base material.39

Figure 3-11 - Schematic illustration of the TEM sample extraction from a microflat tensile specimen and its electropolishing.39

Figure 3-12 – Illustration of the measurements performed on TEM images using Leica QWin software. (a) Determination of precipitate average size and population, (b) grain area.40

Figure 4-1 - Thermal cycles obtained close to the SZ during FSW of Al-Mg-Sc joints, produced applying WP1.33, WP2 and WP4. Average thermal cycles measured from thermocouples fixed in the backing bar.43

Figure 4-2 - Thermal cycles obtained close to the HAZ/TMAZ during FSW of Al-Mg-Sc joints, produced applying WP1.33, WP2 and WP4. Average thermal cycles measured from thermocouples fixed in the workpiece.43

Figure 4-3 – Microhardness profile obtained in the mid thickness of the transverse section, across the BM and FSW zones of the Al-Mg-Sc joint, for the three energy inputs investigated.45

Figure 4-4 – Tensile behaviour of the Al-Mg-Sc FSW joints using energy inputs WP4, WP2 and WP1.33, in association with results from the BM.....47

Figure 4-5 – Macrographs of the rupture location for the different parameter conditions: (a) low HI - WP1.33, (b) intermediate HI - WP2 and (c) high HI - WP4.47

Figure 4-6 – Yield strength profiles from microflat tensile testing across the BM and FSW zones of the WP1.33 (low HI), WP2 (intermediate HI) and WP4 (high HI) parameters.....49

Figure 4-7 – Tensile strength profiles from microflat tensile testing across the BM and FSW zones of the WP1.33 (low HI), WP2 (intermediate HI) and WP4 (high HI) parameters.50

Figure 4-8 - Elongation profiles from microflat tensile testing across the BM and FSW zones of the WP1.33 (low HI), WP2 (intermediate HI) and WP4 (high HI) parameters.50

Figure 4-9 – Microflat tensile behaviour of the Al-Mg-Sc alloy BM in comparisson with transverse flat tensile behaviour from BM.51

Figure 4-10 - Transversal section overview of the weld seam of the Al-Mg-Sc FSW joint by optical microscopy. (a) Detail of the microstructure interface, delimiting SZ and TMAZ/HAZ regions and in (b) the microstructure of the HAZ/BM.53

Figure 4-11 - SEM micrographs of the transversal sections of the Al-Mg-Sc FSW joints, showing equiaxed grains in the SZ of conditions: (a) high HI - WP4, (b) intermediate HI-WP2, (c) low HI - WP1.33 and (d) representing distorted microstructure from the TMAZ.....	55
Figure 4-12 - Bright-field TEM micrographs of the grain structure present in the base material and different FSW regions of Al-Mg-Sc alloy. (a) BM, (b) TMAZ and (c) SZ.	57
Figure 4-13 - Bright-field micrographs from Al-Mg-Sc alloy, showing typical dislocation features in (a) BM in $[\bar{1}11]_{Al}$ ($g = 202$), (b) TMAZ in $[001]_{Al}$ ($g = 200$) and (c) SZ close to $[011]_{Al}$ zone axis.....	59
Figure 4-14 - Bright field micrographs of Al-Mg-Sc alloy showing particular substructural aspects. (a) Parallel bands in BM pancake grain, and (b) initial stages of sub-grain formation in TMAZ of WP4 condition.	60
Figure 4-15 - TEM analysis presenting precipitate features in the BM. (a) Micrograph showing precipitates appearance and distribution along pancake grains. (b) SADP in $[001]_{Al}$ zone axis. (c) EDS peaks from precipitates presented in the micrograph.	61
Figure 4-16 - TEM analysis presenting precipitate features in the SZ. (a) Micrograph showing precipitate characteristics and interactions with dislocations in equiaxed grain. (b) SADP in $[011]_{Al}$ zone axis. (c) EDS peaks from precipitates presented in the micrograph.	63
Figure 4-17– Orowan’s mechanism occurring in TMAZ of hot parameter (WP4 joint), in $[011]_{Al}$ zone axis, $g = 200$	64
Figure 4-18 - TEM bright-field micrographs, representing Al_3Sc precipitates in different FSW zones and BM indicated in the macrograph of a Al-Mg-Sc joint. (a) BM, (b) TMAZ and (c) SZ.	65
Figure 4-19 - Precipitate (Ppt) size and distribution of the Al-Mg-Sc FSW joints using three different input parameters (high HI - WP4, intermediate HI - WP2 and low HI - WP1.33) along TMAZ, SZ and BM.	68
Figure 4-20 – Correlation between precipitation stability and thermal cycles obtained in (a) SZ and (b) TMAZ of Al-Mg-Sc joints.....	69
Figure 4-21 – APB and Orowan strengthening mechanisms due to resistance to dislocation movement, predicted for 1.5, 2.5 and 3.5% volume fraction [80].	71
Figure 4-22 - Thermal cycles obtained close to the SZ during FSW of AA2024 T351 joints produced applying WP2, WP4 and WP8. Average thermal cycles measured from thermocouples fixed in the backing bar.	74

Figure 4-23 - Thermal cycles obtained close to the HAZ/TMAZ during FSW of AA2024 T351 joints produced applying WP2, WP4 and WP8. Average thermal cycles measured from thermocouples fixed in the workpiece.75

Figure 4-24 - Microhardness profiles obtained in the mid thickness of the transverse section, across the BM and FSW zones of the AA2024-T351 joint for the three energy inputs investigated.....77

Figure 4-25 – Tensile behaviour of the AA2024 T351 FSW joints, using energy inputs WP2, WP4 and WP8 in association with results from the BM.....79

Figure 4-26 - Macrographs of the rupture location for the different parameter conditions: (a) low HI - WP2, (b) intermediate HI - WP4 and (c) high HI - WP8.79

Figure 4-27 – Yield strength profiles from microflat tensile testing across the BM and FSW zones of the WP2 (low HI), WP4 (intermediate HI) and WP8 (high HI) parameters.....81

Figure 4-28 – Tensile strength profiles from microflat tensile testing across the BM and FSW zones of the WP2 (low HI), WP4 (intermediate HI) and WP8 (high HI) parameters.81

Figure 4-29 - Elongation profiles from microflat tensile testing across the BM and FSW zones of the WP2 (low HI), WP4 (intermediate HI) and WP8 (high HI) parameters.....82

Figure 4-30 - Microflat tensile behaviour of the AA2024 T351 alloy BM in comparison with transverse flat tensile behaviour from BM.....83

Figure 4-31 - Transversal section overview of the weld seam of the AA2024 T351 FSW joint by optical microscopy. (a) Detail of the microstructure interface delimiting SZ and TMAZ/HAZ in the advancing side and in (b) the retreating side.85

Figure 4-32 - SEM micrographs of the transversal sections of the AA2024 T351 FSW joints, showing equiaxed grains in the SZ of conditions: (a) WP8, (b) WP4, (c) WP2 and (d) representing distorted microstructure from TMAZ (WP2).87

Figure 4-33 – Precipitation in the base material of AA2024-T351 alloy. (a) Nearly oriented dispersoids, (b) S phase thin strengthening precipitates with respectives (c) EDS peaks of dispersoids and (d) EDS peaks of small S phase precipitates.89

Figure 4-34 – Precipitation in the SZ of FSW AA2024-T351 joints. (a) and (b) are coarse round particles and round type precipitates with coherency contrast in the equiaxed grains (WP2); (c) and (d) are dispersoids with different morphologies, randomly distributed in intermediate HI (WP4) and high HI (WP8) conditions, respectively.91

Figure 4-35 – Precipitation in the TMAZ of FSW AA2024-T351 joints. (a) Low HI WP2; (b) and (c) Intermediate HI WP4 and (d) high HI WP8.93

Figure 4-36 – Particular precipitation feature in TMAZ. (a) Bright field micrograph of heterogeneous nucleation sites for S' precipitates and (b) SADP showing the respective precipitate reflections in $[011]_{Al}$ zone axis.....	94
Figure 4-37 – PFZ and precipitate coarsening along the grain boundaries of TMAZ in (a) intermediate HI WP4 and (b) high HI WP8 of the AA2024-T351 joints.	95
Figure 4-38 – Correlation between precipitation stability and thermal cycles obtained in (a) SZ and (b) TMAZ of AA2024 T351 joints.....	97
Figure 4-39 - Thermal cycles obtained close to the SZ during FSW of AA6013 T6 joints produced applying WP1.33, WP2 and WP4. Average thermal cycles measured from thermocouples fixed in the backing bar.	99
Figure 4-40 - Thermal cycles obtained close to the HAZ/TMAZ during FSW of AA6013 T6 joints produced applying WP1.33, WP2 and WP4. Average thermal cycles measured from thermocouples fixed in the workpiece.	99
Figure 4-41 - Microhardness profile obtained in the mid thickness across the base material and welded zones of the AA6013-T6 joint for all the welding parameters investigated.....	102
Figure 4-42 – Tensile behaviour of the AA6013 T6 FSW joints for energy inputs WP1.33, WP2 and WP4 in association with results from the base material.....	105
Figure 4-43 - Macrographs of the rupture location for the different parameter conditions: (a) cold WP1.33, (b) intermediate WP2 and (c) hot WP4.....	105
Figure 4-44 – Yield strength profiles from microflat tensile testing across the BM and FSW zones of the WP1.33 (low HI), WP2 (intermediate HI) and WP4 (high HI) joints.	107
Figure 4-45 – Tensile strength profiles from microflat tensile testing across the BM and FSW zones of the WP1.33 (low HI), WP2 (intermediate HI) and WP4 (high HI) joints.	108
Figure 4-46 - Elongation profiles from microflat tensile testing across the BM and FSW zones of the WP1.33 (low HI), WP2 (intermediate HI) and WP4 (high HI) joints.....	108
Figure 4-47 - Overview of the transverse section of the AA6013 T6 FSW joint by optical microscopy. (a) HAZ/TMAZ/SZ interface on the advancing side, (b) retreating side, (c) detail of the grain structure in TMAZ/SZ , and (d) SZ.	110
Figure 4-48 - SEM micrographs of the transverse sections of the AA6013 T6 FSW joints, showing equiaxed grains in the stir zone of conditions: (a) WP4, (b) WP2, (c) WP1.33 and (d) representing the interface between SZ and TMAZ.	112
Figure 4-49 – Precipitation in AA6013-T6 alloy (BM). (a) and (b) Needle-type precipitates (β'') Preferentially oriented in a Widmanstätten structure, (c) SADP along the $[011]_{Al}$ zone axis.	114

Figure 4-50 - Precipitation in the SZ of FSW AA6013-T6 joints. (a) High HI (WP4) and (b) EDS analysis of dispersoid; (c) Intermediate HI (WP2) close to $[112]_{Al}$ and (d) respective SADP; (e) low HI (WP1.33) in $[011]_{Al}$ and (f) respective SADP.117

Figure 4-51 – Precipitation of Q-phase in the SZ of FSW AA6013-T6 joint. (a) BF micrograph of the precipitates; (b) EDS analysis indicating Cu peaks.....118

Figure 4-52 - Precipitation in the TMAZ of FSW AA6013-T6 joints. (a) high HI (WP4) and (b) SADP along $[001]_{Al}$ zone axis; (c) Intermediate HI (WP2) in $[011]_{Al}$ zone axis and (d) respective SADP; (e) low HI (WP1.33) in $[001]_{Al}$ zone axis and (f) respective SADP.121

Figure 4-53 – Precipitation of Q-phase in the TMAZ of FSW AA6013-T6 joint. (a) bright field micrograph of the precipitates; (c) EDS analysis, indicating Cu peaks.122

Figure 4-54 - PFZ and precipitate coarsening along the grain boundaries of TMAZ in high HI (WP4) of the AA6013-T6 joints in (a) and (b) at slightly higher magnification.123

Figure 4-55 – Correlation between precipitation evolution and thermal cycles obtained in (a) SZ and (b) TMAZ of AA6013 T6 joints.....124

LIST OF TABLES

Table 2-1 - Al ₃ Sc precipitate features and recrystallization temperature (t_r^s) [17].	14
Table 2-2 – Effect of scandium on Tensile properties of annealed Al-Mg alloy [17].	15
Table 3-1- Chemical composition of the aluminium alloys base material [(%) weight]	29
Table 3-2 – Terminology and FSW parameters employed.	31
Table 4-1 – Thermal history of Al-Mg-Sc FSW joints using WP1.33, WP2 and WP4, low intermediate and high HI, respectively.	42
Table 4-2 – Tensile test results of Al-Mg-Sc FSW joints WP4, WP2 and WP1.33 followed by a comparison with the results from BM.	46
Table 4-3 – Thermal history of AA2024 T351 FSW joints using WP2, WP4 and WP8, low HI, intermediate HI and high HI, respectively.	73
Table 4-4 – Tensile test results of AA2024 T351 weld joints WP 8, 4 and 2 followed of comparison with results from base material.	78
Table 4-5 – Thermal history of AA6013 T6 FSW joints using WP1.33, WP2 and WP4, low HI, intermediate HI and high HI, respectively.	98
Table 4-6 – Tensile test results of AA6013 T6 weld joints WP1.33, WP2 and WP4 followed of comparison with results from BM.	103

LIST OF SYMBOLS AND ABBREVIATIONS

S''	Strengthening metastable Al_2MgCu precipitate
S'	Metastable Al_2MgCu precipitate
S	Stable Al_2MgCu precipitate
β''	Strengthening metastable Mg_2Si precipitate
β'	Metastable Mg_2Si precipitate
β	Stable Mg_2Si precipitate
Q'	Metastable quaternary (Al-Mg-Si-Cu) precipitate
Q	Stable quaternary (Al-Mg-Si-Cu) precipitate
$q(r)$	Heat Input (Watt/m ²)
r_0	Radius of the Shoulder
r_i	Radius of the Pin
r	Radius
Q_T	Total Rate of Heat Input to the Workpiece
F	Force
ω	Tool Rotation Speed (rpm)
μ	Frictional Coefficient
a, b and c	Lattice Parameters
t_r^s	Recrystallization Temperature
f	Volume Fraction of Precipitates
L	Interparticle Spacing
$\sigma_{0.2}^T$	Yield Strength of an Al-Mg-Sc
$\sigma_{0.2}^B$	Yield Strength of a binary Al-Mg alloy
$\Delta\sigma_{0.2}$	Increment of Yield Strength due to Sc addition
Rm	Tensile Strength
Rp _{0.2}	Yield Strength
A	Elongation
$\sigma_{0.2}^0$	Yield Strength of an Al-Mg Single Crystal
$\sigma_{0.2}'$	Strengthening Contribution due to Dislocation Density
$\sigma_{0.2}''$	Strengthening Contribution due to the Precipitates
$\sigma_{0.2}^{calc}$	Yield Strength of a Deformed Alloy (analytically determined)

σ_i	Stress required to move the dislocation inside the grain
D	Grain Size
K	Ability of plastic deformation to be transferred between grains
B	Burgers Vector
Ω	Al ₂ Cu Dispersoids
SSS	Solubilized Solid Solution
α	Aluminium CFC phase
T_M	Melting Temperature
FSW	Friction Stir Welding
PWHT	Post Weld Heat Treatment
HAZ	Heat Affected Zone
TMAZ	Thermomechanical Affected Zone
SZ	Stir Zone
BM	Base Material
GP	Guinier Preston
GPB	Guinier Preston Bagariastkij
HI	Heat Input
OM	Optical Microscopy
SEM	Scanning Electron Microscopy
TEM	Transmission Electron Microscopy
STEM	Scanning Transmission Electron Microscope
HRTEM	High Resolution Transmission Electron Microscopy
EDS	Energy Dispersive Spectrometer
BSE	Back Scattered Electrons
DSC	Differential scanning calorimetry
SADP	Selected Area Diffraction Pattern
SAED	Selected Area Electron Diffraction
WP	Weld Pitch
SFC	Strain Field Contrast
APB	Anti-phase Boundary
PFZ	Precipitate Free Zone
BF	Bright-Field
ppts	Precipitates